

Université du Québec  
Institut National de la Recherche Scientifique  
Centre Energie, Matériaux et Télécommunications

**INVESTIGATIONS ON PHOTOVOLTAIC EFFICIENCY, STABILITY,  
AND MECHANISM OF ORGANIC SOLAR CELLS**

Par  
Pandeng Li

Thèse présentée pour l'obtention du grade de  
Philosophiae doctor (Ph.D.)  
en sciences de l'énergie et des matériaux

**Jury d'évaluation**

Président du jury et examinateur interne	Ana Tavares INRS-EMT
Examinateur externe	Changqi Ma CAS-SINANO
Examinateur externe	Giovanni Fanchini Western University
Directeur de recherche	Dongling Ma INRS-EMT
Codirecteur de recherche	Baoquan Sun Soochow University-FUNSOM

## ACKNOWLEDGEMENTS

Foremost I would like to show my deep gratitude to my supervisor Prof. Dongling Ma for admitting me into her research group and offering me a precious opportunity to pursue my PhD degree in INRS-EMT. She provides a warm and opening research atmosphere for us and it is my very honor to work with her. I also would like to communicate with her, in the useful discussions of my whole PhD stages, her constructive advices and immense knowledge largely contributed to the achievements in my research work. I am extremely grateful for her dedicated guidance on my research work and writing of research papers. More importantly, her stringent careful attitude toward academic research has greatly influenced and motivated me to be a better researcher.

Meanwhile, I would like to give my sincere acknowledgment to my co-supervisor Prof. Baoquan Sun. When I joined his research group through the program between INRS and FUNSOM of Soochow University, I am infected by the good research atmosphere of the group which is the solidarity and friendly family (Sun family). It is my pleasure to work with him in the warm family, and I have benefited a lot from his professional guidance on the choice of the research project, the methods of solving problems, and the scientific way of thinking. In addition, his positive and optimistic attitude towards life also influences me. I believe what I have learned in Prof. Sun's research group will continue to support me in my future career.

Additionally, I am enormously grateful to Prof. Ricardo Izquierdo for kindly allowing me to work in his laboratory. I am also thankful for Prof. Mario Leclerc and Prof. Maojie Zhang who provides related photovoltaic materials for my research work.

It is my pleasure to thank the contributions to my projects made by my collaborators, Dr. Yuliang Zhang, Dr. Yusheng Wang, and Dr. Jin Fang during my Ph.D. study. I learned a lot from them with respect to scientific research and handling troubles in my daily life. In addition, I want to give my thanks to Prof. Tao Song for his invaluable help and comments on my research. I would like to thank Jean-Philippe Masse at Ecole Polytechnique and Dr. Yingguo Yang at Shanghai Synchrotron Radiation Facility for carrying out the related measurements, respectively.

I would like to thank the group members in Prof. Ma's group for their help. These people include Dr. Tong Tan, Dr. Qingzhe Zhang, Dr. Deepak Thrithamarassery Gangadharan, Shengyun Huang, Ting Yu, Yong Wang, Wanting He. I am grateful to be part of this group.

I am also grateful to all the group members in Prof. Sun's group for their help. These people include Dr. Yajuan Li, Dr. Yatao Zou, Haihua Wu, Lei Cai, Beibei Shao, Guohua Zhang, Ya Li, Xuechun Wang, Qingyao Zhang, Dong Liang, Jiaqing Zang, Guilin Bai, Zhiwei Hong, Yanfei Wu, and Chang Shu. They altogether created a hardworking and inspiring group.

Lastly, I am eternally grateful to my parents, for their constant support and encouragement throughout all of my studies. I would like to thank my dear wife, Lijuan Jin, who loves me deeply and supports me selflessly.

## RÉSUMÉ

### **Enquêtes sur l'efficacité photovoltaïque, la stabilité et le mécanisme des cellules solaires organiques**

L'utilisation actuelle de l'énergie repose principalement sur des combustibles fossiles non renouvelables et polluants, ce qui entraîne des conséquences non durables sur les plans sociétal, économique, géopolitique et environnemental. L'exploitation de l'énergie solaire est l'une des sources d'énergie renouvelable les plus prometteuses pour répondre à la demande énergétique mondiale, qui ne cesse de croître. Les cellules solaires, qui convertissent directement l'énergie solaire en électricité par l'effet photovoltaïque (PV), ont été considérées comme l'une des technologies les plus propres et les plus prometteuses pour résoudre les problèmes énergétiques actuels. Depuis que la première cellule solaire au silicium d'une efficacité de 6 % a été réalisée avec succès par le Bell Lab en 1954, l'efficacité des cellules solaires n'a cessé d'être améliorée et différents types de cellules solaires ont été explorés. Aujourd'hui, les diverses cellules solaires inorganiques basées sur le silicium cristallin, le tellurure de cadmium ou le sélénium de cuivre, d'indium et de germanium (CIGS) ont obtenu un rendement de conversion de puissance élevé (PCE) d'environ 15 à 27 % et occupent la plupart des technologies PV disponibles dans le commerce. Toutefois, les processus de fabrication complexes des cellules solaires inorganiques susmentionnées, le coût élevé des matières premières et les problèmes environnementaux connexes ont entravé leur déploiement à grande échelle. Ils ont encouragé des recherches intensives pour développer des technologies PV à haut rendement, à faible coût et respectueuses de l'environnement, parmi lesquelles les cellules solaires organiques (OSC) constituent une alternative prometteuse en raison de leurs avantages remarquables: faible coût, flexibilité, légèreté et simplicité des processus de fabrication. Aujourd'hui, le meilleur PCE des OSC à simple jonction a atteint plus de 18 % en laboratoire, ce qui les rend plus que jamais attrayants pour d'éventuelles applications commerciales.

Cependant, certains problèmes liés aux OSC doivent être soigneusement résolus avant que les OSC puissent être largement appliqués. Premièrement, l'efficacité des OSC est toujours inférieure à celle du silicium. Il est très difficile de régler avec précision la ségrégation de phase de l'hétérojonction en vrac pour une dissociation efficace des excitons et le transport des charges, bien que de nombreux paramètres de traitement aient été ajustés, notamment le recuit thermique, le recuit à la vapeur de solvant et l'ingénierie des additifs de solvant. Parmi eux, l'ajout d'additifs de solvant est le moyen le plus simple et le plus efficace sans augmenter la complexité de fabrication des OSC, en particulier les additifs de solvant binaires. Cependant, le rôle du composant unique dans les additifs de solvant binaire n'a pas été entièrement divulgué dans les rapports susmentionnés. Deuxièmement, bien que l'efficacité des OSC se soit considérablement améliorée,

la plupart des OSC sont toujours fabriqués dans une atmosphère inerte en raison de la sensibilité à l'air des matériaux photovoltaïques organiques, des couches d'interface et des matériaux d'électrode. L'aptitude au traitement à l'air et la stabilité à long terme des OSC ont donc attiré davantage l'attention et certaines stratégies ont été mises en oeuvre, comme l'utilisation de la structure inversée du dispositif, les oxydes métalliques comme couches d'extraction d'électrons, les oxydes métalliques à haute fonction de travail comme couches d'interface anodiques et la modification des films photoactifs. Cependant, la stratégie la plus prometteuse et la plus efficace pour obtenir des OSC stables et à haut rendement consiste à explorer les matériaux photovoltaïques stables et traitables à l'air dans diverses conditions. Parallèlement, il convient d'améliorer encore les performances des dispositifs correspondants et d'examiner en détail la stabilité à long terme de ces dispositifs traités par air dans différentes conditions ambiantes. Enfin, la percée des matériaux accepteurs non fullerènes fait progresser rapidement l'efficacité des dispositifs. Les caractéristiques les plus significatives des dispositifs à base de non-fullerène à haute performance sont la faible perte de tension et, par conséquent, la séparation efficace des charges avec une force motrice faible (ou négligeable). Jusqu'à présent, la plupart des recherches se sont concentrées sur les nouveaux accepteurs non fullerènes pour les dispositifs à haute performance avec une faible perte de tension. La dissociation d'exciton pour les dispositifs à base de nonfullerène avec une faible perte de tension (ou une petite force motrice) n'est pas entièrement claire, et les facteurs d'influence doivent être étudiés. Pour répondre aux questions ci-dessus, les trois parties de la thèse ci-dessous ont fourni des explorations significatives.

Dans la première partie, pour sonder le principe de combinaison des additifs de solvant binaire et l'effet d'un seul composant dans les additifs de solvant binaire sur l'amélioration des performances du dispositif, nous avons développé un additif solvant binaire alternatif de 1,8-diiodooctane (DIO) et un p-anisaldéhyde (AA) et avons sondé son effet sur le dispositif basé sur le poly[(5,6-difluoro-2,1,3- benzothiadiazol-4,7-diyl)-alt-(3,3"-di(2-octyldodecyl) 2,2' ;5',2";5",2"" -quaterthio-phen- 5,5"-diyle)] (PffBT4T-2OD) comme donneur et l'ester méthylique de l'acide [6,6]-phényl-C<sub>61</sub>-butyrique (PC<sub>61</sub>BM) comme accepteur. Les mesures correspondantes ont été effectuées par spectroscopie d'absorption optique, diffraction des rayons X en incidence rasante (GIXRD), microscopie à force atomique (AFM) à module de Derjaguin-Muller-Toporov (DMT) et cartographie de l'énergie plasmonique par microscopie électronique à transmission à balayage (STEM). Il a été constaté que l'AA facilitait principalement l'ordre du polymère PffBT4T-2OD et sa haute cristallinité. Par contre, le DIO pouvait diffuser le PC<sub>61</sub>BM dans la matrice polymère PffBT4T-2OD pour élargir les interfaces D-A. Le film photoactif a donc obtenu de grandes dimensions de D-A. Ainsi, le film photoactif a obtenu de grandes interfaces D-A et un transport de porteurs de charge plus équilibré en combinant DIO et AA. Par conséquent, l'effet synergique bénéfique a conduit à un courant de court-circuit ( $J_{sc}$ ) et à un facteur de remplissage (FF) élevés, et a finalement atteint un PCE de 10.64 %, qui a été amélioré de 16 % par rapport au dispositif de contrôle. Par conséquent, ce cas dévoile un mécanisme général

d'exploration d'un nouvel additif de solvant binaire avec un effet synergique sur le film photoactif pour améliorer le dispositif OSCs.

En outre, pour améliorer l'efficacité du dispositif par l'ingénierie des additifs de solvant, la stabilité du dispositif dans différentes conditions, qui est un autre aspect du dispositif à haute performance, doit être prise en compte. Dans la deuxième partie, basée sur un terpolymère à faible bande interdite stable dans l'air (PDPPPPTD) de notre collaborateur, les OSCs traités dans l'air, composés de PDPPPPTD comme donneur et de PC<sub>61</sub>BM comme accepteur, ont atteint avec succès un PCE élevé de 6.34%, et les stabilités des performances du dispositif dans différentes conditions ambiantes ont été étudiées. Il a été constaté que le dispositif correspondant présentait une stabilité thermique, une photostabilité et une stabilité à long terme supérieures dans une atmosphère ambiante avec une humidité appropriée, par rapport à de nombreux OSC rapportés. En outre, compte tenu du grand potentiel, un additif solvant p-anisaldéhyde (AA) non toxique et sans iodé a été essayé, puis l'efficacité supérieure de 7.41% a été fabriquée avec succès, ce qui est l'une des efficacités les plus élevées des OSCs stables et traités à l'air. De plus, avec le traitement AA, la reproductibilité et la stabilité des performances du dispositif dans différentes conditions ambiantes ont été améliorées. Par conséquent, cela présente une voie pour développer des OSCs traités à l'air pour une application commerciale dans le futur.

Dans la troisième partie, pour comprendre la dissociation efficace des excitons sous une petite force motrice avec une perte de tension réduite dans les dispositifs photovoltaïques à base de non fullerène, une nouvelle méthode de mesure précise des constantes diélectriques a été utilisée dans les différents dispositifs à base de non fullerène consistant en un polymère PM6 à base de thiényl benzodithiophène fluoré (BDT-2F) comme donneur commun, et une série sélectionnée de matériaux non fullerènes comme accepteurs. Il a été constaté que, par rapport aux dérivés du fullerène, la plupart des matériaux non fullerènes présentaient des constantes diélectriques plus élevées. De plus, les films de mélange correspondants présentaient des constantes diélectriques plus élevées et des différences de constantes diélectriques plus importantes entre le donneur polymère PM6 et les accepteurs non fullerènes, confirmées par microscopie optique à champ proche à balayage de type diffusion. Les résultats indiquent que les dispositifs à base de nonfullerène diminuent l'énergie de liaison des excitons et la perte par recombinaison des porteurs, tout en augmentant la séparation des charges, ce qui est cohérent avec la dissociation efficace des excitons sous une petite force motrice. En outre, le chevauchement entre le spectre d'émission du donneur de polymère PM6 et les spectres d'absorption des accepteurs non fullerènes a permis le transfert d'énergie de résonance du donneur de polymère PM6 à l'accepteur dans les dispositifs non fullerènes. Cela a été confirmé en comparant les spectres d'émission changeant des films donneurs (et accepteurs) vierges et des films de mélange correspondants. Le transfert d'énergie de résonance a amélioré la diffusion efficace des excitons. L'effet

synergique de la propriété diélectrique élevée et du transfert d'énergie sur la séparation des charges, a donc interprété la dissociation efficace des excitons pour la performance élevée du dispositif sous une petite force motrice. En même temps, le travail a donné une voie possible pour éclairer le mécanisme physique intrinsèque de fonctionnement des OSCs non-fullerènes.

Mots-clés: cellules solaires organiques, additifs de solvant binaire, cellules solaires traitées à l'air, haute stabilité, constante diélectrique, transfert d'énergie, séparation des charges.

## ABSTRACT

The current energy use mainly relies on nonrenewable and polluting fossil fuels, which causes unsustainable consequences for societal, economical, geopolitical, and environmental issues. Harnessing solar energy is one of the most promising renewable energy sources to meet the world's large and growing energy demand. Solar cells, which directly convert solar energy to electricity via the photovoltaic (PV) effect, have been considered as one of the cleanest and most promising technologies to tackle today's energy issues. Since the first silicon solar cell with the efficiency of 6% was successfully achieved by Bell Lab in 1954, the efficiency of solar cells was continuously improved and different kinds of solar cells were explored. Nowadays, the various inorganic solar cells based on crystalline silicon, cadmium telluride, or copper indium germanium selenide (CIGS) obtained a high power conversion efficiency (PCE) of about 15-27% and occupied most of the PV technologies available commercially. However, the complex manufacturing processes of the above inorganic solar cells, the high cost of raw materials, and the related environmental issues have impeded their widespread deployment. They encouraged intensive researches to develop high-efficiency, low-cost, and eco-friendly PV technologies, of which organic solar cell (OSC) is a promising alternative because of their remarkable advantages of low-cost, flexibility, light weight, and simple fabrication processes. Now the best PCE of single-junction OSC has reached up to over 18% in the lab, which makes them more than ever attractive for possible commercial applications.

However, some issues in OSCs required to be carefully addressed before the OSCs likely can be widely applied. Firstly, the efficiency of OSC still lags behind silicon one. It is very difficult to precisely tune the bulk-heterojunction phase segregation for efficient exciton dissociation as well as charge transport, although many related processing parameters have been adjusted, including thermal annealing, solvent vapor annealing, and solvent additives engineering. Among them, adding solvent additive is the simplest and very effective way without increasing the fabricated complexities of OSCs, especially the binary solvent additives. However, the role of the single component in binary solvent additives has not been fully disclosed in the aforementioned reports. Second, regardless of the fact that the efficiency of OSC achieved huge improvement, most of the OSCs are still fabricated in an inert atmosphere due to the air sensitivity of organic photovoltaic materials, interface layers, and electrode materials. So the air processability and long-term stability of OSCs have attracted more attention and some strategies have been conducted, such as employing the inverted device structure, the metal oxides as electron extraction layers, the high work-function metal oxides as anode interface layers, and modification of photoactive films. However, the most promising and effective strategy for stable and high-efficiency OSCs is to explore the air-processable and stable photovoltaic materials under various conditions. Meanwhile, the related device performance should be further improved and the long-term stabilities of these air-processed devices under different ambient

conditions should be examined in detail. Lastly, the breakthrough of non-fullerene acceptor materials makes the device's efficiency rapidly progresses. And the most significant features of high-performance non-fullerene based devices are the low voltage loss and consequently the efficient charge separation with a small (or negligible) driving force. Until now, most researches mainly focus on the novel non-fullerene acceptors for high-performance devices with lower voltage loss. Exciton dissociation for non-fullerene based device with a low voltage loss (or a small driving force) is not entirely clear, and the influencing factors are highly required to be investigated. To answer the above questions, below three parts in the thesis have provided meaningful explorations.

In the first part, to probe the combination principle of binary solvent additives and the effect of a single component in binary solvent additives on the improvement of device performance, we developed an alternative binary solvent additive of 1,8-diiodooctane (DIO) and a p-anisaldehyde (AA) and probed its effect on the device based on poly[(5,6-difluoro-2,1,3- benzothiadiazol-4,7-diyl)-alt-(3,3'''-di(2-octyldodecyl) 2,2';5',2'';5'',2''' -quaterthio-phen- 5,5'''-diyl)] (PffBT4T-2OD) as the donor and [6,6]-phenyl-C<sub>61</sub>-butyric acid methyl ester (PC<sub>61</sub>BM) as the acceptor. Related measurements were conducted by optical absorption spectroscopy, grazing- incidence X-ray diffraction (GIXRD), Derjaguin-Muller-Toporov (DMT) modulus atomic force microscopy (AFM), and plasmon energy mapping via scanning transmission electron microscopy (STEM). It was found that AA mainly facilitated PffBT4T-2OD polymer order and high crystallinity. Differently, DIO could diffuse PC<sub>61</sub>BM into the PffBT4T-2OD polymer matrix for enlarged D-A interfaces. So the photoactive film obtained large D-A interfaces and more balanced charge carrier transport by combining DIO and AA. Hence, the beneficial synergistic effect led to the high short circuit current ( $J_{sc}$ ) and fill factor (FF), and finally reached to PCE of 10.64%, which was improved by 16% compared with the control device. Therefore, the case unveils a general mechanism of exploring new binary solvent additive with synergistic effect on the photoactive film to enhance the OSCs device.

In addition, to improve device efficiency by solvent additives engineering, the device stabilities under different conditions as another aspect of the high-performance device, should be considered. In the second part, based on an air-stable low bandgap terpolymer (PDPPPPTD) from our collaborator, the air-processed OSCs consisting of PDPPPPTD as the donor and PC<sub>61</sub>BM as the acceptor, successfully achieved a high PCE of 6.34%, and the stabilities of device performance under different ambient conditions were studied. It was found that the related device exhibited superior thermal stability, photo-stability, and long-term stability in an ambient atmosphere with suitable humidity compared with lots of the reported OSCs. Besides, considering the great potential, a nontoxic and iodine-free p-anisaldehyde (AA) solvent additive was attempted, then the higher efficiency of 7.41% was successfully fabricated, which is one of the highest efficiency of air-processed and stable OSCs. Moreover, with AA treatment, the related device performance

reproducibility and stability under different ambient conditions were further improved. Therefore, it presents a pathway to develop air-processed OSCs for commercial application in the future.

In the third part, to figure out the efficient excitons dissociation under a small driving force with reduced voltage loss in non-fullerene based photovoltaic devices, a novel method of accurately measuring dielectric constants was used in the different non-fullerene based devices consisting of fluorinated-thienyl benzodithiophene (BDT-2F)-based polymer PM6 as the common donor, and a selected series of non-fullerene materials as the acceptors. It was found that compared with fullerene derivatives, most non-fullerene materials showed higher dielectric constants. Moreover, the corresponding blend films exhibited the higher dielectric constants and the larger dielectric constant differences between PM6 polymer donor and non-fullerene acceptors confirmed by scattering-type scanning near-field optical microscopy. The results indicated that the non-fullerene based devices decreased exciton binding energy and carrier recombination loss, and meanwhile increased charge separation, which is consistent with the efficient exciton dissociation under a small driving force. In addition, the overlap between the emission spectrum of PM6 polymer donor and absorption spectra of non-fullerene acceptors allowed the resonance energy transfer from PM6 polymer donor to the acceptor in the non-fullerene based devices. It was further confirmed by comparing the emission spectra changing of pristine donor (and acceptor) films and corresponding blend films. The resonance energy transfer enhanced the efficient exciton diffusion. The synergistic effect of high dielectric property and energy transfer on charge separation, therefore, interpreted efficient exciton dissociation for the high device performance under a small driving force. Meanwhile, the work gave a possible path to illuminate the intrinsic physical working mechanism of non-fullerene OSCs.

Keywords: organic solar cells, binary solvent additives, air-processed solar cells, high stability, dielectric constant, energy transfer, charge separation.

## CONTENTS

<b>CHAPTER 1 INTRODUCTION .....</b>	1
1.1    Introduction of Organic Solar Cells .....	2
1.1.1 <i>Mechanism of organic solar cells</i> .....	2
1.1.2 <i>Device parameters of organic solar cells</i> .....	3
1.1.3 <i>Device architectures of organic solar cells</i> .....	4
1.2    Classification of Organic Solar Cells .....	6
1.2.1 <i>Polymer solar cells</i> .....	6
1.2.2 <i>All polymer solar cells</i> .....	10
1.2.3 <i>Small molecular solar cells</i> .....	14
1.3    Current Issues of Organic Solar Cells .....	16
1.3.1 <i>Current situation of device efficiency</i> .....	16
1.3.2 <i>Current situation of device stability</i> .....	17
1.3.3 <i>Issue of charge separation in non-fullerene based devices</i> .....	19
1.4    Thesis Objectives and Organization.....	22
1.4.1 <i>Objectives</i> .....	22
1.4.2 <i>Thesis organization</i> .....	23
<b>CHAPTER 2 EXPERIMENTAL.....</b>	25
2.1    Chemicals and Materials .....	25
2.2    Preparation of ZnO Precursor Solution .....	25
2.3    Synthesis of PDPPPPTD Polymer.....	26
2.4    Devices Fabrication.....	26
2.4.1 <i>Fabrication of PffBT4T-2OD:PC<sub>61</sub>BM based device</i> .....	26
2.4.2 <i>Fabrication of PDPPPPTD:PC<sub>61</sub>BM based device</i> .....	26
2.4.3 <i>Fabrication of PM6:non-fullerene acceptors based devices</i> .....	27
2.4.4 <i>Fabrication of photoactive films for dielectric constant measurement</i> .....	27
2.4.5 <i>Fabrication of bilayer heterojunction films</i> .....	28
2.5    Characterizations .....	28

**CHAPTER 3 UNVEILING PHOTOVOLTAIC PERFORMANCE ENHANCEMENT  
MECHANISM OF POLYMER SOLAR CELLS VIA SYNERGISTIC EFFECT OF BINARY  
SOLVENT ADDITIVES.....**.....30

3.1	Introduction .....	31
3.2	Experimental Section .....	33
3.2.1	<i>Reagent and Materials</i> .....	33
3.2.2	<i>Preparation of ZnO Precursor Solution</i> .....	33
3.2.3	<i>Fabrication of Solar Cell Devices</i> .....	33
3.2.4	<i>Characterizations</i> .....	34
3.3	Results and Discussion.....	35
3.4	Conclusion.....	43
3.5	References .....	43
3.6	Supporting Information .....	46

**CHAPTER 4 AIR-PROCESSED, ORGANIC SOLAR CELLS WITH HIGH POWER  
CONVERSION EFFICIENCY OF 7.41%.....**.....50

4.1	Introduction .....	51
4.2	Experimental Section .....	53
4.2.1	<i>Reagent and Materials</i> .....	53
4.2.2	<i>Synthesis of PDPPPPTD Polymer</i> .....	54
4.2.3	<i>Preparation of ZnO Precursor Solution</i> .....	54
4.2.4	<i>Fabrication of Solar Cell Devices</i> .....	54
4.2.5	<i>Characterization</i> .....	55
4.3	Results and Discussion.....	55
4.4	Conclusion.....	65
4.5	References .....	65
4.6	Supporting Information .....	69

**CHAPTER 5 SYNERGISTIC EFFECT OF DIELECTRIC PROPERTY AND ENERGY  
TRANSFER ON CHARGE SEPARATION IN NON-FULLERENE BASED SOLAR CELLS.....**.....79

5.1	Introduction .....	80
5.2	Experimental Section .....	82
5.2.1	<i>Reagent and Materials</i> .....	82
5.2.2	<i>Dielectric Constant Measurement</i> .....	83
5.2.3	<i>Fabrication of Bilayer Heterojunction Films</i> .....	83

5.2.4	<i>Fabrication of Solar Cells .....</i>	84
5.2.5	<i>Characterization.....</i>	84
5.3	Results and Discussion.....	85
5.3.1	<i>Photovoltaic Output of the OPV Devices .....</i>	85
5.3.2	<i>Simulated Charge Transfer Rate .....</i>	86
5.3.3	<i>Dielectric Constants Measurement of the Films .....</i>	87
5.3.4	<i>Scanning Near-field Optical Microscopy of the Films .....</i>	90
5.3.5	<i>Energy Transfer Between Donor and Acceptor.....</i>	92
5.3.6	<i>Mechanism of Exciton Dissociation and Charge Transfer.....</i>	94
5.4	Conclusion.....	95
5.5	References .....	96
5.6	Supporting Information .....	102
<b>CHAPTER 6 CONCLUSIONS AND PERSPECTIVES .....</b>		111
6.1	Conclusions .....	111
6.2	Perspectives .....	113
6.2.1	<i>Application of s-SNOM measurement in non-fullerene based devices .....</i>	113
6.2.2	<i>Further investigation of energy transfer in non-fullerene based devices .....</i>	113
6.2.3	<i>Air-processed and semi-transparent organic solar cells.....</i>	114
<b>REFEREENCES .....</b>		115
<b>RÉSUMÉ.....</b>		130

## LIST OF FIGURES

**Figure 1.1** The operating principle of organic solar cells and the process mainly consists of four steps: (a) Light harvesting/Exciton generation, (b) Exciton diffusion, (c) Exciton dissociation, (d) Charge transfer/generation.<sup>11</sup>

**Figure 1.2** (a) Current density-voltage ( $J-V$ ) curves of the typical photovoltaic device in the dark and illumination<sup>13</sup> (b) the schematic energy diagram between donor and acceptor.<sup>11</sup>

**Figure 1.3** Different device architectures of organic solar cells (a) Single-layer device, (b) Bilayer device, (c) Bulk heterojunction device.

**Figure 1.4** (a) Conventional forward device architecture, (b) Inverted device architecture of organic solar cells

**Figure 1.5** The chemical structures of (a) Wide-bandgap polymers, (b) Narrow bandgap polymers, (c) Middle-bandgap polymers.

**Figure 1.6** The chemical structures of (a) The fullerene derivatives acceptors, (b) The non-fullerene acceptors.

**Figure 1.7** The chemical structures of major NDI-based P<sub>as</sub>s in all PSCs categorized by their design strategies (a) Side-chains engineering, (b) Backbone modification engineering, (c) The random copolymer engineering.

**Figure 1.8** The chemical structures of major PDI-based P<sub>as</sub>s in all PSCs.

**Figure 1.9** The chemical structures of new classes P<sub>as</sub>s in all PSCs. (a) The P<sub>as</sub>s based on different aromatic imide-based moieties, (b) The electron-deficient BNBP-based P<sub>as</sub>s, (c) The polymerized non-fullerene P<sub>as</sub>s.

**Figure 1.10** Chemical structures of BDT-based P<sub>ds</sub> in all-PSCs.

**Figure 1.11** The chemical structures of small molecular donors for small molecular solar cells

**Figure 1.12** Schematic diagram of the degradation factors limiting the device stability.<sup>130</sup>

**Figure 1.13** Typical organic photovoltaic materials and their ESP distributions in vacuum.<sup>138</sup>

**Figure 1.14** ESP of the donor and acceptors and their impact on the intermolecular interactions. (a) ESP distributions of the donor and acceptors (b) The intermolecular binding energies between

PTO2 and the acceptors at different points parallel to the PTO2 backbone (ESP of PTO2 in the moving direction is shown as red) at an intermolecular distance and (d) Vertical with backbone.<sup>139</sup>

**Figure 1.15** GIXRD characterization of Y6 based systems. (a)-(f) Two-dimensional GIXRD patterns (top) and profiles (bottom) of (a) and (d) The pristine Y6, (b) and (e) Pristine PBDB-T-2F, and (c) and (f) PBDB-T-2F:Y6 films, respectively.<sup>140</sup>

# LIST OF CHEMICAL COMPOUNDS, ABBREVIATIONS AND SYMBOLS

## Chemical Compounds

Ag	silver
Al	aluminum
C	carbon
CdS	cadmium sulfide
CdO	cadmium oxide
CH <sub>3</sub> OCH <sub>2</sub> CH <sub>2</sub> OH	2-methoxyethanol
MoO <sub>3</sub>	molybdenum oxide
N <sub>2</sub>	nitrogen gas
NH <sub>2</sub> CH <sub>2</sub> CH <sub>2</sub> OH	ethanolamine
ZnO	zinc oxide
Zn(CH <sub>3</sub> COO) <sub>2</sub> ·2H <sub>2</sub> O	zinc acetate dehydrate

## Abbreviations

DSSCs	dye-sensitized solar cells
QDSCs	quantum dot solar cells
PVSCs	perovskite solar cells
OSCs	organic solar cells
PSCs	polymer solar cells
PCE	power conversion efficiency
D-A	donor-acceptor
P <sub>d</sub> S	polymeric donor
P <sub>a</sub> S	polymeric acceptor
HOMO	highest occupied molecular orbital
LUMO	lowest unoccupied molecular orbital
D/A	donor/acceptor
ESP	electrostatic potential
CT	charge transfer state
EQE	external quantum efficiency
EQE <sub>EL</sub>	electroluminescence quantum efficiency

IQE	internal quantum efficiency
AFM	atomic force microscopy
FTIR	Fourier transform infrared spectroscopy
HR TEM	high resolution transmission electron microscopy
ITO	indium tin oxide
J-V	current-voltage
PDMS	polydimethylsiloxane
PFN-Br	poly[(9,9-bis(3'-(N,N-dimethyl)-nethylammonium-propyl)-2,7-fluorene)-alt-2,7-(9,9dioctylfluorene)]dibromide
PC <sub>61</sub> BM	phenyl-C61-butyric acid methyl ester
PC <sub>71</sub> BM	phenyl-C71-butyric acid methyl ester
PCE	power conversion efficiency
PEDOT:PSS	poly(3,4-ethylenedioxythiophene):polystyrene sulfonate
PL	photoluminescence
BHJ	bulk heterojunction
PV	photovoltaic
OPV	organic photovoltaic
P3HT	poly (3-hexylthiophene)
UV	ultraviolet
Vis	visible
XPS	X-ray photoelectron spectroscopy
XRD	X-ray diffraction
s-SNOM	scattering-type scanning near-field optical microscopy
GIXRD	grazing-incidence X-ray diffraction
CV	cyclic voltammetry
RMS	root-mean-square roughness
DIO	1,8-diiodooctane
AA	p-anisaldehyde
CB	chlorobenzene
ODCB	1,2-dichlorobenzene
DCM	dichloromethane
CF	chloroform

## Symbols

$\mu$	micro
$J_{sc}$	short circuit current
$V_{oc}$	open circuit voltage
$R_{sh}$	shunt resistance
$R_s$	series resistance
FF	fill factor
$\lambda$	wavelength
$J_{ph}$	photocurrent density
$V_{eff}$	effective applied voltage
$\epsilon_r$	relative dielectric constant
$\epsilon_o$	absolute dielectric permittivity
$E_g$	optical gap

## LIST OF PUBLICATIONS AND CONFERENCE CONTRIBUTIONS

### Journal Publications

- 1) **Pandeng Li<sup>1</sup>**, Jin Fang<sup>1</sup>, Yusheng Wang<sup>1</sup>, Sergei Manzhos, Lei Cai, Zheheng Song, Yajuan Li, Tao Song, Xuechun Wang, Xia Guo, Maojie Zhang, Dongling Ma, Baoquan Sun, Synergistic Effect of Dielectric Property and Energy Transfer on Charge Separation in Non-fullerene Based Solar Cells, *Angew. Chem. Int. Ed.* 2021, DOI: 10.1002/anie.202103357.
- 2) **Pandeng Li<sup>1</sup>**, Yuliang Zhang<sup>1</sup>, Ting Yu, Qingzhe Zhang, Jean-Philippe Masse, Yingguo Yang, Ricardo Izquierdo, Baoquan Sun, Dongling Ma, Unveiling Photovoltaic Performance Enhancement Mechanism of Polymer Solar Cells via Synergistic Effect of Binary Solvent Additives, *Sol. RRL* 2020, 2000239.
- 3) **Pandeng Li**, Mathieu Mainville, Yuliang Zhang, Mario Leclerc, Baoquan Sun, Ricardo Izquierdo, Dongling Ma, Air-Processed, Stable Organic Solar Cells with High Power Conversion Efficiency of 7.41%, *Small* 2019, 15, 1804671.
- 4) Long Tan<sup>1</sup>, **Pandeng Li<sup>1</sup>**, Baoquan Sun, Mohamed Chaker, Dongling Ma, Stabilities related to near infrared quantum dot-based solar cells: the role of surface engineering, *ACS Energy Lett.* 2017, 2, 1573-1585.
- 5) Long Tan<sup>1</sup>, **Pandeng Li<sup>1</sup>**, Baoquan Sun, Mohamed Chaker, Dongling Ma, Development of photovoltaic devices based on near infrared quantum dots and conjugated polymers, *ChemNanoMat*, 2016, 2, 601-615.
- 6) Long Tan, **Pandeng Li**, Qingzhe Zhang, Ricardo Izquierdo, Mohamed Chaker, Dongling Ma, Toward enhancing solar cell performance: an effective and “green” additive, *ACS Appl. Mater. Interfaces* 2018, 10, 6498-6504.
- 7) Shengyun Huang, Qingzhe Zhang, **Pandeng Li**, Fuqiang Ren, Aycan Yurtsever, Dongling Ma, High-Performance Suspended Particle Devices Based on Copper-Reduced Graphene Oxide Core-Shell Nanowire Electrodes, *Adv. Energy Mater.* 2018, 8, 1703658.
- 8) Long Tan, Fan Yang, Mee Rahn Kim, **Pandeng Li**, Deepak Thrithamarassery Gangadharan, Joëlle Margot, Ricardo Izquierdo, Mohamed Chaker, and Dongling Ma, Enhanced Long-term and Thermal Stability of Polymer Solar Cells in Air at High Humidity with the Formation of Unusual Quantum Dot Networks, *ACS Appl. Mater. Interfaces* 2017, 9, 26257-26267.
- 9) Shengyun Huang, Qingzhe Zhang, Fan Yang, Deepak Thrithamarassery Gangadharan, **Pandeng Li**, Fuqiang Ren, Baoquan Sun, Dongling Ma, A Facile Way for Scalable Fabrication of Silver Nanowire

Network Electrodes for High-performance and Foldable Smart Windows, *J. Mater. Chem. A* **2020**, *8*, 8620-8628.

**10)** Liang Kuai, Junnan Li, Yajuan Li, Yusheng Wang, **Pandeng Li**, Yuanshuai Qin, Tao Song, Yingguo Yang, Zhuoying Chen, Xingyu Gao, Baoquan Sun, Revealing Crystallization Dynamics and the Compositional Control Mechanism of 2D Perovskite Film Growth by In Situ Synchrotron- Based GIXRD, *ACS Energy Lett.* **2019**, *5*, 8-16.

**11)** Lei Cai, Fei Yang, Yafeng Xu, Jianzhong Fan, Ya Li, Yue Zhao, Dong Liang, Yatao Zou, **Pandeng Li**, Lu Wang, Chuankui Wang, Youyong Li, Jian Fan, Baoquan Sun, Dual Functionalization of Electron Transport Layer via Tailoring Molecular Structure for High- Performance Perovskite Light-Emitting Diodes, *ACS Appl. Mater. Interfaces* **2020**, *12*, 37346- 37353.

### Conference Presentations

1. **Pandeng Li**, Mathieu Mainville, Yuliang Zhang, Mario Leclerc, Baoquan Sun, Ricardo Izquierdo, Dongling Ma. Air-Processed, Stable Organic Solar Cells with High Power Conversion Efficiency (102nd Canadian Chemistry Conference and Exhibition (CCCE2019)). July 03-07, 2019, Quebec, Canada (Oral presentation).

## CHAPTER 1 INTRODUCTION

With the rapid development of the economy and society, fossil fuels are increasingly consumed, which causes serious environmental pollution and energy crisis that influence human life. The photovoltaic (PV) technology that generates electricity directly from sunlight, is a promising solution to solve the above problems. So the solar cells have been an important direction of research and real applications for developing new energy in the world. Since the p-n junction silicon solar cell with the efficiency of 6% was successfully fabricated by Bell Lab in 1954,<sup>1</sup> the efficiency of solar cells have been continuously improved. And the various inorganic solar cells (such as silicon, III-V semiconductors, CIGS, and CdTe) occupied most of the PV market.<sup>2</sup> However, Due to the complex fabrication process, the high cost of raw materials, and the related environmental issues, their application regions were limited and couldn't successfully replace grid electricity. Currently, only 2.6% of global electricity generation came from PV solar cells.<sup>3</sup> Therefore, more efforts should be devoted to exploring high-efficiency, stable, low-cost, and eco-friendly PV devices.

In the past decades, the researchers generally focused on the third-generation PV devices that include the dye-sensitized solar cells (DSSCs), the quantum dot solar cells (QDSCs), the perovskite solar cells (PVSCs), and the organic solar cells (OSCs).<sup>4-7</sup> Especially, the PVSCs and OSCs have attracted much attention because of the huge improvement of device performance. Although the PVSCs obtained a higher efficiency than OSCs, considering the environmental detriment of poisonous heavy metals in PVSCs, the OSCs have a great prospect of development, such as developing ultrathin OSCs and providing the electrical energy for the internet of things. The organic photovoltaic device generally consists of photoactive film and two electrodes with different work functions, whose promising advantages are the low cost, flexibility, light weight, and simple device fabrication process. In 1986, Tang's group successfully fabricated OSCs with an efficiency of 1%, which is a milestone in the developed history of OSCs.<sup>8</sup> With the enormous efforts to synthesis novel photovoltaic materials, to design stable device structure, and to modify fabrication methods, and to manipulate the morphology of photoactive films, the power conversion efficiency (PCE) of OSCs have been hugely improved and the best PCE of single-junction photovoltaic device was boosted to over 18%.<sup>9</sup> In addition, the 1.05 cm<sup>2</sup> photovoltaic device fabricated by blade-coating achieved the enhanced PCE of 14.25%.<sup>10</sup> The remarkable progress make them more than ever attractive for large-scale fabrication, an imperative step toward possible commercial applications. We believe that: As researchers make unremitting efforts for improving the organic photovoltaic device performance, the dream that OSCs are widely used in human life will be finally realized in the future.

## 1.1 Introduction of Organic Solar Cells

### 1.1.1 Mechanism of organic solar cells

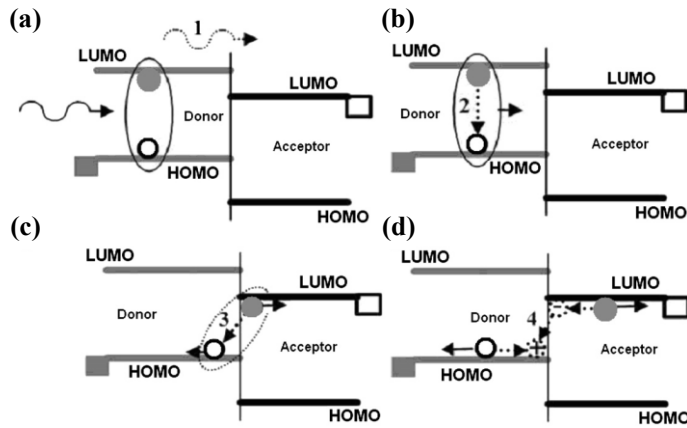


**Figure 1.1 The operating principle of organic solar cells and the process mainly consists of four steps:** (a) Light harvesting/Exciton generation, (b) Exciton diffusion, (c) Exciton dissociation, (d) Charge transfer/generation. Reprinted from ref. 11. Copyright © 2013 Elsevier Ltd..

Organic solar cell called organic photovoltaic device can be used to produce electricity from sunlight. Its core part is the organic photovoltaic film, which can absorb photons when sunlight is absorbed. The fundamental photophysical mechanism in Figure 1.1 includes four steps as followed, starting from the absorbed photons and ending with charge carriers collected by different electrodes.<sup>11</sup>

- (1) Creation of excitons: In Figure 1.1a, when the photoactive film absorb the photons, the electrons are excited from the ground state to the excited state. Due to the low dielectric constant of organic photovoltaic materials ( $\epsilon_r \approx 2\text{-}4$ ), the tightly bound electron-hole pairs (called the Frenkel excitons) are formed.
- (2) Diffusion of excitons: In Figure 1.1b, because of the short exciton lifetime and diffusion length ( $\sim 10$  nm) in organic photovoltaic materials, the excited excitons efficiently diffuse towards the donor-acceptor (D-A) interfaces for free charge carriers.<sup>8</sup>
- (3) Dissociation of charge carriers: In Figure 1.1c, under the built-in electric field at D-A interfaces, the tightly bound excitons at D-A interfaces are dissociated into the free electrons and holes called the free charge carriers.<sup>8</sup> the free electrons are transferred from the lowest unoccupied molecular orbital (LUMO) of a donor to that of the acceptor, while holes transfer from highest occupied molecular orbital (HOMO) of acceptor to that of the donor.
- (4) Transport and collection of charge carriers: In Figure 1.1d, after the free charge carriers are transferred between donor and acceptor, they are respectively transported in donor and acceptor by the concentration gradient. Finally, the free electrons and holes are collected by different electrodes.<sup>12</sup>

It is noted that the corresponding loss mechanisms exist in the above steps. Namely, non-absorbed photons in the creation process of excitons, exciton decay in the process of excitons diffusion, geminate recombination in the process of excitons dissociation, and the bimolecular recombination in the processes of transport and collection of free charge carriers. Hence, the high-performance OSCs would be realized by decreasing the above loss processes.

### 1.1.2 Device parameters of organic solar cells

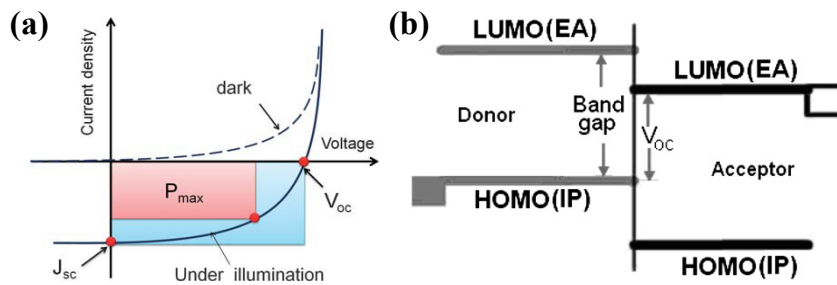


**Figure 1.2 (a)** Current density-voltage ( $J$ - $V$ ) curves model of the typical photovoltaic device in the dark and illumination, Reprinted from ref. 13. Copyright 2010 Royal Society of Chemistry., (b) The schematic energy diagram between donor and acceptor. Reprinted from ref. 11. Copyright © 2013 Elsevier Ltd..

The current density-voltage ( $J$ - $V$ ) curves of OSCs are measured under the AM 1.5G simulated illumination ( $100 \text{ mW cm}^{-2}$ ), which is a direct characterization method of device performance. As illustrated in Figure 1.2a, the  $J$ - $V$  curves are measured under illumination and dark conditions, respectively. The fundamental device parameters are as followed:

- (1) Open-circuit voltage ( $V_{oc}$ ): The  $V_{oc}$  is the measured output voltage between anode and cathode under the open-circuit condition of the related device circuit. Especially in the heterojunction organic photovoltaic device, the  $V_{oc}$  shown in Figure 1.2 b is defined as the difference between the HOMO of a donor and the LUMO of an acceptor.<sup>11</sup>
  - (2) Short-circuit current density ( $J_{sc}$ ): When the voltage is zero under the short-circuit condition, the measured current is the short-circuit current. Namely, a few charge carriers at the D-A interfaces completely pass through the external circuit, which results in the maximum photogenerated current.
  - (3) Fill factor (FF): FF is an important parameter of device performance, is defined as the ratio of the maximum output power  $P_{max}$  ( $V_{max} * J_{max}$ ) to the product of  $J_{sc}$  and  $V_{oc}$ , and the  $V_{max}$  and  $J_{max}$  is related voltage and current density of the  $P_{max}$ . FF can be influenced by many factors, such as the charge carrier mobility, the lifetime of excitons, the thickness of photoactive films, contact quality of photoactive layer and two electrodes, and the leakage current caused by different traps in photovoltaic devices.<sup>14-15</sup>
- The related equation is as followed:

$$FF = \frac{P_{max}}{V_{oc}J_{sc}} = \frac{V_{max}J_{max}}{V_{oc}J_{sc}}$$

- (4) Power conversion efficiency (PCE): It is defined as the ratio of the maximum output power  $P_{max}$  and incident sunlight power  $P_{light}$ . The corresponding equation is as followed: under the constant  $P_{light}$ , the PCE is mainly dependent on the FF,  $V_{oc}$ , and  $J_{sc}$ .

$$PCE = \frac{P_{max}}{P_{light}} = \frac{J_{sc}V_{oc}FF}{P_{light}}$$

- (5) Quantum efficiency: it includes external quantum efficiency (EQE) and internal quantum efficiency (IQE). The EQE is the ratio of the generated electrons in the device and the incident photons under the monochromatic light, which show in below equation. Differently, the IQE is defined as the ratio of the generated electrons and the absorbed photons of device under the same condition. And the relationship between EQE and IQE is as followed :

$$\eta_{EQE} = 1240 \times \frac{J_{sc}}{P_{light} \times \lambda}$$

$$\eta_{EQE} = \eta_{IQE} * \eta_A$$

Note:  $\eta_A$ : photons absorption efficiency;  $P_{light}$ : the incident monochromatic light power in the case.

### 1.1.3 Device architectures of organic solar cells

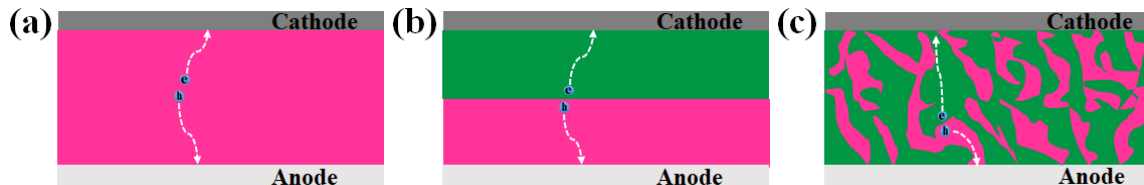


**Figure 1.3 Different device architectures of organic solar cells (a) single-layer device, (b) bilayer device, (c) bulk heterojunction device.**

Besides synthesizing new photovoltaic materials for high-efficiency photovoltaic devices, the development of device architectures also contributes to improving device performance. Until now three typical device architectures have been widely applied, such as a single layer, bilayer, and bulk heterojunction as schematically illustrated in Figure 1.3. Before the middle of the 1980 year, the single-layer architecture (Figure 1.3a) is the primary device configuration, which consists of a single photoactive material sandwiched between two electrodes with different work functions, typically indium tin oxide (ITO) and a low work functions metals, such as Al, Ca, and Mg.<sup>16-17</sup> The built-in electric field mainly derives from the work-function differences of two electrodes and the Schottky potential barriers between electrodes and photoactive materials and can provide a driving force for excitons dissociation and free charge carriers

transport toward their respective electrodes.<sup>18-19</sup> However, it is difficult to overcome the strong recombination of electrons and holes, resulting in the low device performance of single-layer devices.<sup>20</sup>

Since the breakthrough that a bilayer organic photovoltaic device was successfully fabricated with the efficiency of 1% in 1986, the bilayer device architecture was widely investigated.<sup>8,21</sup> It is the donor-acceptor bilayer heterojunction as the photoactive layer between two electrodes, which has two distinct advantages compared with the single-layer device (Figure 1.3b). Firstly, the energy offset between donor and acceptor results in the interface potential field at the planar D-A interfaces, which facilitates the dissociation of the efficient excitons. Secondly, Bilayer architecture provides a direct pathway for charge carrier transport. Namely, the electron-donor layer as a p-type organic semiconductor is used for free hole transport while the electron-acceptor layer as an n-type organic semiconductor for electron transport.<sup>22</sup> However, the short exciton diffusion length of photovoltaic materials indicates that only generated excitons near the D-A interface could be efficiently dissociated into charge carriers. Moreover, it limits the photoactive film thickness of ~ 100 nm, which is detrimental to efficiently absorb the incident photons. Finally, these restrain further improvement of bilayer device performance.<sup>23-24</sup>

To eliminate the influence of short exciton diffusion length on device performance, the most popular bulk heterojunction architecture was developed in the 1991 year.<sup>25</sup> That is, the photoactive film is a bicontinuous and interpenetrating network through the bulk mixing of donor and acceptor, which is beneficial for the improvement of device performance. Firstly, sufficient mixing between donor and acceptor introduces more D-A interfaces for efficient exciton dissociation. Secondly, the nanoscale phase separation (5-20 nm) between donor and acceptor in the bulk heterojunction architecture is closed to the exciton diffusion length, which means more excitons can diffuse to the D-A interfaces for dissociation, eventually decreasing the exciton decay probability. Lastly, the phase-separated domains in an interpenetrated network form the effective pathways, which promotes quick transport of the free electrons and holes to different respective electrodes and eventually minimizes charge carrier recombination.<sup>26</sup> Therefore, in a bulk heterojunction device, the preferable morphology of photoactive film with suitable phase separation largely influences device performance. Until now many strategies have been carried out to optimized the morphology of photoactive films, such as thermal annealing, solvent annealing, additives, tuning the ratio of donor to acceptor, the different solvents processing, film thickness, deposition methods, and so on.

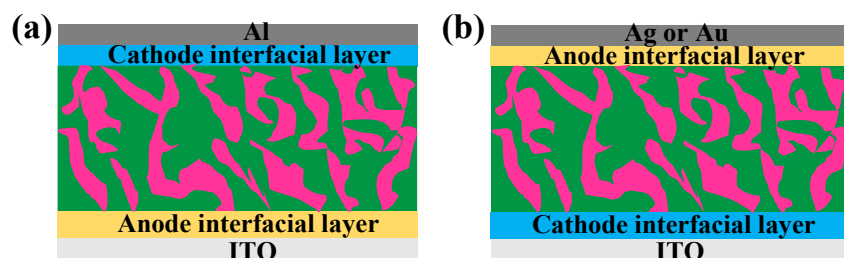


**Figure 1.4 (a) conventional forward device architecture, (b) Inverted device architecture of organic solar cells**

In addition, device architectures could be divided into conventional forward device architecture and inverted device architecture. As shown in Figure 1.4, in conventional forward device architecture, the ITO as an anode electrode collects free holes while the low work function metal (Al) as a cathode electrode for free electrons collection. Meanwhile, the Poly(3,4-ethylenedioxythiophene)-poly(styrenesulfonate) (PEDOT:PSS) to improve device performance, As shown in Figure 1.4, in the forward device architecture, the ITO as an anode electrode collects free holes while the low work-function metal (Al) as a cathode electrode for free electrons collection. Meanwhile, the PEDOT:PSS is always used as an anode interfacial layer to improve device performance. However, the PEDOT:PSS has some corrosive effect on the ITO electrode, and the low work-function metal electrode is easily oxidized. Therefore, the issues can decrease the stability of the device performance.<sup>27</sup>

To solve the above issues, the inverted device architecture was introduced since the 2006 year, in which the ITO as a cathode electrode collects free electrons and the high work-function metal electrodes (Au or Ag) are used as an anode electrode for free holes collection. Additionally, stable metal oxides (ZnO or TiO<sub>2</sub>) are used as the cathode interfacial layer. The difference with that of forwarding device architecture makes the inverted device more stable.<sup>28</sup> Now the inverted device architecture has been widely applied in the field of OSCs.

## 1.2 Classification of Organic Solar Cells

As all known, according to the development and types of organic photovoltaic (OPV) materials, the OPV devices are mainly divided into three different categories, such as the polymer solar cells, all polymer solar cells, and small molecular solar cells. Therefore, in the section, the three classifications of OSCs are introduced mainly based on the development of different types of OPV materials.

### 1.2.1 Polymer solar cells

Polymer solar cells (PSCs) generally consist of a conjugated polymer as an electron donor and a small molecular as an electron acceptor. The C<sub>60</sub> derivatives have been used as popular acceptors because of their strong electronegativity and high electron mobility.<sup>29</sup> At the beginning of the 1990s, the ultrafast electron transfer between a conjugated polymer and a fullerene derivative was demonstrated, and the researcher successfully fabricated planar heterojunction PSCs.<sup>30-31</sup> To further eliminate the limitations of the small D-A interface area and the low exciton dissociation efficiency in planar junction devices, the bulk heterojunction concept was introduced to firstly achieve efficient bulk heterojunction PSCs.<sup>32</sup> In addition, the morphology with suitable D-A phase separation was another key factor for obtaining preferable charge channels for transporting the free electrons and holes to different electrodes.<sup>33</sup> Therefore, through designing

new conjugated polymers and acceptors, optimizing photoactive film, and modification of the interface layers between photoactive films and electrodes, the device performance of PSCs made rapid progress. Among them, the synthesis of novel polymers and acceptors mainly dominated the development of PSCs.

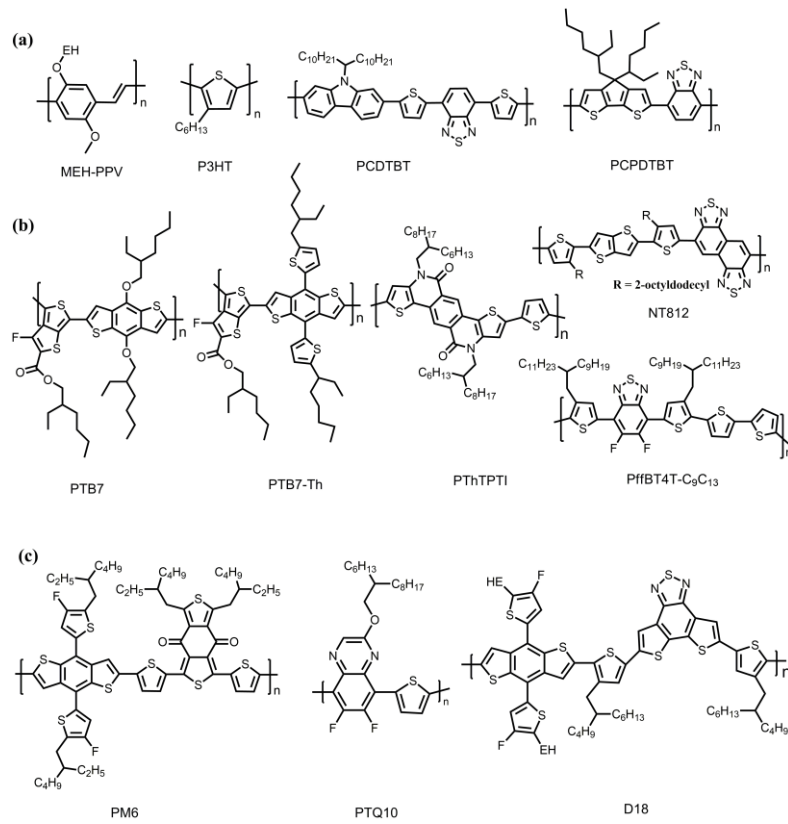


**Figure 1.5. The chemical structures of (a) Wide-bandgap polymers, (b) Narrow bandgap polymers, (c) Middle-bandgap polymers.**

Therefore, the device performance breakout of PSCs has always been mainly accompanied by the innovations in polymer donors and small molecular acceptors. Figure 1.5 indicates the chemical structures of some representative polymers. In the earliest stage of PSCs, the researchers developed the poly[2-methoxy-5-(2'-ethylhexyloxy)-p-phenylene vinylene (MEH-PPV) to blend with C<sub>60</sub> and its derivatives, resulting in the first high-performance PSC, which is a milestone in the application of polymer of organic photovoltaic devices.<sup>34</sup> After optimization, the efficiency of PPV-based PSCs was improved to more than 3%.<sup>35</sup> However, the relatively low hole mobility and narrow light absorption range prevented the further improvement of PPV-based PSCs' efficiency. Then the standard polymer poly(3-hexylthiophene) (P3HT) with an optical bandgap of 1.9 eV, was applied in OPVs, because it showed a higher hole mobility and a wider optical absorption spectrum than them of PPV-based polymers.<sup>36</sup> Combining with the fullerene derivative [6,6]-phenyl-C<sub>61</sub>-butyric acid methyl ester (PC<sub>61</sub>BM) as an acceptor, the typical PCEs of P3HT based devices reached to 3.5-4%. Through morphology optimization, interface modification, and blending

with [6,6]-phenyl C71-butyric acid methyl ester ( $\text{PC}_{71}\text{BM}$ ) acceptor, the related PCEs were achieved to 4-5%.<sup>33</sup> However, the limited absorption (below 600 nm) of P3HT wasn't beneficial for higher device efficiency.

To further improve light harvesting of PSCs, the D-A alternating conjugated polymers that incorporate one electron-rich moiety (D) and one electron-deficient moiety (A) have been developed via careful selection of relative monomers and proper side chains. As seen from Figure 1.5, the carbazole derivative with thermal and photochemical stability as an electron-donating unit could be conjugated with the benzothiadiazole moiety as an electron-deficient unit via a thiophene bridge, finally forming the material known as PCDTBT, the related PCE over 6% was achieved by combining with  $\text{PC}_{71}\text{BM}$  as an acceptor and interface modifications.<sup>37</sup> Similarly, conjugating a benzothiadiazole moiety to a dithiophene unit obtained the low-bandgap polymer of PCPDTBT with the absorption extends up to 900 nm, and the corresponding device efficiency achieved 5.5% by treatment of alkanedithiol additives.<sup>38</sup> For the narrow-bandgap polymer, the impressive polymer PTB7 composed of thieno[3,4-b]-thiophene(TT) and benzodithiophene (BDT) alternating units was designed, and the device efficiency based on the PTB7:[6,6]-phenyl-C71-butyric acid methyl ester ( $\text{PC}_{71}\text{BM}$ ) blend film reached up to 9.2%.<sup>39-40</sup> To further enhance the performance of D-A alternating conjugated polymers, the researcher added the two-dimensional BDT unit to obtain the donor PTB7-Th, which showed a better PCE of 9.35%.<sup>41</sup> In addition, some fused-ring units, such as pentacyclic aromatic lactam unit TPTI and naphtho[1,2-c:5,6-c']bis([1,2,5]thiadiazole) (NT), were introduced to construct the efficient donors (PThTPTI and NT812), and the related device PCEs reached up to 7.8% and 10.33%, respectively.<sup>42-43</sup> Moreover, based on the modification of side-chains, Yan *et al* systematically studied the effects of side-chains on the device performance of conjugated polymer PffBT4T. Combining the 2-nonyltridecanyl as a side chain, the named PffBT4T-C9C13 based device exhibited an efficiency of 11.7%, which is the highest device performance in the fullerene derivatives based PSCs.<sup>44</sup>

Besides the conjugated polymers, many efforts have been made to develop the efficient fullerene derivative acceptors shown in Figure 1.6a. For example, the  $\text{IC}_{60}\text{BA}$  was first reported and the 6.8% PCE was obtained in P3HT: $\text{IC}_{60}\text{BA}$  device.<sup>45</sup> And the  $\text{IC}_{70}\text{BA}$  with stronger light absorption was introduced to further improve to 7.4% for P3HT: $\text{IC}_{70}\text{BA}$ .<sup>46</sup> However, the modification of fullerene derivatives didn't change the weak light-harvesting capability of fullerene acceptors, which caused insufficient light absorption in fullerene based devices and then limits the improvement of the device performance. Hence, the non-fullerene acceptors with strong light-harvesting capability and complementary absorption with polymer donors were designed and shown in Figure 1.6b. Firstly, Zhan *et al* synthesized some A-D-A non-fullerene acceptors with a narrow bandgap and a strong visible (or near infrared) absorption, such as the ITIC and IDIC. And the related devices gave the PCEs of 6.8% and 11.03%, respectively.<sup>47-48</sup> Furthermore, the fluorine

substitution was introduced into A units to obtain the acceptor IT-4F, and the IT-4F based device afforded a PCE of 13.1%.<sup>49</sup> Additionally, Ding *et al* used the strong electron-donating core units, and the carbon-oxygen-bridge ladder-type units with stronger electron-donating capability and larger molecular plane to design the efficient A-D-A acceptor with a lower bandgap (1.26 eV). The resulted acceptor (CO<sub>8</sub>DFIC) based device exhibited a PCE of 12.16% with the higher  $J_{sc}$ .<sup>50</sup> In addition, the more exciting thing is that the highly efficient A-D-A acceptor Y6 was reported in two years. The related PCEs exceeded 15% by combining the suitable polymer donors.<sup>51-52</sup>

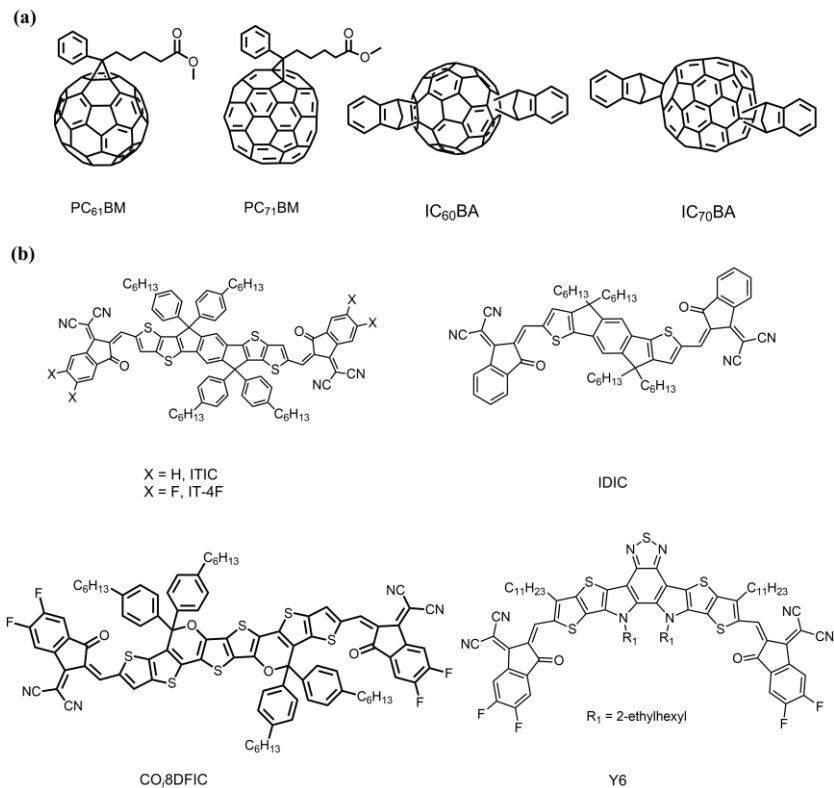


**Figure 1.6. The chemical structures of (a) The fullerene derivatives acceptors, (b) The non-fullerene acceptors.**

With the rapid improvement of non-fullerene acceptors based device performance, the matching middle-bandgap polymer donors that showed the complementary absorption with that of the low-bandgap non-fullerene acceptors are in demand and shown in Figure 1.5c, some of which have the preferable device efficiencies.<sup>53</sup> For example, the D-A copolymer PM6 was designed and then yielded a higher device efficiency of 17%.<sup>54</sup> Similarly, the polymer PTQ10 by simple synthesis and the related device that is combined with Y6 showed a PCE of 16.53%.<sup>55</sup> Recently, a more efficient polymer D18 with the fused-ring A unit dithieno[3',2':3,4;2',3':5,6]benzo[1,2-c][1,2,5]thiadiazole (DTBT) displayed a better molecular plane with higher hole mobility, and the related device gave the highest PCE of 18.22%.<sup>9</sup> However, there

is still room to improve the device efficiency by further exploiting the novel non-fullerene acceptors and the matching donors, and optimized the interface layers to improve the charge transport.

### 1.2.2 All polymer solar cells

Compared with the above polymer solar cells, all-polymer solar cells (all-PSCs) composed of a polymeric donor ( $P_d$ ) and a polymeric acceptor ( $P_a$ ) in the photoactive layer, exhibit the unique thermally and mechanically stable morphologies due to the higher solution viscosity, which have attracted great interest.<sup>56</sup> Before 2014, the improvement of all-PSCs efficiency was very sluggish, which exhibited a low PCE of around 1-2%.<sup>57</sup> It could be attributed to the major challenges of limiting device efficiency as followed: firstly, it showed the inferior electron transport mobility and low electron affinity of  $P_a$ s, which couldn't balance the charge carriers transport. In addition, the undesirable morphological feature with the large phase separation and the polymers ( $P_a$ s and  $P_d$ s) packing structure/orientation were commonly observed in photoactive layers, seriously influencing excitons dissociation at D-A interfaces.<sup>58-59</sup> To overcome the limitations, more efficient  $P_a$ s with high electron mobility were designed and more efficient  $P_d$ s that are easily compatible with new designed  $P_a$ s were discovered.<sup>60-62</sup> Then rapid improvements in the PCE of all-PSCs were attained.

An important breakthrough was made in exploiting many kinds of naphthalene diimide (NDI)- based  $P_a$ s as electron acceptors in all-PSCs, due to the preferable electron transport property and the high electron affinity of the NDI core unit. And some representative NDI-based  $P_a$ s are shown in Figure 1.7. Firstly, the side chain engineering of NDI-based  $P_a$ s as a simple approach effectively controls the crystallinity and morphology of photoactive films, such as tuning side chain length, changing branching point of the side chain, breaking the symmetry of side chains, and introducing heteroatoms into side chains.<sup>63-66</sup> The corresponding device efficiencies were improved. Secondly, the backbone modifications of NDI-based  $P_a$ s are another tactic for high-efficiency all-PSCs. One successful modification is combining the NDI core with small bulky units that include furan- vinylene-furan (FVF), thiophene-phenyl-thiophene (TPT), and thiophenes (Ts), which obviously decrease  $P_a$ s steric hindrance and then closely contact with  $P_d$ s. The PCEs of related all-PSCs exceeded 4%.<sup>67-69</sup> Furtherly, introducing various functional heteroatoms (such as fluorine, cyanovianylene, and selenophene) into the small bulky units can effectively modulate the energy levels and electrical properties of NDI-based  $P_a$ s (Figure 1.7). With appropriate  $P_d$ s, higher PCEs could be achieved.<sup>70-72</sup> Lastly, the random copolymers are designed to finely optimized various properties of NDI-based  $P_a$ s to maximize all PSCs' efficiency. For example, new n-type random copolymer PNDI-T10 with decreased crystallinity showed better miscibility with the  $P_d$  (PTB7-Th), resulting in a high PCE of 7.6%.<sup>73</sup> The random copolymer NOE10 synthesized by adding 10mol% of linear oligoethylene oxide (OE) chains into P(NDI2OD-T2) simultaneously optimized the polymer packing, phase separation, and vertical phase

gradation of a related photoactive layer, achieving a high PCE of 8.1%.<sup>74</sup> Differently, the copolymer PNDI-FT10 with fluorinated bithiophenes could increase the dielectric constant (from 2.88 to 4.10) of the photoactive film (PTB7-Th:PNDI-T10), finally enhancing the  $J_{sc}$  values of all-PSCs.<sup>75</sup>

Additionally, another kind of  $P_{as}$  is the perylene diimide (PDI)-based n-type polymers with desirable properties (high electron affinity and decent electron transport ability) for high-efficiency all-PSCs. So the design strategies of PDI-based  $P_{as}$  are highly similar to those of NDI-based  $P_{as}$ . Combining the PDI-based backbone with the small bulky units could produce the efficient PDI-based  $P_{as}$  (Figure 1.8), such as the PDI-V consisting of PDI unit and a simple vinylene linker, and the PPDIODT consisting of PDI unit and the small T group. The related all PSCs efficiencies reached to 6.58% and 7.57%, respectively.<sup>76-77</sup> To overcome the severe steric hindrance of PDI units with a nonplanar structure, the covalently fused PDI (FPDI) units were designed. Then both combining the small bulky units (such as selenophene unit) with FPDI unit and designing the new fused PDI-based  $P_{as}$  produced the high-efficiency all-PSCs.<sup>78</sup>

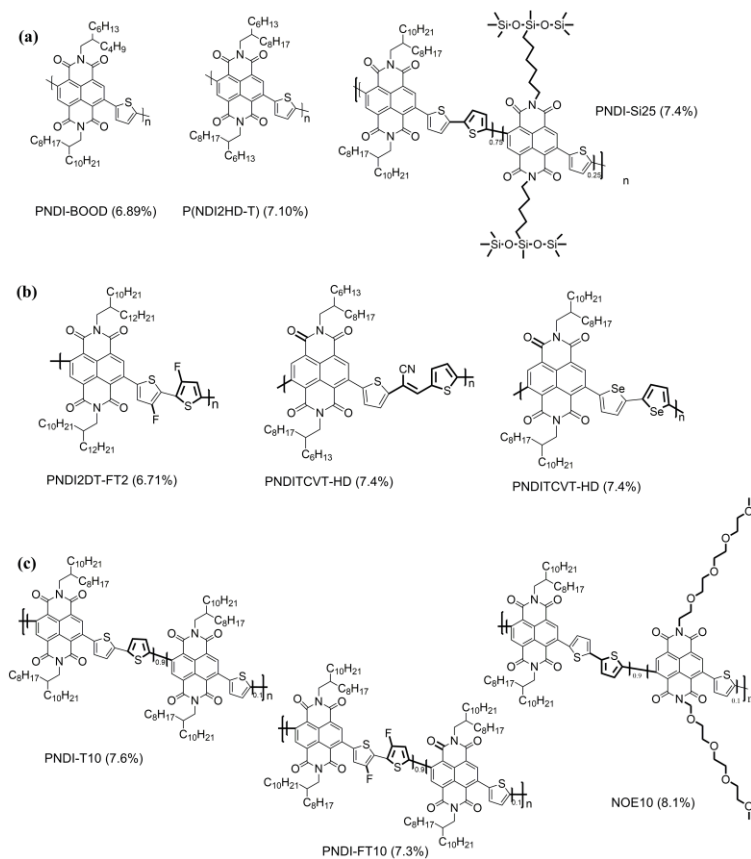


**Figure 1.7. Chemical structures of major NDI-based  $P_{as}$  in all-PSCs are categorized by their design strategies (a) Side-chain engineering, (b) Backbone modification engineering, (c) random copolymer engineering.**

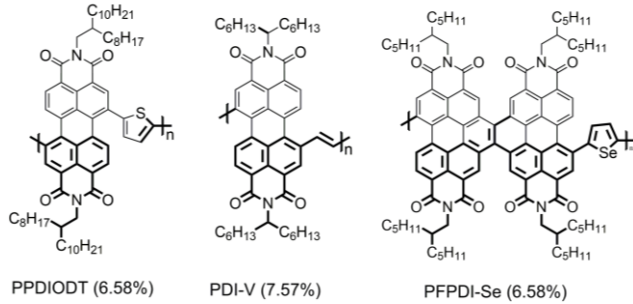


**Figure 1.8 Chemical structures of major PDI-based  $P_a$ s in all PSCs.**

However, due to the low absorption coefficient and the strongly localized electrons caused by the fixed low-lying LUMO energy levels in NDI/PDI-based  $P_a$ s, the three new classes of  $P_a$ s have been developed and shown in Figure 1.9. One is based on various aromatic imide-based moieties, including the diketopyrrolopyrrole (DPP), isoindigo (IID), and thieno[3,4-c]pyrrole-4,6-dione (TPD), and a ring-fused bithiophene imide (f-BTI).<sup>79-82</sup> Another kind of  $P_a$ s is based on the electron-deficient BNBP-based  $P_a$ s with high electron mobility and improved light absorption in the visible range, which resulted in a higher  $V_{oc}$  in related devices.<sup>83-84</sup> However, most of the devices based on the above kinds of  $P_a$ s exhibited lower PCEs than those based on NDI/PDI-based  $P_a$ s. Recently, the polymerization of non-fullerene materials could yield the  $P_a$ s with enhanced light absorption and obtained higher PCEs. For example, the PCE of single-junction all-PSCs based on the polymeric non-fullerene material (PF5-Y5) reached over 14%.<sup>85</sup> Furthermore, the new narrow-bandgap polymer acceptors (PZT- $\gamma$ ) were successfully synthesized by inserting the benzotriazole (BTz)-core fused-ring segment, and the corresponding devices achieved a high PCE of 15.8%.<sup>86</sup>

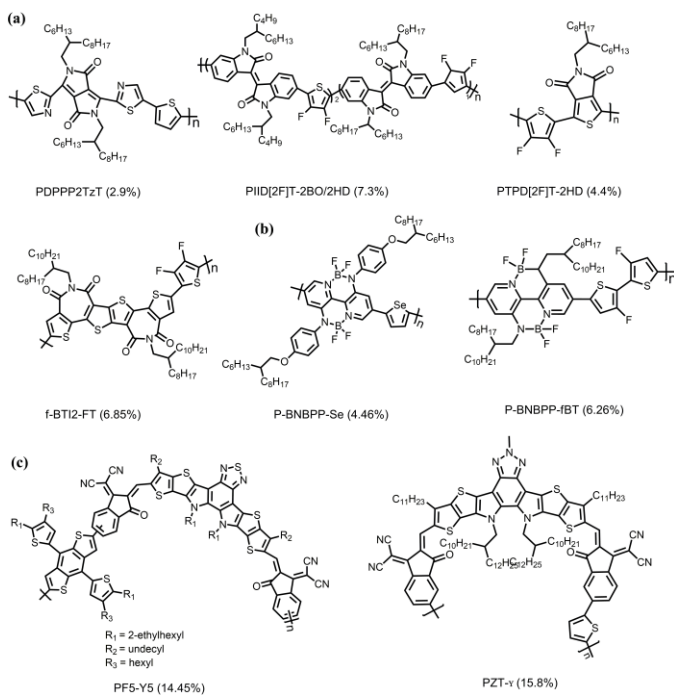


**Figure 1.9. Chemical structures of new classes P<sub>a</sub>s in all PSCs. (a) The P<sub>a</sub>s based on different aromatic imide-based moieties, (b) The electron-deficient BNBP-based P<sub>a</sub>s, (c) The polymerized non-fullerene P<sub>a</sub>s.**

Besides designing many P<sub>a</sub>s for high-efficiency all-PSCs, the progress of P<sub>d</sub>s also facilitates all-PSCs efficiency. It is found that many benzodithiophene (BDT)-based P<sub>d</sub>s have been applied in all-PSCs. Compared with the devices based on P<sub>d</sub>s without BDT backbone, the BDT-based P<sub>d</sub>s can produce higher-efficiency all PSCs, which are attributed that the BDT-based P<sub>d</sub>s have the suppressed crystalline-driven aggregation and good compatibility with NDI/PDI- based P<sub>a</sub>s.<sup>71, 87</sup> To further improve the all-PSCs efficiencies, the different strategies of BDT-based P<sub>d</sub>s structure modifications have been exploited, such as inserting thiophene π-bridge into the backbone between BDT units and electron-deficient units, the fluorination of BDT-based P<sub>d</sub>s, and the side-chain modifications of P<sub>d</sub>s.<sup>88-90</sup> And the corresponding devices based on BDT-based P<sub>d</sub>s showed the higher PCEs shown in Figure 1.10.

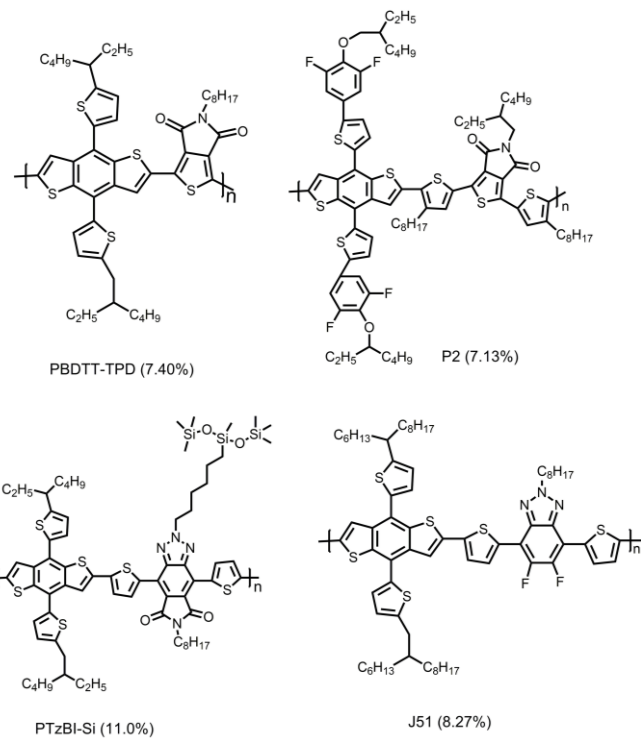


**Figure 1.10. Chemical structures of BDT-based P<sub>d</sub>s in all PSCs.**

In addition to the preferable P<sub>a</sub>s and P<sub>d</sub>s for high-performance all-PSCs, the preferable morphology for high-efficiency all-PSCs is the essential condition, which commonly exhibits finely phase-separated, high purity P<sub>d</sub> and P<sub>a</sub> domains, and the face-on orientation of both P<sub>a</sub> and P<sub>d</sub> for efficient charge separation and transport in all-PSCs. And several optimized strategies should be taken into account for phase-separated optimization. Firstly, the selection of P<sub>d</sub> and P<sub>a</sub> pairs with low interfacial tension could suppress the phase separation of all-PSCs.<sup>91</sup> Secondly, tuning the molecular weight and crystallinity of P<sub>d</sub>s and P<sub>a</sub>s also obtained the suitable

phase-separated morphology for high-efficient all-PSCs.<sup>62, 92</sup> Lastly, according to the two properties (the volatility and the solubility) of processing solvents, tuning the processing solvents is another method to achieve preferable all-polymer blend morphology with suitable phase-separation.<sup>93</sup> For the higher purity P<sub>d</sub> and P<sub>a</sub> domains to improve charge separation and transport without increasing charge recombination of all-polymer blend films, the high-boiling point solvent additives were introduced. Furtherly, the face-on polymer orientation promoted the vertical transport of free charge carriers to the different electrodes by the  $\pi$ -orbitals of conjugated polymers, which has been by different approaches, including controlling the molecular weight of the polymer, random copolymerization, side-chain engineering, fluorination, selection of processing solvent or additives, and post-treatments of blend films.<sup>64, 70, 94-97</sup> In a word, although the efficiency of all-PSCs is lower than that of PSCs based on non-fullerene acceptors. With the design of new P<sub>d</sub>s and P<sub>a</sub>s, optimized blend film with suitable phase separation, and face-on polymer orientation, the all-PSCs still exhibit huge potential in the improvement of device efficiency.

### 1.2.3 Small molecular solar cells

In comparison with the polymer solar cells, the small molecular solar cell that is composed of a small molecular donor and a small molecular acceptor possesses some promising advantages of easy purification, well-defined molecular structure, and small batch-to-batch variations of their device efficiency. So it is suitable for commercial-scale manufacturing.<sup>98-99</sup> And the device efficiency is mainly dependent on the development of small molecular donors.

In the sections, some representative small molecular donors were described and shown in Figure 1.11. Firstly, dye-based molecules were used in organic photovoltaic devices, such as phthalocyanine, subnaphthalocyanine (SubNc), and diketopyrrolopyrroles.<sup>100-102</sup> The dye-based molecules had a high efficiency of over 6% because of the strong absorption of the materials. Secondly, the fused acenes with high hole mobility, broad absorption, and good thermal stability have been successfully applied. For example, the polycrystalline pentacene and anthracene derivatives were explored and the corresponding devices exhibited the PCEs of 2.7% and 1.12% by combining the fullerene and its derivatives, which were attributed that the high crystallinity of fused acenes led to a large phase-separation scale when blending with fullerene acceptors.<sup>103-104</sup> Third, the one-dimensional oligothiophenes with pull-push units exhibited promising device efficiency. For example, the oligothiophenes with electron-withdrawing end groups yielded very high PCEs up to 6.10% by combining the PC<sub>61</sub>BM.<sup>105</sup> Moreover, the oligothiophenes with some fused rings showed better device performance.<sup>106</sup> Lastly, the triphenylamine (TPA) and its derivatives with the D-A-A structure displayed amazing results in device performance, with PCEs up to 6.4%.<sup>107</sup> Meanwhile, the three-dimensional pull-push small molecular donor with core TPA also gave a high PCE up to 4.3%.<sup>108</sup>

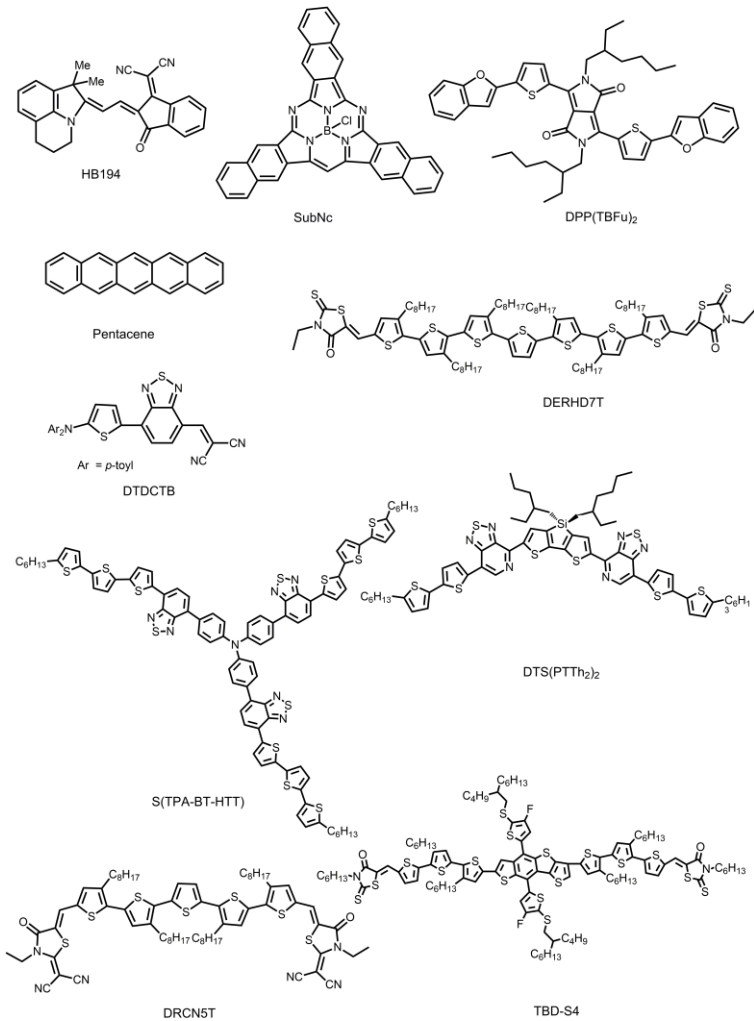


**Figure 1.11. The chemical structures of small molecular donors for small molecular solar cells**

In recent years, the new design strategies for new small molecular donors shown in Figure 1.11 were applied and the related device performance was hugely improved. For example, the dithienosilole-based small molecular solar cells (DTS(PTTh<sub>2</sub>)<sub>2</sub>) possessed a PCE of 6.7%.<sup>109</sup> Furtherly, the oligothiophene-based small molecular solar cells (DRCN5T) formed a well-constructed blend morphology in favor of exciton dissociation and diffusion and were the first to exhibit a PCE of over 10.0%.<sup>110</sup> and the novel BDT-based small molecular donor material (BDTID-Cl) was designed and the device showed a PCE of 10.5%.<sup>111</sup> Another novel A-D-A asymmetric small molecule donor TBD-S4 with 3-ethylrhodanine as the electron-withdrawing unit and furobenzodithiophene (FBD) as the asymmetric core was synthesized. It matched well with Y6, resulting in a PCE of 15.10%.<sup>112</sup> The results indicate that many efforts should be made to catch up with the device performance based on polymer solar cells with non-fullerene acceptors through further exploiting new small molecular photoactive materials.

## 1.3 Current Issues of Organic Solar Cells

### 1.3.1 Current situation of device efficiency

Nowadays, the efficiencies of OSCs reached over 18% for polymer solar cells, over 15% for all-polymer solar cells, and small molecular solar cells, respectively.<sup>9, 86, 113</sup> The efficiencies are still lower than that of inorganic solar cells (Si-based solar cells: 26.7% and Perovskite solar cells: 25.2%).<sup>113</sup> Many efforts should be made to explore various methods for high-efficiency OSCs. Designing novel photoactive materials is a primary method to break through the bottleneck of OSCs' efficiency. For example, through the development of non-fullerene acceptors, the efficiency of polymer solar cells break the limit of 10% and was hugely improved in recent years.<sup>114</sup> Similarly, the all-PSCs device efficiency was dramatically improved with the polymerization of non-fullerene acceptors, such as PF5-Y5 and PZT- $\gamma$ .<sup>85-86</sup> In the field of small molecular solar cells, designing more novel and efficient small molecular donor matching with non-fullerene acceptors was a promising way for higher device efficiency.<sup>112</sup>

In terms of photoactive layers, pursuing the ideal morphology of photoactive film with enough D-A interfaces and meanwhile an interpenetrating network is another effective approach, which obtains the high exciton dissociation and the effective charge carrier transport. For optimizing the morphology, many methods have been utilized, such as thermal annealing, solvent vapor annealing, and solvent additive engineering.<sup>115-117</sup> The thermal annealing process that the photoactive films are treated by the optimized thermal annealing temperature, not only improved the crystallinity of photoactive materials with better-ordered structure but also fine-tuned the phase separation for a better interpenetrating network.<sup>115, 118-119</sup> In addition, the solvent vapor annealing in which a photoactive film is placed in a chamber with a high-concentration solvent vapor that penetrates into the photoactive film, could prolong the reorganizational time for better molecular ordering and tune the nanoscale phase-separated photoactive film.<sup>116, 120</sup> They could be correlated with the solubility and polarity of polar solvents, such as the chloroform, pyridine, and methanol.<sup>121-123</sup> Another advantage is that it could be conducted without a high temperature. However, both methods add to the steps of the device fabrication process. Differently, solvent additive engineering without additional steps is the simplest and effective way for a high-efficiency device. Based on the fundamental principles of selected solvent additives that are the higher boiling point and lower vapor pressure than the host solvents and the selective solubility to one of the photoactive components, many kinds of solvent additives have been successfully developed, such as the nonaromatic solvent additives (1,8-diiodooctane (DIO), 1-methyl-2-pyrrolidone (NMP), 1-methylnaphthalene (Me-naph), and 1,2,3,4-tetrahydronaphthalene), and the aromatic solvent additives (chloronaphthalene (1-CN) and diphenyl ether (DPE)).<sup>117</sup> It was found that the different solvent additives in different devices showed a different role in the morphology evolutions of photoactive films.<sup>124-126</sup> Therefore, combining different solvent additives may

integrate the respective effects on photoactive films to further improve device efficiency. For example, binary solvent additive engineering was explored, such as the combinations of 1-CN and ODT, DIO and NMP, and DIO and pyridine.<sup>127-129</sup> However, the combined principle of binary solvent additive and how a single component affects the photoactive film are not fully clear for high-performance devices.

### 1.3.2 Current situation of device stability

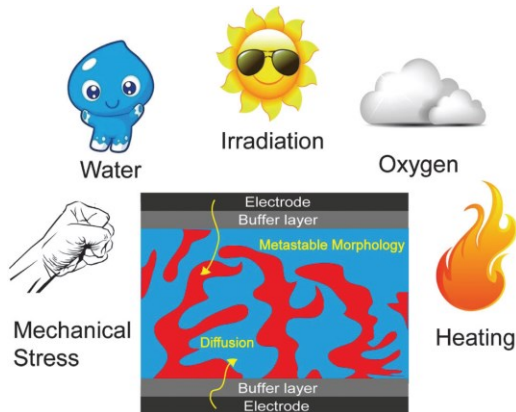


**Figure 1.12.** Schematic diagram of the degradation factors limiting the device stability. Reprinted from ref. 130. Copyright 2016 Royal Society of Chemistry.

Although the efficiency of OSCs has been achieved a huge improvement. The device stabilities in different ambient conditions are still the bottleneck for commercial application. In addition, air-processed device should be considered to decrease the cost in the future. As all known, the degradation factors of OSCs should be considered, which affect the photoactive layer, the transport layers, and the interface contacts between the adjacent layers. And they could be generally divided into intrinsic and extrinsic factors. For example, the extrinsic factors are oxygen and water diffusion, oxidation and rusting of a low work-function electrode (Al) due to water, delamination of metal electrode contacts due to oxygen and water, electromigration induced shunts, and mechanically induced stress.<sup>130</sup> Moreover, the photoinduced and thermal degradation of photoactive films under sunlight in ambient conditions, the chemical evolution of photoactive materials, and the photo bleaching as the intrinsic factors, also occurred in OSCs. Generally, as shown in Figure 1.12, the combined influences of intrinsic and extrinsic factors limited the device stability. To improve the stability of OSCs, the electrodes, the interfacial layers, the photoactive layer, and their interfaces should resist the influences of the above degradation factors. Until now, many strategies have been conducted to address the stability concerns of OSCs.

Firstly, the top electrode of conventional OSCs is made of the low work-function Al, through which oxygen and water can easily diffuse into the whole device and thereby decrease the device performance. To solve this problem, the inverted device structure was explored. That is, the more stable and higher work-

function metal was used as the top electrode, instead, in the inverted device, leading to much better stability. For example, in P3HT:PC<sub>61</sub>BM based inverted device, the Ag anode electrode enhanced the device stability.<sup>131</sup> Compared with Al electrode, the Ag top electrode was employed in PTB7:PC<sub>71</sub>BM based inverted devices, which simultaneously exhibited high device stability and efficiency.<sup>132</sup>

Additionally, the interfacial layers between electrodes and the photoactive layer as another aspect of device degradation significantly reduced device performance. And several alternatives have been carried out to enhance interfacial stability for more stable device. In conventional OSCs, the acidic and hygroscopic PEDOT:PSS, as the commonly employed hole transport layer (HTL), is detrimental to device stability, because it corrodes ITO substrate and further diffuses into a photoactive layer. So the high work-function metal oxides based HTLs, such as NiO, V<sub>2</sub>O<sub>5</sub>, WO<sub>3</sub>, CuO, and MoO<sub>3</sub>, were the main alternatives to efficiently enhance device stabilities, all of which could be deposited by solution. Similarly, the most common electron transport layers (ETLs), such as LiF, Ca, and ZnO, are unstable in ambient conditions because of their reactivity with oxygen, moisture, air, and illumination. To solve the issues, new metal oxides (such as CrO<sub>x</sub>, Cs<sub>2</sub>CO<sub>3</sub>, and TiO<sub>2</sub>) and many electron-extracting organic materials have been explored for stable ETLs.<sup>130</sup> And the modifications of metal oxides are the alternative way, such as the metal doping ZnO ETL, the modifications of ZnO (or TiO<sub>2</sub>) with many organic molecules, and other structures of metal oxides.<sup>133</sup> These not only achieved high device efficiency but also enhanced device stability.

Lastly, due to the short excitons diffusion length of OPV materials, the domain size of donor and acceptor in the photoactive film should be carefully optimized to realize the interpenetrating network morphology for efficient charge carrier transport and the suitable phase separation for efficient excitons dissociation. However, the metastable morphology of photoactive film is easily changed by the ambient conditions, including the photo-oxidation reactions of donor and acceptor, and the coarse phase separation. To diminish the above degradations of photoactive films, introducing the third component into a photoactive film is a popular pathway. For example, the addition of a modified fullerene derivative as a cross-linker improved the thermal stability of the device.<sup>134</sup> And the iodine-free solvent additive was used in PTB7-Th:PC<sub>71</sub>BM based photoactive film, resulting in improved air stability.<sup>135</sup> But these methods couldn't impede the chemical evolution of OPV materials that are still sensitive to the ambient conditions and most of them were fabricated in an inert atmosphere. Therefore, the most effective strategy is to design air-processable and stable OPV materials under various ambient conditions. And related researches have been carried out. Integrating stable units into the skeletons of donor polymers obtained the enhanced thermal stability and photo-stability of related devices.<sup>136</sup> the air-processed low band-gap polymer based device yielded 7.7%, and the air-processed devices based on the twisted perylene diimide (PDI) acceptors achieved the PCE of

7.49%.<sup>137</sup> Obviously, the related devices' efficiencies were still low and related device stabilities under various ambient conditions should be investigated. In a word, it is vast potential to further exploring stable OPV materials for high-efficiency, high-stability, and air-processed OSCs.

### 1.3.3 Issue of charge separation in non-fullerene based devices

In recent years, the development of non-fullerene acceptors has catalyzed the rapid improvement of OSCs device efficiency. An important feature of the non-fullerene based devices is the efficient charge separation at a small driving force with the low voltage loss, which is different from the fullerene derivatives based devices with a significant driving force. The related reasons have been probed now and the respective results or conclusions were shown as followed:

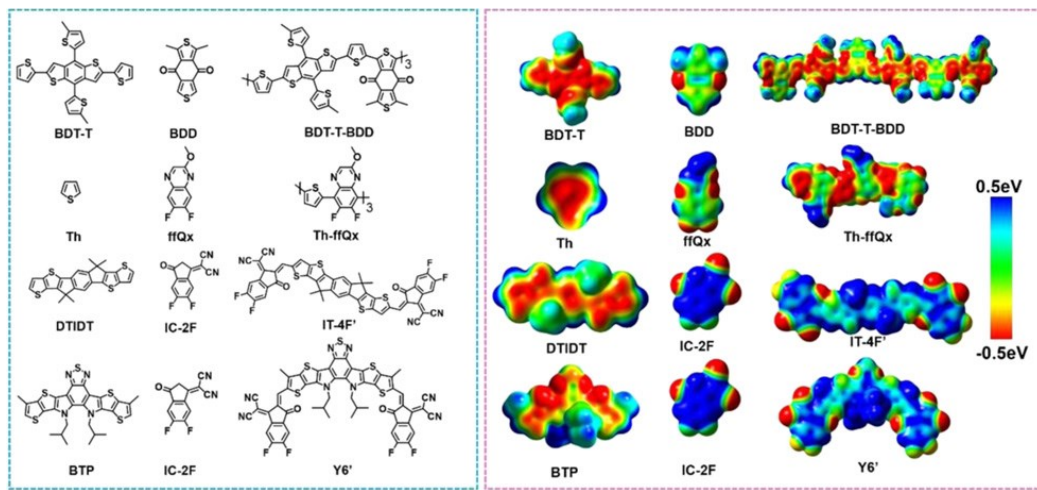


**Figure 1.13. Typical organic photovoltaic materials and their ESP distributions in vacuum.** Reprinted from ref. 138. Copyright 2020 IOP Publishing Ltd..

Firstly, Hou's group presented that the electrostatic potential (ESP) of photovoltaic materials played a crucial role in the charge separation of non-fullerene based devices.<sup>138</sup> As seen from Figure 1.13, the type donor-acceptor alternating polymers displayed the negative ESP values although some electron-withdrawing substitutes were attached to the polymers' backbones. They indicated their electron-donating properties. Differently, in most non-fullerene acceptors with the acceptor-donor-acceptor structures, some electron-rich units (such as DTIDT and BT) with the negative ESP have located the center position of non-fullerene acceptors. And the electron-poor units (such as IC-2F) with primary positive and high ESP regions were attached to the above electron-rich cores. So the resulted non-fullerene acceptors exhibited positive ESP, indicating a strong electron-accepting property. It was noted that the ESP differences between donor and non-fullerene acceptors at the D-A interface could form an intermolecular electrical field (IEF), which facilitates excitons dissociation. As seen from the study on the effect of the ESP on exciton dissociation in PTO<sub>2</sub>:IT-4F system (Figure 1.14), the large ESP difference in PTO<sub>2</sub>:IT-4F blend film caused a stronger

IEF compared with that of PTO<sub>2</sub>:PC<sub>71</sub>BM blend film, which may promote the formation of more loosely bound excitons and then suppressed excitons recombination.<sup>139</sup> Hence, tuning ESP of photovoltaic materials' molecular for large IEF is a feasible strategy to obtain high efficient charge separation at a low driving force. However, it only considers ESP of the blend between single donor and acceptor molecules and ignores the influence of intermolecular packing on charge separation.

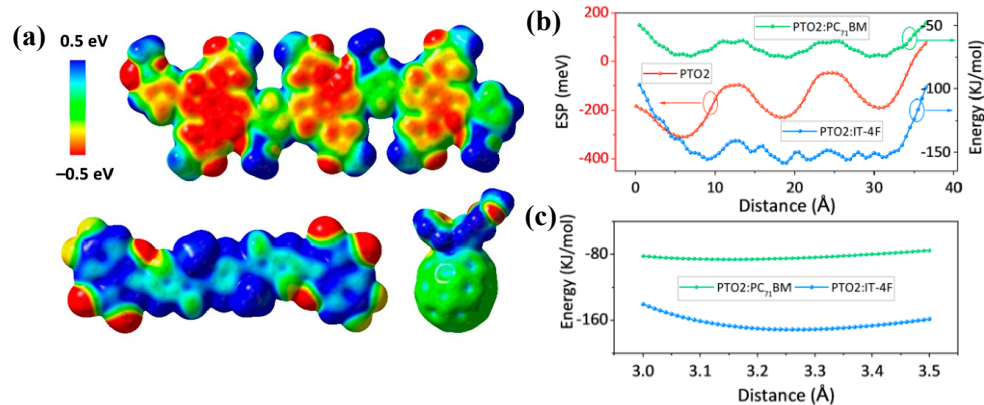


**Figure 1.14. ESP of the donor and acceptors and their impact on the intermolecular interactions. (a)** ESP distributions of the donor and acceptors **(b)** The intermolecular binding energies between PTO<sub>2</sub> and the acceptors at different points parallel to the PTO<sub>2</sub> backbone (ESP of PTO<sub>2</sub> in the moving direction is shown as red) at an intermolecular distance and **(d)** Vertical with backbone. Reprinted from ref. 139. Copyright 2019 American Chemical Society.

To further evaluate the effect of molecular packing of acceptor on the electronic processes in non-fullerene based devices, the PBDB-T:Y6 based device was investigated.<sup>140</sup> It was found that as similar in single crystals of Y6 molecules, the Y6 had distinctive molecular stacking in the blend film and the pristine film evidenced by grazing-incidence X-ray diffraction (GIXRD) results (Figure 1.15). So the delocalized and emissive excitons were formed and reduced the non-radiative voltage loss. In addition, it resulted in the efficient delocalization of electron wave-functions at D-A interfaces, significantly decreasing the interfacial Coulomb attraction of electron-hole pairs in the charge transfer (CT) state. Finally, these helped explain the dissociation of the highly efficient excitons in the above Y6 based device with a small driving force. Similarly, as seen from the time-resolved optical spectroscopy measurement of non-fullerene based devices, the free charge carriers were generated by the thermally activated dissociation of interfacial CT states, the related process was slower than the comparable fullerene-based devices. Meanwhile, an equilibrium between excitons, CT states, and the free charge carriers was set up. These findings indicated the long-lived and disorder-free CT states in non-fullerene based devices was formed, which closes to the quasi-thermodynamic conditions with no need for energy offsets to drive interfacial excitons dissociation and suppresses non-radiative recombination.<sup>141</sup>

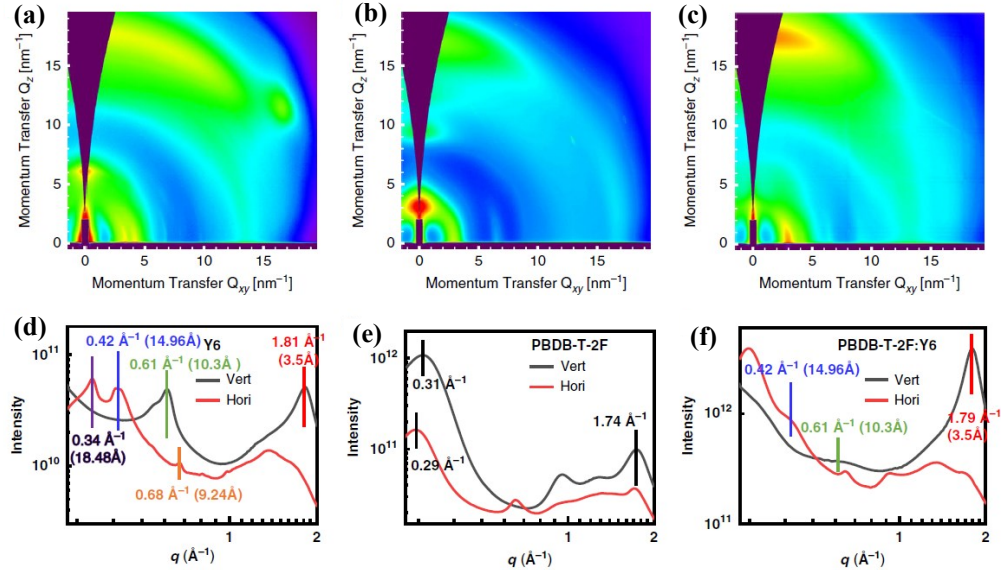


**Figure 1.15. GIXRD characterization of Y6 based systems.** (a)-(f) Two-dimensional GIXRD patterns (top) and profiles (bottom) of (a) and (d) The pristine Y6, (b) and (e) Pristine PBDB-T-2F, and (c) and (f) PBDB-T-2F:Y6 films, respectively. Reprinted from ref. 140. Copyright 2020, rights managed by Nature Publishing Group.

In addition, according to the broadband transient absorption (TA) measurement of PM6:Y6 based devices with high efficiency, an intra-moiety excimer (i-EX) state converted from the primary local excitation (LE) state was formed on an ultrafast time scale of  $\sim 0.2$  ps in Y6 pristine film and blend film, which is faster than formation time of interfacial charge transfer (xCT) state that was used as the intermediate state for charge transfer in conventional OSCs. It depended on the intermolecular coupling in Y6 domains. Therefore, in the Y6 based device, the i-EX state acted as the intermediate for hole transfer channel on  $\sim 15$  ps in blend film, and the interfacial electron transfer still mainly depended on the formation of xCT state due to the sufficient interfacial energy offset between LUMO levels of PM6 donor and Y6 acceptor.<sup>142</sup> These results not only explain the highly efficient hole transfer with a small HOMO energy offset but also present an alternative strategy for further improving device performance via manipulating the intra-moiety molecular interaction toward optimizing the energy landscape and electron coupling between the i-EX state and other exciting species.

Differently, reconsidering the common feature of efficient excitons dissociation under a small driving force with reduced energy loss in high-efficiency non-fullerene based devices, we infer that the dielectric constant ( $\epsilon_r$ ) of photovoltaic materials as a fundamental photophysical parameter and the efficient exciton diffusion as a fundamental photophysical process may be two factors that can't be ignored. Therefore, many efforts should be made to explore the effect of dielectric constant and efficient exciton dissociation on the above common feature of non-fullerene based devices.

## 1.4 Thesis Objectives and Organization

### 1.4.1 Objectives

Based on the above current problems in the field of OSCs, such as the pursuit of higher device efficiency, low stability of device performance, and the controversial charge separation in non-fullerene based devices, three research parts in the thesis are carried out as following:

#### **Part I: Investigating photovoltaic performance enhancement mechanism of polymer solar cells via the synergistic effect of binary solvent additives (DIO and AA)**

As all know, besides designing device structure and interface layers, and combing new photovoltaic materials with complementary light absorption, achieving the ideal morphology of photoactive film with suitable phase separation and interpenetrating network is another important strategy to improve device efficiency. Until now it is difficult to predict the optimized morphology although many methods have been used.<sup>33, 38, 143-144</sup> Among them, solvent additive engineering is the simplest and effective way for ideal photoactive film's morphology. However, most works mainly focused on the effect of the single solvent additive on device efficiency, and a few cases that binary solvent additive improved the device efficiency were reported.<sup>145-147</sup> Moreover, the principle of binary solvent additive and how the single component in binary solvent additive affects the device aren't clear. Therefore, to figure out the issue, a new binary solvent additive (DIO and AA) is explored, and the role of a single component and the general combination principle in binary solvent additive are investigated in detail.

#### **Part II: Fabrication of air-processed and stable organic solar cells with higher device performance through air-stability photovoltaic material (PDPPPTD polymer)**

In the last decades, the works on OSCs were mainly focused on the improvement of device efficiency. Most OSCs are fabricated in an inert atmosphere because of the air sensitivity of organic photovoltaic materials, which is not compatible with the large manufacturing process in the future. Although many strategies have been explored to improve the stability of photovoltaic devices, such as inverted device structure, stable interface materials and interface modification, more stable acceptor materials, and introduction of the third component.<sup>134-135, 148-150</sup> However, few researches about air-stable polymer donor are reported for high-stability devices. Hence, to collaborate with Prof. Mario Leclerc's group, the obtained air-stable PDPPPTD polymer donor, a metal oxide (ZnO) as an electron transport layer, and a favorable solvent additive (p-anisaldehyde: AA) are combined to pursue high-efficiency and more stable photovoltaic device.

#### **Part III: Synergistic effect of dielectric property and energy transfer on charge separation in non-fullerene based solar cells**

In recent years, thanks to the breakthroughs in non-fullerene acceptor materials, the device efficiency has been improved a lot, and the best efficiency of non-fullerene based device reached over 18%.<sup>9</sup> Interestingly, the remarkable features of the high-efficiency non-fullerene based devices exhibit a low voltage loss and efficient charge separation under a small driving force.<sup>151</sup> It is very different from the traditional fullerene derivatives based devices where enough driving force (generally > 0.3 eV) is needed for charge separation because of the low dielectric property of organic photovoltaic materials.<sup>152</sup> Although the researches about the dominant factors influencing the efficient charge separation of non-fullerene based devices at a small driving force with reduced voltage loss have been carried out, and it is still disputed. As considered from fundamental physical processes in non-fullerene based devices, the efficient exciton diffusion and the dielectric constants in the photovoltaic films are the important physical parameters for the efficient charge separation process. Therefore, to collaborate with Prof. Maojie Zhang's group, the synergistic effects of dielectric property and energy transfer on charge separation of non-fullerene based devices are investigated in detail.

#### 1.4.2 Thesis organization

The thesis is divided into six chapters which are organized as follows:

**Chapter 1** Introduction: This chapter introduces the basic background and knowledge of organic photovoltaic devices and the current problems in the field. In addition, the objectives also are presented here.

**Chapter 2** Experimental and characterization: This section describes the preparation of ZnO precursor solution and related film, a simple introduction of synthesizing PDPPPTD polymer, and different device fabrications, such as PffBT4T-2OD:PC<sub>61</sub>BM based device, PDPPPTD:PC<sub>61</sub>BM based device, and PM6:non-fullerene acceptors based devices. In addition, fabricating the photoactive films for dielectric constant measurement and the related bilayer heterojunction films are included. Finally, the main characterization techniques of photovoltaic films and devices are presented.

**Chapter 3** This chapter mainly discusses the investigation of the photovoltaic performance enhancement mechanism of polymer solar cells via the synergistic effect of new binary solvent additive (DIO and AA). Related results are published in the journal of *Solar RRL* (Sol. RRL 2020, 2000239).

**Chapter 4** This chapter is mainly about the fabrication of air-processed and stable organic solar cells with higher device performance through air-stability photovoltaic material (PDPPPTD polymer). Related results are published in the journal of *Small* (Small 2019, 15, 1804671).

**Chapter 5** This chapter mainly discusses the effect of high dielectric property and energy transfer on charge separation in non-fullerene based devices. Related manuscript is published in the journal of *Angew. Chem. Int. Ed.*.

**Chapter 6** Conclusions and Perspectives: Main conclusions are summarized based on the results and discussions, and potential works in the field of organic photovoltaic devices are proposed.

In this thesis, most of the work was completed by Pandeng Li, however, some materials and measurements were conducted through the collaborations. More specifically, the PDPPPTD polymer was synthesized from Prof. Mario Leclerc's group, and the PM6 donor and the non-fullerene acceptors were provided by Prof. Maojie Zhang's group. The plasmon energy-shift imaging (PESI) of photovoltaic films was measured by Jean-Philippe Masse at Polytechnique Montréal. Grazing-incidence x-ray diffraction (GIXRD) measurements were carried out by the Shanghai Synchrotron Radiation Facility (SSRF). Dr. Yusheng Wang assisted me with the measurement of scattering-type scanning near-field optical microscopy (s-SNOM). Dr. Jin Fang helped me fabricate some photovoltaic devices. Lastly, the density functional theory simulations are conducted by Prof. Sergei Manzhos from INRS-EMT.

## **2 CHAPTER 2 EXPERIMENTAL**

In the chapter, the experimental details for the preparation of related materials of photovoltaic devices and the different fabrication processes of photovoltaic devices are described. Firstly, the simple method of preparing the ZnO precursor solution for ZnO film as electron transport layers is introduced. And the synthesis of PDPPPPTD polymer from our collaborator (Prof. Mario Leclerc's group) is simply depicted. Secondly, fabrication processes of the PffBT4T-2OD:PC<sub>61</sub>BM based devices, the PDPPPPTD:PC<sub>61</sub>BM based devices, and the PM6:non-fullerene acceptors based devices are described in detail. In addition, I show the fabrication and dielectric constant measurement of photoactive films. In the end, many characterizations on film samples, and devices are presented. Devices testing conditions are also included.

### **2.1 Chemicals and Materials**

Patterned ITO coated glass substrates were bought from Shenzhen Huayu Union Technology Co., LTD (China) ( $R_s \leq 10 \Omega/\square$   $T_r \geq 83\%$ ). Zinc acetate dehydrate ( $Zn(CH_3COO)_2 \cdot 2H_2O$ , 99.9%), ethanolamine ( $NH_2CH_2CH_2OH$ , 99.5%), 2-methoxyethanol ( $CH_3OCH_2CH_2OH$ , 99.8%), 1,8-diiodooctane (DIO), p-Anisaldehyde (AA), chlorobenzene (CB), 1,2-dichlorobenzene (ODCB), dichloromethane (DCM), 1-chloronaphthalene (CN), and 1,8-diiodooctane (DIO) were bought from Sigma-Aldrich and used as received without any purification. PEDOT:PSS (VP Al 4083) and MoO<sub>3</sub> were purchased from H.C. Starck and Alfa Aesar, respectively. In chapter 5, the polydimethylsiloxane (PDMS) precursor and curing agent was obtained from Sylgard 184 Silicone Elastomer, the eutectic Ga-In (EGaIn) was purchased from Sigma-Aldrich, and the poly[(9,9-bis(3'-(N,N-dimethyl)-nethylammonium-propyl)-2,7-fluorene)-alt-2,7 (9,9-diethylfluorene)]dibromide (PFN-Br) was bought from Solarmer Materials Inc.. The electron donor PffBT4T-2OD polymer, PTB7 polymer, and electron acceptor PC<sub>61</sub>BM in chapter 3 and chapter 4 were bought from 1-Material Inc.. Differently, the PC<sub>61</sub>BM and another popular donor P3HT polymer used in Chapter 5 were obtained from Solaris Chem Inc.. According to previous reports, PM6 and the related acceptors (such as ITIC, IT-4F, F8IC, Y6, and IEICO) were synthesized by our collaborator--Prof. Maojie Zhang's group. Similarly, the PDPPPPTD Polymer was synthesized by our collaborator--Prof. Mario Leclerc's group.

### **2.2 Preparation of ZnO Precursor Solution**

The ZnO precursor solution was prepared by using a previously reported procedure.<sup>153</sup> Briefly, zinc acetate dehydrate ( $Zn(CH_3COO)_2 \cdot 2H_2O$ , 1 g) was dissolved in 2-methoxyethanol ( $CH_3OCH_2CH_2OH$ , 10 mL) followed by the addition of ethanolamine ( $NH_2CH_2CH_2OH$ , 0.28 g) under vigorous stirring overnight in ambient conditions. Then the resulted ZnO precursor solution was filtered with PTFE filter (0.45  $\mu m$ ) before use. By the way, in high humidity, the ZnO films should be fabricated in the glovebox.

## 2.3 Synthesis of PDPPPPTD Polymer

According to our previous work,<sup>154</sup> firstly, 3,8-dibromo-6-octyloxyphenanthridine (M1) and 3,8- dibromo-5-octylphenanthridin-6-one (M2) were easily synthesized from commercially available 2,7-dibromo-9-fluorenone via a simple two-step procedure (including a Schmidt reaction and alkylation reaction). In addition, 2,5-bis(2-octyldodecyl)-3,6-di(thien-2-yl)pyrrolo[3,4-c]pyrrole- 1,4-dione (M3) was obtained following a procedure reported in the literature.<sup>155</sup> To synthesize the electron donor PDPPPPTD ter-polymer (M<sub>n</sub>: 53 kDa and PDI: 3.2), the monomers, M1 (0.35 eq) and M2 (0.65 eq), were copolymerized with M3 (1 eq) via simple direct heteroarylation polymerization. The lowest unoccupied molecular orbital (LUMO) and the highest occupied molecular orbital (HOMO) levels of PDPPPPTD are -5.43 eV and -3.92 eV, respectively.

## 2.4 Devices Fabrication

### 2.4.1 Fabrication of PffBT4T-2OD:PC<sub>61</sub>BM based device

All the devices were fabricated onto patterned indium tin oxide (ITO)-coated glass substrates (1 inch × 1 inch) that were sequentially cleaned with detergent, deionized water, acetone, and isopropanol before being dried with a nitrogen stream. The resulted ZnO precursor solution was deposited onto the cleaned ITO/glass substrates, which were subsequently treated with O<sub>2</sub> plasma for 10 min. The ZnO film was then heated at 200 °C for 60 min in the air and the final thickness was ~30 nm. For the preparation of the precursor solution for photoactive layer deposition, PffBT4T- 2OD (30 mg/mL; mixed solvent: ODCB:CB = 1:1) and PC<sub>61</sub>BM (36 mg/mL; mixed solvent: ODCB:CB = 1:1) solutions were first separately stirred overnight at 120 °C and 60 °C, respectively. They were then mixed according to the pre-determined concentration ratio of PffBT4T-2OD-to- PC<sub>61</sub>BM (15:18 mg/mL) in the final mixture solution and stirred at 120 °C for at least 2 h. Meanwhile, different solvent additives (DIO, DIO+AA, and AA) with different concentrations were separately added in the above stock solution. Before spin-coating the stock solution, the ITO substrates covered with ZnO film and the tips of the pipette need to be preheated on a hotplate at 120 °C. The warm stock solution was then deposited onto ITO substrates covered with ZnO film at 800 rpm for 120 s. Finally, photoactive layers (~300 nm in thickness) were dried on the hotplate at 90 °C for 5 min. All the above steps were carried out in a glovebox. Device fabrication was completed by the thermal deposition of 15 nm of MoO<sub>3</sub> and 100 nm of Ag as the anode under a vacuum of about 1×10<sup>-6</sup> mbar. The effective device area was 0.06 cm<sup>2</sup>.

### 2.4.2 Fabrication of PDPPPPTD:PC<sub>61</sub>BM based device

The patterned ITO-coated glass substrates (1 inch × 1 inch) were cleaned with detergent, deionized water, acetone and isopropyl alcohol in sequence, for 15 min in total, in an ultrasonic bath before being dried with

a nitrogen stream. The resulted ZnO precursor solution was spin-coated onto the cleaned ITO/glass substrates which were subsequently treated with plasma for 20 min followed by thermal annealing at 200 °C for 30 min. For preparing the photoactive layer solution, PDPPPTD solution (20 mg/mL; solvent: ODCB) and PC<sub>61</sub>BM solution (40 mg/mL, solvent: ODCB) were first separately stirred at 175 °C and 60 °C, respectively. They were mixed according to the pre-determined concentration ratio of PDPPPTD:PC<sub>61</sub>BM (10:20 mg/mL) in the final mixture solution and stirred overnight at 150 °C. Then the blend solution was filtered through a 0.45 µm poly(tetrafluoroethylene) (PTFE) filter at elevated temperature. Before the deposition of photoactive layers, the photoactive solution and the substrates should be maintained at 90 °C. The filtered and warm photoactive solution was spin-coated onto the ZnO film at 2500 rpm for 60 s (thickness: 80-90 nm). For process optimization, certain photoactive layers were annealed at different temperatures (100 °C, 110 °C, 120 °C) for 10 min. All steps were conducted in the air. Finally, device fabrication was completed by thermal evaporation of 15 nm of MoO<sub>3</sub> and 100 nm of Ag as anode under a vacuum of about  $1 \times 10^{-6}$  mbar. The effective device area was 0.06 cm<sup>2</sup>.

#### 2.4.3 Fabrication of PM6:non-fullerene acceptors based devices

Patterned ITO-coated glass substrates were cleaned with a series of detergent, deionized water, acetone, and absolute ethyl alcohol for 15 min in an ultrasonic bath before being dried with a nitrogen stream. Then PEDOT:PSS solution was spin-coated onto the cleaned ITO/glass substrates treated with plasma for 15 min followed by thermal annealing at 150 °C for 10 min. All the different photoactive films were deposited onto PEDOT:PSS films according to optimized device conditions in the glove-box. The PFN-Br that is the ethanol solution with a concentration of 0.5 mg/mL, was then spin-coated onto the photoactive layers. Finally, the devices were completed by thermal evaporation of 100 nm Al under a vacuum of ca.  $1 \times 10^{-6}$  mbar. The effective device area was 0.04 cm<sup>2</sup>.

#### 2.4.4 Fabrication of photoactive films for dielectric constant measurement

The same steps mentioned above in the preparation of the device with EGaIn, were followed until the spin coating of photoactive solutions. All the measured films were spun from the optimized photoactive solutions that obtained higher device performance and the related pristine acceptor solutions in the glovebox. After the fabrication of films, polydimethylsiloxane (PDMS) channels was placed onto the above films. The PDMS model was fabricated by stirring precursor and curing agent (Sylgard 184 Silicone Elastomer) in a 10:1 (V:V) ratio, then was poured over the mask in a plastic petri dish, finally was heated at 60 °C for 2 h. The EGaIn was injected into the PDMS channels. To avoid any direct contact between liquid EGaIn and test clamp connector, the thin copper wire was buried in the top of the PDMS channels (Figure S5a), which could contact with the injected EGaIn in the PDMS channels and was used as the bridge of liquid EGaIn and test clamp connector. During the capacitance measurement, the EGaIn was injected into the

PDMS channels. One test clamp connector touched the ITO electrode, and another one contacted with copper wires electrode. The real capacitor device was shown in Figure S5b, in which the four clamps allowed the PDMS model to adhere tightly to the organic films. Besides, because the contacts, junctions, and feed wires (as the resistive or inductive influence factors) were in real capacitor devices, a suitable equivalent circuit model in which the above wires could be assigned to the different circuit elements (such as  $R_s$  and  $R_p$ ), was employed and the same wires were used in the whole measurement process. The strategies could provide the fixed value from the effects of the above wires, which is beneficial for accurately measuring the capacitance of organic films. The capacitance response was measured in the range of 100 Hz to 120 MHz by the precision impedance analyzer (Wayne Kerr 6500B series) with a small AC drive voltage of 10 mV. The measurements were carried out at ambient conditions. The measured capacitance versus frequency plots are fitted by a polynomial function. According to the fitted capacitance value ( $C$ ), the relative dielectric constant ( $\epsilon_r$ ) could be calculated by the equation ( $C = \epsilon_0 \epsilon_r A/d$ ), in which  $\epsilon_0$  is the absolute dielectric permittivity ( $8.85 \times 10^{-12}$  F/m),  $A$  is the knowing contact area, and  $d$  is the knowing thickness of the organic film.

#### 2.4.5 Fabrication of bilayer heterojunction films

In the floating film method, neat PM6 and Y6 were separately dissolved in CF at 60 °C and stirred overnight. Then neat PM6 solution (12 mg/mL) was spin-casted on polystyrene sulfonate (PSS) coated glass while Y6 solution (20 mg/mL) was spin-casted on pre-cleaned Si substrate. The neat PM6 and Y6 films were vacuum ( $1 \times 10^{-6}$  mbar) dried at room temperature for a day to remove the residual amount of processing solvent before fabricating a bilayer sample. PM6 film was floated onto DI water and picked up with the supported Y6 film, finally forming a bilayer of PM6/Y6 on the Si substrate. In the orthogonal solvent method, ITO substrates were sequentially cleaned by ultrasonication with distilled water, acetone, and isopropanol. PM6 dissolved in CB with a concentration of 10 mg/mL was spin-casted with different rotational speeds to fabricate the PM6 layers with different thicknesses. Then the selected non-fullerene acceptor (IT-4F) in DCM with a concentration of 6 mg/mL were deposited on PM6 layer.

### 2.5 Characterizations

In the below chapters, optical absorption spectra were recorded using a Lambda 750 UV-vis-NIR spectrophotometer (Perkin Elmer), a Cary 5000 UV-vis-NIR spectrophotometer (Varian), and UV-vis spectrometer (SPECORD S 600), respectively. The photoluminescence (PL) spectrum was measured by an IHR 320 (Horiba Instruments Inc.). Fourier transform Infrared (FTIR) spectroscopy with attenuated total reflection (ATR) mode (Thermo Scientific, Nicolet 6700/Smart iTR) was used to detect the variation in chemical structure of the organic materials in photoactive layers. External quantum efficiency (EQE) measurements were done using an IQE200B system (Newport Corporation) by scanning from 300 to 850

nm with a 10 nm resolution in chapter 3 and 4. Differently, in chapter 5, the Solar Cell Spectral Response Measurement System (QE-R3011, Enli Technology CO., Ltd.) was used to measure EQE by scanning from 300 to 1000 nm with a 10 nm resolution, the light intensity at each wavelength was calibrated with a standard single-crystal Si photovoltaic cell. Film thickness was measured by a profile meter (Dektak 150). The surface morphology and film roughness of the photoactive layers were analyzed using atomic force microscopy (AFM) with the ScanAsyst mode, and the phase images were taken using the tapping mode. The Derjaguin-Muller-Toporov (DMT) modulus mapping images of photoactive layers were carried out by the NanoScope Analysis software, PeakForce QNM air mode using NanoScope software. The surface morphology and optical amplitude images were derived from the scattering-type scanning near-field optical microscopy (s-SNOM) with the tapping mode, and the X-ray photoelectron spectroscopy (XPS) measurement was performed using a VG Escalab 220iXL equipped with an Al Ka source. The crystalline structure of the photoactive layers was characterized with the grazing-incidence X-ray diffraction (GIXRD) measurements that were performed at the BL14B1 beamline of the Shanghai Synchrotron Radiation Facility using X-ray with a wavelength of 1.24 Å. Samples were prepared on a Si substrate under the same conditions as those used for device fabrication. The 10 keV X-ray beam was incident at different grazing incidence angles of (0.15°, 0.05°) to maximize the diffraction intensity from the samples. Device *J-V* characteristics were measured using a Keithley 2400 source measure unit under AM 1.5 G simulated solar light in chapters 3 and 4. In chapter 5, Device J-V curves were using a SS- F5-3A (Enli Technology CO., Ltd.) Solar Simulator (AAA Grade, 50 mm × 50 mm photo-beam size) under 1 sun, AM 1.5G (air mass 1.5 global) (100 mW cm<sup>-2</sup>). 2×2 cm<sup>2</sup> Monocrystalline silicon reference cell (SRC-00019, covered with a KG5 filter window, Enli Technology CO., Ltd) was used to calibrate the light intensity. The FEG-TEM used for plasmon energy shift imaging (PESI) was a JEOL 2100-F operated at 200 kV. The FEG-TEM was used to acquire mappings of Electron Energy Loss Spectroscopy (EELS) spectra over an area of the samples (thickness: ~100 nm) using the Scanning TEM mode (STEM). The spectrometer employed to the acquisitions of the EELS spectra is an Enfina system from Gatan and has an energy resolution of 1 eV. From each individual EELS spectra part of the mappings, the position of the plasmon peak maxima was extracted which resulted in the generation of Plasmon Energy Shift Images (PESI). Impedance spectroscopy was measured in the range of 100 Hz to 120 MHz by the precision impedance analyzer (Wayne Kerr 6500B series) with an AC drive voltage of 10 mV. The electrochemical cyclic voltammetry (CV) was carried out on a Zahner Ennium IM6 Electrochemical Workstation with a glassy carbon disk, a Pt wire, and an Ag/Ag<sup>+</sup> electrode as working electrode, a counter electrode, and reference electrode respectively, in 0.1 mol L<sup>-1</sup> tetrabutylammonium hexafluorophosphate (Bu<sub>4</sub>NPF<sub>6</sub>) acetonitrile solution at a scan rate of 50 mV s<sup>-1</sup>.

### 3 CHAPTER 3 UNVEILING PHOTOVOLTAIC PERFORMANCE ENHANCEMENT MECHANISM OF POLYMER SOLAR CELLS VIA SYNERGISTIC EFFECT OF BINARY SOLVENT ADDITIVES

Pandeng Li, Yuliang Zhang, Ting Yu, Qingzhe Zhang, Jean-Philippe Masse, Yingguo Yang, Ricardo Izquierdo, Baoquan Sun, Dongling Ma Sol. RRL, **2020**, *4*, 2000239

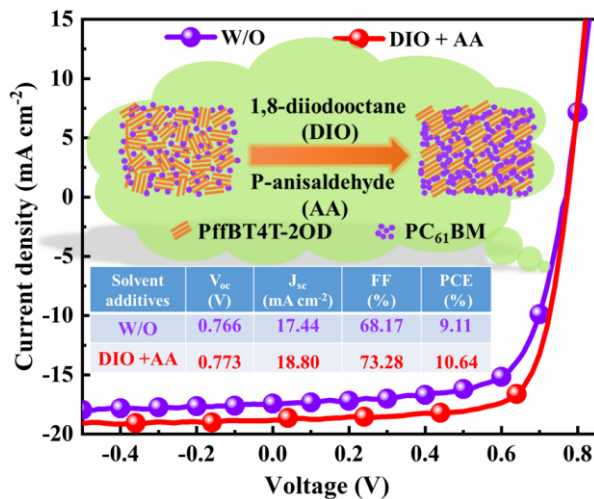


Figure of Table of Contents for This Section Work

As all know, except for designing the novel photoactive materials to improve the efficiency of organic photovoltaic devices, achieving the ideal morphology of photoactive film is another way and several methods have been used to adjust the morphology of photoactive film, such as thermal annealing, solvent annealing, and solvent additive engineering. Among them, the solvent additive engineering is a simple and effective method without increasing the complicity of the fabrication process. Until now many solvent additives have been explored, such as the aromatic solvent additives and non-aromatic solvent additives. They displayed the different effects on the improvement of device efficiency. Therefore, exploiting the binary solvent additive based on two kinds of solvent additives with different effects is a promising way to further optimize photoactive films for high-efficiency organic photovoltaic devices. However, the effect of a single component on the improvement of device performance and the combination principle of binary solvent additive are unclear yet. Therefore, in this section, we mainly focus on the device efficiency improvement of traditional fullerene based organic solar cells through the binary solvent additive strategy, and the new binary solvent additive of (DIO) and less-toxic, iodine-free p-anisaldehyde (AA) was explored to probe the influence on device performance of organic solar cells based on poly[(5,6-difluoro-2,1,3-benzothiadiazol-4,7-diyl)-alt-(3,3"-di(2-octyldodecyl)2,2';5',2";5",2"-quaterthio-phen-5,5"-diyl)] (PffBT4T-2OD) and [6,6]-phenyl-C<sub>61</sub>-butyric acid methyl ester (PC<sub>61</sub>BM). And synchrotron-based grazing incident X-ray diffraction, Derjaguin-Muller-Toropov modulus atomic force microscopy, and plasmon

energy shift imaging acquired in scanning transmission electron microscopy are used to investigate the effect of the binary solvent additive on the morphology of the composite film. It is found that AA additive mainly favors polymer order and the high crystallinity of PffBT4T-2OD. Meanwhile, DIO with selective solubility of PC<sub>61</sub>BM mainly enables PC<sub>61</sub>BM diffusing into PffBT4T-2OD polymer matrix and the large donor-acceptor (D-A) interfaces are obtained accordingly. As expected, by combining AA and DIO, the composite film provides a large D-A interface and a more balanced charge carrier transport. Consequently, the beneficial synergistic effect of binary solvent additive results in enhanced short circuit current and fill factor, and thereby increased power conversion efficiency of 10.64%, improved by 16% with respect to the control device. Herein, a general mechanism of enhancing photovoltaic device performance via the combination of solvent additives with different contributions to photoactive film is unveiled.

In this work, I got help from Dr. Yuliang Zhang for the preliminary work and some useful advice. In addition, Jean-Philippe helped to characterize photovoltaic films by plasmon energy shift imaging acquired in scanning transmission electron microscopy. And Dr. Yingguo Yang measured the synchrotron-based grazing incident X-ray diffraction data of the photovoltaic films. The related work was published in the journal of *Solar RRL* (Sol. RRL 2020, 2000239).

**Keywords:** effective donor-acceptor interface, balanced charge carrier transport, binary solvent additives, synergistic effect, preferable device performance

### 3.1 Introduction

In recent decades, bulk heterojunction (BHJ) organic photovoltaic (OPV) devices have attracted continuous attention because of their unique advantages over inorganic silicon-based photovoltaic devices, such as flexibility, light weight, a simple fabrication process and low fabrication cost, and the possibility of large-scale roll-to-roll production.<sup>[1]</sup> The certified power conversion efficiency (PCE) of single-junction OPV devices has been boosted to over 17%, demonstrating their great potential for practical applications.<sup>[2]</sup> Based on the fundamental of OPV devices, choosing favorable materials with a low bandgap or combining materials with complementary light absorption ranges (such as ternary solar cells) as photoactive layers to capture more light photons, and designing suitable device structure and interface layers to enhance carrier transport and collection are very effective strategies for highly efficient BHJ OPV devices.<sup>[3]</sup> The other important approach towards improved efficiency is centered around achieving the ideal morphology of photoactive film with suitable phase separation at the nanoscale that exhibits maximum donor-acceptor (D-A) interfaces for exciton dissociation and simultaneously an interpenetrating network for effective carrier transport.<sup>[4]</sup> So far it is still unlikely to predict exactly the optimum morphology for a specific D-A system, although numerous methodologies to pursue favorable nano-morphology by adjusting processing parameters have been used, including thermal annealing,<sup>[5]</sup> solvent vapor annealing,<sup>[6]</sup> and solvent additive engineering.<sup>[7]</sup>

The combination of solvent vapor and thermal annealing processes was also carried out.<sup>[8]</sup> Among them, solvent additive engineering is the simplest yet very effective way, which does not increase the steps and complexities of OPV device fabrication.

A general principle of solvent additive selection is that a solvent should have a higher boiling point and lower vapor pressure than the host solvent to prolong the solvent drying time for photoactive molecular reorientation. Meanwhile, selective solubility to one of the components is also necessary to induce better distribution during photoactive film formation. Following these guidelines, many kinds of solvent additives, such as 1,8-diiodooctane (DIO), 1-chloronaphthalene (1-CN), 1-methyl-2-pyrrolidone (NMP), 1-methylnaphthalene, 1,2,3,4-tetrahydronaphthalene, and diphenyl ether (DPE), have been used to tune the nano-morphology of photoactive layers.<sup>[9]</sup> However, the exact role of solvent additives in different OPV systems could be quite different. For example, it was found that nonaromatic solvent additives, such as DIO, octane dithiol (ODT), and 1,8-dichlorooctane (DCO), could improve the donor polymers order, promote the diffusion of fullerenes derivatives into aggregated polymer chains, and/or decrease domain size in photoactive films.<sup>[10]</sup> On the other hand, 1-CN and DPE, as the aromatic solvent additives, tend to facilitate better miscibility between donor and acceptor materials, produce pure domains of each component in the photoactive layer, form a bicontinuous network of the photoactive layer in a vertical direction, or reduce  $\pi$ - $\pi$  packing distance of the donor polymer.<sup>[11]</sup> Clearly, different morphology evolutions can be expected with the addition of various solvent additives. Combining different kinds of solvent additives may integrate their respective advantages to further optimize photoactive films for higher device performance. Indeed, as a promising approach, the binary solvent additives engineering has been attempted, including the combinations of DIO and 1-CN, 1-CN and ODT, and DIO and NMP, and better morphologies and device performance have been achieved.<sup>[12]</sup> Unfortunately, the role of the single component in binary solvent additives in the aforementioned reports has not been fully disclosed. Interestingly, in another work involving pyridine and DIO as binary solvent additives, pyridine was found to promote mixing between donor and acceptor materials, and DIO assembled fullerene derivatives and crystalline donor polymer. As such, a preferable morphology was obtained and device performance improved.<sup>[13]</sup> However, more insights into the principle of binary solvent additives and more understanding on how single components in binary solvent additives affect device performance are needed in this research area. As a result, it is highly desired to unveil the role of each additive to provide a general principle for solvent additive selection.

Here, we investigate the mechanism of a new combination of DIO and a non-toxic, iodine-free AA to enhance OPV devices based on PffBT4T-2OD and PC<sub>61</sub>BM. Their molecular structures are shown in **Figure 1a**. The ratio optimization of the binary solvent additives boosts the PCE from 9.11% to 10.64%. Various characterizations, such as optical absorption spectroscopy, grazing-incidence X-ray diffraction

(GIXRD), Derjaguin-Muller-Toporov (DMT) modulus atomic force microscopy (AFM), and plasmon energy mapping via scanning transmission electron microscopy (STEM), were conducted to probe the influence of binary solvent additives on the photoactive film. It was found that compared with the cases without any additives or with a single solvent additive, the crystallinity and nano-morphology of photoactive films were considerably varied due to the distinctly different contributions of DIO and AA, leading to improved device performance. The results unveil the nano-morphology of photoactive film tuned by the synergistic effect of binary solvent additives, which may provide a general principle for binary solvent additive engineering.

### 3.2 Experimental Section

#### 3.2.1 Reagent and Materials

Patterned ITO coated glass substrates were bought from Shenzhen Huayu Union Technology Co., LTD (China) ( $R_s \leq 10 \Omega/\square$   $T_r \geq 83\%$ ). Both the electron acceptor PC<sub>61</sub>BM and the electron donor PffBT4T-2OD were bought from 1-Material Inc. MoO<sub>3</sub> was purchased from Alfa Aesar. Zinc acetate dehydrate ( $Zn(CH_3COO)_2 \cdot 2H_2O$ , 99.9%), ethanolamine ( $NH_2CH_2CH_2OH$ , 99.5%), 2-methoxyethanol ( $CH_3OCH_2CH_2OH$ , 99.8%), 1,8-diiodooctane (DIO), p-Anisaldehyde (AA), chlorobenzene (CB), and 1,2-dichlorobenzene (ODCB) were bought from Sigma-Aldrich and used as received without any purification.

#### 3.2.2 Preparation of ZnO Precursor Solution

ZnO precursor solution was prepared by using a previously reported procedure.<sup>[15a]</sup> Briefly, zinc acetate dehydrate ( $Zn(CH_3COO)_2 \cdot 2H_2O$ , 1 g) was dissolved in 2-methoxyethanol ( $CH_3OCH_2CH_2OH$ , 10 mL), followed by the addition of ethanolamine ( $NH_2CH_2CH_2OH$ , 0.28 g) under vigorous stirring overnight in ambient conditions. Then the resultant ZnO precursor solution was filtered with a PTFE filter (0.45  $\mu m$ ) before use.

#### 3.2.3 Fabrication of Solar Cell Devices

All the devices were fabricated onto patterned indium tin oxide (ITO)-coated glass substrates (1 inch  $\times$  1 inch) that were sequentially cleaned with detergent, deionized water, acetone and isopropanol before being dried with a nitrogen stream. The resultant ZnO precursor solution was deposited onto the cleaned ITO/glass substrates, which were subsequently treated with O<sub>2</sub> plasma for 10 min. The ZnO film was then heated at 200 °C for 60 min in air and the final thickness was ~30 nm. For the preparation of the precursor solution for photoactive layer deposition, PffBT4T-2OD (30 mg/mL; mixed solvent: ODCB:CB = 1:1) and PC<sub>61</sub>BM (36 mg/mL; mixed solvent: ODCB:CB = 1:1) solutions were first separately stirred overnight at 120 °C and 60 °C, respectively. They were then mixed according to the predetermined concentration ratio of PffBT4T-2OD-to- PC<sub>61</sub>BM (15:18 mg mL<sup>-1</sup>) in the final mixture solution and stirred at 120 °C for at

least 2 h. Meanwhile, the different solvent additives (DIO, DIO + AA, and AA) with different concentrations were separately added to the above stock solution. Before spin coating the stock solution, the ITO substrates covered with ZnO film, and the tips of the pipette had to be preheated on a hotplate at 120 °C. The warm stock solution was then deposited onto ITO substrates covered with ZnO film at 800 rpm for 120 s. Finally, the photoactive layers (~300 nm in thickness) were dried on the hotplate at 90 °C for 5 min. All the above steps were conducted in a glovebox. The device fabrication was completed by thermal deposition of 15 nm of MoO<sub>3</sub> and 100 nm of Ag as the anode under vacuum of about  $1\times 10^{-6}$  mbar. The effective device area was 0.06 cm<sup>2</sup>.

### 3.2.4 Characterizations

Optical absorption spectra were recorded using a Lambda 750 UV-vis-NIR spectrophotometer (Perkin Elmer). Film thickness was measured by a profile meter (Dektak 150). Surface morphology and film roughness were analyzed using AFM with the ScanAsyst mode. The DMT modulus mapping images of photoactive films were conducted by the NanoScope Analysis software, PeakForce QNM air mode using NanoScope software. XPS was performed using a VG Escalab 220iXL equipped with an Al Ka source. The crystalline structure of the photoactive layers was characterized with GIXRD measurements that were carried out at the BL14B1 beamline of the Shanghai Synchrotron Radiation Facility using X-ray with a wavelength of 1.24 Å. Samples were prepared on a Si substrate under the same conditions as those used for device fabrication. The 10 keV X-ray beam was incident at a grazing incidence angle of 0.15° to maximize the diffraction intensity from the samples. Device J-V characteristics were measured using a Keithley 2400 source measure unit under AM 1.5G simulated solar light. EQE measurements were done using an IQE200B system (Newport Corporation) by scanning from 300 to 850 nm with a 10 nm resolution. The field-emission gun transmission electron microscopy (FEG-TEM) used for PESI was a JEOL 2100-F operated at 200 kV. FEG-TEM was used to acquire mappings of Electron Energy Loss Spectroscopy (EELS) spectra over an area of the samples (the thickness: ~100 nm) using STEM. The spectrometer used for the acquisitions of the EELS spectra was an Enfina system from Gatan and had an energy resolution of 1 eV. From each individual EELS spectra part of the mappings, the position the plasmon peak maxima was extracted which resulted in the generation of PESI.

### 3.3 Results and Discussion

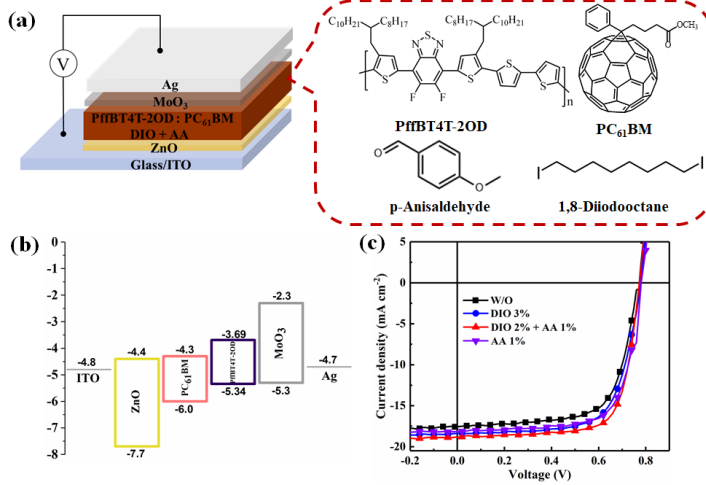


**Figure 1.** (a) Schematic illustration of the inverted device architecture with the photoactive film of PffBT4T-2OD:PC<sub>61</sub>BM, molecular structures of PffBT4T-2OD, PC<sub>61</sub>BM, DIO, and AA; (b) Corresponding energy level diagram of the device, all the values are taken from the references; (c) *J-V* characteristics of the PffBT4T-2OD:PC<sub>61</sub>BM devices with/without different solvent additives (DIO 3%, DIO 2% + AA 1%, and AA 1%).

The inverted device structure is shown in **Figure 1a** along with ZnO as a cathode interface layer and MoO<sub>3</sub> as an anode interface layer. Details of device fabrication can be found in Experimental Section. Both DIO and AA were selected as solvent additives herein. DIO is one of highly recommended additives based on the basic additive selection principle.<sup>[14]</sup> However, it is toxic, which can be a concern for the scale-up of device fabrication. Compared with DIO, AA is a less-toxic, iodine-free additive. As a new combination of binary solvent additives, the required amount of DIO was decreased. In addition, AA can bring extra advantages for device performance as will be discussed later. The energy levels of the device constituent components are shown in **Figure 1b**, and the favorable energy level cascade is formed, which facilitates charge carrier transport and reduces charge carrier recombination.<sup>[15]</sup> The *J-V* characteristics of the devices with different solvent additives are shown in **Figure 1c** and the electrical parameters are listed in **Table 1**. The device without solvent additive (W/O) as the control device yields a PCE up to 9.11% with an open-circuit voltage ( $V_{oc}$ ) of 0.766 V, a  $J_{sc}$  of 17.44 mA/cm<sup>2</sup>, and a fill factor (FF) of 68.17%, under simulated air mass (AM) 1.5 irradiation (100 mW•cm<sup>-2</sup>). With the incorporation of 3 vol% (denoted as 3% hereafter) DIO, a PCE of 9.84% is obtained, which is mainly attributed to the enhanced  $J_{sc}$  from 17.44 mA/cm<sup>2</sup> to 18.41 mA/cm<sup>2</sup>. In contrast, the device with 1 vol% AA (denoted as 1% hereafter) yields a PCE of 10.00% because of simultaneous improvements of  $J_{sc}$ ,  $V_{oc}$ , and FF (optimized concentration, **Figure S1**, and **Table S1**, Supporting Information). These results reveal that DIO and AA played different roles on these parameters (especially on  $J_{sc}$  and FF), which should be correlated with the differences in their boiling points and vapor pressure that influence the solvent drying time of the photoactive film. As expected, the PCE

was further improved to 10.55% by using binary solvent additives of DIO (3%) and AA (1%). After ratio optimization (DIO 2% + AA 1%), PCE was further improved to 10.64%. The statistical electrical outputs of the devices with and without different additives (W/O, DIO 3%, DIO 2% + AA 1%, and AA 1%) are shown in **Figure S2**, Supporting Information, which exhibited good device reproducibility. In addition, the external quantum efficiency (EQE) of the device was improved after incorporating binary solvent additives. The  $J_{EQE}$  values integrated from the EQE spectra of the devices without and with different solvent additives were consistently lower than those from the J-V curves, as shown in **Figure S3a**, Supporting Information, likely caused by the device degradation during the EQE measurements in air, resulting in the rapid reduction of  $J_{sc}$ .<sup>[16]</sup> However, the variation tendency of the  $J_{EQE}$  values is the same as that of the  $J_{sc}$  from the corresponding devices.

**Table 1.** Summary of the photovoltaic parameters of PffBT4T-2OD:PC<sub>61</sub>BM devices with/without different solvent additives (DIO 3%, DIO (3 %, 2%, 1%) + AA 1%, and AA 1%) as well as the ratio of PffBT4T-2OD polymer film absorption maxima (1) and (2),  $\alpha_1/\alpha_2$ , as defined in **Figure S3b**.

Solvent Additives	V <sub>oc</sub> [V]	J <sub>sc</sub> [mA/cm <sup>2</sup> ]	FF [%]	PCE [%]	$\alpha_1/\alpha_2$
W/O	0.766 <sup>a)</sup> (0.767 ± 0.003) <sup>b)</sup>	17.44 (17.01 ± 0.41)	68.17 (68.47 ± 1.16)	9.11 (8.93 ± 0.15)	1.03
DIO 3%	0.778 (0.769 ± 0.008)	18.41 (18.25 ± 0.23)	68.70 (68.60 ± 0.61)	9.84 (9.63 ± 0.16)	1.10
DIO 3%+AA 1%	0.771 (0.775 ± 0.004)	18.74 (18.28 ± 0.24)	73.03 (73.06 ± 0.48)	10.55 (10.30 ± 0.12)	
DIO 2 %+AA 1%	0.773 (0.773 ± 0.002)	18.80 (18.58 ± 0.17)	73.28 (72.79 ± 0.42)	10.64 (10.46 ± 0.14)	1.12
DIO 1%+AA 1%	0.785 (0.780 ± 0.003)	18.50 (18.14 ± 0.27)	72.42 (72.48 ± 0.31)	10.51 (10.25 ± 0.18)	
AA 1%	0.783 (0.781 ± 0.001)	17.90 (17.91 ± 0.15)	71.35 (70.82 ± 0.48)	10.00 (9.91 ± 0.10)	1.08

<sup>a)</sup>The maximum value of device performance. <sup>b)</sup>The average value is obtained in twelve devices from two batches.

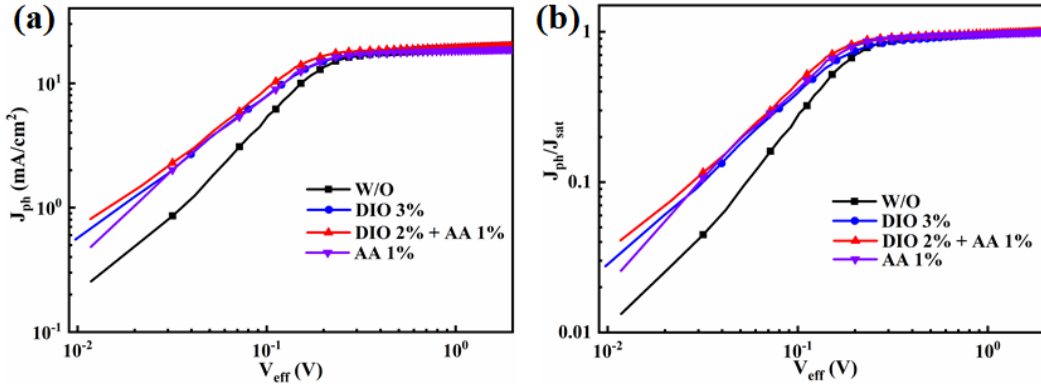


**Figure 2.** (a) Plots of  $J_{ph}$  against  $V_{eff}$  for the photovoltaic devices with/without different solvent additives (DIO 3%, DIO 2% + AA 1%, and AA 1%), (b) Corresponding plots of  $J_{ph}/J_{sat}$  with respect to  $V_{eff}$  in the devices.

Firstly, to probe the effect of different solvent additives on exciton dissociation and charge collection properties, the photocurrent density ( $J_{ph}$ ) versus effective applied voltage ( $V_{eff}$ ) was investigated.  $J_{ph}$  is the difference between  $J_L$  and  $J_D$ , where  $J_L$  and  $J_D$  are the photocurrent density under light illumination and in the dark, respectively, and  $V_{eff} = V_0 - V_a$ , where  $V_0$  is the voltage at  $J_{ph} = 0$  and  $V_a$  is the applied voltage.<sup>[17]</sup> As shown in **Figure 2a** and **Table S2**, Supporting Information,  $J_{ph}$  increased linearly with increasing  $V_{eff}$  and then reached saturation ( $J_{sat}$ ) current level when  $V_{eff}$  approached 2 V.  $J_{sat}$  of the devices with different solvent additives were 19.22 (W/O), 20.10 (DIO 3%), 19.77 (DIO 2% + AA 1%), and 18.81 mA/cm<sup>2</sup> (AA 1%), respectively. Moreover, as shown in **Figure 2b** and **Table S2**, Supporting Information, the corresponding exciton dissociation probabilities estimated by  $J_{ph}/J_{sat}$  under the short circuit condition were 95.23%, 95.31%, 96.49%, and 96.70%, respectively. The probabilities of charge collection estimated by  $J_{ph}/J_{sat}$  at the maximal power output condition were 70.66% (W/O), 74.50% (DIO 3%), 83.95% (DIO 2% + AA 1%), and 81.14% (AA 1%), respectively.<sup>[18]</sup> Obviously, the device with DIO displayed the maximal  $J_{sat}$  but the lower probabilities of exciton dissociation and charge collection with respect to those involving the AA additive. On the contrary, the device with AA exhibited minimal  $J_{sat}$  but higher exciton dissociation and charge collection probabilities. Hence, their combination leads to increased probabilities of exciton dissociation and charge collection efficiency as well as balanced charge carrier transport, which results in improved  $J_{sc}$  and FF.

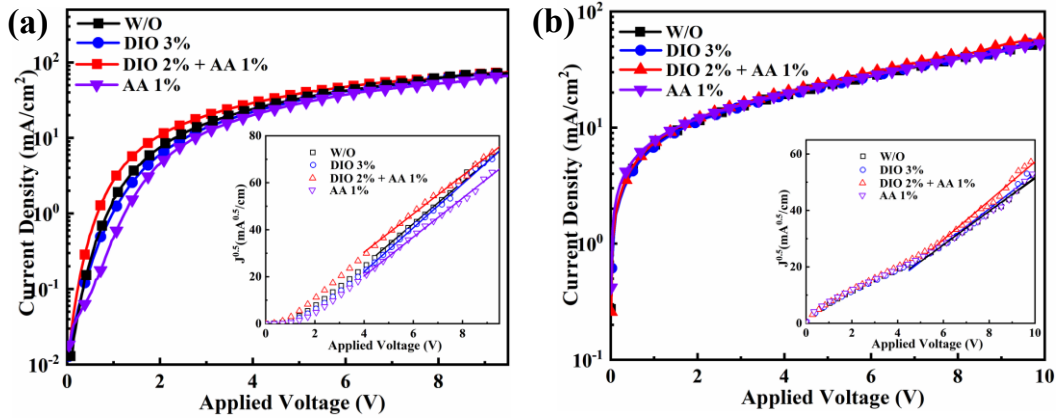


**Figure 3.** (a)  $J_D$ - $V$  characteristics of electron-only devices of ITO/ZnO/PffBT4T-2OD:PC<sub>6</sub>1BM/LiF/Ag by SCLC model, (b)  $J_D$ - $V$  characteristics of hole-only devices of ITO/PEDOT:PSS/PffBT4T-2OD:PC<sub>6</sub>1BM/MoO<sub>3</sub>/Ag by SCLC model. The insets are the corresponding  $J^{0.5}$ - $V$  characteristics for SCLC single-carrier mobility and fitting lines.

In addition, because charge transport properties in photoactive layers would be affected by different solvent additives, hole and electron single-carrier mobilities were measured. The values were extracted from  $J$ - $V$  characteristics of single-carrier devices using the space-charge-limited current (SCLC) model according to Mott-Gurney square law ( $J = (9/8)\epsilon_0\epsilon_r\mu(V^2/L^3)$ ), where  $\epsilon_0\epsilon_r$  is the dielectric permittivity of the photoactive layer,  $\mu$  is the drift mobility of each charge carrier,  $V$  is the effective applied voltage, and  $L$  is the thickness of the photoactive layer.<sup>[19]</sup> The detailed results are summarized in **Figure 3** and **Table S3**, Supporting Information. Compared with the electron ( $\mu_e$ ) and hole ( $\mu_h$ ) mobilities of the control device, both  $\mu_e$  and  $\mu_h$  increase simultaneously after adding DIO solvent additive. However, the ratio ( $\mu_e/\mu_h$ ) remains almost constant, which is consistent with the small difference of FF observed with the introduction of DIO. In contrast, the  $\mu_e/\mu_h$  ratio of the device with AA drops to 2.06, implying more balance between electron and hole mobility and thus explaining the achievement of higher FF. Based on this analysis, upon the incorporation of binary solvent additives,  $\mu_h$  increases to  $3.17 \times 10^{-3} \text{ cm}^2 \text{ V}^{-1}\text{s}^{-1}$  and  $\mu_e$  decreases to  $5.27 \times 10^{-3} \text{ cm}^2 \text{ V}^{-1}\text{s}^{-1}$ , and the minimum ratio ( $\mu_e/\mu_h$ : 1.66) is achieved, being consistent with the highest FF of 73.28%. In a word, DIO could simultaneously improve the  $\mu_e$  and  $\mu_h$ , whereas the AA incorporation results in a slight increment of hole mobility and decreased electron mobility. The combined effects of these different factors lead to improved device performance.

Ultraviolet-visible (UV-vis) absorption spectra were probed for the composite films with different solvent additives (W/O, DIO, DIO+AA, and AA), as shown in **Figure S3b**, Supporting Information. Two main absorption peaks of PffBT4T-2OD polymer at  $\sim 689$  nm (1) and  $\sim 625$  nm (2) display the different relative amplitudes  $\alpha_1$  and  $\alpha_2$ . The peak ratios ( $\alpha_1/\alpha_2$ ) from different samples are listed in **Table 1**. As the peak at  $\sim 689$  nm is ascribed to  $\pi$ - $\pi$  stacking of polymer molecules, higher values of  $\alpha_1/\alpha_2$  ratios suggest improved polymer order.<sup>[20]</sup> Compared with a peak ratio (1.03) of PffBT4T-2OD polymer in the control photoactive

film, the ratios in photoactive films deposited using different solvent additives (DIO, AA, and DIO + AA) were increased to 1.10, 1.08, and 1.12 respectively, which reveals that the single solvent additive facilitated  $\pi$ - $\pi$  stacking of PffBT4T-2OD polymer molecules. In the presence of binary solvent additives, the polymer  $\pi$ - $\pi$  stacking was further enhanced. Such increased polymer order can in principle promote charge carrier transport, yielding a higher  $J_{sc}$  and FF.<sup>[14, 21]</sup> Therefore, the fact that the photoactive film deposited using binary solvent additives exhibits the strongest absorption intensity is consistent with the highest EQE, implying that the use of solvent additives might lead to a more favorable morphology of the photoactive film.

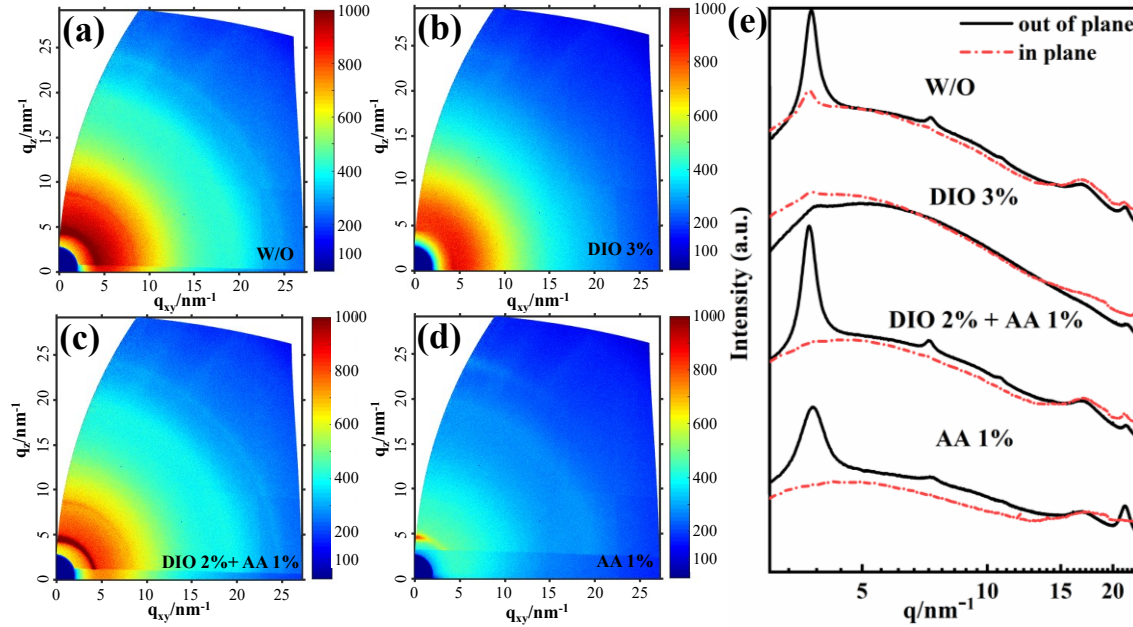


**Figure 4.** Synchrotron-based 2D GIXRD patterns of the PffBT4T-2OD:PC<sub>61</sub>BM photoactive films with/without different solvent additives: (a) W/O, (b) DIO 3%, (c) DIO 2% + AA 1%, and (d) AA 1%, respectively; (e) Synchrotron-based GIXRD patterns along OOP and IP scattering geometry for different photoactive films.

To investigate the effect of solvent additives on the morphology of photoactive films, the synchrotron-based GIXRD of photoactive films with different solvent additives was measured. GIXRD patterns in in-plane (IP) and out-of-plane (OOP) directions are shown in **Figure 4** and **Figure S4**, Supporting Information. Different processing conditions of photoactive films and polymers of different molecular weights likely exhibited different GIXRD results.<sup>[22]</sup> Along the OOP direction of the control photoactive film with low polymer molecular weight deposited at a low spin-coating speed from a higher concentration solution at 120 °C, the diffraction peak values ( $q$ ) of  $\sim 3.8 \text{ nm}^{-1}$ ,  $\sim 7.3 \text{ nm}^{-1}$ ,  $\sim 10.9 \text{ nm}^{-1}$ , and  $\sim 21.5 \text{ nm}^{-1}$  correspond to the lamellar stacking ((100), (200), (300)), and  $\pi$ - $\pi$  stacking (010) of PffBT4T-2OD polymer, respectively.<sup>[15b]</sup> The diffraction peak of PC<sub>61</sub>BM is located at  $\sim 17.0 \text{ nm}^{-1}$ . Moreover, the strong lamellar

and  $\pi$ - $\pi$  stacking peaks are still shown in the IP direction. The results suggest that the PffBT4T-2OD polymer possesses high crystallinity and there is co-presence of both face-on and edge-on stacking in the control photoactive film. Very differently, after treatment with DIO, the diffraction peaks of PC<sub>61</sub>BM and the lamellar packing peaks (1 0 0) of PffBT4T-2OD polymer along both the OOP and IP directions were dramatically suppressed. The results reveal that the more isotropic orientation of PffBT4T-2OD polymer crystallites that display the Debye-Scherrer like rings was formed.<sup>[23]</sup> Meanwhile, DIO incorporation allowed more PC<sub>61</sub>BM to diffuse into PffBT4T-2OD polymer side chains in all directions, which led to improved exciton dissociation at D-A interfaces. In addition, only the  $\pi$ - $\pi$  stacking peak in the OOP line profile remained unchanged; it means that the polymer order along OOP direction didn't change, which is beneficial for hole transport.<sup>[24]</sup> When the photoactive film was treated with AA, the intensity of the lamellar stacking peak along the OOP direction was slightly decreased and the corresponding  $\pi$ - $\pi$  stacking peak obviously increased. However, the lamellar stacking peaks along IP direction disappeared. Compared with that of DIO solvent additive, these results may reveal better polymer order and increased crystallinity in OOP direction along with the main diffusion of PC<sub>61</sub>BM into PffBT4T-2OD polymer side chains in the IP direction. After the combination of DIO and AA, the photoactive film not only displayed better crystallinity and polymer order of PffBT4T-2OD based on the preferred orientation along (100) lamellar stacking peak in OOP direction and the  $\pi$ - $\pi$  stacking peaks both in IP and OOP direction, but also showed large D-A interface based on the disappeared lamellar stacking peak in the IP direction through mixing PC<sub>61</sub>BM into PffBT4T-2OD polymer side chains. In other words, the use of a binary additive improved the exciton dissociation (large D-A interface) and charge transport (preferred orientation) in the photoactive film.

Considering different physical properties of DIO and AA (AA solvent exhibits a much higher vapor pressure than DIO solvent [ $P_{AA} = 4.3 \times 10^{-2}$  mbar vs  $P_{DIO} = 3.1 \times 10^{-4}$  mbar] at room temperature), the above results suggest that the AA additive can shorten the drying time of the photoactive film as compared with the DIO additive. Meanwhile, the DIO additive exhibits selected dissolution capability for fullerene derivatives (such as PC<sub>61</sub>BM and PC<sub>71</sub>BM).<sup>[14, 20a]</sup> Therefore, in this case, we may speculate that the treatment with DIO mainly promotes a better mix of PC<sub>61</sub>BM into the PffBT4T-2OD polymer matrix, building more D-A interfaces between PffBT4T-2OD polymer and PC<sub>61</sub>BM, in line with GIXRD results. Differently, the AA solvent additive mainly helps to maintain a high polymer order and crystallinity in a short drying time, which leads to more balanced carrier mobility. Hence, combining the different contributions (synergistic effect) of DIO and AA on photoactive film results in better polymer order and enlarged D-A interfaces, facilitating device performance.

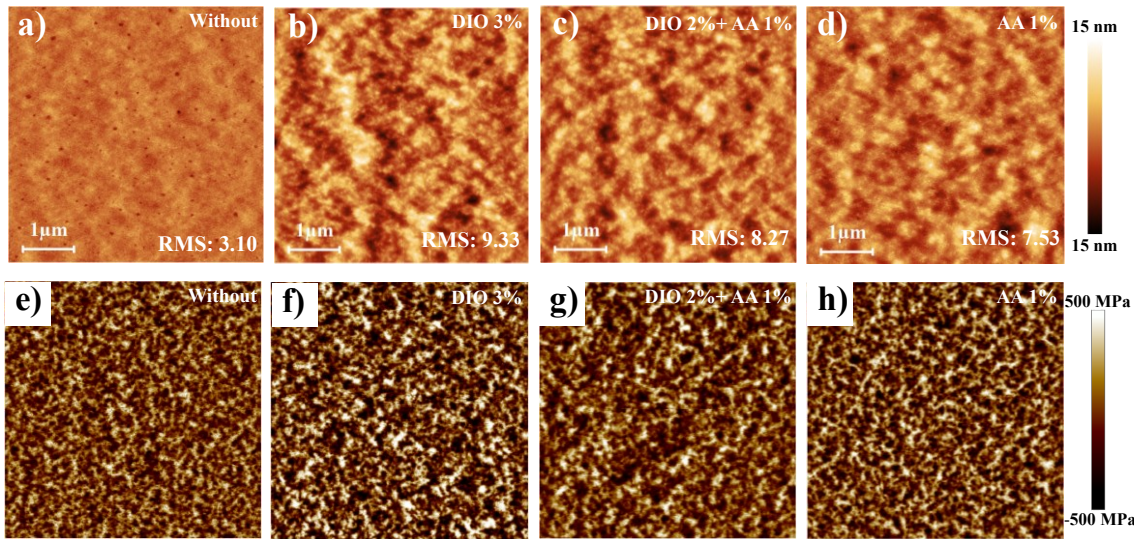


**Figure 5.** Surface topographic images (a, b, c, and d) and the DMT modulus images (e, f, g and h) of the PffBT4T-2OD:PC<sub>61</sub>BM photoactive layers prepared (a) and (e): without solvent additives, or with different solvent additives (b) and (f): DIO 3%, (c) and (g): DIO 2% + AA 1%, and (d) and (h): AA 1%. Scan size: 5 μm × 5 μm.

Surface topographic images of AFM were acquired to further confirm the morphology variation of photoactive layers with different solvent additives, as shown in **Figure 5a-5d**. The control photoactive film appeared smoother, with a root-mean-square (RMS) of 3.10 nm. With DIO incorporation, the roughness of the resulted photoactive film sharply increased to 9.33 nm, which likely resulted from a high mixing ratio between PC<sub>61</sub>BM and PffBT4T-2OD polymer and the domain coarsening of photoactive film assisted by the solvent additives and thermal annealing.<sup>[23, 25]</sup> However, increased roughness (7.53 nm) of the photoactive film with AA additive was mainly ascribed to enhanced polymer order and crystallinity in the OOP direction. As expected, the photoactive film with binary solvent additives showed a similar roughness value (8.27 nm). The DMT modulus of photoactive films highly relies on morphology variation.<sup>[26]</sup> Moreover, the stiffness of PC<sub>61</sub>BM is much stronger than that of PffBT4T-2OD polymer (**Figure S5**, Supporting Information). Therefore, DMT modulus mapping of photoactive films with different solvent additives could be used to probe the surface composition distribution and the phase-separated morphological variation of photoactive films with different solvent additives (**Figure 5e-h**).<sup>[24]</sup> The dark areas represent PffBT4T-2OD polymer or PffBT4T-2OD polymer-rich, and the bright areas stand for PC<sub>61</sub>BM or PC<sub>61</sub>BM-rich. In addition, the brown regions are ascribed to the mixed areas between PC<sub>61</sub>BM and PffBT4T-2OD polymer or well-crystallized PffBT4T-2OD polymer. Compared with the control photoactive film, the surface of a photoactive film made with DIO treatment shows more bright areas and distinctly decreased brown areas. Considering the related GIXRD results, this observation is in line with more PC<sub>61</sub>BM diffusing into PffBT4T-2OD polymer side chains and decreased crystallinity of PffBT4T-

2OD polymer. Accordingly, more D-A interfaces and charge carrier transport paths are expected, which could facilitate  $J_{sc}$ , although the roughness was increased. Differently, after AA treatment, there is negligible change in dark and brown areas, and only smaller bright areas were slightly enlarged in photoactive film (**Figure 5h**), which is consistent with the slight crystallinity decrement of PffBT4T-2OD polymer. Finally, with binary solvent additives, the brown areas are enlarged, which reveals the distribution of more PffBT4T-2OD polymer on the surface (beneficial for charge collection) and/or large D-A interfaces in the photoactive film (beneficial for charge separation) (**Figure 5g**).

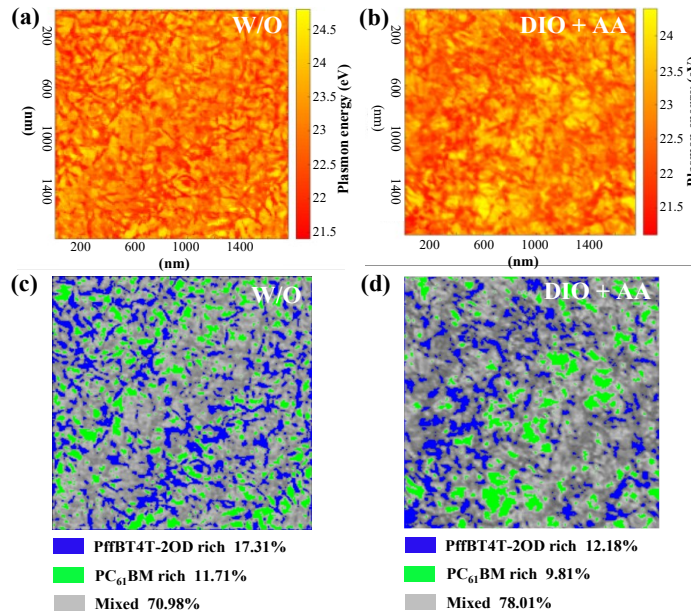


**Figure 6.** Plasmon energy shift imaging (PC<sub>61</sub>BM: 24.8 eV and PffBT4T-2OD: 21.4 eV) acquired in STEM mode of the PffBT4T-2OD:PC<sub>61</sub>BM photoactive films, (a) without solvent additive, (b) with binary solvent additives (DIO 2% + AA 1%). (c) and (d) segmentation of the corresponding plasmon energy mapping into enriched and mixed domains, which were obtained using the ImageJ software.

Furthermore, the change of surface composition of the photoactive film with different solvent additives was investigated by X-ray photoelectron spectroscopy (XPS).<sup>[27]</sup> The sulfur was used as a characteristic element of PffBT4T-2OD polymer because of the absence of sulfur in PC<sub>61</sub>BM. The sulfur/carbon ratio (R<sub>s/c</sub>) is shown in **Table S4**, Supporting Information. With incorporating DIO, R<sub>s/c</sub> decreased from 0.159 (control film) to 0.137. The reduction of R<sub>s/c</sub> indicates that DIO incorporation facilitates the diffusion of more PC<sub>61</sub>BM onto the film surface, which provides more D-A interfaces. On the contrary, the R<sub>s/c</sub> values of the films with AA and binary solvent additives treatments only slightly decreased to 0.145 and 0.143, respectively, resulting in a slight decrement of PffBT4T-2OD polymer content. It means that the AA solvent additive can restrain the diffusion of excess PC<sub>61</sub>BM to the surface of the photoactive film. Therefore, the combination of DIO and AA not only tunes the mixing capability between PC<sub>61</sub>BM and PffBT4T-2OD

polymer in association with enough D-A interfaces but also maintains the polymer concentration on the surface to favor charge carrier transport. We further investigate the film morphology with and without binary solvent additive by plasmon energy shift imaging (PESI) acquired in STEM<sup>[28]</sup>, as shown in **Figure 6**. According to the plasmon energy-shift images, we can observe that the control composite film exhibits less mixed domains between PffBT4T-2OD and PC<sub>61</sub>BM in comparison with that with binary solvent additive, which is consistent with the aforementioned DMT modulus images. In a word, binary solvent additive enables the composite with a more D-A interface and balanced charge carrier transport, which is beneficial for the improvement of  $J_{sc}$  and FF.

### 3.4 Conclusion

In conclusion, we have clearly unveiled the mechanism for binary DIO and AA additives to enhance OPV device performance *via* synchrotron-based GIXRD, DMT modulus AFM, and STEM. We find that DIO solvent additive mainly promotes the diffusion of more PC<sub>61</sub>BM into PffBT4T-2OD polymer matrix. AA, a less-toxic and iodine-free solvent additive, mainly improves the polymer order with preferred stacking orientation. Hence, based on the different contributions of DIO and AA on photoactive films, the binary solvent additive further improves polymer order, maintains high crystallinity, and obtains preferable morphology of photoactive film (more effective D-A interfaces), which facilitates more balanced charge carrier transport, and higher exciton dissociation and charge collection probabilities. As a result, the binary solvent additive results in enhanced  $J_{sc}$  and FF, and a PCE of 10.64% is obtained. Our findings provide a new strategy to exploit binary solvent additive with the synergistic effect on photoactive film, which would provide a simple path *via* smartly designing solvent additive tactics to enhance the OPV device.

### 3.5 References

- [1] a) M. Kaltenbrunner, M. S. White, E. D. Głowacki, T. Sekitani, T. Someya, N. S. Sariciftci, S. Bauer, *Nat. Commun.* **2012**, *3*, 770; b) X. Gu, Y. Zhou, K. Gu, T. Kurosawa, Y. Guo, Y. Li, H. Lin, B. C. Schroeder, H. Yan, F. Molina-Lopez, C. J. Tassone, C. Wang, S. C. B. Mannsfeld, H. Yan, D. Zhao, M. F. Toney, Z. Bao, *Adv. Energy Mater.* **2017**, *7*, 1602742; c) C. J. Brabec, N. S. Sariciftci, J. C. Hummelen, *Adv. Funct. Mater.* **2001**, *11*, 15.
- [2] Q. Liu, Y. Jiang, K. Jin, J. Qin, J. Xu, W. Li, J. Xiong, J. Liu, Z. Xiao, K. Sun, S. Yang, X. Zhang, L. Ding, *Sci. Bull.* **2020**, *65*, 272.

- [3] a) Y. Lin, J. Wang, Z.-G. Zhang, H. Bai, Y. Li, D. Zhu, X. Zhan, *Adv. Mater.* **2015**, *27*, 1170; b) Z. He, C. Zhong, S. Su, M. Xu, H. Wu, Y. Cao, *Nature Photon.* **2012**, *6*, 593; c) T. Yang, M. Wang, C. Duan, X. Hu, L. Huang, J. Peng, F. Huang, X. Gong, *Energy Environ. Sci.*, **2012**, *5*, 8208.
- [4] a) L.-M. Chen, Z. Hong, G. Li, Y. Yang, *Adv. Mater.* **2009**, *21*, 1434; b) Y. Huang, E. J. Kramer, A. J. Heeger, G. C. Bazan, *Chem. Rev.* **2014**, *114*, 7006.
- [5] W. Ma, C. Yang, X. Gong, K. Lee, A. J. Heeger, *Adv. Funct. Mater.* **2005**, *15*, 1617.
- [6] G. Li, Y. Yao, H. Yang, V. Shrotriya, G. Yang, Y. Yang, *Adv. Funct. Mater.* **2007**, *17*, 1636.
- [7] J. Peet, J. Y. Kim, N. E. Coates, W. L. Ma, D. Moses, A. J. Heeger, G. C. Bazan, *Nat. Mater.* **2007**, *6*, 497.
- [8] a) J. Gao, J. Wang, Q. An, X. Ma, Z. Hu, C. Xu, X. Zhang, F. Zhang, *Sci. China Chem.* **2019**, *63*, 83; b) J. Gao, W. Gao, X. Ma, Z. Hu, C. Xu, X. Wang, Q. An, C. Yang, X. Zhang, F. Zhang, *Energy Environ. Sci.*, **2020**, *13*, 958.
- [9] S. Kwon, H. Kang, J.-H. Lee, J. Lee, S. Hong, H. Kim, K. Lee, *Adv. Energy Mater.* **2017**, *7*, 1601496.
- [10] Y. Gu, C. Wang, T. P. Russell, *Adv. Energy Mater.* **2012**, *2*, 683.
- [11] a) C. V. Hoven, X. D. Dang, R. C. Coffin, J. Peet, T. Q. Nguyen, G. C. Bazan, *Adv. Mater.* **2010**, *22*, E63; b) T. L. Nguyen, H. Choi, S. J. Ko, M. A. Uddin, B. Walker, S. Yum, J. E. Jeong, M. H. Yun, T. J. Shin, S. Hwang, J. Y. Kim, H. Y. Woo, *Energy Environ. Sci.* **2014**, *7*, 3040.
- [12] a) D. H. Wang, A. K. K. Kyaw, J.-R. Pouliot, M. Leclerc, A. J. Heeger, *Adv. Energy Mater.* **2014**, *4*, 1300835; b) C. Liu, X. Hu, C. Zhong, M. Huang, K. Wang, Z. Zhang, X. Gong, Y. Cao, A. J. Heeger, *Nanoscale* **2014**, *6*, 14297; c) Q. Wan, X. Guo, Z. Wang, W. Li, B. Guo, W. Ma, M. Zhang, Y. Li, *Adv. Funct. Mater.* **2016**, *26*, 6635.
- [13] K. Gao, J. Miao, L. Xiao, W. Deng, Y. Kan, T. Liang, C. Wang, F. Huang, J. Peng, Y. Cao, F. Liu, T. P. Russell, H. Wu, X. Peng, *Adv. Mater.* **2016**, *28*, 4727.
- [14] J. K. Lee, W. L. Ma, C. J. Brabec, J. Yuen, J. S. Moon, J. Y. Kim, K. Lee, G. C. Bazan, A. J. Heeger, *J. Am. Chem. Soc.* **2008**, *130*, 3619.
- [15] a) Y. Sun, J. H. Seo, C. J. Takacs, J. Seifter, A. J. Heeger, *Adv. Mater.* **2011**, *23*, 1679; b) Y. Liu, J. Zhao, Z. Li, C. Mu, W. Ma, H. Hu, K. Jiang, H. Lin, H. Ade, H. Yan, *Nat. Commun.* **2014**, *5*, 5293; c) Y. Sun, M. Wang, X. Gong, J. H. Seo, B. B. Y. Hsu, F. Wudl, A. J. Heeger, *J. Mater. Chem.* **2011**, *21*, 1365.
- [16] N. Li, J. D. Perea, T. Kassar, M. Richter, T. Heumueller, G. J. Matt, Y. Hou, N. S. Guldal, H. Chen, S. Chen, S. Langner, M. Berlinghof, T. Unruh, C. J. Brabec, *Nat. Commun.* **2017**, *8*, 14541.
- [17] Z. He, C. Zhong, X. Huang, W. Y. Wong, H. Wu, L. Chen, S. Su, Y. Cao, *Adv. Mater.* **2011**, *23*, 4636.
- [18] Q. Zhang, B. Kan, F. Liu, G. Long, X. Wan, X. Chen, Y. Zuo, W. Ni, H. Zhang, M. Li, Z. Hu, F. Huang, Y. Cao, Z. Liang, M. Zhang, T. P. Russell, Y. Chen, *Nature Photon.* **2014**, *9*, 35.

- [19] a) J. W. Jung, W. H. Jo, *Adv. Funct. Mater.* **2010**, *20*, 2355; b) M. A. Lampert, P. Mark, *Current Injection in Solids* Academic Press, New York, NY 1970.
- [20] a) C. Sprau, F. Buss, M. Wagner, D. Landerer, M. Koppitz, A. Schulz, D. Bahro, W. Schabel, P. Scharfer, A. Colsmann, *Energy Environ. Sci.* **2015**, *8*, 2744; b) H. Y. Chen, J. Hou, A. E. Hayden, H. Yang, K. N. Houk, Y. Yang, *Adv. Mater.* **2010**, *22*, 371; c) J. A. Bartelt, J. D. Douglas, W. R. Mateker, A. E. Labban, C. J. Tassone, M. F. Toney, J. M. J. Fréchet, P. M. Beaujuge, M. D. McGehee, *Adv. Energy Mater.* **2014**, *4*, 1301733.
- [21] Q. Fan, Q. Zhu, Z. Xu, W. Su, J. Chen, J. Wu, X. Guo, W. Ma, M. Zhang, Y. Li, *Nano Energy* **2018**, *48*, 413.
- [22] W. Ma, G. Yang, K. Jiang, J. H. Carpenter, Y. Wu, X. Meng, T. McAfee, J. Zhao, C. Zhu, C. Wang, H. Ade, H. Yan, *Adv. Energy Mater.* **2015**, *5*, 1501400.
- [23] Y. Zhang, A. J. Parnell, F. Pontecchiani, J. F. Cooper, R. L. Thompson, R. A. Jones, S. M. King, D. G. Lidzey, G. Bernardo, *Sci. Rep.* **2017**, *7*, 44269.
- [24] L. M. J. Moore, M. Bhattacharya, Q. Wu, S. G. Youm, E. E. Nesterov, S. E. Morgan, *ACS Appl. Mater. Interfaces* **2017**, *9*, 22764.
- [25] A. K. K. Kyaw, D. H. Wang, C. Luo, Y. Cao, T.-Q. Nguyen, G. C. Bazan, A. J. Heeger, *Adv. Energy Mater.* **2014**, *4*, 1301469.
- [26] a) O. Awartani, B. I. Lemanski, H. W. Ro, L. J. Richter, D. M. DeLongchamp, B. T. O'Connor, *Adv. Energy Mater.* **2013**, *3*, 399; b) L. Li, J. Liang, H. Gao, Y. Li, X. Niu, X. Zhu, Y. Xiong, Q. Pei, *ACS Appl. Mater. Interfaces* **2017**, *9*, 40523; c) D. Wang, F. Liu, N. Yagihashi, M. Nakaya, S. Ferdous, X. Liang, A. Muramatsu, K. Nakajima, T. P. Russell, *Nano Lett.* **2014**, *14*, 5727.
- [27] X. Guo, M. Zhang, W. Ma, L. Ye, S. Zhang, S. Liu, H. Ade, F. Huang, J. Hou, *Adv. Mater.* **2014**, *26*, 4043.
- [28] a) S. B. Dkhil, M. Pfannmöller, M. I. Saba, M. Gaceur, H. Heidari, C. Videlot-Ackermann, O. Margeat, A. Guerrero, J. Bisquert, G. Garcia-Belmonte, A. Mattoni, S. Bals, J. Ackermann, *Adv. Energy Mater.* **2017**, *7*, 1601486; b) Y. Sun, G. C. Welch, W. L. Leong, C. J. Takacs, G. C. Bazan, A. J. Heeger, *Nat. Mater.* **2011**, *11*, 44.

### 3.6 Supporting Information

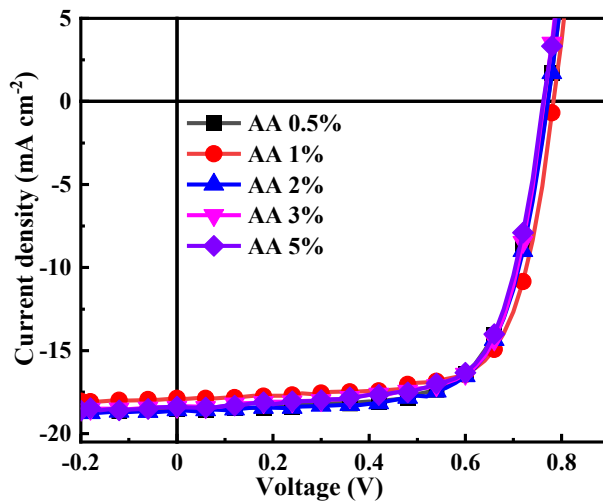


**Figure S1.**  $J$ - $V$  characteristics of the PffBT4T-2OD:PC<sub>61</sub>BM devices with different concentration AA additive (AA 0.5%, 1%, 2%, 3%, and 5%).

**Table S1.** Summary of the photovoltaic parameters of PffBT4T-2OD:PC<sub>61</sub>BM devices with different concentration AA additive (AA 0.5%, 1%, 2%, 3%, and 5%).

Solvent Additives	V <sub>oc</sub> (V)	J <sub>sc</sub> (mA/cm <sup>2</sup> )	FF (%)	PCE (%)
AA 0.5%	0.771 <sup>a</sup> (0.772) <sup>b</sup>	18.53 (18.36)	68.93 (68.48)	9.85 (9.71)
AA 1%	0.781 (0.782)	17.97 (17.89)	71.54 (71.21)	10.04 (9.96)
AA 2%	0.772 (0.773)	18.61 (18.41)	69.27 (69.69)	9.95 (9.92)
AA 3%	0.763 (0.764)	18.37 (18.34)	70.63 (69.55)	9.90 (9.74)
AA 5%	0.762 (0.763)	18.41 (18.00)	70.01 (69.76)	9.82 (9.59)

<sup>a</sup> Average values are obtained in five devices. <sup>b</sup> Peak values.

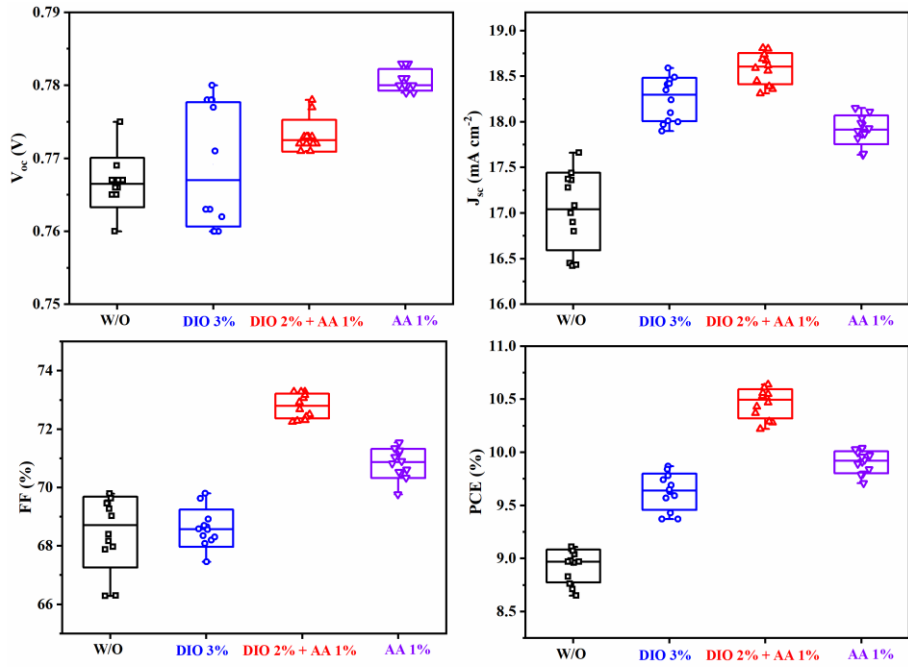


**Figure S2.** The statistical electrical outputs of the devices (twelve devices from two batches) based on PffBT4T-2OD: PC<sub>61</sub>BM blend films with/without different solvent additives (W/O, DIO 3%, DIO 2% + AA 1%, and AA 1%).

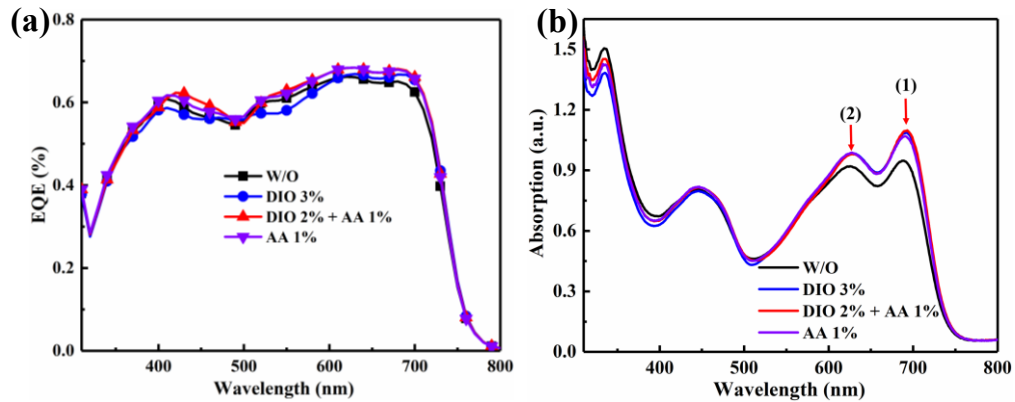


**Figure S3.** (a) EQE spectra of the devices without or with solvent additives, the devices were measured in the air without encapsulation. (b) UV-visible absorption spectra of PffBT4T-2OD:PC<sub>61</sub>BM films with/without different solvent additives (W/O, DIO 3%, DIO 2% + AA 1%, and AA 1%). The red arrows (1) and (2) denote the main absorption maxima of PffBT4T-2OD.

**Table S2.** Key photovoltaic parameters calculated from the  $J_{ph}$ - $V_{eff}$  curves of PffBT4T-2OD:PC<sub>61</sub>BM devices processed without or with different solvent additives.

Solvent Additives	$J_{sat}^a$ [mA·cm <sup>-2</sup> ]	$J_{ph}^b$ [mA·cm <sup>-2</sup> ]	$J_{ph}^c$ [mA·cm <sup>-2</sup> ]	$J_{ph}^b/J_{sat}$ [%]	$J_{ph}^c/J_{sat}$ [%]
W/O	19.22	18.30	13.58	95.23	70.66
DIO 3%	20.10	19.16	14.98	95.31	74.50
DIO 2% + AA 1%	19.77	19.08	16.60	96.49	83.95
AA 1%	18.81	18.12	15.26	96.70	81.14

<sup>a</sup> $J_{sat}$  is  $J_{ph}$  under the condition of  $V_{eff} = 2.0$  V, <sup>b</sup> $J_{ph}$  is the data under short circuit condition. <sup>c</sup> $J_{ph}$  is photocurrent under the maximum power output condition.

**Table S3.** Calculated electron and hole mobility values for the PffBT4T2OD:PC<sub>61</sub>BM devices without or with different solvent additives (DIO 3%, DIO 2% + AA 1%, and AA 1%).

Solvent Additives	Electron mobility ( $\mu_e$ )	Hole mobility ( $\mu_h$ )	$\mu_e / \mu_h$
	( $\times 10^{-3}$ cm <sup>2</sup> V <sup>-1</sup> s <sup>-1</sup> )	( $\times 10^{-3}$ cm <sup>2</sup> V <sup>-1</sup> s <sup>-1</sup> )	
W/O	$5.84 \pm 0.26^a$	$2.50 \pm 0.48$	2.34
DIO 3%	$6.17 \pm 0.49$	$2.84 \pm 0.30$	2.17
DIO 2% + AA 1%	$5.27 \pm 0.18$	$3.17 \pm 0.38$	1.66
AA 1%	$5.16 \pm 0.57$	$2.50 \pm 0.42$	2.06

<sup>a</sup>Average values are obtained in four devices.

**Table S4.** XPS element analysis results of the area ratio of S(2p) peak and C(1s) peak for the surface compositions of photoactive films without or with the different solvent additives (DIO 3%, DIO 2% + AA 1%, and AA 1%).

Solvent Additives	Peak ratio of S(2p)/C(1s)
W/O	0.159
DIO 3%	0.137
DIO 2% + AA 1%	0.145
AA 1%	0.143

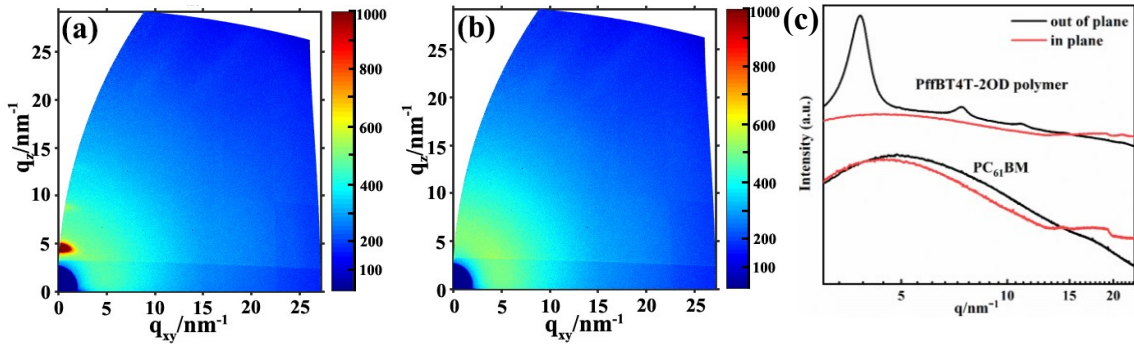


**Figure S4.** Synchrotron-based 2D GIXRD patterns of (a) the pristine PffBT4T-2OD polymer film and (b) PC<sub>61</sub>BM film (c) GIXRD with OOP and IP scattering geometry for pristine PffBT4T-2OD polymer and PC<sub>61</sub>BM.

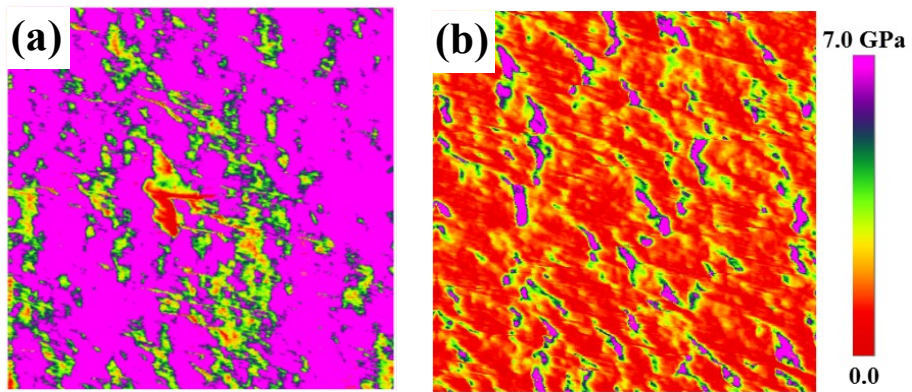


**Figure S5.** Modulus images of the PffBT4T-2OD:PC<sub>61</sub>BM photoactive film based on the different specific ratios between PffBT4T-2OD and PC<sub>61</sub>BM: (a) 20%wt PffBT4T-2OD and 80%wt PC<sub>61</sub>BM and, and (b) 80%wt PffBT4T-2OD and 20%wt PC<sub>61</sub>BM.

## 4 CHAPTER 4 AIR-PROCESSED, ORGANIC SOLAR CELLS WITH HIGH POWER CONVERSION EFFICIENCY OF 7.41%

Pandeng Li, Mathieu Mainville, Yuliang Zhang, Mario Leclerc, Baoquan Sun, Ricardo Izquierdo, and Dongling Ma *Small*, **2019**, *15*, 1804671.

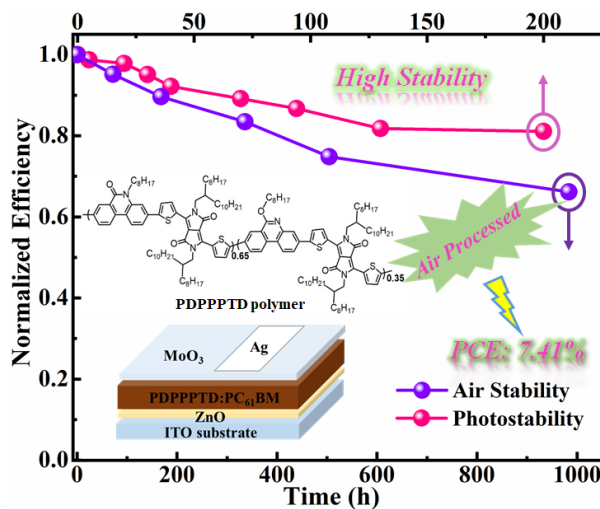


Figure of Table of Contents for This Section Work

In addition to pursuing higher-efficiency organic photovoltaic devices by using the new binary solvent additive, device stability as another serious question should be considered in endeavoring to push forward the real-world application of organic solar cells. To improve the device stability, several methods have been explored, for example, changing device structure, interface modifications, and introducing a third component into photoactive layer. However, the photoactive materials in these devices are still sensitive to environmental conditions and need to be processed in glovebox. So modification of photoactive materials is a more efficient way to improve device stability, such as the modification of donor polymers. This method improved the thermal stability and photo-stability. However, the air stability and the air processability are not so good. The air-stable photoactive materials need to be further investigated. Herein, in this section, an air-processed inverted photovoltaic device built upon a low-bandgap, air-stable, phenanthridinone-based terpolymer ( $C_{15}H_{218}N_6O_6S_4$ )<sub>n</sub> (PDPPPPTD) and [6,6]-phenyl-C<sub>61</sub>-butyric acid methyl ester (PC<sub>61</sub>BM) without involving any additive engineering processes yields a high efficiency of 6.34%. The PDPPPPTD/PC<sub>61</sub>BM devices also exhibit superior thermal stability and photo-stability as well as long-term stability in an ambient atmosphere without any device encapsulation, which shows less performance decay as compared to most of the reported organic solar cells. Because of their great potential, solvent additive engineering via adding p-anisaldehyde (AA) is attempted, leading to a further improved efficiency of 7.41%,

one of the highest efficiencies for all air-processed and stable organic photovoltaic devices. Moreover, the device stability under different ambient conditions is also further improved with the AA additive engineering. Various characterizations are conducted to probe the structural, morphology, and chemical information to correlate the structure with photovoltaic performance. This work paves a way for developing a new generation of air-processable organic solar cells for possible commercial applications.

In this work, I got the related donor polymer (PDPPPTD) from Prof. Mario Leclerc's research group. Dr. Yuliang Zhang provided some advice. In addition, the synchrotron-based grazing incident X-ray diffraction measurement of the photovoltaic films was from Shanghai Synchrotron Radiation Facility (SSRF). The work was published in the journal of *Small* (Small 2019, 15, 1804671).

**Keywords:** Inverted solar cells, air-stable low bandgap polymer, air-processed solar cells, stability, ZnO cathode buffer layer.

#### 4.1 Introduction

The promising advantages of bulk heterojunction organic solar cells (OSCs), such as low cost, flexibility, light weight, and simple device fabrication process, have attracted wide attention.<sup>[1]</sup> Enormous efforts have been made toward achieving high power conversion efficiency (PCE) by synthesizing new donor and acceptor materials,<sup>[2]</sup> designing better device structure,<sup>[3]</sup> modifying fabrication methods,<sup>[4]</sup> and manipulating the morphology of the photoactive layers.<sup>[5]</sup> Up to date, the certified record PCE of single-junction OSCs already exceeded 13%.<sup>[6]</sup> The recent remarkable progress on the PCE of OSCs makes them more than ever attractive for large-scale fabrication, an imperative step toward possible commercial applications. But a similarly important factor, air processability, has received less attention; the work on OSCs has been mainly focused on the improvement of device efficiency in the last decades. In most cases, the OSCs are still fabricated in a nitrogen atmosphere because of the air sensitivity of organic materials. This increases the complexity of device fabrication and is not compatible with future large manufacturing processes either. To overcome these limits and facilitate their real-world applications, aside from further improving device efficiency, the air processability and long-term stability of OSC devices deserve significantly more attention than what they received previously.

Many factors, such as the chemical structure of photoactive materials, charge carrier extraction layer, and electrode materials, and device architecture, can largely influence the stability of OSCs and should be thoroughly and systematically investigated.<sup>[7]</sup> Employing the inverted device structure has been widely demonstrated to be an efficient strategy toward enhanced device stability.<sup>[8]</sup> Different from conventional OSCs structure, where poly(3,4-ethylenedioxythiophene):poly (styrene sulfonate) (PEDOT:PSS) coated indium tin oxide (ITO) anode is typically used to collect holes and a low-work-function metal electrode to

collect electrons, the inverted organic photovoltaic devices use metal oxides (e.g., TiO<sub>2</sub> and ZnO) as electron extraction layers and the high-work-function metal oxides such as MoO<sub>x</sub>, NiO<sub>x</sub>, and CuO as anode buffer layers, have also been explored.<sup>[9]</sup> The combination of the above cathode or anode interface materials can further significantly increase device stability. For example, Sun et al. found that the inverted photovoltaic device based on poly[N-9"-hepta-decanyl-2,7-carbazole-*alt*-5,5-(4',7'-di-2-thienyl-2',1',3'-benzothiadiazole) (PCDTBT)/PC<sub>71</sub>BM, with ZnO as a cathode buffer layer, MoO<sub>x</sub> as an anode buffer layer, and high-work-function Ag as a cathode could preserve 70% of the initial efficiency after storage in air for 30 d, while in clear contrast the performance of conventional devices degraded by a factor of 2 after 16 h.<sup>[10]</sup> To further improve device stability and performance, modification of buffer layers was also attempted, such as the modification of ZnO buffer layer with conjugated polyelectrolyte (poly(ethyleneimine) (PEI)) and the modification of TiO<sub>2</sub> with titanium oxide bis(2,4-pentanedionate).<sup>[11]</sup>

In addition to the above efforts, exploration has also been conducted to directly modify the major device component—the photoactive layer, to impede device degradation in the ambient atmosphere. McCulloch and co-workers presented that the addition of a modified fullerene dimer, bis- [6,6]-phenyl-C<sub>61</sub>-butyric acid ethane-1,2-diylester ((PCB)<sub>2</sub>C<sub>2</sub>) to the PCDTBT/PC<sub>61</sub>BM photoactive layer resulted in enhanced thermal stability by restraining the excessive aggregation and crystallization of fullerene.<sup>[12]</sup> Similarly, our group incorporated PbS/CdS core/shell quantum dots capped with small halide ligands into the poly(3-hexylthiophene) (P3HT)/PC<sub>61</sub>BM photoactive layer, which enhanced the long-term stability of devices under high humidity by forming unique, percolating quantum dot networks in the photoactive layer.<sup>[13]</sup> In another scenario, the photoactive layer of poly[[2,6'-4,8-di(5-ethylhexylthienyl) benzo[1,2-b;3,3-b]dithiophene][3-fluoro-2[(2-ethylhexyl)carbonyl] thieno[3,4-b]thiophenediy]] (PTB7-Th)/PC<sub>71</sub>BM was treated with an iodine-free solvent additive to distinctly improve air-stability and 90% of the initial efficiency could be maintained after 10 d storage in air without encapsulation.<sup>[14]</sup> Introducing the third component into the photoactive layer represents an alternative way to improving device stability. Despite all these endeavors, organic photoactive materials are still sensitive to environmental factors under most circumstances and processing in an inert atmosphere is commonly and highly needed.

The design and use of photovoltaic materials, which are air-processable and stable under various conditions, appear to be the most promising and appealing strategy for realizing the industrial production of stable OSCs in the future. One strategy is the modification of donor polymers by, for example, integrating more stable units into their skeletons, controlling their crystallinity, or adjusting their side chains. Although the thermal stability and photo-stability of the devices based on the modified materials were enhanced, the efficiency and air stability were not sufficiently good; most of the device fabrication processes are still required to be carried out in an inert atmosphere.<sup>[15]</sup> Even though in one case, air-processed low-bandgap

polymer poly(dithienogermole-*alt*-thienopyrrolodione) (p(DTG-TPD)) based solar cells yielded an initial PCE of 7.7%, a significant PCE degradation to 7.07% was observed after 3 h in air.<sup>[16]</sup> Toward realizing high-performance and air-processed photovoltaic devices, new non-fullerene acceptors, such as the twisted perylene diimide (PDI) dimer (tPDI-Hex), and PDI-based molecular acceptors, which are expected to be more stable than currently widely used fullerene derivative acceptors, were also attempted, resulting in the PCE of 7.49%.<sup>[17]</sup> But the lifetime of these non-fullerene acceptors-based devices in the ambient atmosphere remains obscure. Therefore, stable organic materials would offer new opportunities to simultaneously realize high efficiency, high stability, and air processability.

We recently synthesized an air-stable low-bandgap terpolymer (PDPPPTD), which allowed us to fabricate PDPPPTD/PC<sub>61</sub>BM device in the air with polyethylenimine:glycerol diglycidyl ether (PEI:GDE) as a cathode buffer layer and attain a PCE of 5.79%.<sup>[18]</sup> Although the efficiency is still lower than the highest reported values for other low-bandgap polymers-based solar cells fabricated under inert conditions, the air processibility of these PDPPPTD-based solar cells represents an attractive feature. It is worthwhile to further explore them to increase their PCE. Moreover, the long-term stability of these air-processed devices under different ambient conditions, another important factor for photovoltaic devices, was not reported and should be examined in detail.

Here, an air-processed OSC based on the air-stable low-bandgap terpolymer (PDPPPTD) (**Figure 1a**) and PC<sub>61</sub>BM without any solvent additive achieved the high PCE up to 6.34%. The thermal stability, photo-stability, and humidity stability of the developed devices, without any encapsulation, were then probed in detail. It was found that they could remain more than 70% of their initial efficiency after being heated at 85 °C for 75 h. The devices showed good photo-stability under continuous simulated sunlight illumination for 200 h, only losing 20% of efficiency. Meanwhile, the device can also be stored under an ambient atmosphere with suitable humidity for a long time. Additionally, *p*-anisaldehyde (AA) as a nontoxic and iodine-free solvent additive led to enhanced PCE of 7.41% as well as considerably increased performance reproducibility and device stability under different ambient conditions. This work paves a path toward achieving air-processable OSCs via the synthesis of more stable photovoltaic materials.

## 4.2 Experimental Section

### 4.2.1 Reagent and Materials

Patterned ITO-coated glass substrates ( $R_s \leq 10 \Omega \square^{-1}$ ,  $T_r \geq 83\%$ ), PC<sub>61</sub>BM, and MoO<sub>3</sub> were purchased from Shenzhen Huayu Union Technology Co., Ltd. (China), Solaris Chem Inc., and Alfa Aesar, respectively. In addition, zinc acetate dehydrate ( $Zn(CH_3COO)_2 \cdot 2H_2O$ , 99.9%), ethanolamine ( $NH_2CH_2CH_2OH$ , 99.5%),

2-methoxyethanol ( $\text{CH}_3\text{OCH}_2\text{CH}_2\text{OH}$ , 99.8%), 1,2-dichlorobenzene (ODCB), and AA (98%) were obtained from Sigma-Aldrich and used as received without any purification.

#### 4.2.2 Synthesis of PDPPPTD Polymer

According to previous work,<sup>[18]</sup> first M1 and M2 were easily synthesized from commercially available 2,7-dibromo-9-fluorenone via a simple two-step procedure (including a Schmidt reaction and alkylation reaction). In addition, M3 was obtained following a procedure reported in the literature.<sup>[36]</sup> To synthesize the electron donor PDPPPTD terpolymer ( $M_n$ : 53 kDa and PDI: 3.2), the monomers, M1 (0.35 eq), and M2 (0.65 eq), were copolymerized with M3 (1 eq) via simple direct heteroarylation polymerization. The LUMO and the HOMO levels of PDPPPTD are -5.43 and -3.92 eV, respectively.

#### 4.2.3 Preparation of ZnO Precursor Solution

The ZnO precursor solution was prepared according to a reported procedure.<sup>[10]</sup> Zinc acetate dehydrate ( $\text{Zn}(\text{CH}_3\text{COO})_2 \cdot 2\text{H}_2\text{O}$ , 1g), 2-methoxyethanol ( $\text{CH}_3\text{OCH}_2\text{CH}_2\text{OH}$ , 10 mL), and ethanolamine ( $\text{NH}_2\text{CH}_2\text{CH}_2\text{OH}$ , 0.28 g) were mixed and vigorously stirred overnight for the hydrolysis reaction in air.

#### 4.2.4 Fabrication of Solar Cell Devices

The patterned ITO-coated glass substrates (1 in.  $\times$  1 in.) were cleaned with detergent, deionized water, acetone, and isopropyl alcohol in sequence, for 15 min in total, in an ultrasonic bath before being dried with a nitrogen stream. The resulted ZnO precursor solution was spin-coated onto the cleaned ITO/glass substrates which were subsequently treated with plasma for 20 min followed by thermal annealing at 200 °C for 30 min. For preparing the photoactive layer solution, PDPPPTD solution (20 mg mL<sup>-1</sup>; solvent: ODCB) and PC<sub>61</sub>BM solution (40 mg mL<sup>-1</sup>; solvent: ODCB) were first separately stirred at 175 and 60 °C, respectively. They were mixed according to the predetermined concentration ratio of PDPPPTD:PC<sub>61</sub>BM (10:20 mg mL<sup>-1</sup>) in the final mixture solution and stirred overnight at 150 °C. Then the blend solution was filtered through a 0.45 µm poly(tetrafluoroethylene) (PTFE) filter at elevated temperature. Before the deposition of photoactive layers, the photoactive solution and the substrates should be kept at 90 °C. The filtered and warm photoactive solution was spin-coated onto the ZnO film at 2500 rpm for 60 s (thickness: 80-90 nm). For process optimization, certain photoactive layers were annealed at different temperatures (100, 110, and 120 °C) for 10 min. All the steps were carried out in the air. Finally, the device fabrication was completed by thermal evaporation of 15 nm of MoO<sub>3</sub> and 100 nm of Ag as the anode under a vacuum of about  $1 \times 10^{-6}$  mbar. The effective device area was 0.06 cm<sup>2</sup>.

#### 4.2.5 Characterization

Optical absorption spectra were recorded using a Cary 5000 UV-vis-NIR spectrophotometer (Varian). The surface morphology and the film roughness of the photoactive layers were analyzed using AFM. Roughness measurements were conducted in the ScanAsyst mode and phase images were taken using the tapping mode. Film thickness was measured by a profile meter (Dektak150). XPS was performed using a VG Escalab 220iXL equipped with an Al Ka source. The crystalline structure of the photoactive layers was characterized with GIXRD measurement that was performed at the BL14B1 beamline of the Shanghai Synchrotron Radiation Facility using X-ray with a wavelength of 1.24 Å. Samples were prepared on a Si substrate under the same conditions as those used for device fabrication. The 10 keV X-ray beam was incident at a grazing incidence angle of 0.05° to maximize the diffraction intensity from the samples. FTIR spectroscopy with attenuated total reflection (ATR) mode (Thermo Scientific, Nicolet 6700/ Smart iTR) was used to detect the change in the chemical structure of the organic materials in the photoactive layer. Device *J-V* characteristics were measured using a Keithley 2400 source measure unit under AM 1.5G simulated solar light. EQE measurements were done using an IQE200B system (Newport Corporation) by scanning from 300 to 850 nm with a 10 nm resolution.

### 4.3 Results and Discussion

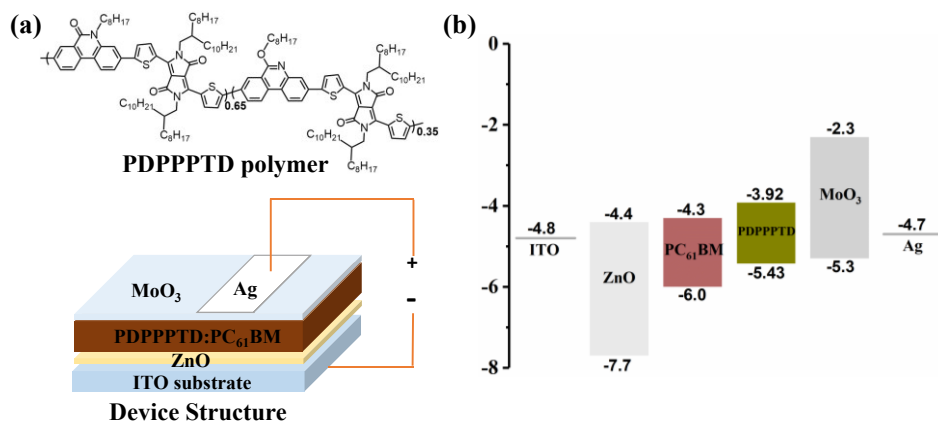


**Figure 1.** (a) Illustration of the structure of PDPPPPTD polymer and the device architecture of inverted PSCs based on the photoactive film of PDPPPPTD and PC<sub>61</sub>BM. (b) Energy level diagram of various components.

The inverted device configuration is presented in Figure 1a along with the chemical structure of the low-bandgap polymer PDPPPPTD, synthesized via a simple direct heteroarylation polymerization of 3,8-dibromo-5-octylphenanthridin-6-one (M2), 3,8-dibromo-6-(octyloxy)phenanthridine (M1), and 2,5-bis(2-octyldodecyl)-3,6-di(thien-2-yl)pyrrolo[3,4-c]pyrrole-1,4-dione (M3) following our previous work.<sup>[18]</sup> The ZnO film as the cathode buffer layer was fabricated via spin-coating the ZnO precursor solution followed

by thermal annealing at 200 °C for 30 min. The photoactive materials, PDPPPPTD and PC<sub>61</sub>BM, were used to construct the photovoltaic device in the ambient atmosphere, thanks to the stability of PDPPPPTD, higher than most of the low-bandgap polymers used so far for OSCs. Meanwhile, the energy levels of photoactive materials and charge carrier extraction materials (ZnO and MoO<sub>3</sub>) as well as electrode materials (ITO and Ag) are illustrated in Figure 1b.<sup>[10,18,19]</sup> It is clear that the appropriate energy level cascade was constructed successfully based on these components. The energy difference between the lowest unoccupied molecular orbital (LUMO) of PDPPPPTD and PC<sub>61</sub>BM is more than 0.3 eV (0.38 eV), which is favorable for efficient electron transfer from PDPPPPTD to PC<sub>61</sub>BM.<sup>[2a,20]</sup> In addition, the conduction band (CB) of the ZnO film is very close to the LUMO of PC<sub>61</sub>BM, allowing the easy transport of electrons to the ITO electrode through the ZnO film. Moreover, the ZnO layer can efficiently block the hole transport from PDPPPPTD to the ITO electrode because the valence bands (VB) of ZnO (-7.7 eV) is a quite low lying relative to the highest occupied molecular orbital (HOMO) levels of PC<sub>61</sub>BM (-6.0 eV) and PDPPPPTD (-5.45 eV). Additionally, as shown in **Figure 2a**, the PDPPPPTD polymer exhibited broad absorption, with the major absorption ranging from 550 to 800 nm and a much weaker absorption ranging from 300 to 450 nm. Since PC<sub>61</sub>BM only displays an absorption range at wavelengths shorter than 400 nm,<sup>[21]</sup> its combination with PDPPPPTD endows the photoactive film with the overall stronger absorption in the range of 300-400 nm, which is beneficial for improving short-circuit current density ( $J_{sc}$ ). Nonetheless, the absorption of the photoactive film is still weak in the range of 450-550 nm, which may be improved by integrating other acceptor or donor materials that can considerably absorb in this range, while allowing for appropriate band alignments.

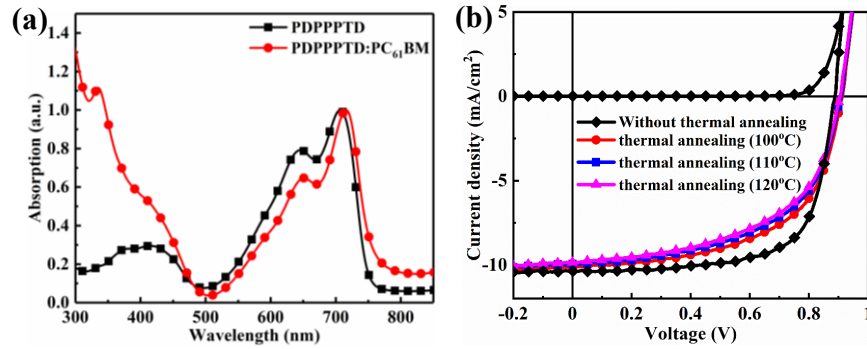


**Figure 2.** (a) Normalized UV-visible absorption spectra of PDPPPPTD films prepared with and without PC<sub>61</sub>BM. (b)  $J$ - $V$  characteristics of devices based on non-annealed PDPPPPTD/PC<sub>61</sub>BM film and those undergoing thermal annealing at different temperatures under AM 1.5G irradiation at 100 mW/cm<sup>2</sup> and in the dark.

With the favorable energy levels of constituent components, the air-processed inverted device, based on PDPPPPTD and PC<sub>61</sub>BM, without any specific ZnO modification and additive engineering, could achieve a relatively high PCE up to 6.34% with an open-circuit voltage ( $V_{oc}$ ) of 0.885 V, a  $J_{sc}$  of 10.38 mA cm<sup>-2</sup>, and a fill factor (FF) of 69.02% under AM 1.5G irradiation (100 mW cm<sup>-2</sup>) (Figure 2b), which represents an

improvement of 9.5% in the device performance compared with that (PCE: 5.79%) of the similar device using PEI:GDE as a cathode buffer layer and 3% of DPE as an additive.<sup>[18]</sup> The external quantum efficiency (EQE) spectrum mimics the absorption spectrum of the photoactive layer except for short wavelengths, as shown in Figure S1 (Supporting Information). Moreover, the effect of thermal annealing on device performance was studied (Figure 2b), and detailed results are summarized in **Table 1**. It was found that with thermal annealing at 100 °C in air, the  $V_{oc}$  of the devices increased from 0.885 to 0.915 V, but both  $J_{sc}$  and FF distinctly decreased, leading to the overall considerable reduction of PCE from 6.34 to 5.32%. With the further increasing temperature to 120 °C,  $V_{oc}$ ,  $J_{sc}$ , and FF decreased gradually. Consequently, PCE dropped from 5.32 to 4.85%. It was clear that the thermal annealing of photoactive layers deteriorated device performance in our case, although the PDPPPPTD polymer by itself is stable up to 400 °C and the deposition of photoactive layer needs hot spin-coating at an elevated temperature.<sup>[18]</sup>

**Table 1.** Electrical output characteristics of the devices built upon the photoactive layers without thermal annealing or undergoing thermal annealing at different temperatures.

Active Layer	$V_{oc}$ [V]	$J_{sc}$ [mA/cm <sup>2</sup> ]	FF [%]	PCE [%]
Without	0.885 (0.885)	10.14 (10.38)	68.62 (69.02)	6.16 ± 0.14 (6.34)
100 °C/10min	0.911 (0.915)	9.86 (10.12)	57.29 (57.44)	5.15 ± 0.14 (5.32)
110 °C/10min	0.909 (0.910)	9.61 (9.94)	55.83 (55.63)	4.88 ± 0.10 (5.03)
120 °C/10min	0.906 (0.905)	9.56 (9.86)	54.26 (54.39)	4.70 ± 0.11 (4.85)

In brackets: the best values obtained.

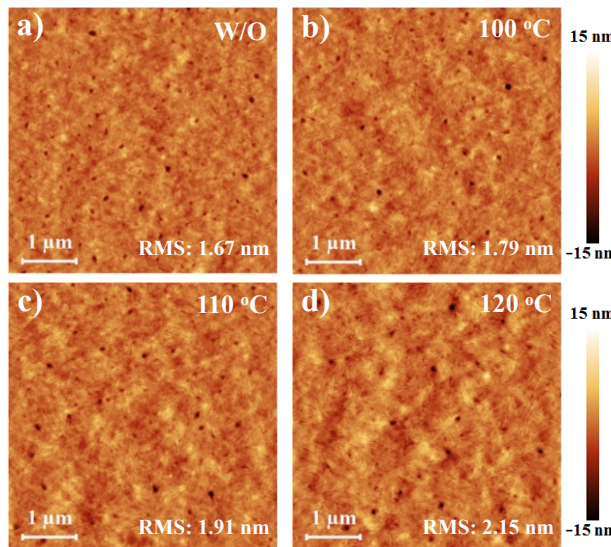


**Figure 3.** AFM height topography images of the PDPPPPTD/PC<sub>61</sub>BM photoactive layers (a) without thermal annealing, and undergoing thermal annealing at (b) 100 °C, (c) 110 °C, and (d) 120 °C for 10 min. Scan size: 5 μm × 5 μm.

To figure out the deteriorated device performance after thermal annealing, the atomic force microscopy (AFM) measurement was conducted to investigate the surface morphology of the photoactive layers. As depicted in the height topography images of **Figure 3**, the photoactive layer without thermal annealing appeared smoother with a lower root-mean-square (RMS) roughness of 1.67 nm with the presence of some pinholes. Upon increasing temperature from 100 to 120 °C, the roughness of annealed photoactive films increased from 1.79 to 2.15 nm. Meanwhile, the number of pinholes decreased while their diameter increased (Figure S2, Supporting Information), inducing the increased leakage current level. In addition, as seen from the phase images of photoactive layers without and with thermal annealing treatment (Figure S3, Supporting Information), the non-annealed film showed relatively homogeneous phase separation between the short and irregular PDPPPTD domains and PC<sub>61</sub>BM. After annealing at 100 °C, the prolonged PDPPPTD fibrillar structure was formed, which was likely formed by connecting adjacent small PDPPPTD polymer domains.<sup>[2a,22]</sup> This could be beneficial for hole transport and meanwhile caused a reduction of electron-hole recombination centers, which led to increased  $V_{oc}$ .<sup>[23]</sup> On the other hand, compared with non-annealed photoactive film, there appeared more PDPPPTD fibrils and fewer PC<sub>61</sub>BM phases on the surface of the photoactive layer after thermal annealing, which reveals enlarged phase segregation between PDPPPTD and PC<sub>61</sub>BM. The larger phase separation would result in less efficient charge transfer at the interface and thereby deteriorating  $J_{sc}$ . The measurements of the hole and electron mobilities of the device processed with thermal annealing at 100 °C for 10 min were also carried out by using the space-charge-limited current (SCLC) model with the Mott-Gurney square law ( $(J = (9/8)\epsilon_0 \epsilon_r \mu(V^2/L^3))$ ) (Table S1, Supporting Information), where  $\epsilon_0 \epsilon_r$  is the dielectric permittivity of the photoactive layer,  $\mu$  is the drift mobility of charge carriers,  $V$  is the applied voltage, and  $L$  is the thickness of the photoactive layer. It was found that the hole mobility ( $\mu_h$ ) was increased from  $9.64 \times 10^{-5}$  to  $1.05 \times 10^{-4}$  cm<sup>2</sup> V<sup>-1</sup> s<sup>-1</sup> because of the formation of PDPPPTD polymer fibrillar structure. Meanwhile, the electron mobility ( $\mu_e$ ) increased from  $1.10 \times 10^{-4}$  to  $1.37 \times 10^{-4}$  cm<sup>2</sup> V<sup>-1</sup> s<sup>-1</sup>, which was likely attributed to PC<sub>61</sub>BM aggregation under thermal annealing. The carrier mobility ratio ( $\mu_e/\mu_h$ ) increased from 1.14 to 1.31, which led to an unbalanced charge collection rate. As a result, inefficient charge collection led to reduced  $J_{sc}$  and FF. Hence, both reduced interface area and unbalanced charge collection ratio are considered to be responsible for the dramatic reduction of the  $J_{sc}$  and the FF upon thermal annealing, and the overall decrease of device performance.<sup>[24]</sup> With further increasing temperature, especially at 120 °C, the PDPPPTD polymer fibrils became larger and longer. The phase segregation between PDPPPTD and PC<sub>61</sub>BM became too large to allow efficient charge transfer, resulting in the drop of all three photovoltaic parameters,  $V_{oc}$ ,  $J_{sc}$ , and FF.<sup>[25]</sup> It could be reasonably concluded that the coarser and prolonged fibrillar structure of PDPPPTD polymer formed under thermal annealing is detrimental to device performance, which is different from P3HTbased photovoltaic devices.<sup>[26]</sup>

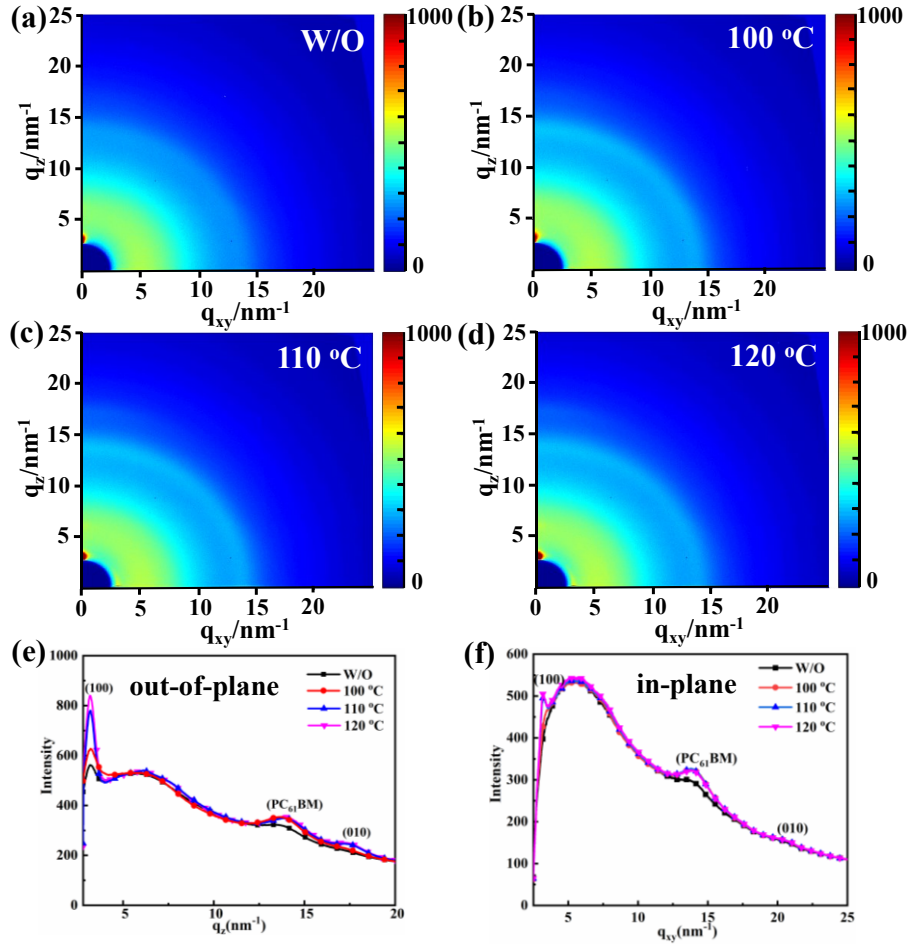


**Figure 4.** 2D GIXRD patterns of the PDPPPPTD/PC<sub>61</sub>BM photoactive layers without and with thermal annealing at different temperature: (a) W/O, (b) 100 °C, (c) 110 °C, and (d) 120 °C, respectively; (e) Related GIXRD with OOP and (f) IP scattering geometry for photoactive layers.

In order to better understand the annealing effect on the mentioned morphology variation, the grazing-incidence X-ray diffraction (GIXRD) measurements were conducted on the photoactive films without and with thermal annealing, and the corresponding out-of-plane (OOP) and in-plane (IP) line-cut profiles are summarized in **Figure 4** and Figure S4 (Supporting Information). The lamellar diffraction peak ((100) at 3.2 nm<sup>-1</sup>) of the photoactive films after thermal annealing became strong along with both the OOP and IP directions, with the former being stronger. Moreover, compared with the unchanged  $\pi$ – $\pi$  stacking peak (010) along the IP direction, the intensity of  $\pi$ – $\pi$  stacking peak along the OOP direction was slightly enhanced with thermal annealing treatment. In addition, the broad peak at  $\approx$ 14.0 nm<sup>-1</sup> was enhanced because of the aggregation of PC<sub>61</sub>BM along with both the OOP and IP directions.<sup>[27]</sup> In a word, after thermal annealing, the enhanced crystallinity and crystal orientation of photoactive films were mainly due to the strong lamellar stacking and the aggregation of PC<sub>61</sub>BM,<sup>[28]</sup> which was consistent with the observed coarser and prolonged fibrillary morphology of PDPPPPTD polymer in AFM phase images.<sup>[29]</sup> Therefore, thermal

annealing in our case was undesirable, which would indeed simplify the device fabrication process. Considering that the entire fabrication process was done under ambient conditions without any interface modification and post-treatments, the device PCE based on the PDPPPPTD/PC<sub>61</sub>BM photoactive layer and the ZnO cathode buffer layer was already impressive.

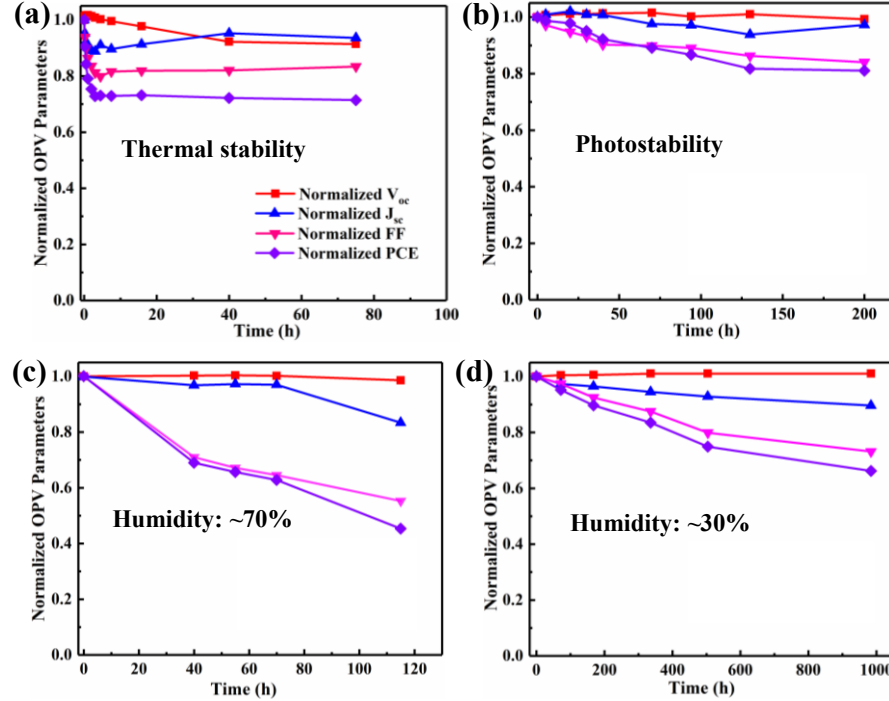


**Figure 5.** Stability of PDPPPPTD/PC<sub>61</sub>BM devices (a) at 85 °C in a glove box, (b) under continuous illumination in a glove box, (c) in air with high humidity of 70% in the dark and (d) in air with low humidity of 30% in the dark.

In addition to the efficiency of air-processed devices, the stability under different conditions should also be considered toward future practical applications. To this end, the thermal stability and photo-stability of above devices were studied by monitoring the evolution of photovoltaic parameters at an elevated temperature of 85 °C (a standard test temperature used by photovoltaic industries) and under continuous, simulated solar irradiation in a glove box, respectively.<sup>[30]</sup> The results are summarized in **Figure 5a,b**, respectively. During the short time period after heating started,  $V_{oc}$  increased slightly and then decreased, which was in line with improved  $V_{oc}$  observed during the thermal annealing mentioned above, because of the reduction of electron-hole recombination centers under the thermal stress.<sup>[23b,c]</sup> Overall,  $V_{oc}$ ,  $J_{sc}$ , and FF decreased quickly, but then stabilized after a certain period. As a consequence, the device efficiency could still remain more than 70% of its initial value after 75 h heating. Differently, under continuous illumination in a glove box,  $V_{oc}$  remained almost constant while  $J_{sc}$  and FF gradually decreased as a function of time, which caused a similar decreasing tendency for PCE. But the decrease was less than 20% after 200 h exposure to illumination, suggesting a quite good photo-stability of photoactive materials and devices. We

further made comparison with typical and commonly studied low-bandgap polymer solar cells, poly[4,8-bis[(2-ethylhexyl)oxy]benzo[1,2-b:4,5-b']dithiophene-2,6-diyl][3-fluoro-2-[(2-ethylhexyl)carbonyl]thieno[3,4-b]thiophenediyl] (PTB7)/PC<sub>71</sub>BM, fabricated and tested under the same conditions. As shown in Figure S5 (Supporting Information), only 52% efficiency was preserved after 11 h heating and after 150 h continuous illumination, the PCE of the device dropped to 65% of the original value. And PTB7/PC<sub>71</sub>BM based devices showed worse thermal stability and photo-stability than those of PDPPPTD/PC<sub>61</sub>BM based ones. Hence, it could safely conclude that the PDPPPTD/PC<sub>61</sub>BM device displays better thermal stability and photo-stability.

Furthermore, the device stability was assessed in the air with different humidity (about 70 and 30%), without device encapsulation. Humidity induces larger decay of PCE performance in comparison with thermal stress and illumination under testing conditions applied herein (Figure 5c,d). Similar to that of the device under continuous illumination, *Voc* remained unchanged under both humidity levels, while FF showed the largest drop, which resulted in dramatically degrading PCE, although *Jsc* was also gradually decreased. Under the high humidity of 70%, the device only preserved 40% of the initial PCE after 115 h, while more than 65% of efficiency remained after 960 h under the low humidity (30%). Meanwhile, the thermal stability, photo-stability, and air stability under different humidity levels of other OSCs based on fullerene derivatives as acceptors are also summarized in Table S2 (Supporting Information). In comparison with the reported OSCs, PDPPPTD/PC<sub>61</sub>BM devices exhibited superior stability performance. Pristine PDPPPTD exhibited favorable crystallinity property, which could contribute to the stronger PDPPPTD polymer network to mitigate the morphology degradation of the photoactive layer and further aggregation of PC<sub>61</sub>BM.<sup>[7d,18]</sup> In addition, the relatively low-energy HOMO (-5.45 eV) level of PDPPPTD provided it a capability against oxidation from the ambient conditions (such as thermal, illumination, humidity, and oxygen).<sup>[31]</sup>

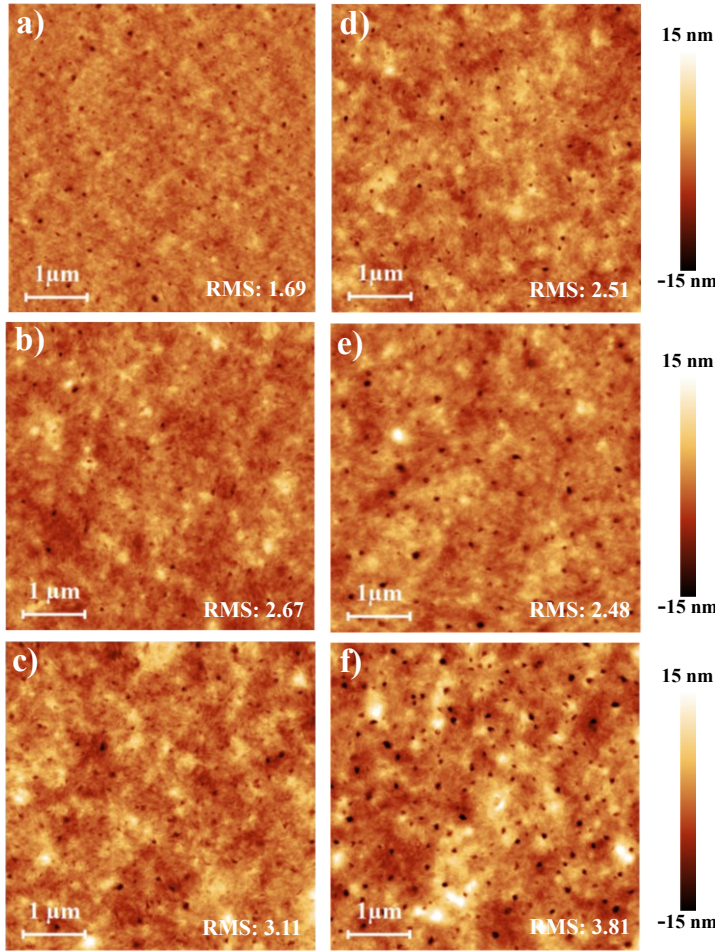


**Figure 6.** (a) J-V characteristics and photovoltaic parameters of the best device, prepared by involving AA as an additive, under AM 1.5G irradiation at  $100\text{ mW/cm}^2$ ; (b) AFM height topography image of PDPPPPTD/PC<sub>61</sub>BM photoactive layer fabricated with additive engineering using AA.

To further figure out the effect of different conditions (thermal, illumination, and humidity) on device performance, X-ray photoelectron spectroscopy (XPS) with depth profiling was used to investigate electrode–photoactive layer interface variation of the device before and after thermal stability testing. As seen from Figure S6 (Supporting Information), the profile of silver distribution along the vertical direction did not change after the thermal stability testing at  $85\text{ }^\circ\text{C}$  for 75 h, which suggests that the electrode–photoactive layer interface was not the main factor of the observed device degradation. So the AFM height images of PDPPPPTD/PC<sub>61</sub>BM photoactive films after conducting different stability tests were taken (**Figure 6**). Compared with a fresh photoactive film (Figure 6a), the RMS roughness of photoactive film heated at  $85\text{ }^\circ\text{C}$  in a glove box first increased from 1.69 to 2.67 nm, and then reached 3.11 nm with the prolongation of heating time (**Figure 6b,c**). Moreover, the pinhole distribution of photoactive films under different stability tests is shown in Figure S7 (Supporting Information). Although the pinhole number and diameter were clearly decreased after being heated for 10 h, the pinhole number was slightly increased with

further heating up to 75 h. Such morphology variation well explained the device performance degradation. In principle, the increased film roughness and the more pinholes could negatively influence charge carrier collection and transport.<sup>[32]</sup> Based on the above-mentioned thermal annealing studies, it is reasonable to anticipate that the heating herein, although at a lower temperature (85 °C vs >100 °C), would also result in a coarser and prolonged fibrillar structure of PDPPPPTD polymer. In contrast, the RMS value for the photoactive film after 200 h continuous illumination in a glove box only increased slightly to 2.51 nm (**Figure 6d**). Regarding the pinholes, only the number was slightly increased and the average diameter was kept constant. All these observations were in line with the smaller variation of photovoltaic parameters in this sample with respect to others. As for the humidity effect, the roughness of the photoactive film stored in air for 960 h with 30% humidity was only increased to 2.48 nm (**Figure 6e**). However, different from the photoactive film under continuous illumination, the average pinhole diameter was dramatically increased. As for the sample under a higher humidity of 70%, even for a shorter testing time of 115 h, the RMS value was largely increased to 3.81 nm. Many more and much larger pinholes were observed, which means the photoactive film is sensitive to high humidity in the air. Similarly, the related hole and electron mobilities of the devices after stability measurements under different conditions (such as at 85 °C for 75 h, under continuous illumination for 200 h, and at high humidity ( $\approx$  70%) for 115 h) were also examined (**Table S1**, Supporting Information). In all the cases, electron mobilities were slightly improved, which may be attributed to the aggregation of PC<sub>61</sub>BM during the degradation of photoactive layers, while the hole mobilities decreased. So the  $\mu_e/\mu_h$  ratio was reduced and was more deviating from 1, which caused imbalanced lower charge collection efficiency.

Additionally, the absorption spectra of photoactive films were measured after heating, illumination, and high humidity tests. As seen from Figure S8a (Supporting Information), the absorption intensity of PC<sub>61</sub>BM and PDPPPPTD polymer decreased with heating time, and the absorption peak ( $\pi-\pi$  stacking peak) of PDPPPPTD showed slight redshift, which is consistent with what has concluded above for thermally annealed films. However, at the beginning of illumination (Figure S8b, Supporting Information), the absorption density of PC<sub>61</sub>BM slightly increased, which was correlated with the redistribution of PC<sub>61</sub>BM in the photoactive film.<sup>[33]</sup> Finally, the optical density of both PC<sub>61</sub>BM and PDPPPPTD polymer dropped under continuous illumination. But the level of decrease was smaller than previously reported similar cases.<sup>[34]</sup> A similar trend of absorption decrease of the photoactive film stored under high humidity is obvious in Figure S8c (Supporting Information). It was found that only the PDPPPPTD polymer was degraded while the absorption band of PC<sub>61</sub>BM did not change too much. In a word, the PDPPPPTD/PC<sub>61</sub>BM films suffer from different degrees of degradation under the above-mentioned different conditions.

To get in-depth insights into the possible effect of different test conditions on the chemical structure of the related materials in the photoactive layers, Fourier transform Infrared (FTIR) spectroscopy measurements were employed and results are shown in Figure S8d (Supporting Information). The characteristic absorption bands for PDPPPTD and PC<sub>61</sub>BM, such as those located at 1737 cm<sup>-1</sup> (C=O stretching vibration of PC<sub>61</sub>BM) and 1556 cm<sup>-1</sup> (C=C vibration in the aromatic ring) and between 1663 and 1605 cm<sup>-1</sup> (amide bond vibration in the aromatic ring) were observed for the photoactive film.<sup>[5a,35]</sup> No obvious changes were observed for all these characteristic absorption bands, which suggests that the chemical structures of PDPPPTD and PC<sub>61</sub>BM were mostly maintained after all the tests. The morphology variation is thus considered the major reason for the performance degradation following the different stability tests. Meanwhile, the results can provide guidelines for further improving the performance and stability of PDPPPTD-based photovoltaic devices under different ambient conditions.

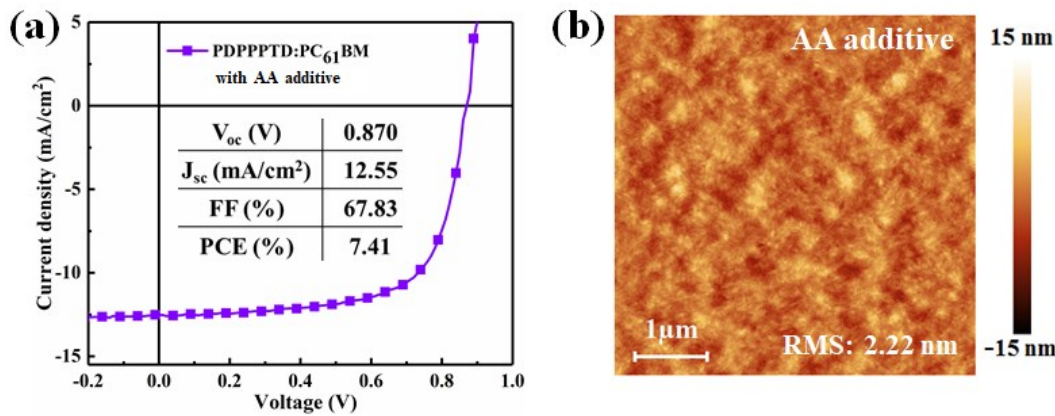


**Figure 7.** (a) J-V characteristics and photovoltaic parameters of the best device, prepared by involving AA as an additive, under AM 1.5G irradiation at 100 mW/cm<sup>2</sup>; (b) AFM height topography image of PDPPPTD/PC<sub>61</sub>BM photoactive layer fabricated with additive engineering using AA.

Although the air-processed device achieved a PCE of 6.34%, the device could be further improved if addressing the following three points. First, in terms of the device fabrication process, to get reasonably good film quality the photoactive material solution before deposition must be filtered at elevated temperature, which was not easy to operate and also caused the reproducibility problem. Second, with the current fabrication conditions, the optimal thickness was found to be limited to only 80–90 nm; further thickness increase caused the decrease of PCE due to morphology deterioration. Nonetheless, it is known that the increased thickness of the photoactive layer would enhance light harvesting. Moreover, multiple pinholes in photoactive films may allow humidity to penetrate the photoactive layer. Therefore, to address these problems, the strategy of solvent additive engineering was considered and the AA, a nontoxic and iodine-free chemical, was selected as an additive and introduced into the device fabrication process. Interestingly, the involvement of AA allowed us to get rid of the filtering process at an elevated temperature

and yet achieve an even higher efficiency of 7.41% (**Figure 7a**), which is better than that of similar photovoltaic devices with PC<sub>71</sub>BM as an acceptor in our previous work and is also superior PCE in the field of air-processed and stable OSCs (Table S3, Supporting Information). Consistently, the morphology of the photoactive layer became much better (**Figure 7b**). Compared with the photoactive layer without AA engineering, the pinholes completely disappeared although the roughness (2.22 nm) was slightly increased, which indicates that a more uniform and homogeneous photoactive layer was formed. These pinhole-free films could alleviate the damage of ambient conditions on device stability. Therefore, the device stability was also dramatically improved (**Figure S9**, Supporting Information). Additionally, the thickness of the photoactive layer with relatively good morphology was increased to 115 nm with the help of AA solvent additive. It is expected that the optimal thickness can be further increased by optimizing AA concentration, leading to an even higher PCE.

#### 4.4 Conclusion

In conclusion, without specific interlayer modification, thermal annealing of the photoactive layer, and device encapsulation, the photovoltaic devices based on a new air-stable low-bandgap PDPPPTD polymer and PC<sub>61</sub>BM completely fabricated in the air achieved an optimized efficiency of 6.34%. These air-processed devices not only exhibited excellent thermal stability and photostability but also showed superior stability in the ambient atmosphere without any device encapsulation. The use of AA, a nontoxic and iodine-free solvent additive, not only simplified device fabrication and enhanced performance reproducibility, but also improved the morphology of the photoactive films, including thicker ones, which further boosted the efficiency to 7.41%. It represents one of the highest PCE of air-processed and stable OSCs, including those fabricated using more expensive PC<sub>71</sub>BM. An additional, important benefit of the AA treatment was further improved device stability. Our work indicated that the low-bandgap PDPPPTD polymer-based solar cells hold huge potential in developing a new generation of air-processable photovoltaic devices of commercial interest in the future.

#### 4.5 References

- [1] a) M. Kaltenbrunner, M. S. White, E. D. Głowacki, T. Sekitani, T. Someya, N. S. Sariciftci, S. Bauer, *Nat. Commun.* **2012**, *3*, 770; b) X. Gu, Y. Zhou, K. Gu, T. Kurosawa, Y. Guo, Y. Li, H. Lin, B. C. Schroeder, H. Yan, F. Molina-Lopez, C. J. Tassone, C. Wang, S. C. B. Mannsfeld, H. Yan, D. Zhao, M. F. Toney, Z. Bao, *Adv. Energy Mater.* **2017**, *7*, 1602742; c) C. J. Brabec, N. S. Sariciftci, J. C. Hummelen, *Adv. Funct. Mater.* **2001**, *11*, 15.
- [2] a) H.-Y. Chen, J. Hou, S. Zhang, Y. Liang, G. Yang, Y. Yang, L. Yu, Y. Wu, G. Li, *Nature Photon.* **2009**, *3*, 649; b) Y. Lin, J. Wang, Z.-G. Zhang, H. Bai, Y. Li, D. Zhu, X. Zhan, *Adv. Mater.* **2015**, *27*, 1170.
- [3] Z. He, C. Zhong, S. Su, M. Xu, H. Wu, Y. Cao, *Nature Photon.* **2012**, *6*, 593.

- [4] a) H. Zhou, Y. Zhang, C.-K. Mai, S. D. Collins, G. C. Bazan, T.-Q. Nguyen, A. J. Heeger, *Adv. Mater.* **2015**, *27*, 1767; b) T. B. Yang, M. Wang, C. H. Duan, X. W. Hu, L. Huang, J. B. Peng, F. Huang, X. Gong, *Energy Environ. Sci.*, **2012**, *5*, 8208.
- [5] a) W. Ma, C. Yang, X. Gong, K. Lee, A. J. Heeger, *Adv. Funct. Mater.* **2005**, *15*, 1617; b) Z. A. Page, Y. Liu, V. V. Duzhko, T. P. Russell, T. Emrick, *Science* **2014**, *346*, 441.
- [6] W. Zhao, S. Li, H. Yao, S. Zhang, Y. Zhang, B. Yang, J. Hou, *J. Am. Chem. Soc.* **2017**, *139*, 7148.
- [7] a) M. O. Reese, A. M. Nardes, B. L. Rupert, R. E. Larsen, D. C. Olson, M. T. Lloyd, S. E. Shaheen, D. S. Ginley, G. Rumbles, N. Kopidakis, *Adv. Funct. Mater.* **2010**, *20*, 3476; b) J. Adams, M. Salvador, L. Lucera, S. Langner, G. D. Spyropoulos, F. W. Fecher, M. M. Voigt, S. A. Dowland, A. Osvet, H.-J. Egelhaaf, C. J. Brabec, *Adv. Energy Mater.* **2015**, *5*, 1501065; c) C. J. Schaffer, C. M. Palumbiny, M. A. Niedermeier, C. Jendrzejewski, G. Santoro, S. V. Roth, P. Muller-Buschbaum, *Adv. Mater.* **2013**, *25*, 6760; d) P. Cheng, X. Zhan, *Chem. Soc. Rev.* **2016**, *45*, 2544.
- [8] L.-M. Chen, Z. Hong, G. Li, Y. Yang, *Adv. Mater.* **2009**, *21*, 1434.
- [9] a) Z. Liang, Q. Zhang, O. Wiranwetchayan, J. Xi, Z. Yang, K. Park, C. Li, G. Cao, *Adv. Funct. Mater.* **2012**, *22*, 2194; b) J. You, C. C. Chen, L. Dou, S. Murase, H. S. Duan, S. A. Hawks, T. Xu, H. J. Son, L. Yu, G. Li, Y. Yang, *Adv. Mater.* **2012**, *24*, 5267; c) Y. Sun, C. J. Takacs, S. R. Cowan, J. H. Seo, X. Gong, A. Roy, A. J. Heeger, *Adv. Mater.* **2011**, *23*, 2226; d) J. R. Manders, S.-W. Tsang, M. J. Hartel, T.-H. Lai, S. Chen, C. M. Amb, J. R. Reynolds, F. So, *Adv. Funct. Mater.* **2013**, *23*, 2993; e) Z. Yu, W. Liu, W. Fu, Z. Zhang, W. Yang, S. Wang, H. Li, M. Xu, H. Chen, *J. Mater. Chem. A* **2016**, *4*, 5130.
- [10] Y. Sun, J. H. Seo, C. J. Takacs, J. Seifter, A. J. Heeger, *Adv. Mater.* **2011**, *23*, 1679.
- [11] a) S. Woo, W. Hyun Kim, H. Kim, Y. Yi, H.-K. Lyu, Y. Kim, *Adv. Energy Mater.* **2014**, *4*, 1301692; b) Y. Yan, F. Cai, L. Yang, J. Li, Y. Zhang, F. Qin, C. Xiong, Y. Zhou, D. G. Lidzey, T. Wang, *Adv. Mater.* **2017**, *29*, 1604044.
- [12] B. C. Schroeder, Z. Li, M. A. Brady, G. C. Faria, R. S. Ashraf, C. J. Takacs, J. S. Cowart, D. T. Duong, K. H. Chiu, C. H. Tan, J. T. Cabral, A. Salleo, M. L. Chabinyc, J. R. Durrant, I. McCulloch, *Angew. Chem. Int. Ed.* **2014**, *53*, 12870.
- [13] L. Tan, F. Yang, M. R. Kim, P. Li, D. T. Gangadharan, J. Margot, R. Izquierdo, M. Chaker, D. Ma, *ACS Appl. Mater. Interfaces* **2017**, *9*, 26257.
- [14] S. Lee, J. Kong, K. Lee, *Adv. Energy Mater.* **2016**, *6*, 1600970.
- [15] a) H. S. Lee, H. G. Song, H. Jung, M. H. Kim, C. Cho, J.-Y. Lee, S. Park, H. J. Son, H.-J. Yun, S.-K. Kwon, Y.-H. Kim, B. Kim, *Macromolecules* **2016**, *49*, 7844; b) C. Müller, J. Bergqvist, K. Vandewal, K. Tvingstedt, A. S. Anselmo, R. Magnusson, M. I. Alonso, E. Moons, H. Arwin, M. Campoy-Quiles, O. Inganäs, *J. Mater. Chem.* **2011**, *21*, 10676; c) P. Verstappen, J. Kesters, L. D'Olieslaeger, J. Drijkoningen,

- I. Cardinaletti, T. Vangerven, B. J. Bruijnaers, R. E. M. Willems, J. D'Haen, J. V. Manca, L. Lutsen, D. J. M. Vanderzande, W. Maes, *Macromolecules* **2015**, *48*, 3873.
- [16] I. Constantinou, T. H. Lai, D. Zhao, E. D. Klump, J. J. Deininger, C. K. Lo, J. R. Reynolds, F. So, *ACS Appl. Mater. Interfaces* **2015**, *7*, 4826.
- [17] a) S. V. Dayneko, A. D. Hendsbee, G. C. Welch, *Chem. Commun.* **2017**, *53*, 1164; b) Y. Guo, Y. Li, O. Awartani, J. Zhao, H. Han, H. Ade, D. Zhao, H. Yan, *Adv. Mater.* **2016**, *28*, 8483; c) S. M. McAfee, S. V. Dayneko, P. Josse, P. Blanchard, C. Cabanetos, G. C. Welch, *Chem. Mater.* **2017**, *29*, 1309.
- [18] M. Guérette, A. Najari, J. Maltais, J.-R. Pouliot, S. Dufresne, M. Simoneau, S. Besner, P. Charest, M. Leclerc, *Adv. Energy Mater.* **2016**, *6*, 1502094.
- [19] Y. Sun, M. Wang, X. Gong, J. H. Seo, B. B. Y. Hsu, F. Wudl, A. J. Heeger, *J. Mater. Chem.* **2011**, *21*, 1365.
- [20] M. C. Scharber, D. Mühlbacher, M. Koppe, P. Denk, C. Waldauf, A. J. Heeger, C. J. Brabec, *Adv. Mater.* **2006**, *18*, 789.
- [21] Z. Jin, J. Wang, *Sci. Rep.* **2014**, *4*, 5331.
- [22] M. Wang, D. Cai, Z. Yin, S. C. Chen, C. F. Du, Q. Zheng, *Adv. Mater.* **2016**, *28*, 3359.
- [23] a) A. Maurano, R. Hamilton, C. G. Shuttle, A. M. Ballantyne, J. Nelson, B. O'Regan, W. Zhang, I. McCulloch, H. Azimi, M. Morana, C. J. Brabec, J. R. Durrant, *Adv. Mater.* **2010**, *22*, 4987; b) K. Vandewal, S. Himmelberger, A. Salleo, *Macromolecules* **2013**, *46*, 6379; c) K. Vandewal, J. Widmer, T. Heumueller, C. J. Brabec, M. D. McGehee, K. Leo, M. Riede, A. Salleo, *Adv. Mater.* **2014**, *26*, 3839.
- [24] a) J. Jo, S.-S. Kim, S.-I. Na, B.-K. Yu, D.-Y. Kim, *Adv. Funct. Mater.* **2009**, *19*, 866; b) M. D. Perez, C. Borek, S. R. Forrest, M. E. Thompson, *J. Am. Chem. Soc.* **2009**, *131*, 9281; c) J. W. Jung, W. H. Jo, *Adv. Funct. Mater.* **2010**, *20*, 2355; d) M. A. Lampert, P. Mark, *Charge Injection in Solids*, Academic, New York **1970**.
- [25] B. C. Thompson, J. M. Fréchet, *Angew. Chem. Int. Ed.* **2008**, *47*, 58.
- [26] G. Li, Y. Yao, H. Yang, V. Shrotriya, G. Yang, Y. Yang, *Adv. Funct. Mater.* **2007**, *17*, 1636.
- [27] Q. Fan, Q. Zhu, Z. Xu, W. Su, J. Chen, J. Wu, X. Guo, W. Ma, M. Zhang, Y. Li, *Nano Energy* **2018**, *48*, 413.
- [28] J. Zhao, S. Zhao, Z. Xu, D. Song, B. Qiao, D. Huang, Y. Zhu, Y. Li, Z. Li, Z. Qin, *ACS Appl. Mater. Interfaces* **2018**, *10*, 24075.
- [29] H.-W. Wang, E. Pentzer, T. Emrick, T. P. Russell, *ACS Macro Lett.* **2013**, *3*, 30.
- [30] M. Jorgensen, K. Norrman, S. A. Gevorgyan, T. Tromholt, B. Andreasen, F. C. Krebs, *Adv. Mater.* **2012**, *24*, 580.
- [31] S. Cho, J. H. Seo, S. H. Park, S. Beaupre, M. Leclerc, A. J. Heeger, *Adv. Mater.* **2010**, *22*, 1253.

- [32] P. Huang, J. Du, S. S. Gunathilake, E. A. Rainbolt, J. W. Murphy, K. T. Black, D. Barrera, J. W. P. Hsu, B. E. Gnade, M. C. Stefan, M. C. Biewer, *J. Mater. Chem. A* **2015**, *3*, 6980.
- [33] S. Chambon, A. Rivaton, J.-L. Gardette, M. Firon, *Sol. Energy Mater. Sol. Cells* **2007**, *91*, 394.
- [34] T. I. Ryu, Y. Yoon, J.-H. Kim, D.-H. Hwang, M. J. Ko, D.-K. Lee, J. Y. Kim, H. Kim, N.-G. Park, B. Kim, H. J. Son, *Macromolecules* **2014**, *47*, 6270.
- [35] T. Khan, A. M.; Kaur, S. K. Dhawan, S. Chand, *J. Appl. Phys.* **2011**, *110*, 044509.
- [36] Y. Zou, D. Gendron, R. d. Badrou-Aich, A. Najari, Y. Tao, M. Leclerc, *Macromolecules* **2009**, *42*, 2891.

## 4.6 Supporting Information

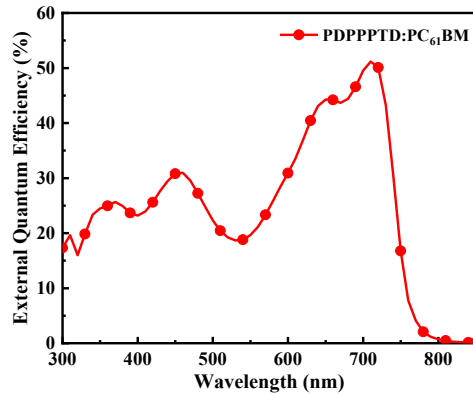


**Figure S1.** EQE of the optimized device based on PDPPPPTD and PC<sub>61</sub>BM as the photoactive layer.

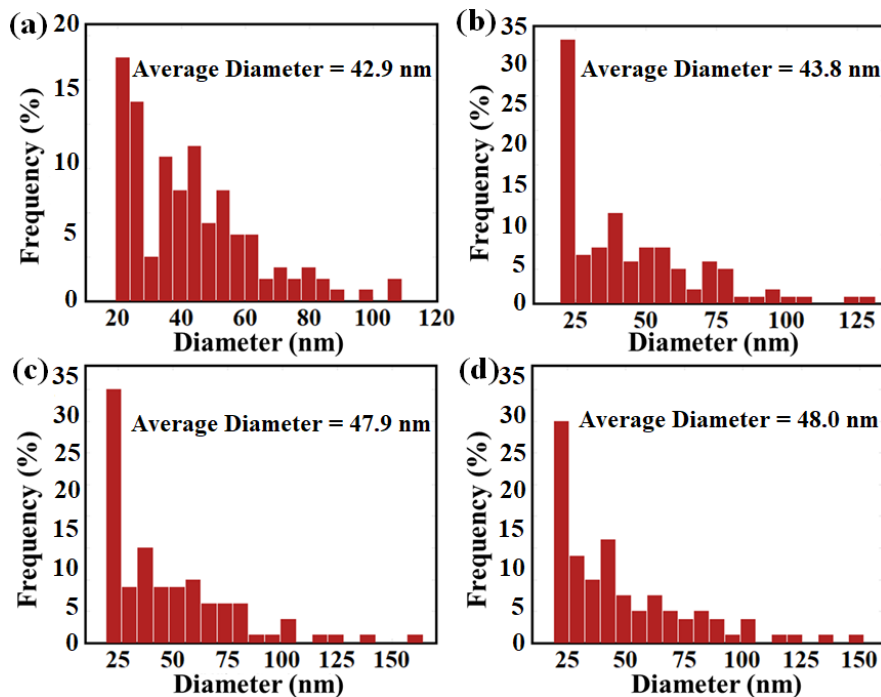


**Figure S2.** Pinhole distribution of PDPPPPTD/PC<sub>61</sub>BM photoactive layers (a) without thermal annealing, and undergoing thermal annealing at (b) 100 °C, (c) 110 °C, and (d) 120 °C for 10 min. The pinhole size distribution and average diameter were obtained using the scanning probe image processor (SPIP) software.

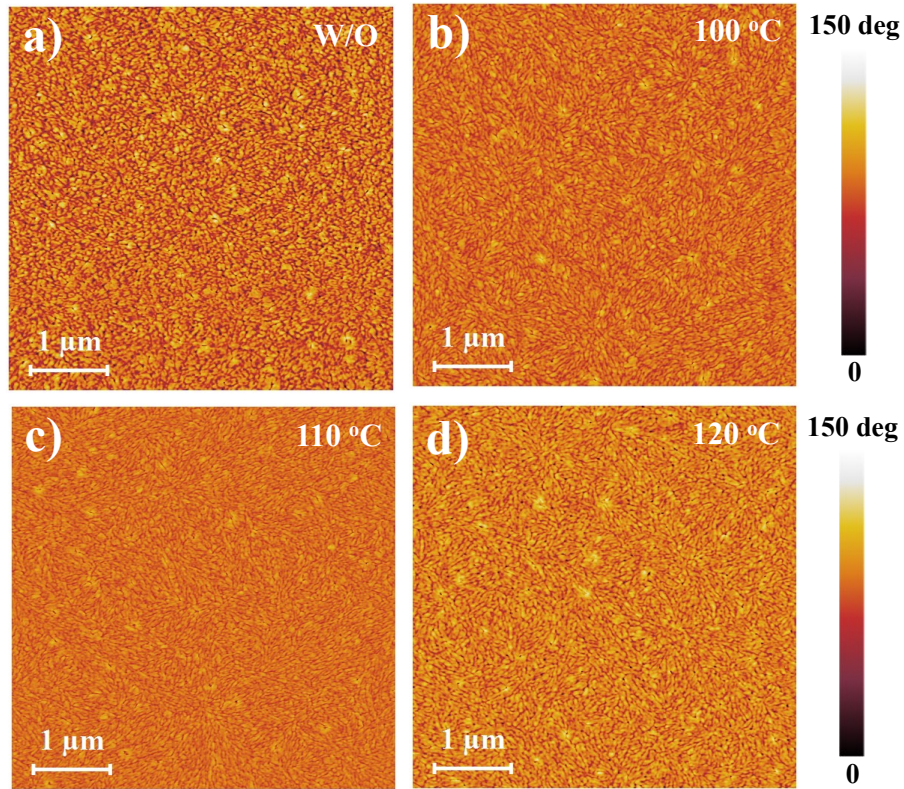


**Figure S3.** AFM phase images of PDPPPPTD/PC<sub>61</sub>BM photoactive layers (a) without thermal annealing, or annealed at different temperatures: (b) 100 °C, 10 min, (c) 110 °C, 10 min, and (d) 120 °C, 10 min. Scan size: 5 μm × 5 μm.

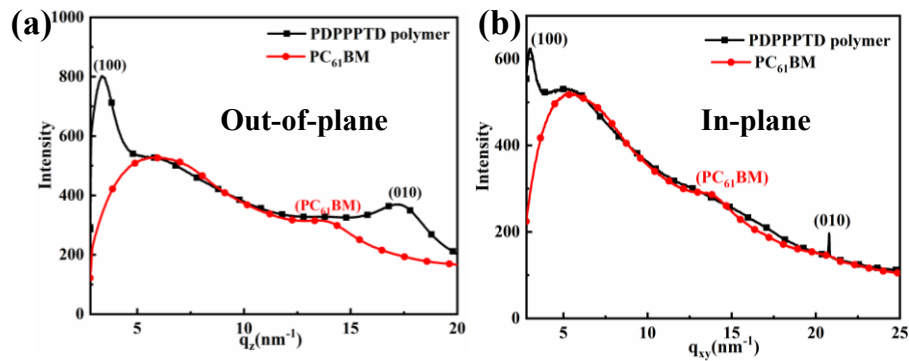


**Figure S4.** (a) GIXRD patterns with OOP direction and (b) IP direction for pristine PDPPPPTD polymer and PC<sub>61</sub>BM.

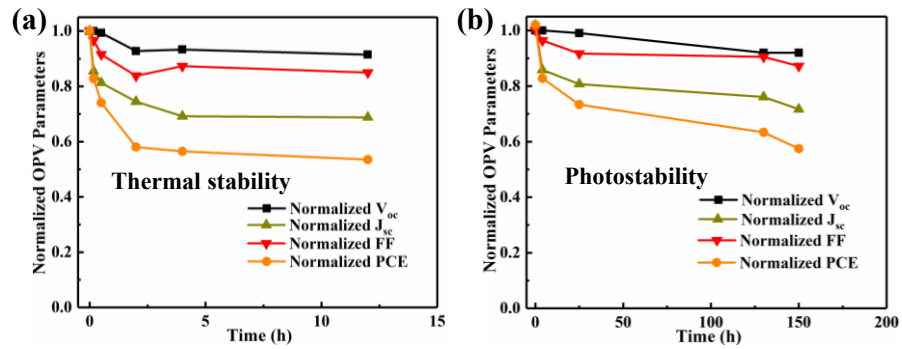


**Figure S5.** (a) Thermal stability of PTB7/PC<sub>71</sub>BM devices at 85 °C in a glovebox. (b) Photo-stability of PTB7/PC<sub>71</sub>BM devices in a glovebox under continuous illumination of simulated solar light.

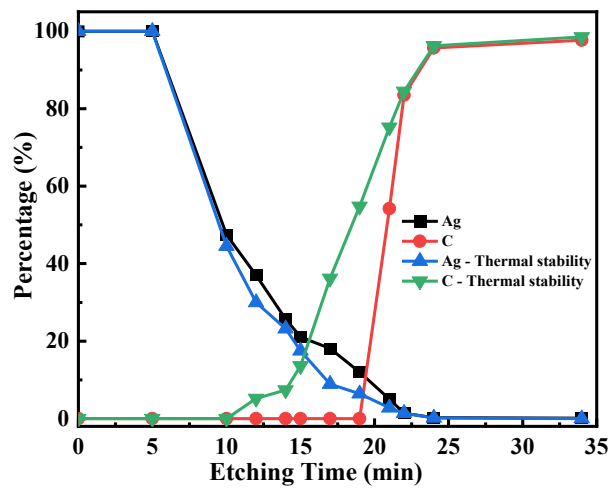


**Figure S6.** Elements of Ag and C percentages across the electrode-photoactive layer interface as a function of etching time measured by XPS with depth profiling.

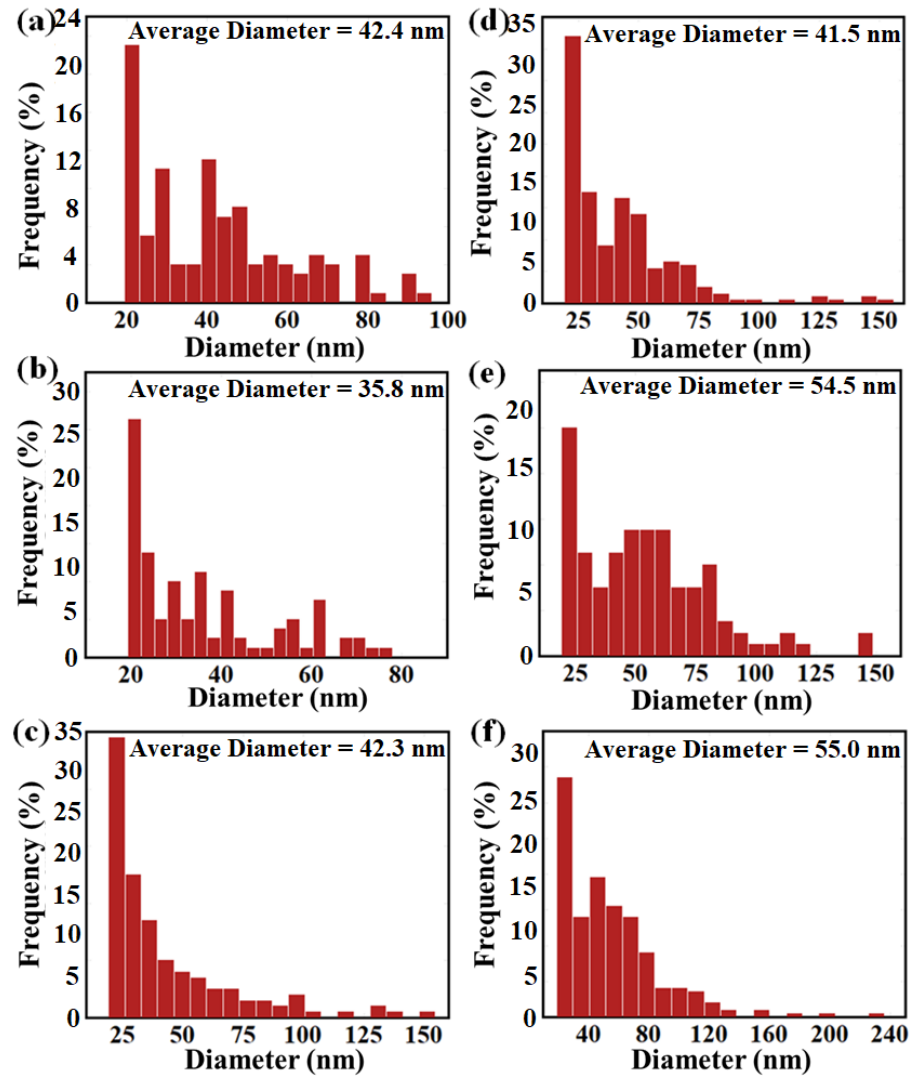


**Figure S7.** The pinhole distribution of photoactive layers under different conditions, (a) freshly prepared, (b) after being heated at 85 °C for 10 h in a glovebox, (c) after being heated at 85 °C for 75 h in a glovebox, (d) after 200 h continuous illumination in a glovebox, (e) after being kept at low humidity of 30% for 960 h in air and (f) after being kept at high humidity of 70% for 115 h in air. The pinhole size distribution and average diameter were obtained using the scanning probe image processor (SPIP) software.

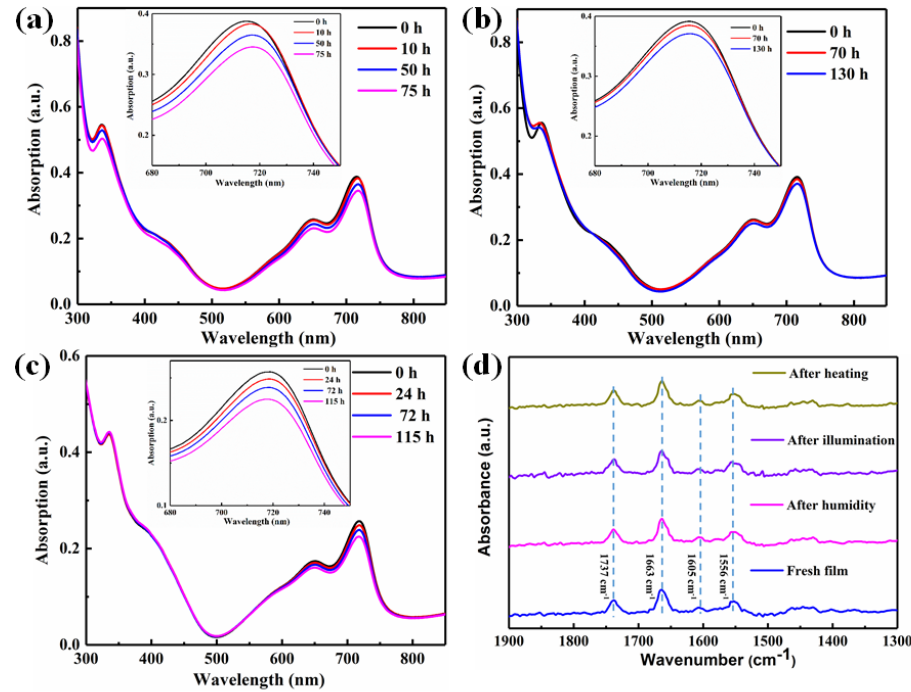


**Figure S8.** Variation of UV-visible absorption spectra of the photoactive layers with time under different conditions: (a) being heated at 85 °C in a glovebox, (b) under continuous simulated solar irradiation in a glovebox, and (c) at high humidity (70%) in the dark and d) FTIR spectra of the freshly prepared photoactive film and the films after stability tests at 85 °C, under continuous illumination, or at high humidity (70%).

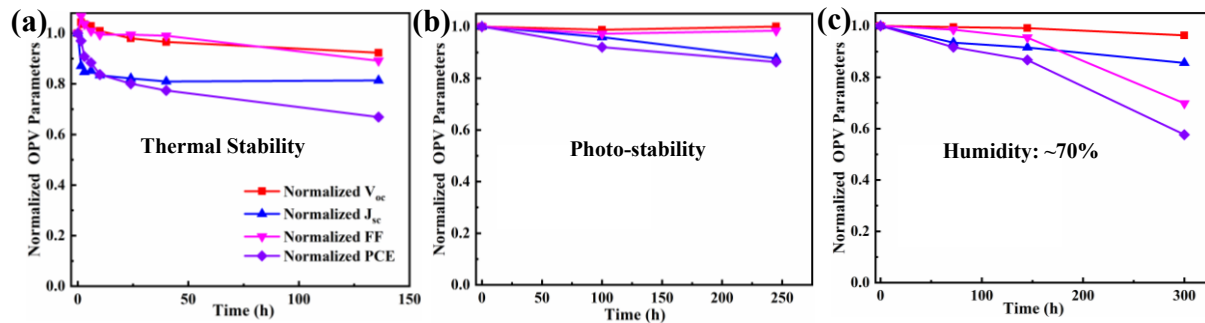


**Figure S9.** Stability measurements of PDPPPTD/PC<sub>61</sub>BM devices after additive treatment with AA: (a) at 85 °C in a glove box, (b) under continuous illumination in a glove box, (c) in the air with high humidity of 70% in the dark.

**Table S1.** Electron and hole mobility values for PDPPPTD/PC<sub>61</sub>BM devices based on the electron-only devices of ITO/ZnO/PDPPPTD:PC<sub>61</sub>BM/LiF/Al and the hole-only devices of ITO/PEDOT:PSS/PDPPPTD:PC<sub>61</sub>BM/MoO<sub>3</sub>/Ag by space-charge-limited current (SCLC) measurements under different conditions (such as after thermal annealing at 100 °C for 10 min, after thermal stability at 85 °C for 75 h, after photo-stability under continuous illumination for 200 h, and after humidity stability at high humidity (~70%) for 115 h).

Different Conditions	Electron mobility ( $\mu_e$ )	Hole mobility ( $\mu_h$ )	$\mu_e / \mu_h$
	(cm <sup>2</sup> V <sup>-1</sup> s <sup>-1</sup> )	(cm <sup>2</sup> V <sup>-1</sup> s <sup>-1</sup> )	
Fresh Sample	$1.10 \times 10^{-4}$	$9.64 \times 10^{-5}$	1.14
100 °C/10min	$1.37 \times 10^{-4}$	$1.05 \times 10^{-4}$	1.31
Thermal Stability	$1.36 \times 10^{-4}$	$8.05 \times 10^{-5}$	1.69
Photo-Stability	$1.26 \times 10^{-4}$	$7.20 \times 10^{-5}$	1.74
Humidity Stability (~70%)	$1.32 \times 10^{-4}$	$5.47 \times 10^{-5}$	2.42

**Table S2.** A summary of stability data of the organic solar cells based on fullerenes derivatives (PC<sub>61</sub>BM and PC<sub>71</sub>BM) as acceptors in recent years.

Device Structure	Storage Condition	Storage Time	Device Degradation	Ref.
ITO/PEDOT:PSS/PTB7:PC <sub>61</sub> BM (with BABP)/Ca/Al	150 °C in glovebox	15 h	14.8 %	[1]
ITO/TiO <sub>x</sub> /PDPPTBT:PC <sub>71</sub> BM (with BABP)/MoO <sub>3</sub> /Ag	150 °C in glovebox	15 h	40 %	[1]
ITO/PEDOT:PSS/SiIDT-BT:PC <sub>71</sub> BM/Ca/Al (with bis-azide DAZH)	85 °C in glovebox	130 h	≥ 20 %	[2]
ITO/PEDOT:PSS/P2:PC <sub>71</sub> BM/Ca/Al	85 °C in glovebox	100 h	30 %	[3]
ITO/TiO <sub>x</sub> /PTB7-Th:Alloy acceptor/Ca/Al	130 °C in glovebox	2 h	10 %	[4]
ITO/ZnO/PDPPPTD:PC <sub>61</sub> BM/MoO <sub>3</sub> /Ag	85 °C in glovebox	75 h	30 %	This work
ITO/ZnO/PDPPPTD:PC <sub>61</sub> BM (with AA additives)/MoO <sub>3</sub> /Ag	85 °C in glovebox	130 h	30 %	This work
ITO/ZnO/P3HT:PC <sub>61</sub> BM/MoO <sub>3</sub> /Al	Illumination in glovebox	80 h	43 %	[5]
ITO/MoO <sub>3</sub> /P3HT:PC <sub>61</sub> BM/LiF/Al	Illumination in glovebox	168 h	10%	[6]
ITO/ZnO (withPA)/P3HT:ICBA/MoO <sub>3</sub> /Ag	Illumination in air	200 h	20 %	[7]
ITO/PEDOT:PSS/PThBDTP:PC <sub>71</sub> BM/PFN/Al (without or with DIO)	Illumination	2 h	10% (W/O) 18% (DIO)	[8]
ITO/ZnO/PDPPPTD:PC <sub>61</sub> BM/MoO <sub>3</sub> /Ag	Illumination in glovebox	200 h	20 %	This work
ITO/ZnO/PDPPPTD:PC <sub>61</sub> BM (with AA additives)/MoO <sub>3</sub> /Ag	Illumination in glovebox	245 h	15 %	This work
ITO/PEDOT:PSS/PCDTBT:PC <sub>71</sub> BM/TiO <sub>x</sub> /Al	Humidity: 50 % in air	36 h	20 %	[9]
ITO/ZnO/PTB7-Th:PC <sub>71</sub> BM (with TCB additive)/MoO <sub>3</sub> /Ag	Humidity: ~35 % in air	240 h	10 %	[10]
ITO/ZnO/PTB7:PC <sub>71</sub> BM/CzPAF-SBF/Ag	Humidity: ~28 % in air	~500 h	10 %	[11]
ITO/ZnO/PCE-11:PC <sub>71</sub> BM/MoO <sub>3</sub> /Ag	Humidity: < 40 % in air	100 h	70 %	[12]
ITO/ZnO/PDPPPTD:PC <sub>61</sub> BM/MoO <sub>3</sub> /Ag	Humidity: 30 % in air	960 h	> 35 %	This work
ITO/ZnO/PDPPPTD:PC <sub>61</sub> BM (with AA additives)/MoO <sub>3</sub> /Ag	Humidity: 70 % in air	300 h	40 %	This work

**Table S3.** Photoactive layer deposition method and device performance of the single-junction, air-processed organic solar cells reported in recent years.

Active Layers	Deposition Method	V <sub>oc</sub> [V]	J <sub>sc</sub> [mA/cm <sup>2</sup> ]	FF [%]	PCE [%]	Ref.
PDPPPTD:PC <sub>71</sub> BM	Spin-Coating	0.85	11.72	67	6.70	[13]
P9:PC <sub>71</sub> BM	Spin-Coating	0.85	13.17	64	7.13	[14]
PTB7-Th:tPDI-Hex	Spin-Coating	0.94	11.6	43.7	4.8	[15]
P3HT:Si-PCPDTBT:PCBM	Blade-Coating	0.6	12.0	55.8	4.0	[16]
PCDTBT:GNF-EDNB60:PC <sub>71</sub> BM	Spin-Coating	0.896	12.56	57.1	6.41	[17]
p(DTGTPD):PC <sub>71</sub> BM	Spin-Coating	0.85	14.6	62	7.7	[18]
P3HT:DPP-Pht <sub>2</sub>	Spin Coating	0.89	5.91	50	3.28	[19]
PCDTBT:PC <sub>61</sub> BM	Printing	0.89	9.95	56.78	5.05	[20]
PCDTBT:PC <sub>71</sub> BM	Spin-Coating	0.894	11.54	56.4	5.82	[21]
PTB7-Th: PDI-DPP-PDI	Spin-Coating	0.98	11.32	50.1	5.6	[22]
PFQ2T-BDT:PC <sub>61</sub> BM	Spin Coating	0.87	8.70	55	4.2	[23]
P2:PC <sub>71</sub> BM	Spray-Cast	0.90	10.00	54	5.0	[24]
P3HT:PCBM	Spin-Coating	0.61	10.87	71	4.71	[25]
PBDT-TS1:PPDIODT	Blade-Coating	0.744	12.79	53.42	5.07	[26]
PBDT-TSR:PC <sub>71</sub> BM	Blade-Coating	0.780	16.48	62.37	8.02	[26]
PDPPPTD:PC <sub>61</sub> BM	Spin-Coating	0.870	12.55	67.83	7.41	This work

## References

- [1] L. Derue, O. Dautel, A. Tournebize, M. Drees, H. Pan, S. Berthumeyrie, B. Pavageau, E. Cloutet, S. Chambon, L. Hirsch, A. Rivaton, P. Hudhomme, A. Facchetti, G. Wantz, *Adv. Mater.* **2014**, *26*, 5831.
- [2] J. W. Rumer, R. S. Ashraf, N. D. Eisenmenger, Z. Huang, I. Meager, C. B. Nielsen, B. C. Schroeder, M. L. Chabiny, I. McCulloch, *Adv. Energy Mater.* **2015**, *5*, 1401426.
- [3] J. Kesters, P. Verstappen, J. Raymakers, W. Vanormelingen, J. Drijkoningen, J. D'Haen, J. Manca, L. Lutsen, D. Vanderzande, W. Maes, *Chem. Mater.* **2015**, *27*, 1332.
- [4] P. Cheng, C. Yan, Y. Wu, J. Wang, M. Qin, Q. An, J. Cao, L. Huo, F. Zhang, L. Ding, Y. Sun, W. Ma, X. Zhan, *Adv. Mater.* **2016**, *28*, 8021.
- [5] C. Zhang, L. Qi, Q. Chen, L. Lv, Y. Ning, Y. Hu, Y. Hou, F. Teng, *J. Mater. Chem. C* **2014**, *2*, 8715.

- [6] G. Williams, Q. Wang, H. Aziz, *Adv. Funct. Mater.* **2013**, *23*, 2239.
- [7] B. A. MacLeod, B. J. Tremolet de Villers, P. Schulz, P. F. Ndione, H. Kim, A. J. Giordano, K. Zhu, S. R. Marder, S. Graham, J. J. Berry, A. Kahn, D. C. Olson, *Energy Environ. Sci.* **2015**, *8*, 592.
- [8] H. Li, D. He, P. Mao, Y. Wei, L. Ding, J. Wang, *Adv. Energy Mater.* **2017**, *7*, 1602663.
- [9] J. Kong, S. Song, M. Yoo, G. Y. Lee, O. Kwon, J. K. Park, H. Back, G. Kim, S. H. Lee, H. Suh, K. Lee, *Nat. Commun.* **2014**, *5*, 5688.
- [10] S. Lee, J. Kong, K. Lee, *Adv. Energy Mater.* **2016**, *6*, 1600970.
- [11] S. S. Reddy, K. Gunasekar, J. H. Heo, S. H. Im, C. S. Kim, D. H. Kim, J. H. Moon, J. Y. Lee, M. Song, S. H. Jin, *Adv. Mater.* **2016**, *28*, 686.
- [12] D. Baran, R. S. Ashraf, D. A. Hanifi, M. Abdelsamie, N. Gasparini, J. A. Rohr, S. Holliday, A. Wadsworth, S. Lockett, M. Neophytou, C. J. Emmott, J. Nelson, C. J. Brabec, A. Amassian, A. Salleo, T. Kirchartz, J. R. Durrant, I. McCulloch, *Nature Mater.* **2017**, *16*, 363.
- [13] M. Guérette, A. Najari, J. Maltais, J.-R. Pouliot, S. Dufresne, M. Simoneau, S. Besner, P. Charest, M. Leclerc, *Adv. Energy Mater.* **2016**, *6*, 1502094.
- [14] A. Najari, S. Beaupré, N. Allard, M. Ouattara, J.-R. Pouliot, P. Charest, S. Besner, M. Simoneau, M. Leclerc, *Adv. Energy Mater.* **2015**, *5*, 1501213.
- [15] S. V. Dayenko, A. D. Hendsbee, G. C. Welch, *Chem. Commun.* **2017**, *53*, 1164.
- [16] T. Ameri, J. Min, N. Li, F. Machui, D. Baran, M. Forster, K. J. Schottler, D. Dolfen, U. Scherf, C. J. Brabec, *Adv. Energy Mater.* **2012**, *2*, 1198.
- [17] F. Bonaccorso, N. Balis, M. M. Stylianakis, M. Savarese, C. Adamo, M. Gemmi, V. Pellegrini, E. Stratakis, E. Kymakis, *Adv. Funct. Mater.* **2015**, *25*, 3870.
- [18] I. Constantinou, T. H. Lai, D. Zhao, E. D. Klump, J. J. Deininger, C. K. Lo, J. R. Reynolds, F. So, *ACS Appl. Mater. Interfaces* **2015**, *7*, 4826.
- [19] P. Josse, C. Dalinot, Y. Jiang, S. Dabos-Seignon, J. Roncali, P. Blanchard, C. Cabanetos, *J. Mater. Chem. A* **2016**, *4*, 250.
- [20] S. Jung, A. Sou, K. Banger, D.-H. Ko, P. C. Y. Chow, C. R. McNeill, H. Sirringhaus, *Adv. Energy Mater.* **2014**, *4*, 1400432.
- [21] T. Kim, S. J. Yang, S. K. Kim, H. S. Choi, C. R. Park, *Nanoscale* **2014**, *6*, 2847.
- [22] S. M. McAfee, S. V. Dayenko, P. Josse, P. Blanchard, C. Cabanetos, G. C. Welch, *Chem. Mater.* **2017**, *29*, 1309.
- [23] M. Prosa, M. Tessarolo, M. Bolognesi, O. Margeat, D. Gedefaw, M. Gaceur, C. Videlot-Ackermann, M. R. Andersson, M. Muccini, M. Seri, J. Ackermann, *ACS Appl. Mater. Interfaces* **2016**, *8*, 1635.

- [24] T. Wang, N. W. Scarratt, H. Yi, A. D. F. Dunbar, A. J. Pearson, D. C. Watters, T. S. Glen, A. C. Brook, J. Kingsley, A. R. Buckley, M. W. A. Skoda, A. M. Donald, R. A. L. Jones, A. Iraqi, D. G. Lidzey, *Adv. Energy Mater.* **2013**, *3*, 505.
- [25] Z. Hu, J. Zhang, Y. Zhu, *Appl. Phys. Lett.* **2013**, *102*.
- [26] L. Ye, Y. Xiong, H. Yao, A. Gadisa, H. Zhang, S. Li, M. Ghasemi, N. Balar, A. Hunt, B. T. O'Connor, J. Hou, H. Ade, *Chem. Mater.* **2016**, *28*, 7451.

## 5 CHAPTER 5 SYNERGISTIC EFFECT OF DIELECTRIC PROPERTY AND ENERGY TRANSFER ON CHARGE SEPARATION IN NON-FULLERENE BASED SOLAR CELLS

Pandeng Li, Jin Fang, Yusheng Wang, Sergei Manzhos, Lei Cai, Zheheng Song, Yajuan Li, Tao Song, Xuechun Wang, Xia Guo, Maojie Zhang, Dongling Ma, Baoquan Sun Angew. Chem. Int. Ed., 2021, DOI: 10.1002/anie.202103357



Figure of Table of Contents for This Section Work

Another challenge is from the non-fullerene based devices. In recent years, through designing the new non-fullerene acceptors with strong light-harvesting capability, the device efficiency of non-fullerene based devices has been rapidly improved and brokes through the limitation of the 10% efficiency of the fullerene derivatives based devices, which has achieved the best efficiency of over 18%. In the non-fullerene solar cells, a striking feature in the non-fullerene based devices is the efficient charge separation even under a tiny driving force (tens of meV) with reduced energy loss. It means that we can improve  $V_{oc}$  and  $J_{sc}$  at the same time. That is, the driving force isn't the main factor of charge separation for non-fullerene based devices, which is very different from different from the fullerene derivatives based devices. So what is the main factor for the charge separation in non-fullerene solar cells, which remains unclear yet. Here, dielectric constants of different non-fullerene based solar cells consisting of fluorinated-thienyl benzodithiophene (BDT-2F)-based polymer PM6 as the common donor, and a selected series of non-fullerene acceptors were precisely measured by a novel method. It was found that most of the non-fullerene acceptors exhibited higher dielectric constants than fullerene derivatives ( $PC_{61}BM$  and  $PC_{71}BM$ ). The corresponding photoactive films exhibited not only higher dielectric constants but also the larger dielectric constant differences between donor and non-fullerene acceptors. These would result in lower exciton binding energy and increased charge dissociation possibility with low geminate losses. Additionally, the overlap between the emission spectrum of donor and absorption spectra of non-fullerene acceptors allowed the resonance energy transfer from donor to the acceptor in these non-fullerene based devices, which was confirmed by

investigating the emission spectra of pristine donor (and acceptor) films and corresponding blend films. Such an energy transfer process enhanced the efficient exciton diffusion, promising improved device performance. Based on the synergistic effect of higher dielectric property and energy transfer on charge separation of selected non-fullerene based photovoltaic devices, therefore, these results provided strong hints to interpret efficient charge separation for the high device performance with a tiny driving force. Our work paves an alternative path to elucidate the intrinsic physical working mechanism on non-fullerene organic solar cells.

In this work, I got the help from Dr. Jin Fang and Yusheng Wang for the preliminary work and some useful advice. For example, Jin Fang helped to characterize related photovoltaic devices for *J-V* curves and EQE measurements. Yusheng Wang helped to do scattering-type scanning near-field optical microscopy measurements. In addition, Prof. Sergei Manzhos gave the theoretical calculation about the charge transfer rate. The work was published to the journal of *Angew. Chem. Int. Ed.*

**Keywords:** non-fullerene acceptors, photovoltaic devices, dielectric constant, resonance energy transfer

## 5.1 Introduction

With the advantages of flexibility, light weight, and simple device fabrication process, organic photovoltaic(OPV) devices have obtained much attention and achieved high power conversion efficiency (PCE) as a result of the development of new photovoltaic materials, device fabrication methods designing, and the morphology optimization of photoactive layers.<sup>1-3</sup> In particular, thanks to the breakthroughs in non-fullerene acceptor materials, the device performance made rapid progress, and the certified PCE of a single heterojunction OPV device has been over 17%<sup>4</sup> Interestingly, the most striking feature of high-performance non-fullerene based devices is the low voltage loss and consequently the efficient charge separation with a small (even negligible) driving force, namely the energetic offset between the bandgap ( $E_{\text{gap}}$ ) of donor/acceptor materials and the energy of charge transfer state ( $E_{\text{CT}}$ ). The case is very different from the fullerene derivatives-based OPV devices, where a significant driving force (generally  $> 300$  meV) is required because of the low dielectric constants of organic compounds.<sup>5, 6</sup> Until now, most researches are mainly focused on high-performance devices with lower voltage loss by designing novel non-fullerene acceptors.<sup>7-9</sup> Only a few researchers pay attention to how excitons dissociate into free charge carriers in non-fullerene-based OPV devices at a small driving force with reduced voltage loss. For example, the pioneering work pointed out that intermolecular electrical field (IEF) induced by the electrostatic potential (ESP) differences between the donor and non-fullerene acceptor, facilitated highly efficient charge separation at a small driving force. However, it considered the ESP difference between single donor and acceptor molecules as the only factor, which completely ignored the influence of intermolecular packing on the charge separation.<sup>10-12</sup> Furthermore, the molecule Y6 with distinctive  $\pi$ - $\pi$  molecular packing resulted

in delocalized and emissive excitons according to the research of Yip's group. And non-radiative voltage loss was suppressed in association with the delocalization of electron wave functions at the donor-acceptor (D-A) interface. In that case, the Coulomb attraction between interfacial electron-hole pairs was dramatically reduced by increasing the distance between interfacial electron-hole pairs.<sup>13</sup> Similarly, the research results suggested that the long-lived and disorder-free charge-transfer states in non-fullerene-based devices were formed, which was close to the quasi-thermodynamic conditions without energy offsets to drive interfacial excitons dissociation and suppress non-radiative recombination.<sup>14</sup> Differently, an alternative result revealed that the intramolecular coupling in the popular fluorinated non-fullerene acceptor (Y6) domains led to the formation of an intra-moiety intermediate state in 0.2 ps following a hole transfer process which was independent of energy alignment and electron coupling at the D-A interface. As a result, efficient hole transfer would occur even under a tiny highest occupied molecular orbital energy offset ( $\Delta\text{HOMO}$ ) in non-fullerene-based photovoltaic devices.<sup>15</sup> In addition, the hole transfer and efficient exciton dissociation in high-performance devices with small  $\Delta\text{HOMO}$  was independent of HOMO offsets.<sup>16-18</sup> Hence, the whole picture of exciton dissociation for the non-fullerene based device with a low voltage loss (or a small driving force) is still unclear yet. An understanding of the dominant factors influencing the efficient charge separation is highly indispensable to make even higher-performance OPV.

In a bulk heterojunction OPV device, efficient exciton diffusion is of fundamental importance for a high-performance device. Under a photoactive film with favorable phase separation, the exciton diffusion length is the main factor for efficient exciton diffusion, which is influenced by intermolecular spacing and molecular interaction.<sup>19-21</sup> Interestingly, it is confirmed that some non-fullerene acceptors display high exciton diffusion length.<sup>22,23</sup> Besides efficient exciton diffusion, the dielectric constant ( $\mathcal{E}_r$ ) of OPV materials is another fundamental physical parameter. It is inversely proportional to exciton binding energy ( $E_b$ ) obeying the equation  $E_b = q^2/4\pi \mathcal{E}_0 \mathcal{E}_r r_o$ , where  $q$ ,  $\mathcal{E}_0$ ,  $\mathcal{E}_r$ ,  $r_o$  are the elementary charge, the absolute dielectric permittivity, the relative dielectric constant, and the distance between the electron and hole, respectively.<sup>24</sup> Therefore, efforts have been made to boost up the dielectric constant by anchoring polar groups (such as fluorine atoms or cyano-ended side chains) to the backbones structure of OPV materials and in order to establish a relationship between dielectric constant and device performance. For example, a polar cyano-ended side chain was incorporated into diketopyrrolopyrrole (DPP) unit of an indacenodithiophene (IDT)-based copolymer (PIDT-DPP-CN) to increase its dielectric constant, thereby improving both open-circuit voltage ( $V_{oc}$ ) and short-circuit density ( $J_{sc}$ ).<sup>25</sup> The increased blend dielectric constant, influenced by better polymer-fullerene derivatives interaction, led to more efficient exciton dissociation and delocalization.<sup>26,27</sup> On the contrary, the performance of devices with cyano-containing polymers was inferior to that of the devices with parent polymers because the increased energetic disorder of cyano-containing polymers with strong local permanent dipoles decreased the hole mobility.<sup>28</sup> Similarly, the enhanced dielectric constant of

the fullerene derivative *via* the addition of triethylene glycol appendage (TEG-PC<sub>61</sub>BM) did not increase exciton dissociation possibility, which would be ascribed to the incorporation of trapping sites into the photoactive film by TEG-chain.<sup>29</sup> As it is, more insights are required to rationally tune the dielectric constants of OPV materials for the high-performance device. Regarding the non-fullerene-based devices, the fluorinated non-fullerene acceptor (IT-4F) improved charge dissociation with low geminate loss and balanced charge extraction and recombination, eventually prompting device performance. It is ascribed to the enlarged dielectric constant.<sup>30</sup> Differently, the fluorinated non-fullerene acceptor (Y6), as an additional component in the photoactive film to tune down the final blend dielectric constant, resulted in enhanced ternary device performance *via* better balancing the exciton dissociation and carrier recombination.<sup>31</sup> It is to say, the reported correlations between dielectric constants and device performance of non-fullerene-based devices are controversial. In addition, it is very challenging to accurately determine the dielectric constants of OPV materials because of metal diffusion into organic films based on current methods.<sup>32,33</sup> Therefore, it is difficult to figure out the influence of dielectric constant on the relevant photophysical processes of non-fullerene based OPV device with a small driving force. What is urgently needed now is to develop an alternative method to accurately extract the dielectric constant to possibly provide a clear physical picture for exciton dissociation and charge transfer process in non-fullerene based OPV.

Here, a novel method to extract dielectric constants of organic photoactive films was developed. It was found that most of the non-fullerene acceptors in the study displayed higher dielectric constants than the conventional fullerene derivatives (PC<sub>61</sub>BM and PC<sub>71</sub>BM) in the frequency range of 100 Hz to ~ MHz. The results indicate that the non-fullerene-based OPV devices decrease the carrier recombination loss and meanwhile contribute to the charge separation. Meanwhile, scattering-type scanning near-field optical microscopy (s-SNOM) measurement exhibited the larger dielectric constant differences between PM6 polymer donor and non-fullerene acceptors. The differences led to lower exciton binding energy and more efficient exciton dissociation, which is consistent with the high device performance under a small driving force. Besides, the emission spectral ranges of the donor (PM6) and the absorption band of the non-fullerene acceptors displayed large overlap, which allows the energy transfer from the donor to the acceptors in non-fullerene-based OPV devices. The synergistic effect of dielectric property and energy transfer occurring in non-fullerene OPV devices allowed us to interpret their high device performance with a small driving force.

## 5.2 Experimental Section

### 5.2.1 Reagent and Materials

Patterned ITO-coated glass substrates were purchased from Shenzhen Huayu Union Technology Co., LTD (China) ( $R_s \leq 10 \Omega/\square$   $T_r \geq 83\%$ ). PM6 and the related acceptors (such as ITIC, IT-4F, Y6, IEICO, and F8IC) were synthesized according to our previous reports. PEDOT:PSS (VP Al 4083) were obtained from H.C.

Starck. Other related solvents, such as 1-chloronaphthalene (CN), 1,8-diiodooctane (DIO), chloroform (CF) and the chlorobenzene (CB), dichloromethane (DCM) were bought from Sigma-Aldrich and used as received.

### 5.2.2 Dielectric Constant Measurement

Patterned ITO-coated glass substrates were cleaned with a series of detergent, deionized water, acetone, and absolute ethyl alcohol for 15 min in an ultrasonic bath before being dried with a nitrogen stream. Then PEDOT:PSS solution was spin-coated onto the cleaned ITO/glass substrate treated with plasma for 15 min followed by thermal annealing at 150 °C for 10 min. All the measured films were spun from the optimized photoactive solutions that obtained higher device performance and the related pristine acceptor solutions in glovebox. After the fabrication of films, polydimethylsiloxane (PDMS) channels (**Figure S5a**) was placed onto the above films. The PDMS model was fabricated by stirring precursor and curing agent (Sylgard 184 Silicone Elastomer) in a 10:1 (V:V) ratio, then was poured over the mask in a plastic petri dish, finally was heated at 60 °C for 2 h. The EGaIn was injected into the PDMS channels. To avoid any direct contact between liquid EGaIn and test clamp connector, the thin copper wire was buried in the top of the PDMS channels (Figure S5a), which could contact with the injected EGaIn in the PDMS channels and was used as the bridge of liquid EGaIn and test clamp connector. During the capacitance measurement, the EGaIn was injected into the PDMS channels. One test clamp connector touched the ITO electrode, and another one contacted with copper wires electrode. The real capacitor device was shown in Figure S5b, in which the four clamps allowed the PDMS model to adhere tightly to the organic films. Besides, because the contacts, junctions, and feed wires (as the resistive or inductive influence factors) were in real capacitor devices, a suitable equivalent circuit model (**Figure S5a**) in which the above wires could be assigned to the different circuit elements (such as  $R_s$  and  $R_p$ ), was employed and the same wires were used in the whole measurement process. The strategies could provide the fixed value from the effects of the above wires, which is beneficial for accurately measuring the capacitance of organic films. The capacitance response was measured in the range of 100 Hz to 120 MHz by the precision impedance analyzer (Wayne Kerr 6500B series) with a small AC drive voltage of 10 mV. The measurements were carried out at ambient conditions. The measured capacitance versus frequency plots are fitted by a polynomial function. According to the fitted capacitance value ( $C$ ), the relative dielectric constant ( $\epsilon_r$ ) could be calculated by the equation ( $C = \epsilon_0 \epsilon_r A/d$ ), in which  $\epsilon_0$  is the absolute dielectric permittivity ( $8.85 \times 10^{-12}$  F/m),  $A$  is the knowing contact area, and  $d$  is the knowing thickness of the organic film.

### 5.2.3 Fabrication of Bilayer Heterojunction Films

In the floating film method, neat PM6 and Y6 were separately dissolved in CF at 60 °C and stirred overnight. Then neat PM6 solution (12 mg/mL) was spin-casted on polystyrene sulfonate (PSS) coated glass while Y6

solution (20 mg/mL) was spin-casted on pre-cleaned Si substrate. The neat PM6 and Y6 films were vacuum ( $1 \times 10^{-6}$  mbar) dried at room temperature for a day to remove the residual amount of processing solvent before fabricating a bilayer sample. PM6 film was floated onto DI water and picked up with the supported Y6 film, finally forming a bilayer of PM6/Y6 on the Si substrate. In the orthogonal solvent method, ITO substrates were sequentially cleaned by ultrasonication with distilled water, acetone, and isopropanol. PM6 dissolved in CB with a concentration of 10 mg/mL was spin-casted with different rotational speeds to fabricate the PM6 layers with different thicknesses. Then the selected non-fullerene acceptors (IT-4F and Y6) in DCM with a concentration of 6 mg/mL were deposited on PM6 layer.

#### 5.2.4 Fabrication of Solar Cells

The same steps mentioned above in the preparation of the device with EGaIn, were followed until the spin coating of photoactive solutions. The different photoactive layers were deposited onto PEDOT:PSS film according to optimized device conditions in glovebox. The poly[(9,9-bis(3'-(N,N-dimethyl)-nethylammonium-propyl)-2,7-fluorene)-alt-2,7-(9,9-diethylfluorene)]dibromide (PFN-Br) that is a ethanol solution with a concentration of 0.5 mg/mL, was then spin-coated onto the top of photoactive layers. Finally, the device fabrication was completed by thermal evaporation of 100 nm Al under a vacuum of ca.  $1 \times 10^{-6}$  mbar. Device current-voltage ( $J-V$ ) characteristics were measured under the illumination of AM 1.5G (100 mW/cm<sup>2</sup>) using a SS-F5-3A solar simulator (AAA grade, 50 × 50 mm<sup>2</sup> photobeam size) of Enli Technology CO., Ltd.. A 2 × 2 cm<sup>2</sup> monocrystalline silicon reference cell (SRC-00019) was obtained from Enli Technology CO., Ltd.

#### 5.2.5 Characterization

Optical absorption spectra were recorded using a UV-vis spectrometer (SPECORD S 600), and PL spectrum was measured by an IHR 320 (Horiba Instruments Inc.), and excited wavelength of PM6, ITIC, IT-4F, Y6, and IEICO are 560 nm, 682 nm, 710 nm, 687 nm, and 685 nm, respectively. Film thickness was measured by a profile meter (Dektak 150). The surface morphology and optical amplitude images were derived from the scattering-type scanning near-field optical microscopy (s-SNOM) with the tapping mode. Device J-V curves were using a Keithley 2400 source measure unit under AM 1.5G simulated solar light. An IQE200B system (Newport Corporation) was used to measure external quantum efficiency (EQE) by scanning from 300 to 1000 nm with a 10 nm resolution. Impedance spectroscopy was measured in the range of 100 Hz to 120 MHz by the precision impedance analyzer (Wayne Kerr 6500B series) with an AC drive voltage of 10 mV. The electrochemical cyclic voltammetry (CV) was carried out on a Zahner Ennium IM6 Electrochemical Workstation with a glassy carbon disk, a Pt wire, and a Ag/Ag<sup>+</sup> electrode as working

electrode, the counter electrode, and the reference electrode respectively, in 0.1 mol L<sup>-1</sup> tetrabutylammonium hexafluorophosphate ( $\text{Bu}_4\text{NPF}_6$ ) acetonitrile solution at a scan rate of 50 mV s<sup>-1</sup>.

### 5.3 Results and Discussion

#### 5.3.1 Photovoltaic Output of the OPV Devices

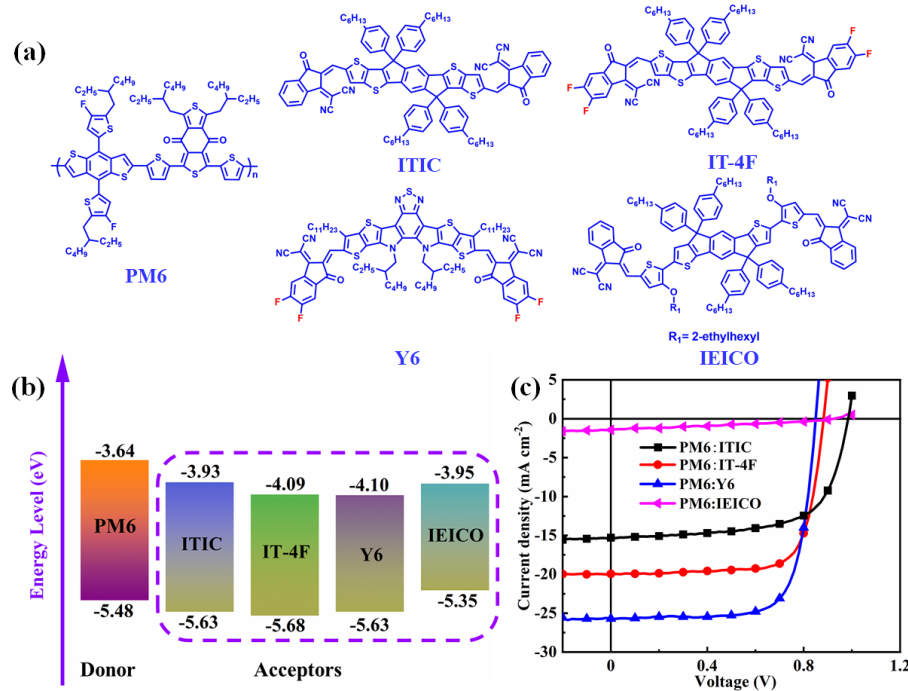


**Figure 1.** (a) Chemical structure of donor material (PM6) and related acceptor ones (ITIC, IT- 4F, Y6, and IEICO), (b) Corresponded energy level diagrams of PM6 and related acceptor materials, and (c)  $J$ - $V$  characteristics of the devices based on PM6 and related acceptor materials.

Four representative systems of non-fullerene-based photovoltaic devices were selected to explore the correlation between dielectric constant and device performance. The wide-bandgap polymer PM6 containing fluorinated thienyl benzodithiophene unit acted as a typical donor, and the narrow bandgap non-fullerenes of ITIC, IT-4F, Y6, and IEICO served as acceptors, respectively. Their corresponding chemical structures and the related energy level diagrams extracted from cyclic voltammetry (CV) are shown in **Figure 1a**, **Figure 1b**, and **Figure S1**.<sup>34</sup> It was found that all the blend systems displayed relatively large electron affinity offsets ( $\Delta\text{LUMO} > 290$  meV, as shown in **Table 1**), which are usually correlated with the driving force of electron transfer from a donor to an acceptor. However, they all exhibited small ionization potential offsets ( $\Delta\text{HOMO}$ ), which act as the driving force of hole transfer from an acceptor to a donor. Especially regarding the donor/acceptor pair of PM6:IEICO, the ionization potential offset was even negative (-0.13 eV). In spite of the tiny ionization potential offset, the efficient charge separation still occurred, according to a previous report.<sup>35</sup> As seen from the absorption spectra of blend films shown in

**Figure S2**, all donor/acceptor pairs exhibited favorable and complementary optical absorption. Three of them (PM6:IT-4F, PM6:Y6, and PM6:IEICO) showed relatively wide optical absorption spectra reaching the near-infrared region, which means that more excitons should be generated. *J-V* characteristics of the devices based on these four donor/acceptor pairs are shown in **Figure 1c**. The electrical parameters are summarized in **Table 1**. It was found that the blend devices of PM6:ITIC, PM6:IT-4F, and PM6:Y6, displaying ionization potential offsets of over 150 meV, yielded PCEs of 9.97%, 13.16%, and 16.26%, respectively. The respective external quantum efficiency (EQE) spectra profiles (**Figure S3**) were consistent with optical spectra of the related blend films, which was indicated of efficient charge separation occurring in all three devices. A voltage loss is defined by the difference between the optical gap ( $E_g$ ) of the lower bandgap materials and  $V_{oc}$ , where  $E_g$  is estimated from the cross point between the normalized absorption and emission spectra of the lower bandgap materials (**Figure S4**).<sup>5</sup> The high-efficiency devices display small voltage losses (**Table 1**), which are close to the empirical threshold of 0.6 eV. On the contrary, the PM6:IEICO device yielded significantly inferior device performance (PCE: 0.407%) with lower short current density ( $J_{sc}$ ) regardless of its smallest voltage loss and widened optical absorption spectrum. We suspect that the negative ionization potential offset (-130 meV) in the donor/acceptor pair of PM6:IEICO is likely responsible for the inferior PCE of PM6:IEICO because of inefficient charge separation as confirmed by the lowest EQE.

### 5.3.2 Simulated Charge Transfer Rate

To further gain insights into the relationships among differences in band alignments, charge transport, and device performance, the density functional theory simulations on molecules as well as on donor-acceptor dimers were conducted. The calculated details are discussed in **Supporting Text 1** and are summarized in **Table S2**. According to the model, the differences of LUMO levels between the PM6 donor and the selected non-fullerene acceptors (0.36 eV, 0.44 eV, and 0.74 eV for IEICO, ITIC, and IT-4F, respectively) should be large enough to allow appreciable electron transfer rates. Two acceptor molecules displayed the electron transfer rates in the order of  $10^{12}\text{-}10^{13}\text{ s}^{-1}$ . However, IEICO exhibited an order of magnitude lower electron transfer rate of  $10^{11}\text{ s}^{-1}$ , and the detailed reason is unclear. On the other hand, the alignment of the HOMO levels was correlated with hole transfer rate. Here, ITIC and IT-4F (with  $\Delta\text{HOMO}$  of 0.42 eV, and 0.68 eV, respectively) is favorable for hole transfer. Although the HOMO level of IEICO was only 40 meV higher than that of PM6 donor, the tiny  $\Delta\text{HOMO}$  only led to a modest hole transfer rate (on the order of  $10^{11}\text{ s}^{-1}$ ), which is an order lower than that of ITIC/IT-4F pair (on the order of  $10^{12}\text{ s}^{-1}$ ). Both lower electron and hole rates likely result in inferior PCE of IEICO based device. The results reveal that in a non-fullerene-based device with a low voltage loss, the  $\Delta\text{LUMO}$  (and  $\Delta\text{HOMO}$ ) between the PM6 donor and the selected non-fullerene acceptors do not seem to be the dominant factor of hole/electron transfer rate.<sup>9</sup>

**Table 1.** Summary of photovoltaic parameters and related voltage loss of devices based on different materials systems.

Active Layer	V <sub>oc</sub> (V)	J <sub>sc</sub> (mA/cm <sup>2</sup> )	FF (%)	PCE (%)	ΔHOMO <sup>a</sup>	ΔLUMO <sup>b</sup>	E <sub>g/q</sub> (V)	E <sub>g/q</sub> – V <sub>oc</sub> (V)
PM6:ITIC	0.984 (0.983 ± 0.001)	15.29 (15.11 ± 0.16)	66.28 (64.06 ± 1.60)	9.97 <sup>c</sup> (9.53 ± 0.34) <sup>d</sup>	0.15	0.29	1.66	0.68
PM6:IT-4F	0.883 (0.883 ± 0.001)	19.95 (19.39 ± 0.51)	74.75 (75.44 ± 0.57)	13.17 (12.91 ± 0.24)	0.20	0.45	1.58	0.70
PM6:Y6	0.853 (0.850 ± 0.003)	25.75 (25.92 ± 0.22)	74.07 (73.27 ± 0.74)	16.26 (16.14 ± 0.08)	0.15	0.46	1.40	0.55
PM6:IEICO	0.923 (0.954 ± 0.025)	1.433 (0.844 ± 0.41)	30.78 (40.68 ± 7.11)	0.41 (0.30 ± 0.08)	-0.13	0.31	1.44	0.52

<sup>a</sup>ΔHOMO = HOMO (donor) - HOMO (acceptor) <sup>b</sup>ΔLUMO = LUMO (donor) - LUMO (acceptor) <sup>c</sup>The maximum value of device performance. <sup>d</sup>The average value is obtained in five devices.

### 5.3.3 Dielectric Constants Measurement of the Films

As mentioned above, the voltage loss is correlated with two factors. One is the driving force that does not contribute to the V<sub>oc</sub>. The other is the charge recombination in OPV devices, including radiative and non-radiative ones. The radiative recombination originating from the absorption above the bandgap is unavoidable in all kinds of solar cells. The non-radiative recombination is inversely proportional to electroluminescence quantum efficiency (EQE<sub>EL</sub>) and would be suppressed *via* minimizing voltage loss. The decreased driving force results in high EQE<sub>EL</sub> and consequently suppressed non-radiative recombination. Clearly, the driving force accounts for an important part of OPV devices.<sup>5,6</sup> In the case of non-fullerene-based devices, the significant feature is that effective charge dissociation and suppressed charge recombination is realized under a small driving force with a low voltage loss. It can be attributed to low exciton binding energy, which depends on the dielectric constant of photovoltaic materials.<sup>9</sup> In this regard, the accurate measurement of the dielectric constant of involved photovoltaic materials in a non-fullerene-based device is indispensable to understand low voltage loss deeply.<sup>26,36,37</sup>

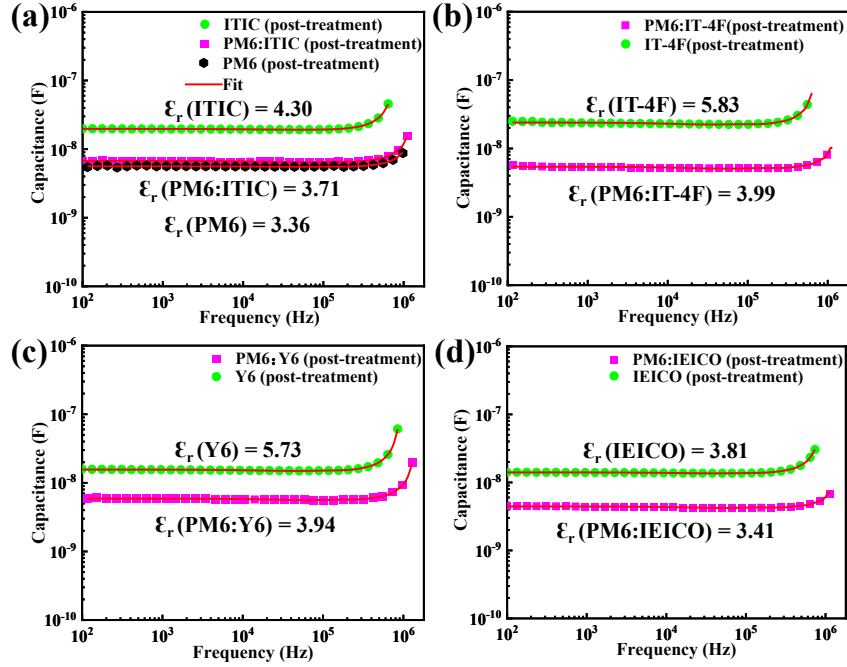


**Figure 2.** Capacitance *versus* frequency plots for (a) pristine ITIC film, pristine PM6 film, and the PM6 and ITIC blend film with post-treatment, (b) Pristine IT-4F film, and the PM6 and IT-4F blend film with post-treatment, (c) Pristine Y6 film, and the PM6 and Y6 blend film with post-treatment, and (d) Pristine IEICO film, and the PM6 and IEICO blend film with post-treatment. The red lines represent the simulated fitting curves over the measured data by a polynomial function.

Dielectric constant ( $\epsilon_r$ ) in the frequency range of 100 Hz to several megahertz (MHz) is considered to be reversely proportional to bimolecular recombination. However, it is still challenging to precisely extract these values of organic semiconductors by the parallel-plate-capacitance measurement with impedance spectroscopy because space charge polarizations or ionic movements would occur when the dielectric material is sandwiched between parallel electrodes.<sup>38</sup> The damage/contamination of the top thermal evaporated electrode would result in space charge polarizations or ionic movements. In order to eliminate the undesirable effect, a more precise method was invented to extract relative dielectric constant ( $\epsilon_r$ ) for soft, organic semiconductor materials, as shown in **Figure S5**. It yields  $\epsilon_r$  by measuring the capacitance of a capacitor device made of a thin organic film as a function of frequency by impedance spectroscopy. A thin organic film is deposited on ITO/poly(3,4-ethylenedioxythiophene):poly(styrenesulfonate) (PEDOT:PSS), and the eutectic Ga-In (EGaIn) is used as the top electrode. A soft poly(dimethylsiloxane) micro-channel is specially designed to hold liquid eutectic EGaIn.<sup>36</sup> The channels are enlarged to assure the full contact area between EGaIn and the organic layer as well as to provide a facile device fabrication process. The detailed fabrication and measurement processes are described in the Experimental Section. According to the fitted capacitance value from the capacitance *versus* frequency curve, the  $\epsilon_r$  can be derived according to the equation ( $C = \epsilon_0 \epsilon_r A/d$ ), where  $\epsilon_0$  is the absolute dielectric permittivity ( $8.85 \times 10^{-12} \text{ F/m}$ )

of vacuum,  $A$  is the contact area, and  $d$  is the thickness of the organic film, as shown in **Figure S5a**. To validate the modified method for dielectric constant measurements, poly (3-hexylthiophene-2,5-diyl) (P3HT) and fullerene derivative ( $\text{PC}_{61}\text{BM}$ ) with the well-known  $\mathcal{E}_r$  were measured with different top electrodes by impedance spectroscopy. As shown in **Figure S6**, the measured  $\mathcal{E}_r$  of P3HT and  $\text{PC}_{61}\text{BM}$  with Al as the top electrode showed the overestimated values with large standard deviation, which is attributed to the frequency-dependent capacitance caused by the space charge polarizations or ionic movements.<sup>39,40</sup> Differently, the measured capacitance values based on EGaIn as the top electrode is weakly dependent on the frequency, and the corresponding averaged  $\mathcal{E}_r$  is 3.36 for P3HT and 3.99 for  $\text{PC}_{61}\text{BM}$  with tiny standard deviations, respectively, which agrees well with the previous works.<sup>41</sup> It means that our modified method is reliable and can be used to measure the dielectric property of the non-fullerene acceptor materials in the frequency range of 100 Hz to several MHz.

The  $\mathcal{E}_r$  of pristine non-fullerene acceptors films (ITIC, IT-4F, Y6, and IEICO), pristine PM6 film, and corresponding blend films with post-treatments (such as solvent additive engineering and thermal annealing) was measured (**Figure 2**). The measured  $\mathcal{E}_r$  values were 4.30, 5.83, and 5.73 for ITIC, IT-4F, and Y6, respectively. Interestingly, compared with the fullerene derivative ( $\text{PC}_{61}\text{BM}$ :  $\mathcal{E}_r = 3.9$ ), most of the selected non-fullerene acceptors exhibited higher dielectric properties except for the IEICO acceptor ( $\mathcal{E}_r = 3.81$ ). If the chemical structure difference between fullerene derivatives and non-fullerene acceptors is considered, there are the polar units in the terminal group of non-fullerene acceptors, such as cyano and fluoro units. These polar units with a large dipole moment would further strengthen the intramolecular dipole, which can enhance  $\mathcal{E}_r$ .<sup>38,42</sup> In addition, the dielectric constants of fluorinated non-fullerene acceptors, *i.e.*, IT-4F and Y6, were higher than those of non-fullerene acceptors without fluorine atoms (ITIC and IEICO), which are ascribed to their stronger intermolecular dipole. In addition, as shown in **Figure S7** and **Table S1**, the ITIC, IT-4F, and Y6 without post-treatments showed the lower dielectric constants. It suggests that the post-treatments likely further strengthen intermolecular interactions, such as  $\pi$ - $\pi$  stacking, and change the molecular arrangement in pristine organic films. These factors may be beneficial for the improvement of the dielectric property of non-fullerene acceptors, further reducing the exciton binding energy in non-fullerene acceptors.<sup>43</sup> In a word, the dielectric property of pristine organic films is dependent on the presence of polar molecular units, the intermolecular interaction, and the molecular arrangement.

Furthermore, the increased blend dielectric constant is confirmed to decrease exciton binding energy for efficient exciton dissociation in the fullerene-based devices.<sup>27,44,45</sup> Moreover, a higher dielectric constant of fullerene derivatives-based blend film effectively reduces the bimolecular recombination and voltage loss.<sup>26,46</sup> Hence, the dielectric properties of non-fullerene based blend films in the frequency range of 100 Hz to  $\sim$  MHz should be investigated, and the results are shown in **Figure 2**. All the dielectric constants of

blend films were higher than that of PM6 donor but lower than that of corresponding non-fullerene acceptors. The dielectric constants of blend composition PM6:ITIC, PM6:IT-4F, and PM6:Y6 were 3.71, 3.99, and 3.94, respectively, which are positively associated with the dielectric constants of corresponding non-fullerene acceptors and suggest the lower bimolecular recombination in the above blend films. However, in the case of IEICO based device with poor device performance, PM6:IEICO based blend film coincided with exhibiting the lowest dielectric constants of 3.41. The lower blend dielectric constants indicate that a larger driving force is required for effective exciton dissociation. Unfortunately, the PM6:IEICO pair showed the lowest ionization potential offset (-130 meV), which indicates its smaller driving force. As a result, exciton dissociation is likely impeded in association with a high possibility of bimolecular recombination. On the contrary, although the PM6:F8IC based device (**Figure S8**) exhibited negative ionization potential offset (-40 meV), higher dielectric constants of pristine F8IC ( $\mathcal{E}_r = 4.78$ ) film and PM6:F8IC ( $\mathcal{E}_r = 3.68$ ) blend film likely assure their charge transfer process. Namely, the higher dielectric constant of non-fullerene acceptors and related blend films correlate with improved device performance through the lower bimolecular recombination; this correlation seems to hold independent of the energy offsets between HOMO levels. In addition, a high dielectric constant value is correlated with the strong interface dipole in association with the enhanced exciton delocalization in blend film.<sup>45</sup> These results would promise efficient exciton dissociation.

#### 5.3.4 Scanning Near-field Optical Microscopy of the Films

To further investigate the dielectric property of aforementioned non-fullerene based blend films in the gigahertz (GHz) range that mainly influences the exciton binding energy,<sup>47</sup> in a sub-micrometer scale, the scattering-type scanning near-field optical microscopy (s-SNOM) at the optical-frequency ( $10^{14}$  Hz) was used to investigate the dielectric property of blend films through the complex analytical expressions between the optical scattering amplitude and the dielectric constant in **Supporting Text 2**. And the optical scattering amplitude contrast is correlated with the difference of the dielectric constants of components in organic semiconductor films.<sup>48,49</sup> The four optimized blend films with high device performance were selected to characterize the optical amplitude images shown in **Figure 3d-g** and the corresponding phase images in **Figure S9**. In order to distinguish the components associated with “dark brown” and “bright” domains shown in optical amplitude images, a bilayer film consisting of PM6 component (top left) and Y6 one (bottom right) was fabricated, and the detailed fabrication is shown in Experimental Section. The corresponding topography, phase, and optical amplitude images are presented in **Figure 3a-c**. It was found that in the phase image, PM6 film displayed a higher stiffness than Y6 film because of the stronger  $\pi$ - $\pi$  interaction in the former. In the optical amplitude image, PM6 film appeared as a dark brown region while Y6 a brighter region. It means that the PM6 polymer exhibits a lower dielectric property at the optical

frequency ( $10^{14}$  Hz) than Y6, which is consistent with the fact that the dielectric constants of non-fullerene acceptors are higher than that of PM6 polymer in the 100 Hz to  $\sim$  MHz range. Therefore, the brighter region with stronger scattering light intensity should be assigned to non-fullerene acceptors (ITIC, IT-4F, Y6, and IEICO) while the dark region in optical amplitude images corresponds to PM6.<sup>50,51</sup> Among the optimized blend films, IEICO based blend film with the lowest device performance showed the lowest optical amplitude contrast ( $\sim 1 \mu\text{V}$ ) similar to its lowest dielectric constants difference ( $\Delta\epsilon = 0.45$ ) in the 100 Hz to  $\sim$  MHz range (**Figure 2d**). In contrast, the optical amplitude contrast ( $\sim 2.5 \mu\text{V}$ ) of ITIC based blend film was enhanced. Further, IT-4F and Y6 based blend films exhibited even higher optical amplitude contrasts ( $\sim 4.0 \mu\text{V}$ ). It was found that the variation tendency of optical amplitude contrast at the optical-frequency ( $10^{14}$  Hz) was consistent with changing of the dielectric constant differences ( $\Delta\epsilon = 0.94$  for ITIC based blend film,  $\Delta\epsilon = 2.47$  for IT-4F based blend film, and  $\Delta\epsilon = 2.37$  for Y6 based blend film) in the 100 Hz to  $\sim$  MHz range (**Figure 2a-c**). The results reveal that the non-fullerene acceptors (ITIC, IT-4F, and Y6) have the higher dielectric constants at the optical frequency ( $10^{14}$  Hz), which lead to the large optical amplitude contrast between the donor (PM6) and related acceptors in a sub-micrometer scale. Namely, in a sub-micrometer scale, most non-fullerene acceptors (ITIC, IT-4F, and Y6) of corresponding blend films in the  $\sim$  GHz range also exhibit higher dielectric constants as similar as those of related non-fullerene acceptors in the frequency range of 100 Hz to several MHz. As a result, a lower exciton binding energy and a higher D-A interface dipole would be expected, which lead to more efficient exciton dissociation.<sup>30, 45, 52</sup>

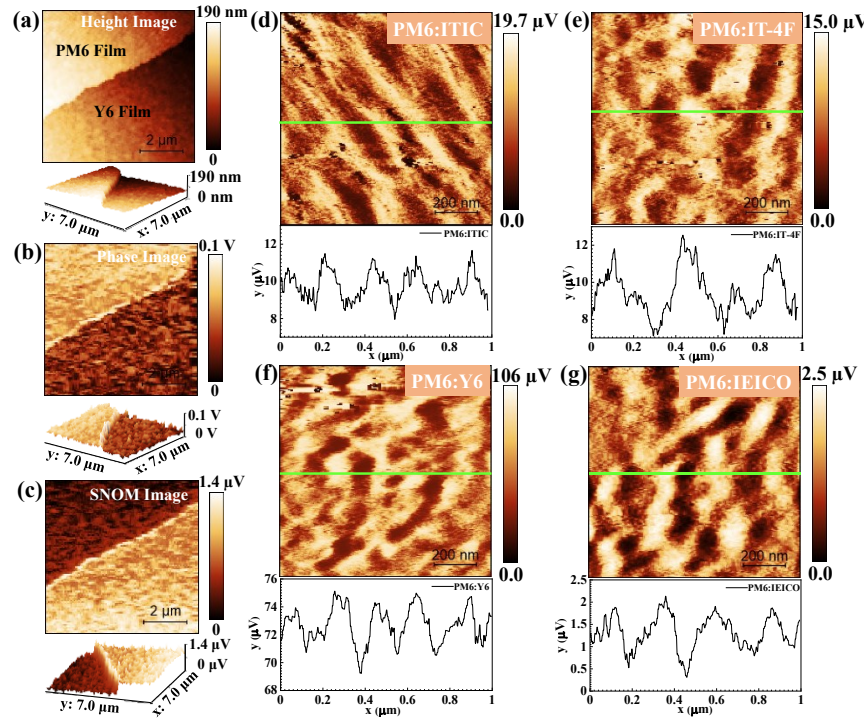


**Figure 3.** (a) Topography, (b) Phase, and (c) optical amplitude image of PM6/Y6 side-by-side arranged film by a floating lamination method. PM6 and Y6 were located top left side and bottom right one, respectively. The topography image and related phase one were collected with AFM. The below 3D images were corresponded with the up ones. Optical amplitude images and corresponded extracted surface profiles of (d) PM6 and ITIC blend film with post-treatment, (e) PM6 and IT-4F blend film with post-treatment, (f) PM6 and Y6 blend film with post-treatment, (g) PM6 and IEICO blend film with post-treatment. The optical amplitude images were derived from s-SNOM.

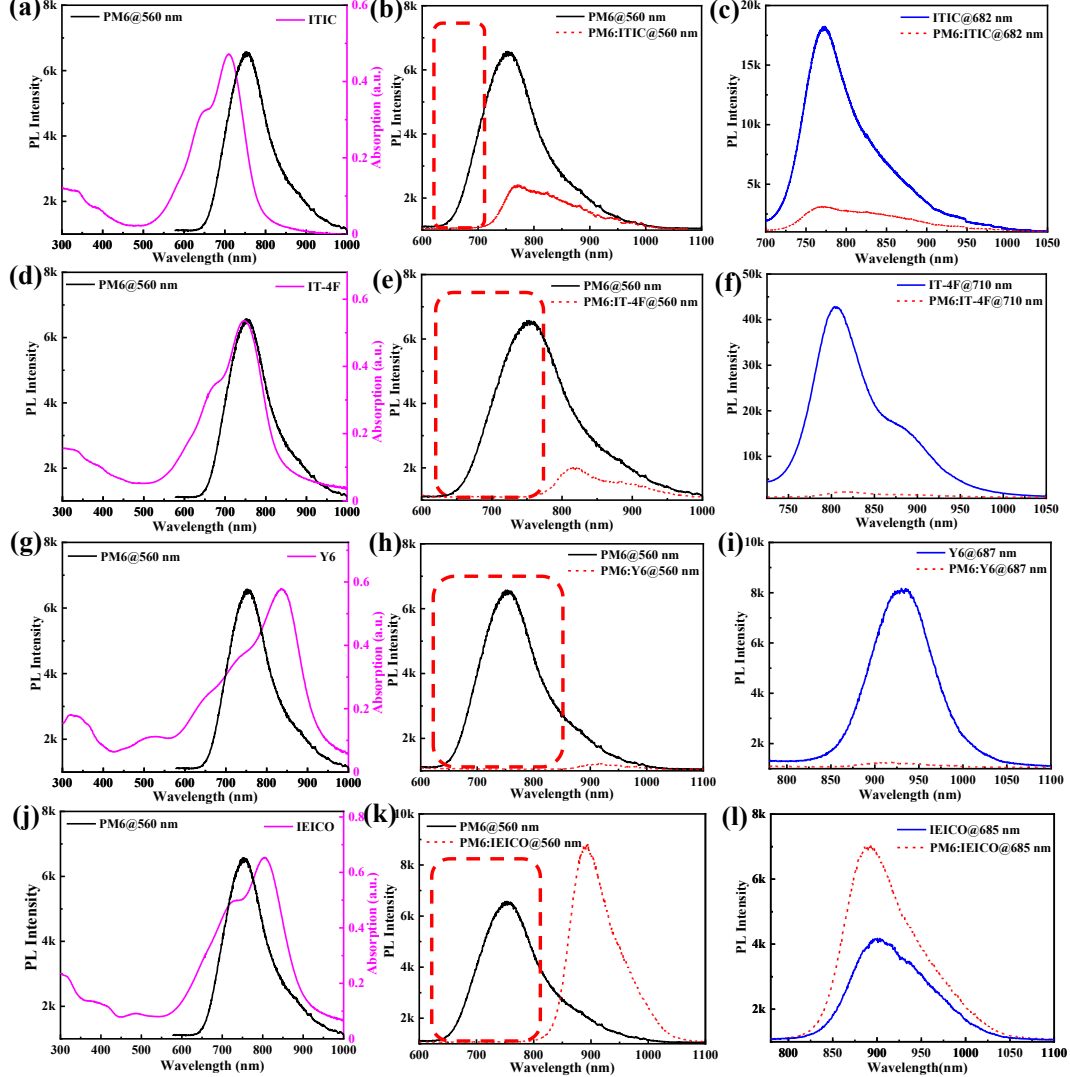


**Figure 4.** Absorption spectra and the emission spectra of pristine PM6 donor, pristine acceptors, and related blend films in different combinations: (a)-(c) PM6:ITIC, (d)-(f) PM6:IT-4F, (g)-(i) PM6:Y6, and (j)-(l) PM6:IEICO (Pumped at 560 nm for PM6 and corresponded blend films, 682 nm for ITIC and corresponded blend film, 710 nm for IT-4F and corresponded film, 687 nm for Y6 and corresponded film, 685 nm for IEICO and corresponded film).

### 5.3.5 Energy Transfer Between Donor and Acceptor

Besides the dielectric constant of non-fullerene acceptors, energy transfer is likely the other key factor affecting exciton dissociation. Energy transfer from polymer donor to non-fullerene acceptor would occur

in the bulk heterojunction non-fullerene-based devices due to their bandgap difference.<sup>53</sup> Optical absorption and photoluminescence (PL) properties of the pristine PM6 film, pristine non-fullerene acceptor films (ITIC, IT-4F, Y6, and IEICO), and corresponding blend films are shown in **Figure 4**. The emission band of PM6 ranged from 650 to 1000 nm, partially overlapping with the absorption spectra of the selected ITIC acceptor. Differently, it nearly completely overlapped with the absorption spectra of IT-4F, Y6, and IEICO acceptors. As shown in PL of PM6 and corresponding blend films at the PM6 excitation wavelength of 560 nm, the PL of PM6 was quenched after blending with the non-fullerene acceptors, and the quenched wavelength range was consistent with the overlapped range between the emission spectra of PM6 and the absorption spectra of selected non-fullerene acceptors. It is to say that the PL intensity of PM6 in ITIC based blend film was partly quenched while the PL intensity of PM6 was completely quenched upon blended with IT-4F, Y6, and IEICO. In addition, the PL spectra of blend films at PM6's excitation wavelength exhibited different peak positions from those of PM6 films. Still, they were the same as those of the blend films at acceptors' excitation wavelength. After comparing the PL peak of non-fullerene acceptors and corresponding blend films at acceptors' excitation wavelength, the PL peak positions of blend films were similar to those of the corresponding pristine acceptor films. The PL peaks of blend films are mainly attributed to blend films' acceptors, even at the different excitation wavelengths. These reveal that resonant energy transfer from the donor to the non-fullerene acceptor may occur in the bulk non-fullerene-based blend films.<sup>54</sup> Especially in the IEICO based blend film, although the PM6's PL intensity in blend film was quenched entirely, the PL intensity of blend film was enhanced, and the peak position was the same as that of the IEICO acceptor. It confirmed resonance energy transfer from donor to the acceptor in non-fullerene-based devices, which would occur in a relatively long-range away from the D-A interface and can be strengthened by designing a strongly coupled donor-acceptor system.<sup>55,56</sup>

In the bilayer heterojunction PM6/IT-4F films, it has been reported that the devices exhibited a negligible mixed region at D-A interfaces. Still, the energy transfer between donor and acceptor is a dominant factor to contribute to the final current.<sup>53</sup> To eliminate the interference factor of charge transfer in bulk heterojunction non-fullerene-based device and further verify the resonance energy transfer between PM6 and non-fullerene acceptors, the bilayer heterojunction films composed of the PM6 film with different thickness and the selected non-fullerene acceptor (IT-4F) film were built by the same procedure.<sup>53</sup> PL spectra of bilayer heterojunction films (PM6/IT-4F) with the PM6 layer thickness varying from 0 to 73 nm are plotted in **Figure S10**. In the PM6/IT-4F bilayer films, the thinner PM6 layers (40 nm, 46 nm, and 52 nm) displayed the completely quenched emission. After the thickness of the PM6 layer beyond 52 nm (such as 65 and 73 nm), the PM6 emission was partially reestablished. Namely, the excitons from the PM6 layer in the range of ~ 50 nm thickness (beyond the general distance of exciton diffusion in organic photovoltaic) was transferred to the IT-4F layer by the resonance energy transfer. Hence, PL measurement of the bilayer

heterojunction films further confirmed that the resonance energy transfer between PM6 and non-fullerene acceptors existed in both bulk heterojunction film and bilayer heterojunction film, which is also consistent with the newest research that showed the important effect of the resonance energy transfer in the bilayer structure on device performance.<sup>57</sup> It could lead to the efficient exciton diffusion between donor and acceptor, consistent with increased exciton delocalization caused by the higher dielectric constant of non-fullerene-based blend films. Additionally, the resonance energy transfer may suppress the exciton recombination loss from PM6 domains in non-fullerene-based blend films because of the quenching of PM6 after combination with non-fullerene acceptors, which finally increased exciton harvesting. In a word, the efficient exciton diffusion caused by resonance energy transfer is beneficial to improve the non-fullerene based device performance.<sup>19-21,23</sup>

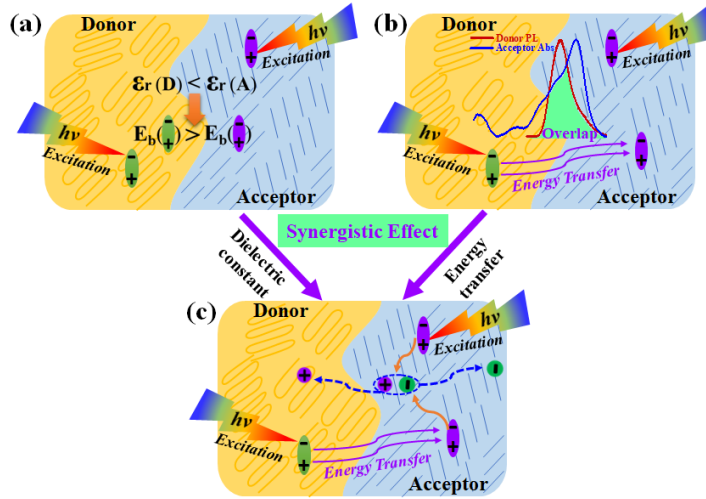


**Figure 5.** The diagram of charge separation and transport process of the non-fullerene based photovoltaic devices: (a) creation of excitons, (b) energy transfer between donor and non-fullerene acceptor, (c) the exciton dissociation and the transport of charge carriers.

### 5.3.6 Mechanism of Exciton Dissociation and Charge Transfer

Once the combined effects of those mentioned above dielectric constant and the resonance energy transfer are considered in the selected non-fullerene-based photovoltaic devices, a likely pathway to charge generation is proposed (**Figure 5**). The heterojunction photoactive layer (containing both the donor and acceptor) generates excitons following photons harvesting. Because of the higher dielectric constant of non-fullerene acceptor than that of PM6 donor, exciton in non-fullerene acceptor has the lower binding energy than that in PM6 donor. Besides, based on the efficient exciton diffusion caused by the favorable resonance energy transfer in a non-fullerene-based device, exciton in the PM6 donor molecules would efficiently diffuse to the adjacent non-fullerene acceptor through D-A interface. That is, the synergistic effect of higher dielectric property of non-fullerene acceptor and energy transfer from donor to non-fullerene acceptor

results in more excitons with low binding energy in the non-fullerene acceptor. The process partly fits well with the two-step exciton dissociation mechanism confirmed in previous fullerene derivative-based photovoltaic devices.<sup>58,59</sup> In such a two-step process, the energy transfer of exciton in the donor occurs from the donor to the acceptor. It then diffuses back to the D-A interface for dissociation through hole transfer to the donor. Differently, in consideration of the ultrafast formation of an intra-moiety intermediate state in non-fullerene acceptor<sup>15</sup> and the lower binding energy of non-fullerene acceptor, it is inferred that the transferred excitons do not require to diffuse back to D-A interface but directly dissociate in the non-fullerene acceptor, and then the free holes can transfer back from non-fullerene acceptor to the donor by simple charge hopping process, which has been confirmed in previous works.<sup>15</sup> It is concluded that the higher dielectric constant of non-fullerene acceptor and the efficient exciton diffusion caused by resonance energy transfer between donor and non-fullerene acceptor are indispensable in the high-performance non-fullerene-based device even with a smaller driving force. However, very differently from direct charge separation in the fullerene-based device, the above processes also raise the new questions or disputation: the traditional charge transfer and energy transfer, as the competing processes, which is the dominant process in non-fullerene based device? To answer the question, firstly, the ratio influenced by the distance between D and A molecules, their relative orientation, and the local dielectric environment should be measured in detail.<sup>60,61</sup> In addition, although it is confirmed that energy transfer from D to A occurs twice faster than charge transfer in conjugated oligomer-fullerene dyads,<sup>62</sup> the rates of charge/energy transfer should be urgently measured if we can answer which one is faster in non-fullerene based device.

#### 5.4 Conclusion

In summary, a combination effect model of dielectric constant of non-fullerene acceptor and resonant energy transfer is developed to interpret the high-efficiency of non-fullerene-based OPV with small voltage loss. Dielectric property variation in different non-fullerene-based photovoltaic devices consisting of PM6 as the typical donor, and ITIC, IT-4F, Y6, and IEICO as non-fullerene acceptors are accurately measured by a novel developed method. It was found that most of the non-fullerene acceptors displayed higher dielectric constants than fullerene derivatives (PC<sub>61</sub>BM and PC<sub>71</sub>BM) in the frequency range of 100 Hz to several MHz. Moreover, most of the blend films also exhibited higher dielectric constants (vs. fullerene derivatives), resulting in reduced bimolecular recombination, and increased charge dissociation possibility with low geminate losses. The s-SNOM measurements also confirmed the large dielectric constant difference in the non-fullerene acceptor-based blend films and the larger dielectric constant of non-fullerene acceptors in the GHz range, leading to the lower exciton binding energy. Additionally, the overlap between the emission spectra of the PM6 donor and the absorption spectra of the correlated non-fullerene acceptors in photovoltaic films suggested that the energy transfer from the donor to the acceptors may occur in non-

fullerene based photovoltaic devices, which enhanced the efficient exciton diffusion for preferable device performance. Therefore, these results well interpret the high device performance with a tiny driving force. Based on the synergistic effect of higher dielectric property and energy transfer on the charge transfer/separation process of selected non-fullerene based photovoltaic devices, the intrinsic physical working mechanism on non-fullerene organic solar cells is proposed. The extent of contribution of the energy transfer to the enhanced photovoltaic performance should be further explored in the future.

## 5.5 References

1. Kaltenbrunner, M.; White, M. S.; Głowacki, E. D.; Sekitani, T.; Someya, T.; Sariciftci, N. S.; Bauer, S., Ultrathin and lightweight organic solar cells with high flexibility. *Nat. Commun.* **2012**, *3*, 770.
2. Gu, X.; Zhou, Y.; Gu, K.; Kurosawa, T.; Guo, Y.; Li, Y.; Lin, H.; Schroeder, B. C.; Yan, H.; Molina-Lopez, F.; Tassone, C. J.; Wang, C.; Mannsfeld, S. C. B.; Yan, H.; Zhao, D.; Toney, M. F.; Bao, Z., Roll-to-Roll Printed Large-Area All-Polymer Solar Cells with 5% Efficiency Based on a Low Crystallinity Conjugated Polymer Blend. *Adv. Energy Mater.* **2017**, *7*, 1602742.
3. Brabec, C. J.; Sariciftci, N. S.; Hummelen, J. C., Plastic Solar Cells. *Adv. Funct. Mater.* **2001**, *11*, 15-26.
4. Q. Liu, Y. Jiang, K. Jin, J. Qin, J. Xu, W. Li, J. Xiong, J. Liu, Z. Xiao, K. Sun, S. Yang, X. Zhang, L. Ding, *Sci. Bull.* **2020**, *65*, 272-275.
5. Liu, J.; Chen, S.; Qian, D.; Gautam, B.; Yang, G.; Zhao, J.; Bergqvist, J.; Zhang, F.; Ma, W.; Ade, H.; Inganäs, O.; Gundogdu, K.; Gao, F.; Yan, H., Fast charge separation in a non-fullerene organic solar cell with a small driving force. *Nat. Energ.* **2016**, *1*, 16089.
6. Yao, J.; Kirchartz, T.; Vezie, M. S.; Faist, M. A.; Gong, W.; He, Z.; Wu, H.; Troughton, J.; Watson, T.; Bryant, D.; Nelson, J., Quantifying Losses in Open-Circuit Voltage in Solution-Processable Solar Cells. *Phys. Rev. Applied* **2015**, *4*, 014020.
7. Wang, Y.; Fan, Q.; Guo, X.; Li, W.; Guo, B.; Su, W.; Ou, X.; Zhang, M., High-performance nonfullerene polymer solar cells based on a fluorinated wide bandgap copolymer with a high open-circuit voltage of 1.04 V. *J. Mater. Chem. A* **2017**, *5*, 22180-22185.
8. Fan, Q.; Zhu, Q.; Xu, Z.; Su, W.; Chen, J.; Wu, J.; Guo, X.; Ma, W.; Zhang, M.; Li, Y., Chlorine substituted 2D-conjugated polymer for high-performance polymer solar cells with 13.1% efficiency via toluene processing. *Nano Energy* **2018**, *48*, 413-420.
9. Zhang, J.; Tan, H. S.; Guo, X.; Facchetti, A.; Yan, H., Material insights and challenges for non-fullerene organic solar cells based on small molecular acceptors. *Nat. Energ.* **2018**, *3*, 720-731.
10. Yao, H.; Qian, D.; Zhang, H.; Qin, Y.; Xu, B.; Cui, Y.; Yu, R.; Gao, F.; Hou, J., Critical Role of Molecular Electrostatic Potential on Charge Generation in Organic Solar Cells. *Chin. J. Chem.* **2018**, *36*, 491-494.

11. Yao, H.; Cui, Y.; Qian, D.; Pонсеа, С. С., Jr.; Honarfar, A.; Xu, Y.; Xin, J.; Chen, Z.; Hong, L.; Gao, B.; Yu, R.; Zu, Y.; Ma, W.; Chabera, P.; Pullerits, T.; Yartsev, A.; Gao, F.; Hou, J., 14.7% Efficiency Organic Photovoltaic Cells Enabled by Active Materials with a Large Electrostatic Potential Difference. *J. Am. Chem. Soc.* **2019**, *141*, 7743-7750.
12. Sun, C.; Qin, S.; Wang, R.; Chen, S.; Pan, F.; Qiu, B.; Shang, Z.; Meng, L.; Zhang, C.; Xiao, M.; Yang, C.; Li, Y., High Efficiency Polymer Solar Cells with Efficient Hole Transfer at Zero Highest Occupied Molecular Orbital Offset between Methylated Polymer Donor and Brominated Acceptor. *J. Am. Chem. Soc.* **2020**, *142*, 1465-1474.
13. Zhang, G.; Chen, X. K.; Xiao, J.; Chow, P. C. Y.; Ren, M.; Kupgan, G.; Jiao, X.; Chan, C. C. S.; Du, X.; Xia, R.; Chen, Z.; Yuan, J.; Zhang, Y.; Zhang, S.; Liu, Y.; Zou, Y.; Yan, H.; Wong, K. S.; Coropceanu, V.; Li, N.; Brabec, C. J.; Bredas, J. L.; Yip, H. L.; Cao, Y., Delocalization of exciton and electron wavefunction in non-fullerene acceptor molecules enables efficient organic solar cells. *Nat. Commun.* **2020**, *11*, 3943.
14. Hinrichsen, T. F.; Chan, C. C. S.; Ma, C.; Palecek, D.; Gillett, A.; Chen, S.; Zou, X.; Zhang, G.; Yip, H. L.; Wong, K. S.; Friend, R. H.; Yan, H.; Rao, A.; Chow, P. C. Y., Long-lived and disorder-free charge transfer states enable endothermic charge separation in efficient non-fullerene organic solar cells. *Nat. Commun.* **2020**, *11*, 5617.
15. Wang, R.; Zhang, C.; Li, Q.; Zhang, Z.; Wang, X.; Xiao, M., Charge Separation from an Intra-Moiety Intermediate State in the High-Performance PM6:Y6 Organic Photovoltaic Blend. *J. Am. Chem. Soc.* **2020**, *142*, 12751-12759.
16. Liu, Y.; Zhang, J.; Zhou, G.; Liu, F.; Zhu, X.; Zhang, F., Electric Field Facilitating Hole Transfer in Non-Fullerene Organic Solar Cells with a Negative HOMO Offset. *J. Phys. Chem. C* **2020**, *124*, 15132-15139.
17. Cha, H.; Zheng, Y.; Dong, Y.; Lee, H. H.; Wu, J.; Bristow, H.; Zhang, J.; Lee, H. K. H.; Tsoi, W. C.; Bakulin, A. A.; McCulloch, I.; Durrant, J. R., Exciton and Charge Carrier Dynamics in Highly Crystalline PTQ10:IDIC Organic Solar Cells. *Adv. Energy Mater.* **2020**, *10*, 2001149.
18. Li, S.; Zhan, L.; Sun, C.; Zhu, H.; Zhou, G.; Yang, W.; Shi, M.; Li, C. Z.; Hou, J.; Li, Y.; Chen, H., Highly Efficient Fullerene-Free Organic Solar Cells Operate at Near Zero Highest Occupied Molecular Orbital Offsets. *J. Am. Chem. Soc.* **2019**, *141*, 3073-3082.
19. Burkhard, G. F.; Hoke, E. T.; Scully, S. R.; McGehee, M. D., Incomplete Exciton Harvesting from Fullerenes in Bulk Heterojunction Solar Cells. *Nano Lett.* **2009**, *9*, 4037-4041.
20. Najafov, H.; Lee, B.; Zhou, Q.; Feldman, L. C.; Podzorov, V., Observation of long-range exciton diffusion in highly ordered organic semiconductors. *Nat. Mater.* **2010**, *9*, 938-943.

21. Menke, S. M.; Luhman, W. A.; Holmes, R. J., Tailored exciton diffusion in organic photovoltaic cells for enhanced power conversion efficiency. *Nat. Mater.* **2013**, *12*, 152-157.
22. Chandrabose, S.; Chen, K.; Barker, A. J.; Sutton, J. J.; Prasad, S. K. K.; Zhu, J.; Zhou, J.; Gordon, K. C.; Xie, Z.; Zhan, X.; Hodgkiss, J. M., High Exciton Diffusion Coefficients in Fused Ring Electron Acceptor Films. *J. Am. Chem. Soc.* **2019**, *141*, 6922-6929.
23. Sajjad, M. T.; Ruseckas, A.; Jagadamma, L. K.; Zhang, Y.; Samuel, I. D. W., Long-range exciton diffusion in non-fullerene acceptors and coarse bulk heterojunctions enable highly efficient organic photovoltaics. *J. Mater. Chem. A* **2020**, *8*, 15687-15694.
24. Koster, L. J. A.; Shaheen, S. E.; Hummelen, J. C., Pathways to a New Efficiency Regime for Organic Solar Cells. *Adv. Energy Mater.* **2012**, *2*, 1246-1253.
25. Cho, N.; Schlenker, C. W.; Knesting, K. M.; Koelsch, P.; Yip, H.-L.; Ginger, D. S.; Jen, A. K. Y., High-Dielectric Constant Side-Chain Polymers Show Reduced Non-Geminate Recombination in Heterojunction Solar Cells. *Adv. Energy Mater.* **2014**, *4*, 1301857.
26. Chen, S.; Tsang, S. W.; Lai, T. H.; Reynolds, J. R.; So, F., Dielectric effect on the photovoltage loss in organic photovoltaic cells. *Adv. Mater.* **2014**, *26*, 6125-6131.
27. Constantinou, I.; Yi, X.; Shewmon, N. T.; Klump, E. D.; Peng, C.; Garakyanaghi, S.; Lo, C. K.; Reynolds, J. R.; Castellano, F. N.; So, F., Effect of Polymer-Fullerene Interaction on the Dielectric Properties of the Blend. *Adv. Energy Mater.* **2017**, *7*, 1601947.
28. Xu, B.; Yi, X.; Huang, T.-Y.; Zheng, Z.; Zhang, J.; Salehi, A.; Coropceanu, V.; Ho, C. H. Y.; Marder, S. R.; Toney, M. F.; Brédas, J.-L.; So, F.; Reynolds, J. R., Donor Conjugated Polymers with Polar Side Chain Groups: The Role of Dielectric Constant and Energetic Disorder on Photovoltaic Performance. *Adv. Funct. Mater.* **2018**, *28*, 1803418.
29. Hughes, M. P.; Rosenthal, K. D.; Dasari, R. R.; Luginbuhl, B. R.; Yurash, B.; Marder, S. R.; Nguyen, T. Q., Charge Recombination Dynamics in Organic Photovoltaic Systems with Enhanced Dielectric Constant. *Adv. Funct. Mater.* **2019**, *29*, 1901269.
30. Zhang, X.; Zhang, D.; Zhou, Q.; Wang, R.; Zhou, J.; Wang, J.; Zhou, H.; Zhang, Y., Fluorination with an enlarged dielectric constant prompts charge separation and reduces bimolecular recombination in non-fullerene organic solar cells with a high fill factor and efficiency >13%. *Nano Energy* **2019**, *56*, 494-501.
31. Duan, L.; Zhang, Y.; Yi, H.; Haque, F.; Deng, R.; Guan, H.; Zou, Y.; Uddin, A., Trade-Off between Exciton Dissociation and Carrier Recombination and Dielectric Properties in Y6-Sensitized Nonfullerene Ternary Organic Solar Cells. *Energy Technol.* **2019**, 1900924.
32. Torabi, S.; Liu, J.; Gordiichuk, P.; Herrmann, A.; Qiu, L.; Jahani, F.; Hummelen, J. C.; Koster, L. J., Deposition of LiF onto Films of Fullerene Derivatives Leads to Bulk Doping. *ACS Appl. Mater. Interfaces* **2016**, *8*, 22623-22628.

33. Torabi, S.; Cherry, M.; Duijnste, E. A.; Le Corre, V. M.; Qiu, L.; Hummelen, J. C.; Palasantzas, G.; Koster, L. J. A., Rough Electrode Creates Excess Capacitance in Thin-Film Capacitors. *ACS Appl. Mater. Interfaces* **2017**, *9*, 27290-27297.
34. Cardona, C. M.; Li, W.; Kaifer, A. E.; Stockdale, D.; Bazan, G. C., Electrochemical Considerations for Determining Absolute Frontier Orbital Energy Levels of Conjugated Polymers for Solar Cell Applications. *Adv. Mater.* **2011**, *23*, 2367-2371.
35. Qian, D.; Zheng, Z.; Yao, H.; Tress, W.; Hopper, T. R.; Chen, S.; Li, S.; Liu, J.; Chen, S.; Zhang, J.; Liu, X. K.; Gao, B.; Ouyang, L.; Jin, Y.; Pozina, G.; Buyanova, I. A.; Chen, W. M.; Inganas, O.; Coropceanu, V.; Bredas, J. L.; Yan, H.; Hou, J.; Zhang, F.; Bakulin, A. A.; Gao, F., Design rules for minimizing voltage losses in high-efficiency organic solar cells. *Nat. Mater.* **2018**, *17*, 703-709.
36. Douvogianni, E.; Qiu, X.; Qiu, L.; Jahani, F.; Kooistra, F. B.; Hummelen, J. C.; Chiechi, R. C., Soft Nondamaging Contacts Formed from Eutectic Ga-In for the Accurate Determination of Dielectric Constants of Organic Materials. *Chem. Mater.* **2018**, *30*, 5527-5533.
37. Xie, S.; Xia, Y.; Zheng, Z.; Zhang, X.; Yuan, J.; Zhou, H.; Zhang, Y., Effects of Nonradiative Losses at Charge Transfer States and Energetic Disorder on the Open-Circuit Voltage in Nonfullerene Organic Solar Cells. *Adv. Funct. Mater.* **2018**, *28*, 1705659.
38. Torabi, S.; Jahani, F.; Van Severen, I.; Kanimozhi, C.; Patil, S.; Havenith, R. W. A.; Chiechi, R. C.; Lutsen, L.; Vanderzande, D. J. M.; Cleij, T. J.; Hummelen, J. C.; Koster, L. J. A., Strategy for Enhancing the Dielectric Constant of Organic Semiconductors Without Sacrificing Charge Carrier Mobility and Solubility. *Adv. Funct. Mater.* **2015**, *25*, 150-157.
39. Shrotriya, V.; Yang, Y., Capacitance-voltage characterization of polymer light-emitting diodes. *J. Appl. Phys.* **2005**, *97*, 054504.
40. Knapp, E.; Ruhstaller, B., The role of shallow traps in dynamic characterization of organic semiconductor devices. *J. Appl. Phys.* **2012**, *112*, 024519.
41. Juška, G.; Genevičius, K.; Österbacka, R.; Arlauskas, K.; Kreouzis, T.; Bradley, D. D. C.; Stubb, H., Initial transport of photogenerated charge carriers in  $\pi$ -conjugated polymers. *Phys. Rev. B* **2003**, *67*, 081201.
42. Liu, X.; Xie, B.; Duan, C.; Wang, Z.; Fan, B.; Zhang, K.; Lin, B.; Colberts, F. J. M.; Ma, W.; Janssen, R. A. J.; Huang, F.; Cao, Y., A high dielectric constant non-fullerene acceptor for efficient bulk-heterojunction organic solar cells. *J. Mater. Chem. A* **2018**, *6*, 395- 403.
43. Zhu, L.; Tu, Z.; Yi, Y.; Wei, Z., Achieving Small Exciton Binding Energies in Small Molecule Acceptors for Organic Solar Cells: Effect of Molecular Packing. *J. Phys. Chem. Lett.* **2019**, *10*, 4888-4894.
44. Lenes, M.; Kooistra, F. B.; Hummelen, J. C.; Van Severen, I.; Lutsen, L.; Vanderzande, D.; Cleij, T. J.; Blom, P. W. M., Charge dissociation in polymer:fullerene bulk heterojunction solar cells with enhanced permittivity. *J. Appl. Phys.* **2008**, *104*, 114517.

45. Leblebici, S. Y.; Chen, T. L.; Olalde-Velasco, P.; Yang, W.; Ma, B., Reducing exciton binding energy by increasing thin film permittivity: an effective approach to enhance exciton separation efficiency in organic solar cells. *ACS Appl. Mater. Interfaces* **2013**, *5*, 10105-10110.
46. Zhang, X.; Zuo, X.; Xie, S.; Yuan, J.; Zhou, H.; Zhang, Y., Understanding charge transport and recombination losses in high performance polymer solar cells with non-fullerene acceptors. *J. Mater. Chem. A* **2017**, *5*, 17230-17239.
47. Horst, J.-W. v. d.; Bobbert, P. A.; Jong, P. H. L. d.; Michels, M. A. J.; Siebbeles, L. D. A.; Warman, J. M.; Gelinck, G. H.; Brocks, G., Predicting polarizabilities and lifetimes of excitons on conjugated polymer chains. *Chem. Phys. Lett.* **2001**, *334*, 303-308.
48. Zhang, W.; Chen, Y., Visibility of subsurface nanostructures in scattering-type scanning near-field optical microscopy imaging. *Opt. Express* **2020**, *28*, 6696-6707.
49. Stanciu, S. G.; Tranca, D. E.; Pastorino, L.; Boi, S.; Song, Y. M.; Yoo, Y. J.; Ishii, S.; Hristu, R.; Yang, F.; Bussetti, G.; Stanciu, G. A., Characterization of Nanomaterials by Locally Determining Their Complex Permittivity with Scattering-Type Scanning Near-Field Optical Microscopy. *ACS Appl. Nano. Mater.* **2020**, *3*, 1250-1262.
50. An, C.; Zheng, Z.; Hou, J., Recent progress in wide bandgap conjugated polymer donors for high-performance nonfullerene organic photovoltaics. *Chem. Commun.* **2020**, *56*, 4750-4760.
51. Pan, M.-A.; Lau, T.-K.; Tang, Y.; Wu, Y.-C.; Liu, T.; Li, K.; Chen, M.-C.; Lu, X.; Ma, W.; Zhan, C., 16.7%-efficiency ternary blended organic photovoltaic cells with PCBM as the acceptor additive to increase the open-circuit voltage and phase purity. *J. Mater. Chem. A* **2019**, *7*, 20713-20722.
52. Zhong, Y.; Ma, J.; Hashimoto, K.; Tajima, K., Electric field-induced dipole switching at the donor/acceptor interface in organic solar cells. *Adv. Mater.* **2013**, *25*, 1071-1075.
53. Lee, T. H.; Park, S. Y.; Park, W.-W.; Du, X.; Son, J. H.; Li, N.; Kwon, O.-H.; Woo, H. Y.; Brabec, C. J.; Kim, J. Y., Efficient Exciton Diffusion in Organic Bilayer Heterojunctions with Nonfullerene Small Molecular Acceptors. *ACS Energy Lett.* **2020**, *5*, 1628-1635.
54. Chen, L.; Roman, L. S.; Johansson, D. M.; Svensson, M.; Andersson, M. R.; Janssen, R. A. J.; Inganäs, O., Excitation Transfer in Polymer Photodiodes for Enhanced Quantum Efficiency. *Adv. Mater.* **2000**, *12*, 1110-1114.
55. Scully, S. R.; Armstrong, P. B.; Edder, C.; Fréchet, J. M. J.; McGehee, M. D., Long- Range Resonant Energy Transfer for Enhanced Exciton Harvesting for Organic Solar Cells. *Adv. Mater.* **2007**, *19*, 2961-2966.
56. Coffey, D. C.; Ferguson, A. J.; Kopidakis, N.; Rumbles, G., Photovoltaic Charge Generation in Organic Semiconductors Based on LongRange Energy Transfer. *ACS Nano* **2010**, *4*, 5437-5445.

57. Park, S. Y.; Chandrabose, S.; Price, M. B.; Ryu, H. S.; Lee, T. H.; Shin, Y. S.; Wu, Z.; Lee, W.; Chen, K.; Dai, S.; Zhu, J.; Xue, P.; Zhan, X.; Woo, H. Y.; Kim, J. Y.; Hodgkiss, J. M., Photophysical pathways in efficient bilayer organic solar cells: The importance of interlayer energy transfer. *Nano Energy* **2021**, *84*, 105924.
58. Liu, Y.-X.; Summers, M. A.; Scully, S. R.; McGehee, M. D., Resonance energy transfer from organic chromophores to fullerene molecules. *J. Appl. Phys.* **2006**, *99*, 093521.
59. Lloyd, M. T.; Lim, Y.-F.; Malliaras, G. G., Two-step exciton dissociation in poly(3-hexylthiophene)/fullerene heterojunctions. *Appl. Phys. Lett.* **2008**, *92*, 143308.
60. Eckert, J.-F. o.; Nicoud, J.-F. o.; Nierengarten, J.-F. o.; Liu, S.-G.; Echegoyen, L.; Barigelli, F.; Armaroli, N.; Ouali, L.; Krasnikov, V.; Hadzioannou, G., Fullerene-Oligophenylenevinylene Hybrids: Synthesis, Electronic Properties, and Incorporation in Photovoltaic Devices. *J. Am. Chem. Soc.* **2000**, *122*, 7467-7479.
61. Scholes, G. D., Long-Range Resonance Energy Transfer in Molecular Systems. *Annu. Rev. Phys. Chem.* **2003**, *54*, 57-87.
62. van Hal, P. A.; Janssen, R. A. J.; Lanzani, G.; Cerullo, G.; Zavelani-Rossi, M.; De Silvestri, S., Two-step mechanism for the photoinduced intramolecular electron transfer in oligo(p-phenylene vinylene)-fullerene dyads. *Phys. Rev. B* **2001**, *64*, 075206.

## 5.6 Supporting Information

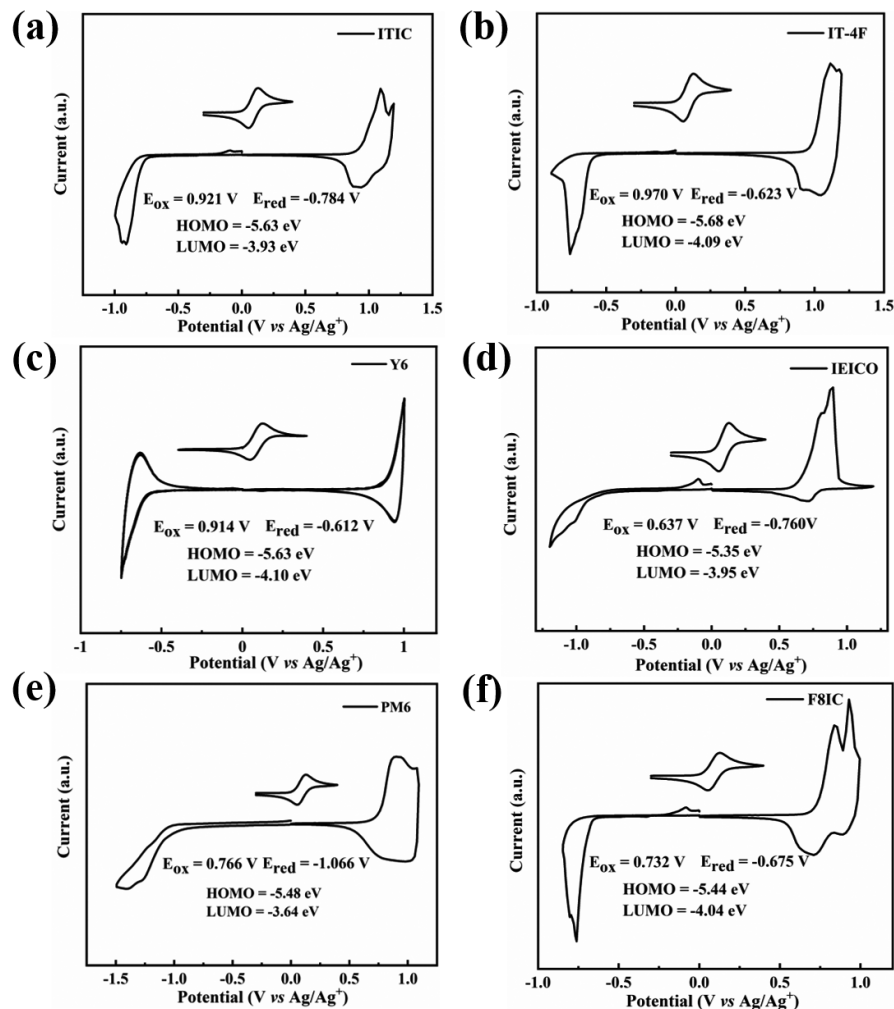


**Figure S1.** Cyclic voltammogram of the corresponded films on a glassy carbon electrode measured in a  $0.1 \text{ mol L}^{-1}$   $\text{Bu}_4\text{NPF}_6$  acetonitrile solution at a scan rate of  $50 \text{ mV s}^{-1}$ , (a) ITIC film, (b) IT-4F film, (c) Y6 film, (d) IEICO film, (e) PM6 film, and (f) F8IC film.

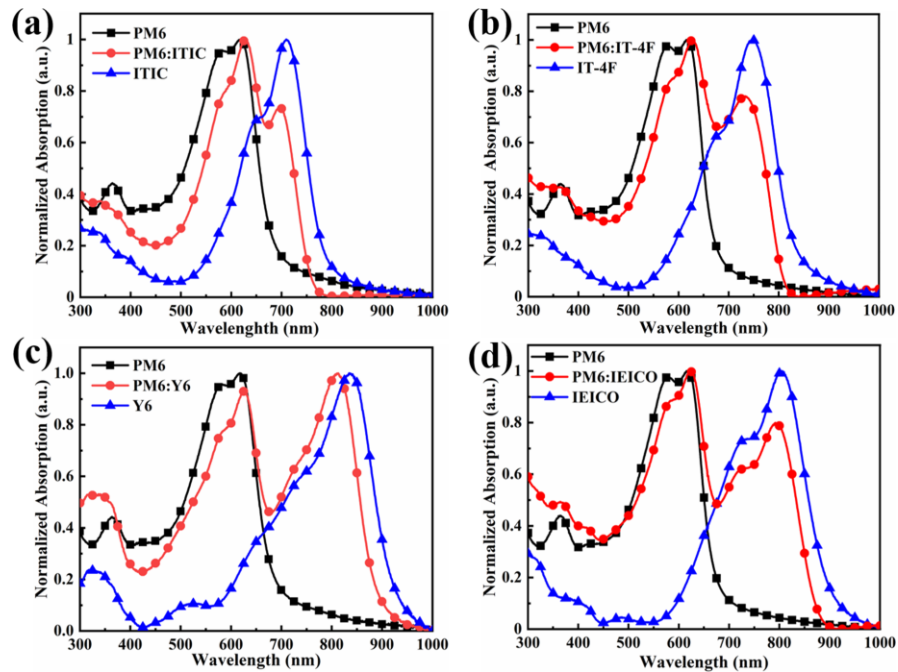


**Figure S2.** Absorption spectra of corresponded blend films on quartz substrates, (a) PM6:ITIC, (b) PM6:IT-4F, (c) PM6:Y6, and (d) PM6:IEICO.

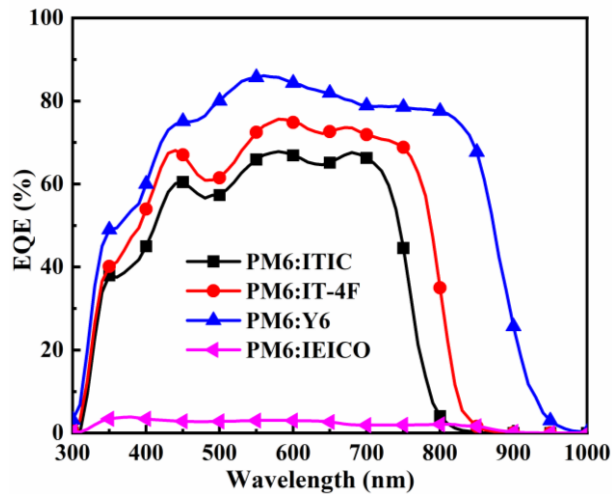


**Figure S3.** EQE spectra of the devices based on PM6 and related acceptor materials (ITIC, IT- 4F, Y6, and IEICO).

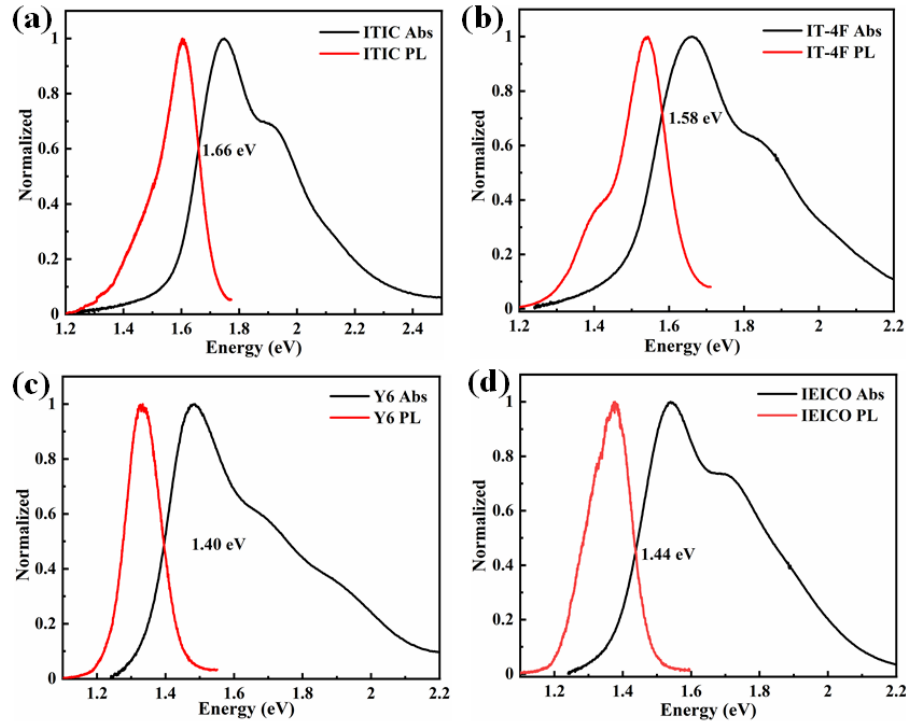


**Figure S4.** Optical gap of non-fullerene acceptors determined by the crossing point between the normalized emission (red) and absorption (black) spectra, (a) ITIC, (b) IT-4F, (c) Y6, and (d) IEICO.

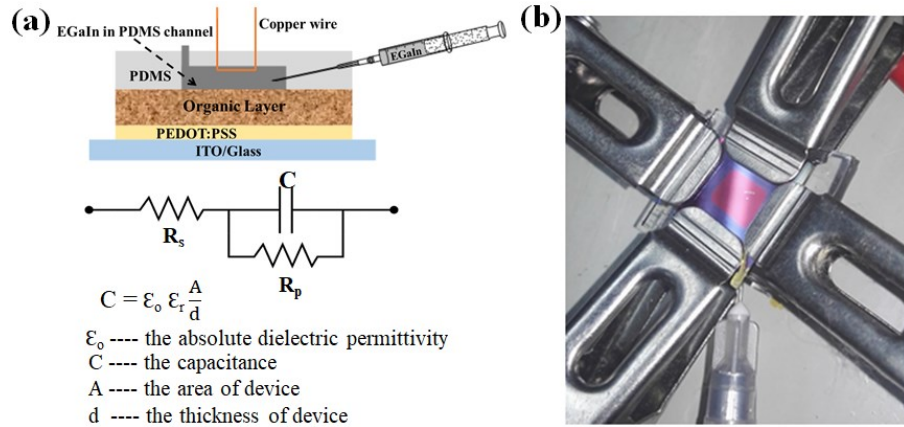


**Figure S5.** (a) Schematic diagram of device architecture with EGaIn as the top electrode. PDMS mask is placed on the top of the film and filled with EGaIn. The equivalent circuit for fitting impedance data and the related equation for relative dielectric constant are at the bottom. (b) Photograph of the capacitor device of related organic materials.

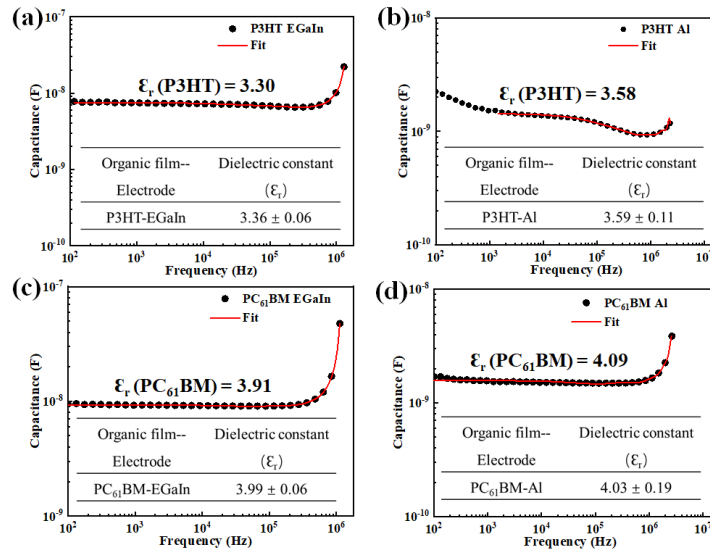


**Figure S6.** Capacitance *versus* frequency plots for (a) Pristine P3HT film with EGaIn electrode, (b) Pristine P3HT film with Al electrode, (c) Pristine PC<sub>61</sub>BM film with EGaIn electrode, (d) Pristine PC<sub>61</sub>BM film with Al electrode. The red lines represent the fit over the measured data by a polynomial function. Inset shows extracted dielectric constants of pristine P3HT and PC<sub>61</sub>BM films.

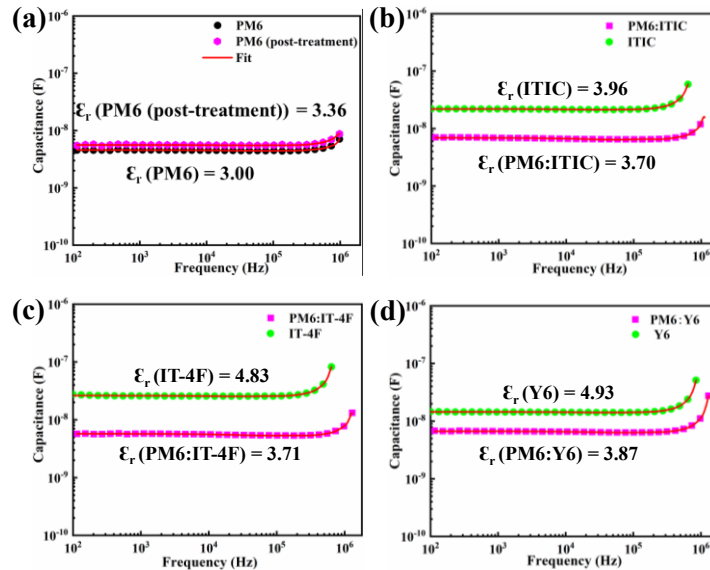


**Figure S7.** Capacitance *versus* frequency plots for (a) Pristine PM6 film without and with post-treatment, (b) Pristine ITIC film and the PM6 and ITIC blend film, (c) Pristine IT-4F film and the PM6 and IT-4F blend film, (d) Pristine Y6 film and the blend PM6 and Y6 film. The red lines represent the fit over the measured data by a polynomial function.

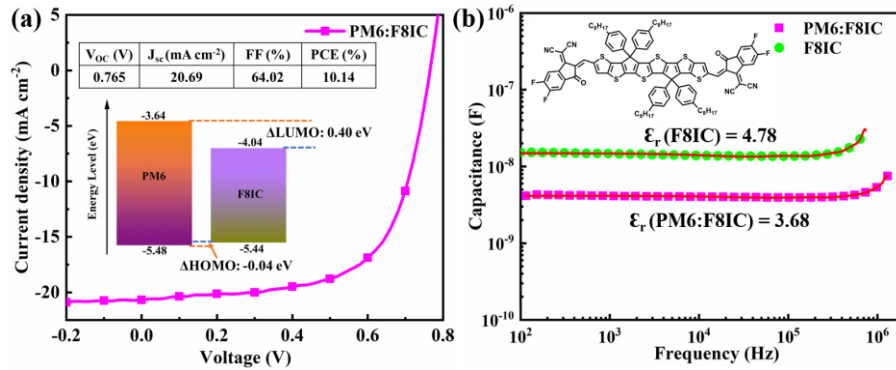


**Figure S8.** (a)  $J$ - $V$  characteristics and corresponded energy level diagram of the device based on donor PM6 and acceptor F8IC. (b) Capacitance *versus* frequency plots for the pristine film of F8IC, and the blend film of PM6 and F8IC. The red lines represent the fit over the measured data by a polynomial function. Inset shows the chemical structure of non-fullerene F8IC molecular.

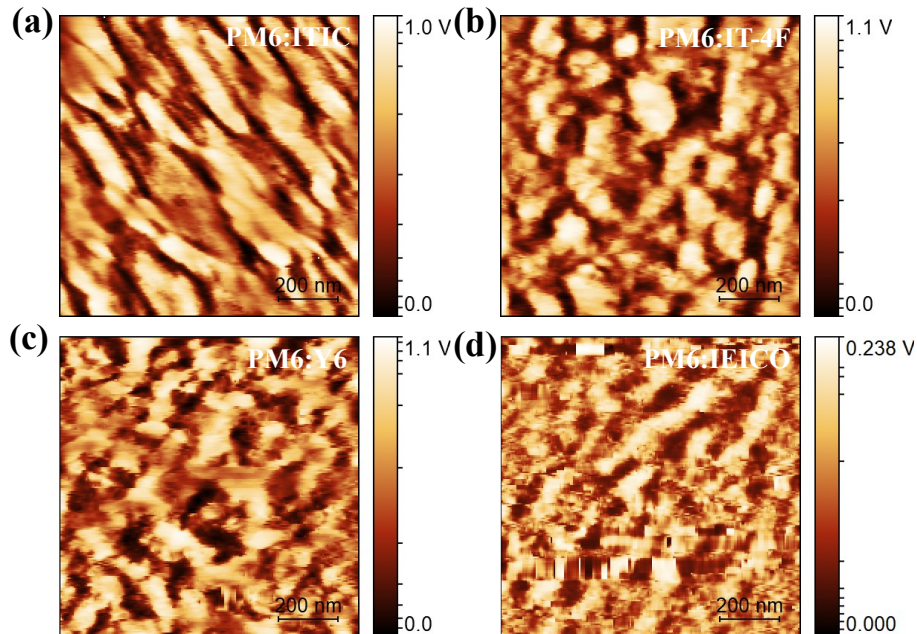


**Figure S9.** The corresponded phase images of blend films based on PM6 and different non-fullerene acceptors (a) PM6 and ITIC blend film, (e) PM6 and IT-4F blend film, (f) PM6 and Y6 blend film, (g) PM6 and IEICO blend film.

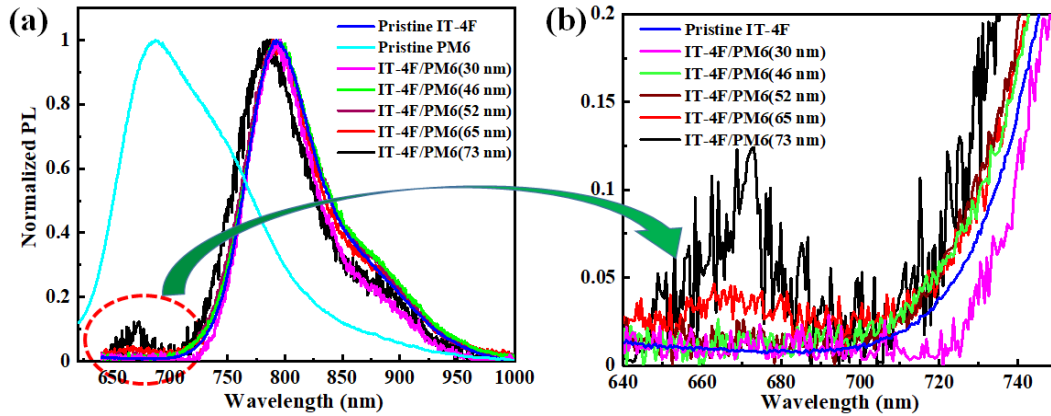


**Figure S10.** Normalized emission spectra variation of pristine PM6 film, pristine non-fullerene acceptor's film, and the corresponded bilayer heterojunction films (a) PM6/IT-4F bilayer films with a different PM6 layer thickness in the wavelength region from 620 to 1000 nm, (b) PM6/IT-4F bilayer films with a different PM6 layer thickness in the wavelength region from 640 to 750 nm. The PL spectra were recorded by PM6 excitation wavelength of 560 nm.

**Table S1.** Extracted dielectric constants of pristine non-fullerene acceptors' films and the corresponded blend films without and with post-treatments.

Photovoltaic films	W/O	After post-treatment
ITIC	$3.96 \pm 0.23^a$	$4.30 \pm 0.15$
IT-4F	$4.83 \pm 0.08$	$5.83 \pm 0.25$
Y6	$4.93 \pm 0.17$	$5.73 \pm 0.15$
IEICO	N/A	$3.81 \pm 0.16$
PM6:ITIC	$3.70 \pm 0.06$	$3.71 \pm 0.03$
PM6:IT-4F	$3.71 \pm 0.07$	$3.99 \pm 0.07$
PM6:Y6	$3.87 \pm 0.11$	$3.94 \pm 0.05$
PM6:IEICO	N/A	$3.41 \pm 0.06$

<sup>a</sup> The variance of the dielectric constant is obtained in three devices.

## Supporting Text 1

### Calculation of Energy Levels and Charge Transfer Rates

DFT calculations were performed on individual molecules to compute frontier orbital energies and reorganization energies as well as on donor-acceptor pairs to approximately estimate the electronic coupling. All calculations were performed in Gaussian.<sup>1</sup> B3LYP functional<sup>2</sup> and Lanl2dz<sup>3</sup> basis sets were used. Spin-polarized calculations were performed for systems with an odd number of electrons. The reorganization energies for hole (electron) ( $h(e)$ ) transfer were evaluated as  $E_{reorg}^{h(e)} = (E_0^{+(-)} - E_0^0) + (E_{+(-)}^0 - E_{+(-)}^{+(-)})$ , where  $E_0^0$  is the energy of the neutral molecule at its equilibrium geometry,  $E_0^{+(-)}$  is the energy of the neutral molecule at the equilibrium geometry of the ion,  $E_{+(-)}^{+(-)}$  is the energy of the ion at its equilibrium geometry, and  $E_{+(-)}^0$  is the energy of the ion at the equilibrium geometry of the neutral molecule. The electronic coupling  $H$  between the donor and the acceptor was estimated from one-half of the HOMO (respectively LUMO) shift in the molecular dimer *vs.* isolated molecules.<sup>4</sup> The PM6 donor was models with a tetramer. On account of a relatively low value of the dielectric constant, the calculations were done in vacuum.

The charge transfer rate ( $k_{CT}$ ) is estimated using the Marcus theory:

$$k_{CT} = \frac{2\pi}{\hbar} H^2 \frac{1}{\sqrt{4\pi\lambda k_B T}} \exp\left(-\frac{(\lambda + \Delta G)^2}{4\lambda k_B T}\right) \quad (1)$$

where the total reorganization energy  $\lambda^{h(e)}$  is the sum of  $E_{reorg}^{h(e)}$  for the donor and the acceptor,  $\Delta G$  is the driving force for charge transfer which is approximated by the difference in HOMO (respectively LUMO) energies between the acceptor and the donor, and  $k_B T$  is the thermal energy (we used room temperature).

The frontier orbital energies, reorganization energies, driving forces, electronic coupling values, and estimated electron and hole transfer rates are given in Table S2. It can be seen from these results that the alignment of LUMO levels between the donor and acceptor is favorable (negative  $\Delta G$ , corresponding to a lower LUMO of the acceptor than that of the donor) with all the non-fullerene acceptors, leading to appreciable electron transfer rates with all molecules; however, IEICO stands out as having an order of magnitude lower computed rate *vs.* the other three acceptor molecules.

The alignment of the HOMO levels relevant for hole transport is, on the contrary, qualitatively different among the acceptor molecules: while the HOMO alignment is favorable with ITIC, IT4F, and F8IC, it is not (HOMO is higher than that of the donor) with IEICO. The  $\Delta G$  is positive, but its magnitude is small,

leading to still an appreciable, albeit the lowest among the four molecules, computed hole transfer rate. These results are consistent with the lowest PCE of the cells using IEICO in the experiments.

**Table S2.** The frontier orbital energy levels, reorganization energies, and hole and electron charge transfer rates between the considered non-fullerene acceptors (ITIC, IT-4F, and IEICO) and PM6.

	HOMO	LUMO	$E_{reorg}^h$	$\Delta G^h$	$H^{2,h}$	$k_{CT}^h$	$E_{reorg}^e$	$\Delta G^e$	$H^{2,e}$	$k_{CT}^e$
	eV	eV	eV	eV	eV <sup>2</sup>	s <sup>-1</sup>	eV	eV	eV <sup>2</sup>	s <sup>-1</sup>
PM6	-5.30	-3.21	0.069				0.076			
IEICO	-5.26	-3.57	0.182	0.041	$6.57 \times 10^{-5}$	$1.58 \times 10^{11}$	0.133	-0.360	$5.76 \times 10^{-5}$	$1.32 \times 10^{11}$
ITIC	-5.72	-3.65	0.167	-0.423	0.0016	$3.59 \times 10^{12}$	0.159	-0.436	0.0018	$4.56 \times 10^{12}$
IT4F	-5.98	-3.96	0.170	-0.675	0.0004	$8.07 \times 10^{11}$	0.151	-0.743	0.0009	$2.17 \times 10^{12}$

## Supporting Text 2

### Relation Between Optical Scattering Amplitude and Dielectric Constant of Organic Films

According to the reference<sup>5,6</sup>, the s-SNOM optical scattering amplitude (S) is directly proportional to the effective polarizability ( $\alpha_{eff}$ ), which is shown in the analytical expression below.

$$S \propto |\alpha_{eff}| \quad (1)$$

The effective polarizability ( $\alpha_{eff}$ ) is introduced to describe the multiple interactions between the probe tip and the mirror dipoles.

$$\alpha_{eff} = \frac{\alpha(1+\beta)}{1-\alpha\beta/[16\pi(R+z)^3]} \quad (2)$$

In the above equation, R is the radius of the approximated metallic sphere of the probe tip, and z is the distance between tip and sample.  $\alpha$  is the probe tip polarizability which is created under the incident near-infrared light field and can be expressed by the equation 3,

$$\alpha = 4\pi R^3 \frac{\varepsilon_t - 1}{\varepsilon_t + 2} \quad (3)$$

in which  $\varepsilon_t$  is the dielectric constant of probe tip that is the knowing value for the probe tip. Therefore, the  $\alpha$  value can be easily calculated. Then the sample is polarized in the z-direction when the probe tip is close

enough to the sample surface. Finally, the mirror dipole is created. (1),  $\beta$  in equation 1 is the surface response function of the sample, which can be expressed by,

$$\beta = 1 - \frac{2}{\varepsilon_s + 1} \quad (4)$$

where  $\varepsilon_s$  is the relative dielectric constant of the sample, as seen from equation 4 and equation 2, the effective polarizability ( $\alpha_{eff}$ ) is proportional to the sample relative dielectric constant ( $\varepsilon_s$ ). Therefore, the s-SNOM optical scattering amplitude (S) is directly proportional to the sample relative dielectric constant ( $\varepsilon_s$ ) inferred from the above equations.

### Supporting References

1. Frisch, M. J. T., G. W.; Schlegel, H. B.; Scuseria, G. E.; Robb, M. A.; Cheeseman, J. R.; Scalmani, G.; Barone, V.; Mennucci, B.; Petersson, G. A.; et al. *Gaussian 09, Revision D.01*, Gaussian, Inc.: Wallingford, CT, 2009.
2. Becke, A. D., *Journal of Chemical Physics* **1993**, *98*, 5648.
3. Dunning Jr., T. H.; Hay, P. J., In Modern Theoretical Chemistry, Schaefer III, H. F., Ed. Plenum: New York, 1977; Vol. 3, pp 1-28.
4. Wang, L.; Nan, G.; Yang, X.; Peng, Q.; Li, Q.; Shuai, Z., Computational methods for design of organic materials with high charge mobility. *Chemical Society Reviews* **2010**, *39*, 423-434.
5. Zhang, W.; Chen, Y., Visibility of subsurface nanostructures in scattering-type scanning near-field optical microscopy imaging. *Optics Express* **2020**, *28*, 6696-6707.
6. Cvitkovic, A.; Ocelic, N.; Hillenbrand, R., Analytical model for quantitative prediction of material contrasts in scattering-type near-field optical microscopy. *Optics Express* **2007**, *15*, 8550-8565.

## **6 CHAPTER 6 CONCLUSIONS AND PERSPECTIVES**

### **6.1 Conclusions**

Nowadays, although the field of OSCs has made huge progress on device efficiency, further improving efficiency is still the main research topic in the field. The solvent additive engineering, especial the binary solvent additive, is the simplest and effective way to improve OSCs' efficiency, so it needs to be carefully studied, in particular the general principle of binary solvent additive for high-efficiency OSCs. Additionally, the stable and air-processable devices under different ambient conditions have attracted much attention, which is beneficial for commercial applications. Among many methods of high device stability, designing stable photovoltaic materials seems to be a more effective way for achieving air-processed and stable OSCs. Lastly, in the non-fullerene based devices, the reason for the dissociation of the efficient excitons under a small driving force is not very clear. The dielectric constant and the efficient exciton diffusion are the fundamental photophysical parameter and the important photophysical process, respectively, which should be deeply investigated to figure out the mentioned reason. Therefore, this thesis mainly explores the suitable strategies, photovoltaic materials, and measurements to overcome the issues, and the results of this thesis are divided into three parts.

In the first part, a new binary solvent additive consisting of DIO and AA has been explored and was used in the OSCs based on PffBT4T-2OD polymer donor and PC<sub>61</sub>BM acceptor. After optimizing the concentration ratio between DIO and AA, the device efficiency increased from 9.11% to 10.64%. The related mechanism was probed by optical absorption spectroscopy, synchrotron-based GIXRD, DMT modulus AFM, and STEM. It was found that AA mainly enhanced the PffBT4T-2OD polymer order with better stacking orientation and high crystallinity. Differently, DIO could facilitate the diffusion of more PC<sub>61</sub>BM into the polymer matrix. Based on the synergistic effect of DIO and AA, the corresponding photoactive film exhibited the preferable polymer order and crystallinity, and more D-A interfaces. These led to high charge dissociation and collection probabilities and balanced charge carrier transport, finally resulting in high-performance OSCs. The case introduced a new way to design binary solvent additives with synergistic effects for the improved OSCs.

In the second part, we combined a new air-stable low-bandgap PDPPPTD polymer as a donor and PC<sub>61</sub>BM as an acceptor to obtain the air-processed photovoltaic device with the PCE of 6.34%. Without any encapsulation and interface modification, the device stabilities under different ambient conditions were checked and the related morphology changing of photoactive films was measured by various characterizations, such as synchrotron-based GIXRD, AFM, and FTIR spectroscopy. We found that the air-processed devices had good thermal stability, photostability, and long-term stability in the ambient atmosphere with suitable humidity. In addition, after introducing a solvent additive AA, the device

reproducibility was enhanced and its efficiency was further improved to 7.41%, which was one of the best PCE in air-processed and stable OSCs. Moreover, the AA treatment further improved device stabilities. This work suggested that designing air-stable photovoltaic materials was a more effective tactic for air-processable and high-performance OSCs.

In the third part, a novel method was developed to probe the variation of the dielectric constant of non-fullerene based devices consisting of the common donor (PM6 polymer) and selected non-fullerene acceptors (ITIC, IT-4F, Y6, and IEICO). We found that except for IEICO, other non-fullerene acceptors had higher dielectric constants than fullerene derivatives ( $PC_{61}BM$  and  $PC_{71}BM$ ) in the frequency range of 100 Hz to  $\sim$  MHz and the corresponding blend films also displayed higher blend dielectric constants, resulting in the reduced bimolecular recombination and the increased charge dissociation possibility with low geminate losses. Moreover, from the s-SNOM measurement of non-fullerene acceptors based blend films, the large dielectric constant differences between donor-rich domains and acceptor-rich domains were confirmed, which indicated the larger dielectric constant of non-fullerene acceptors in the GHz range. The results led to lower exciton binding energy and improved exciton dissociation efficiency. In addition, the overlap between the emission spectra of donor and the absorption spectra of related non-fullerene acceptors and the emission spectra variation of donor and related non-fullerene acceptors in bulk heterojunction and bilayer heterojunction films suggested that the energy transfer from donor to acceptor could occur in non-fullerene based photovoltaic devices, finally extending the efficient exciton diffusion for preferable device performance. Therefore, these results well interpret the high device performance with a tiny driving force. Based on the synergistic effect of higher dielectric property and energy transfer on charge separation/transfer process in selected non-fullerene based devices, another intrinsic photophysical working mechanism of charge separation/transfer in non-fullerene based devices was presented. Particularly, the extent of energy transfer's contribution to the enhanced photovoltaic performance should be further probed in the future.

## 6.2 Perspectives

We have made the preliminary progress in the different aspects of OSCs, such as the improvement of OSCs' efficiency and stability, and the exploration of another fundamental photophysical mechanism of efficient charge separation in non-fullerene based devices. However, they are not enough and significant efforts are still needed for further investigation on the above aspects. Therefore, I propose several interesting research directions in this highly promising field.

### 6.2.1 Application of s-SNOM measurement in non-fullerene based devices

Firstly, in the process of comparing the dielectric constants of the PM6:ITIC, PM6:IT-4F, and PM6:Y6 blend films, we found that the different blend films seem to have the same level of dielectric constants in a macrometer scale. Differently, in a sub-micrometer scale, the different blend films exhibit the dielectric constant difference between donor-rich domains and acceptor-rich domains via the scattering optical amplitude contrast of the s-SNOM measurement.<sup>156-157</sup> So the s-SNOM with its resolution of 10 nm is a useful instrument for measuring dielectric property changing of different components in non-fullerene based devices. During the degeneration of non-fullerene based devices and the optimization process of device performance, we can use the s-SNOM to measure dielectric property changing of photovoltaic blend film's different components, especially the dielectric constant changing in the mixing region of donor and acceptor. These can help to deeply investigate the relationship between device performance or charge separation/transfer process and the dielectric property changing in a sub-micrometer scale.

### 6.2.2 Further investigation of energy transfer in non-fullerene based devices

In the third part, the resonance energy transfer from D to A and the different photophysical working mechanisms of charge separation/transfer occurred in non-fullerene based devices. It causes new disputes: the energy transfer and the traditional charge transfer are considered as the competing processes, which is the dominant process and which one is faster in non-fullerene based devices. To answer the above questions, transient absorption (TA) spectroscopy should be conducted to distinguish energy transfer and traditional charge transfer in non-fullerene based devices, although the energy transfer has twice faster than charge transfer in conjugated oligomer-fullerene dyads.<sup>158</sup> Additionally, as reported in previous work, the energy transfer may be experimentally confirmed via the special multilayer films (the general structure: donor/electron blocking layer/non-fullerene acceptor) that block traditional charge transfer but permit the energy transfer.<sup>159</sup> the related measurements such as the time-resolved microwave conductivity (TRMC) measurement of multilayer films on quartz and EQE measurement of corresponding multilayer films based photovoltaic devices, should be carried out. Meanwhile, the work may further confirm the presented new photophysical working mechanism of charge separation/transfer in the above non-fullerene based devices.

### 6.2.3 Air-processed and semi-transparent organic solar cells

In the second part, we fabricated the air-processed and stable OSCs based on air-stable PDPPPTD polymer as a donor and PC<sub>61</sub>BM as an acceptor with a PCE of 7.41%. As seen from the absorption spectrum of blend film, the blend film shows the huge valleys in the visible region and then the related device can be called the semi-transparent OSC. To further improve device efficiency, the invisible light in the near infrared region and ultra-violet region should be sufficiently utilized without reducing the average photopic transmittance. In recent years, the non-fullerene acceptors (such as IEICO-4F, FOIC, and IUIC) with extended near infrared absorption achieved semi-transparent OSCs with high device performance.<sup>160-162</sup> However, most of the cases were carried out in an inert atmosphere. It is expected that combining the PDPPPTD and non-fullerene acceptor with suitable energy level alignment can lead to the high-performance semi-transparent OSC processed in the air. In addition, another way to improve device efficiency of above air-processed and semi-transparent OSC is adding a non-fullerene material with near infrared absorption into the PDPPPTD:PC<sub>61</sub>BM based device, which can be called the semi-transparent ternary OSCs.

## REFERENCES

1. Chapin, D. M.; Fuller, C. S.; Pearson, G. L., A New Silicon p-n Junction Photocell for Converting Solar Radiation into Electrical Power. *J. Appl. Phys.* **1954**, *25*, 676-677.
2. Green, M. A.; Emery, K.; Hishikawa, Y.; Warta, W.; Dunlop, E. D., Solar cell efficiency tables. *Prog. Photovolt.* **2012**, *20*, 12-20.
3. Q4 2018/Q1 2019 Solar Industry Update. **2019**.
4. Hagfeldt, A.; Boschloo, G.; Sun, L.; Kloo, L.; Pettersson, H., Dye-Sensitized Solar Cells. *Chem. Rev.* **2010**, *110*, 6595-6663.
5. Kamat, P. V., Quantum Dot Solar Cells. Semiconductor Nanocrystals as Light Harvesters. *J. Phys. Chem. C* **2008**, *112*, 18737-18753.
6. Petrus, M. L.; Schlipf, J.; Li, C.; Gujar, T. P.; Giesbrecht, N.; Müller-Buschbaum, P.; Thelakkat, M.; Bein, T.; Hüttner, S.; Docampo, P., Capturing the Sun: A Review of the Challenges and Perspectives of Perovskite Solar Cells. *Adv. Energy Mater.* **2017**, *7*, 1700264.
7. Dou, L.; You, J.; Hong, Z.; Xu, Z.; Li, G.; Street, R. A.; Yang, Y., 25th anniversary article: a decade of organic/polymeric photovoltaic research. *Adv. Mater.* **2013**, *25*, 6642-6671.
8. Tang, C. W., Two-layer organic photovoltaic cell. *Appl. Phys. Lett.* **1986**, *48*, 183-185.
9. Liu, Q.; Jiang, Y.; Jin, K.; Qin, J.; Xu, J.; Li, W.; Xiong, J.; Liu, J.; Xiao, Z.; Sun, K.; Yang, S.; Zhang, X.; Ding, L., 18% Efficiency organic solar cells. *Sci. Bull.* **2020**, *65* (4), 272-275.
10. Liu, S.; Chen, D.; Hu, X.; Xing, Z.; Wan, J.; Zhang, L.; Tan, L.; Zhou, W.; Chen, Y., Printable and Large-Area Organic Solar Cells Enabled by a Ternary Pseudo-Planar Heterojunction Strategy. *Adv. Funct. Mater.* **2020**, *30*, 2003223.
11. Yeh, N.; Yeh, P., Organic solar cells: Their developments and potentials. *Renew. Sust. Energ. Rev.* **2013**, *21*, 421-431.
12. Halls, J. J. M.; Walsh, C. A.; Greenham, N. C.; Marseglia, E. A.; Friend, R. H.; Moratti, S. C.; Holmes, A. B., Efficient photodiodes from interpenetrating polymer networks. *Nature* **1995**, *376*, 498-500.
13. Zhou, Y.; Eck, M.; Krüger, M., Bulk-heterojunction hybrid solar cells based on colloidal nanocrystals and conjugated polymers. *Energy Environ. Sci.* **2010**, *3*, 1851-1864.
14. Schilinsky, P.; Waldauf, C.; Hauch, J.; Brabec, C. J., Simulation of light intensity dependent current characteristics of polymer solar cells. *J. Appl. Phys.* **2004**, *95*, 2816-2819.

15. Riedel, I.; Dyakonov, V., Influence of electronic transport properties of polymer-fullerene blends on the performance of bulk heterojunction photovoltaic devices. *phys. stat. sol. (a)* **2004**, *201*, 1332-1341.
16. Nelson, J., Organic photovoltaic films. *Curr. Opin. Solid State Mater. Sci.* **2002**, *6*, 87-95.
17. G.A.Chamberlain, Organic solar cells: A review. *Solar Cells* **1983**, *8*, 47-83.
18. Loutfy, R. O.; Sharp, J. H.; Hsiao, C. K.; Ho, R., Phthalocyanine organic solar cells: Indium/x-metal free phthalocyanine Schottky barriers. *J. Appl. Phys.* **1981**, *52*, 5218-5230.
19. Tang, C. W.; Albrecht, A. C., Photovoltaic effects of metal-chlorophyll-a-metal sandwich cells. *J. Chem. Phys.* **1975**, *62*, 2139-2149.
20. Wohrle, D.; Meissner, D., Organic Solar Cells. *Adv. Mater.* **1991**, *3*, 129-138.
21. Sariciftci, N. S.; Braun, D.; Zhang, C.; Srdanov, V. I.; Heeger, A. J.; Stucky, G.; Wudl, F., Semiconducting polymer-buckminsterfullerene heterojunctions: Diodes, photodiodes, and photovoltaic cells. *Appl. Phys. Lett.* **1993**, *62*, 585-587.
22. Arango, A. C.; Johnson, L. R.; Bliznyuk, V. N.; Schlesinger, Z.; Carter, S. A.; Hörhold, H. H., Efficient Titanium Oxide/Conjugated Polymer Photovoltaics for Solar Energy Conversion. *Adv. Mater.* **2000**, *12*, 1689-1692.
23. Halls, J. J. M.; Pichler, K.; Friend, R. H.; Moratti, S. C.; Holmes, A. B., Exciton diffusion and dissociation in a poly(p-phenylenevinylene)/C<sub>60</sub> heterojunction photovoltaic cell. *Appl. Phys. Lett.* **1996**, *68*, 3120-3122.
24. Haugeneder, A.; Neges, M.; Kallinger, C.; Spirk, W.; Lemmer, U.; Feldmann, J.; Scherf, U.; Harth, E.; Gügel, A.; Müllen, K., Exciton diffusion and dissociation in conjugated polymer/fullerene blends and heterostructures. *Phys. Rev. B* **1999**, *59*, 15346.
25. Hiramoto, M.; Fujiwara, H.; Yokoyama, M., Three-layered organic solar cell with a photoactive interlayer of codeposited pigments. *Appl. Phys. Lett.* **1991**, *58*, 1062-1064.
26. Brabec, C. J.; Sariciftci, N. S.; Hummelen, J. C., Plastic Solar Cells. *Adv. Funct. Mater.* **2001**, *11*, 15-26.
27. Norrman, K.; Gevorgyan, S. A.; Krebs, F. C., Water-induced degradation of polymer solar cells studied by H<sub>2</sub>O<sup>18</sup> labeling. *ACS Appl. Mater. Interfaces* **2009**, *1*, 102-112.
28. Murase, S.; Yang, Y., Solution processed MoO<sub>3</sub> interfacial layer for organic photovoltaics prepared by a facile synthesis method. *Adv. Mater.* **2012**, *24*, 2459-2462.

29. Hummelen, J. C.; Knight, B. W.; LePeq, F.; Wudl, F.; Yao, J.; Wilkins, C. L., Preparation and Characterization of Fulleroid and Methanofullerene Derivatives. *J. Org. Chem.* **1995**, *60*, 532-538.
30. Sariciftci, N. S.; Smilowitz, L.; Heeger, A. J.; Wudi, F., Photoinduced Electron Transfer from a Conducting Polymer to Buckminsterfullerene. *Science* **1992**, *258*, 1474-1476.
31. ShigenoriMorita; AZakhidov, A.; KatsumiYoshino, Doping effect of buckminsterfullerene in conducting polymer: Change of absorption spectrum and quenching of luminescene. *Solid State Commun.* **1992**, *82*, 249-252.
32. Yu, G.; Gao, J.; Hummelen, J. C.; Wudi, F.; Heeger, A. J., Polymer Photovoltaic Cells: Enhanced Efficiencies via a Network of Internal Donor-Acceptor Heterojunctions. *Science* **1995**, *270*, 1789-1791.
33. Ma, W.; Yang, C.; Gong, X.; Lee, K.; Heeger, A. J., Thermally Stable, Efficient Polymer Solar Cells with Nanoscale Control of the Interpenetrating Network Morphology. *Adv. Funct. Mater.* **2005**, *15*, 1617-1622.
34. Yu, G.; Gao, J.; Hummelen, J. C.; Wudl, F.; Heeger, A. J., Polymer Photovoltaic Cells: Enhanced Efficiencies via a Network of Internal Donor-Acceptor Heterojunctions. *Science* **1995**, *270*, 1789-1791.
35. Wienk, M. M.; Kroon, J. M.; Verhees, W. J. H.; Knol, J.; Hummelen, J. C.; van Hal, P. A.; Janssen, R. A. J., Efficient Methano[70]fullerene/MDMO-PPV Bulk Heterojunction Photovoltaic Cells. *Angew. Chem.* **2003**, *115*, 3493-3497.
36. Padinger, F.; Rittberger, R. S.; Sariciftci, N. S., Effects of Postproduction Treatment on Plastic Solar Cells. *Adv. Funct. Mater.* **2003**, *13*, 85-88.
37. Park, S. H.; Roy, A.; Beaupré, S.; Cho, S.; Coates, N.; Moon, J. S.; Moses, D.; Leclerc, M.; Lee, K.; Heeger, A. J., Bulk heterojunction solar cells with internal quantum efficiency approaching 100%. *Nat. Photonics* **2009**, *3*, 297-302.
38. Peet, J.; Kim, J. Y.; Coates, N. E.; Ma, W. L.; Moses, D.; Heeger, A. J.; Bazan, G. C., Efficiency enhancement in low-bandgap polymer solar cells by processing with alkane dithiols. *Nat. Mater.* **2007**, *6*, 497-500.
39. Liang, Y.; Xu, Z.; Xia, J.; Tsai, S. T.; Wu, Y.; Li, G.; Ray, C.; Yu, L., For the bright future-bulk heterojunction polymer solar cells with power conversion efficiency of 7.4%. *Adv. Mater.* **2010**, *22*, E135-E138.
40. He, Z.; Zhong, C.; Su, S.; Xu, M.; Wu, H.; Cao, Y., Enhanced power-conversion efficiency in polymer solar cells using an inverted device structure. *Nat. Photonics* **2012**, *6*, 591-595.

41. Liao, S. H.; Jhuo, H. J.; Cheng, Y. S.; Chen, S. A., Fullerene derivative-doped zinc oxide nanofilm as the cathode of inverted polymer solar cells with low-bandgap polymer (PTB7-Th) for high performance. *Adv. Mater.* **2013**, *25*, 4766-4771.
42. Cao, J.; Liao, Q.; Du, X.; Chen, J.; Xiao, Z.; Zuo, Q.; Ding, L., A pentacyclic aromatic lactam building block for efficient polymer solar cells. *Energy Environ. Sci.* **2013**, *6*, 3224-3228.
43. Jin, Y.; Chen, Z.; Dong, S.; Zheng, N.; Ying, L.; Jiang, X. F.; Liu, F.; Huang, F.; Cao, Y., A Novel Naphtho[1,2-c:5,6-c']Bis([1,2,5]Thiadiazole)-Based Narrow-Bandgap pi-Conjugated Polymer with Power Conversion Efficiency Over 10. *Adv. Mater.* **2016**, *28*, 9811-9818.
44. Zhao, J.; Li, Y.; Yang, G.; Jiang, K.; Lin, H.; Ade, H.; Ma, W.; Yan, H., Efficient organic solar cells processed from hydrocarbon solvents. *Nat. Energ.* **2016**, *1*, 15027.
45. Zhao, G.; He, Y.; Li, Y., 6.5% Efficiency of polymer solar cells based on poly(3-hexylthiophene) and indene-C(60) bisadduct by device optimization. *Adv. Mater.* **2010**, *22*, 4355-4358.
46. Guo, X.; Cui, C.; Zhang, M.; Huo, L.; Huang, Y.; Hou, J.; Li, Y., High efficiency polymer solar cells based on poly(3-hexylthiophene)/indene-C70 bisadduct with solvent additive. *Energy Environ. Sci.* **2012**, *5*, 7943-7949.
47. Lin, Y.; Wang, J.; Zhang, Z. G.; Bai, H.; Li, Y.; Zhu, D.; Zhan, X., An electron acceptor challenging fullerenes for efficient polymer solar cells. *Adv. Mater.* **2015**, *27*, 1170-1174.
48. Lin, Y.; Zhao, F.; Wu, Y.; Chen, K.; Xia, Y.; Li, G.; Prasad, S. K.; Zhu, J.; Huo, L.; Bin, H.; Zhang, Z. G.; Guo, X.; Zhang, M.; Sun, Y.; Gao, F.; Wei, Z.; Ma, W.; Wang, C.; Hodgkiss, J.; Bo, Z.; Inganás, O.; Li, Y.; Zhan, X., Mapping Polymer Donors toward High-Efficiency Fullerene Free Organic Solar Cells. *Adv. Mater.* **2017**, *29*, 1604155.
49. Zhao, W.; Li, S.; Yao, H.; Zhang, S.; Zhang, Y.; Yang, B.; Hou, J., Molecular Optimization Enables over 13% Efficiency in Organic Solar Cells. *J. Am. Chem. Soc.* **2017**, *139*, 7148-7151.
50. Xiao, Z.; Jia, X.; Li, D.; Wang, S.; Geng, X.; Liu, F.; Chen, J.; Yang, S.; Russell, T. P.; Ding, L.,  $26 \text{ mA cm}^{-2}$   $J_{sc}$  from organic solar cells with a low-bandgap nonfullerene acceptor. *Sci. Bull.* **2017**, *62*, 1494-1496.
51. Yuan, J.; Zhang, Y.; Zhou, L.; Zhang, G.; Yip, H.-L.; Lau, T.-K.; Lu, X.; Zhu, C.; Peng, H.; Johnson, P. A.; Leclerc, M.; Cao, Y.; Ulanski, J.; Li, Y.; Zou, Y., Single-Junction Organic Solar Cell with over 15% Efficiency Using Fused-Ring Acceptor with Electron-Deficient Core. *Joule* **2019**, *3*, 1140-1151.

52. Jiang, K.; Wei, Q.; Lai, J. Y. L.; Peng, Z.; Kim, H. K.; Yuan, J.; Ye, L.; Ade, H.; Zou, Y.; Yan, H., Alkyl Chain Tuning of Small Molecule Acceptors for Efficient Organic Solar Cells. *Joule* **2019**, *3*, 3020-3033.
53. Fu, H.; Wang, Z.; Sun, Y., Polymer Donors for High-Performance Non-Fullerene Organic Solar Cells. *Angew Chem. Int. Ed. Eng.* **2019**, *58*, 4442-4453.
54. Cui, Y.; Yao, H.; Hong, L.; Zhang, T.; Tang, Y.; Lin, B.; Xian, K.; Gao, B.; An, C.; Bi, P.; Ma, W.; Hou, J., 17% efficiency organic photovoltaic cell with superior processability. *Natl. Sci. Rev.* **2020**, *7*, 1239-1246.
55. Wu, Y.; Zheng, Y.; Yang, H.; Sun, C.; Dong, Y.; Cui, C.; Yan, H.; Li, Y., Rationally pairing photoactive materials for high-performance polymer solar cells with efficiency of 16.53%. *Sci. China Chem.* **2019**, *63*, 265-271.
56. Facchetti, A., Polymer donor-polymer acceptor (all-polymer) solar cells. *Mater. Today* **2013**, *16*, 123-132.
57. Lee, C.; Lee, S.; Kim, G. U.; Lee, W.; Kim, B. J., Recent Advances, Design Guidelines, and Prospects of All-Polymer Solar Cells. *Chem. Rev.* **2019**, *119*, 8028-8086.
58. Flesch, H.-G.; Resel, R.; McNeill, C. R., Charge transport properties and microstructure of polythiophene/polyfluorene blends. *Org. Electron.* **2009**, *10*, 1549-1555.
59. McNeill, C. R., Morphology of all-polymer solar cells. *Energy Environ. Sci.* **2012**, *5*, 5653-5667.
60. Yan, H.; Chen, Z.; Zheng, Y.; Newman, C.; Quinn, J. R.; Dotz, F.; Kastler, M.; Facchetti, A., A high-mobility electron-transporting polymer for printed transistors. *Nature* **2009**, *457*, 679-686.
61. Mu, C.; Liu, P.; Ma, W.; Jiang, K.; Zhao, J.; Zhang, K.; Chen, Z.; Wei, Z.; Yi, Y.; Wang, J.; Yang, S.; Huang, F.; Facchetti, A.; Ade, H.; Yan, H., High-efficiency all-polymer solar cells based on a pair of crystalline low-bandgap polymers. *Adv. Mater.* **2014**, *26*, 7224-7230.
62. Kang, H.; Uddin, M. A.; Lee, C.; Kim, K. H.; Nguyen, T. L.; Lee, W.; Li, Y.; Wang, C.; Woo, H. Y.; Kim, B. J., Determining the role of polymer molecular weight for high-performance all-polymer solar cells: its effect on polymer aggregation and phase separation. *J. Am. Chem. Soc.* **2015**, *137*, 2359-2365.
63. Lee, C.; Kang, H.; Lee, W.; Kim, T.; Kim, K. H.; Woo, H. Y.; Wang, C.; Kim, B. J., High-performance all-polymer solar cells via side-chain engineering of the polymer acceptor: the importance of the polymer packing structure and the nanoscale blend morphology. *Adv. Mater.* **2015**, *27*, 2466-2471.

64. You, H.; Kim, D.; Cho, H.-H.; Lee, C.; Chong, S.; Ahn, N. Y.; Seo, M.; Kim, J.; Kim, F. S.; Kim, B. J., Shift of the Branching Point of the Side-Chain in Naphthalenediimide (NDI)-Based Polymer for Enhanced Electron Mobility and All-Polymer Solar Cell Performance. *Adv. Funct. Mater.* **2018**, *28*, 1803613.
65. Jia, T.; Li, Z.; Ying, L.; Jia, J.; Fan, B.; Zhong, W.; Pan, F.; He, P.; Chen, J.; Huang, F.; Cao, Y., Asymmetric Alkyl Side-Chain Engineering of Naphthalene Diimide-Based n-Type Polymers for Efficient All-Polymer Solar Cells. *Macromol. Rapid Commun.* **2018**, *39*, e1700765.
66. Feng, S.; Liu, C.; Xu, X.; Liu, X.; Zhang, L.; Nian, Y.; Cao, Y.; Chen, J., Siloxane-Terminated Side Chain Engineering of Acceptor Polymers Leading to Over 7% Power Conversion Efficiencies in All-Polymer Solar Cells. *ACS Macro Lett.* **2017**, *6*, 1310-1314.
67. Xue, L.; Yang, Y.; Bin, H.; Zhang, Z.-G.; Zhang, J.; Yang, Y.; Li, Y., Synthesis and characterization of arylenevinylenearylene-naphthalene diimide copolymers as acceptor in all-polymer solar cells. *J. Polym. Sci., Part A: Polym. Chem.* **2017**, *55*, 1757-1764.
68. Deng, P.; Ho, C. H.; Lu, Y.; Li, H. W.; Tsang, S. W.; So, S. K.; Ong, B. S., Naphthalene diimide-difluorobenzene-based polymer acceptors for all-polymer solar cells. *Chem. Commun.* **2017**, *53*, 3249-3252.
69. Hwang, Y. J.; Courtright, B. A.; Ferreira, A. S.; Tolbert, S. H.; Jenekhe, S. A., 7.7% Efficient All-Polymer Solar Cells. *Adv. Mater.* **2015**, *27*, 4578-4584.
70. Jung, J. W.; Jo, J. W.; Chueh, C. C.; Liu, F.; Jo, W. H.; Russell, T. P.; Jen, A. K., Fluoro-Substituted n-Type Conjugated Polymers for Additive-Free All-Polymer Bulk Heterojunction Solar Cells with High Power Conversion Efficiency of 6.71. *Adv. Mater.* **2015**, *27*, 3310-3317.
71. Cho, H.-H.; Kim, S.; Kim, T.; Sree, V. G.; Jin, S.-H.; Kim, F. S.; Kim, B. J., Design of Cyanovinylene-Containing Polymer Acceptors with Large Dipole Moment Change for Efficient Charge Generation in High-Performance All-Polymer Solar Cells. *Adv. Energy Mater.* **2018**, *8*, 1701436.
72. Kolhe, N. B.; Lee, H.; Kuzuhara, D.; Yoshimoto, N.; Koganezawa, T.; Jenekhe, S. A., All-Polymer Solar Cells with 9.4% Efficiency from Naphthalene Diimide-Biselenophene Copolymer Acceptor. *Chem. Mater.* **2018**, *30*, 6540-6548.
73. Li, Z.; Xu, X.; Zhang, W.; Meng, X.; Ma, W.; Yartsev, A.; Inganas, O.; Andersson, M. R.; Janssen, R. A.; Wang, E., High Performance All-Polymer Solar Cells by Synergistic Effects of Fine-Tuned Crystallinity and Solvent Annealing. *J. Am. Chem. Soc.* **2016**, *138*, 10935-10944.
74. Liu, X.; Zhang, C.; Duan, C.; Li, M.; Hu, Z.; Wang, J.; Liu, F.; Li, N.; Brabec, C. J.; Janssen, R. A. J.; Bazan, G. C.; Huang, F.; Cao, Y., Morphology Optimization via Side Chain Engineering Enables All-Polymer Solar Cells with Excellent Fill Factor and Stability. *J. Am. Chem. Soc.* **2018**, *140*, 8934-8943.

75. Xu, X.; Li, Z.; Wang, J.; Lin, B.; Ma, W.; Xia, Y.; Andersson, M. R.; Janssen, R. A. J.; Wang, E., High-performance all-polymer solar cells based on fluorinated naphthalene diimide acceptor polymers with fine-tuned crystallinity and enhanced dielectric constants. *Nano Energy* **2018**, *45*, 368-379.
76. Li, S.; Zhang, H.; Zhao, W.; Ye, L.; Yao, H.; Yang, B.; Zhang, S.; Hou, J., Green-Solvent-Processed All-Polymer Solar Cells Containing a Perylene Diimide-Based Acceptor with an Efficiency over 6.5%. *Adv. Energy Mater.* **2016**, *6*, 1501991.
77. Guo, Y.; Li, Y.; Awartani, O.; Zhao, J.; Han, H.; Ade, H.; Zhao, D.; Yan, H., A Vinylene-Bridged Perylenediimide-Based Polymeric Acceptor Enabling Efficient All-Polymer Solar Cells Processed under Ambient Conditions. *Adv. Mater.* **2016**, *28*, 8483-8489.
78. Yin, Y.; Yang, J.; Guo, F.; Zhou, E.; Zhao, L.; Zhang, Y., High-Performance All-Polymer Solar Cells Achieved by Fused Perylenediimide-Based Conjugated Polymer Acceptors. *ACS Appl. Mater. Interfaces* **2018**, *10*, 15962-15970.
79. Li, W.; Roelofs, W. S.; Turbiez, M.; Wienk, M. M.; Janssen, R. A., Polymer solar cells with diketopyrrolopyrrole conjugated polymers as the electron donor and electron acceptor. *Adv. Mater.* **2014**, *26*, 3304-3309.
80. Liu, S.; Firdaus, Y.; Thomas, S.; Kan, Z.; Cruciani, F.; Lopatin, S.; Bredas, J. L.; Beaujuge, P. M., Isoindigo-3,4-Difluorothiophene Polymer Acceptors Yield "All-Polymer" Bulk-Heterojunction Solar Cells with over 7 % Efficiency. *Angew. Chem. Int. Ed.* **2018**, *57*, 531-535.
81. Liu, S.; Kan, Z.; Thomas, S.; Cruciani, F.; Bredas, J. L.; Beaujuge, P. M., Thieno[3,4-c]pyrrole-4,6-dione-3,4-difluorothiophene Polymer Acceptors for Efficient All-Polymer Bulk Heterojunction Solar Cells. *Angew. Chem. Int. Ed.* **2016**, *55*, 12996-13000.
82. Wang, Y.; Yan, Z.; Guo, H.; Uddin, M. A.; Ling, S.; Zhou, X.; Su, H.; Dai, J.; Woo, H. Y.; Guo, X., Effects of Bithiophene Imide Fusion on the Device Performance of Organic Thin-Film Transistors and All-Polymer Solar Cells. *Angew. Chem. Int. Ed.* **2017**, *56*, 15304-15308.
83. Zhao, R.; Bi, Z.; Dou, C.; Ma, W.; Han, Y.; Liu, J.; Wang, L., Polymer Electron Acceptors with Conjugated Side Chains for Improved Photovoltaic Performance. *Macromolecules* **2017**, *50*, 3171-3178.
84. Long, X.; Ding, Z.; Dou, C.; Zhang, J.; Liu, J.; Wang, L., Polymer Acceptor Based on Double B-N Bridged Bipyridine (BNBP) Unit for High-Efficiency All-Polymer Solar Cells. *Adv. Mater.* **2016**, *28* (30), 6504-6508.
85. Fan, Q.; An, Q.; Lin, Y.; Xia, Y.; Li, Q.; Zhang, M.; Su, W.; Peng, W.; Zhang, C.; Liu, F.; Hou, L.; Zhu, W.; Yu, D.; Xiao, M.; Moons, E.; Zhang, F.; Anthopoulos, T. D.; Inganäs, O.; Wang, E., Over 14%

efficiency all-polymer solar cells enabled by a low bandgap polymer acceptor with low energy loss and efficient charge separation. *Energy Environ. Sci.* **2020**, *13*, 5017-5027.

86. Fu, H.; Li, Y.; Yu, J.; Wu, Z.; Fan, Q.; Lin, F.; Woo, H. Y.; Gao, F.; Zhu, Z.; Jen, A. K., High Efficiency (15.8%) All-Polymer Solar Cells Enabled by a Regioregular Narrow Bandgap Polymer Acceptor. *J. Am. Chem. Soc.* **2021**, *143*, 7, 2665-2670.
87. Oh, J.; Kranthiraja, K.; Lee, C.; Gunasekar, K.; Kim, S.; Ma, B.; Kim, B. J.; Jin, S. H., Side-Chain Fluorination: An Effective Approach to Achieving High-Performance All-Polymer Solar Cells with Efficiency Exceeding 7. *Adv. Mater.* **2016**, *28*, 10016-10023.
88. Gao, L.; Zhang, Z. G.; Xue, L.; Min, J.; Zhang, J.; Wei, Z.; Li, Y., All-Polymer Solar Cells Based on Absorption-Complementary Polymer Donor and Acceptor with High Power Conversion Efficiency of 8.27%. *Adv. Mater.* **2016**, *28*, 1884-1890.
89. Chen, S.; An, Y.; Dutta, G. K.; Kim, Y.; Zhang, Z.-G.; Li, Y.; Yang, C., A Synergetic Effect of Molecular Weight and Fluorine in All-Polymer Solar Cells with Enhanced Performance. *Adv. Funct. Mater.* **2017**, *27*, 1603564.
90. Fan, B.; Ying, L.; Zhu, P.; Pan, F.; Liu, F.; Chen, J.; Huang, F.; Cao, Y., All-Polymer Solar Cells Based on a Conjugated Polymer Containing Siloxane-Functionalized Side Chains with Efficiency over 10. *Adv. Mater.* **2017**, *29*, 1703906.
91. Ye, L.; Collins, B. A.; Jiao, X.; Zhao, J.; Yan, H.; Ade, H., Miscibility-Function Relations in Organic Solar Cells: Significance of Optimal Miscibility in Relation to Percolation. *Adv. Energy Mater.* **2018**, *8*, 1703058.
92. Hwang, Y. J.; Earmme, T.; Courtright, B. A.; Eberle, F. N.; Jenekhe, S. A., n-Type semiconducting naphthalene diimide-perylene diimide copolymers: controlling crystallinity, blend morphology, and compatibility toward high-performance all-polymer solar cells. *J. Am. Chem. Soc.* **2015**, *137*, 4424-4434.
93. Pavlopoulou, E.; Kim, C. S.; Lee, S. S.; Chen, Z.; Facchetti, A.; Toney, M. F.; Loo, Y.-L., Tuning the Morphology of All-Polymer OPVs through Altering Polymer-Solvent Interactions. *Chem. Mater.* **2014**, *26*, 5020-5027.
94. Jung, J.; Lee, W.; Lee, C.; Ahn, H.; Kim, B. J., Controlling Molecular Orientation of Naphthalenediimide-Based Polymer Acceptors for High Performance All-Polymer Solar Cells. *Adv. Energy Mater.* **2016**, *6*, 1600504.

95. Jo, J. W.; Jung, J. W.; Ahn, H.; Ko, M. J.; Jen, A. K. Y.; Son, H. J., Effect of Molecular Orientation of Donor Polymers on Charge Generation and Photovoltaic Properties in Bulk Heterojunction All-Polymer Solar Cells. *Adv. Energy Mater.* **2017**, *7*, 1601365.
96. Ye, L.; Jiao, X.; Zhao, W.; Zhang, S.; Yao, H.; Li, S.; Ade, H.; Hou, J., Manipulation of Domain Purity and Orientational Ordering in High Performance All-Polymer Solar Cells. *Chem. Mater.* **2016**, *28*, 6178-6185.
97. Su, W.; Meng, Y.; Guo, X.; Fan, Q.; Zhang, M.; Jiang, Y.; Xu, Z.; Dai, Y.; Xie, B.; Liu, F.; Zhang, M.; Russell, T. P.; Li, Y., Efficient and thermally stable all-polymer solar cells based on a fluorinated wide-bandgap polymer donor with high crystallinity. *J. Mater. Chem. A* **2018**, *6*, 16403-16411.
98. Chen, Y.; Wan, X.; Long, G., High Performance Photovoltaic Applications Using Solution-Processed Small Molecules. *Acc. Chem. Res.* **2013**, *46*, 2645-2655.
99. Collins, S. D.; Ran, N. A.; Heiber, M. C.; Nguyen, T.-Q., Small is Powerful: Recent Progress in Solution-Processed Small Molecule Solar Cells. *Adv. Energy Mater.* **2017**, *7*, 1602242.
100. Steinmann, V.; Kronenberg, N. M.; Lenze, M. R.; Graf, S. M.; Hertel, D.; Meerholz, K.; Bürckstümmer, H.; Tulyakova, E. V.; Würthner, F., Simple, Highly Efficient Vacuum-Processed Bulk Heterojunction Solar Cells Based on Merocyanine Dyes. *Adv. Energy Mater.* **2011**, *1*, 888-893.
101. Ma, B.; Woo, C. H.; Miyamoto, Y.; Fréchet, J. M. J., Solution Processing of a Small Molecule, Subnaphthalocyanine, for Efficient Organic Photovoltaic Cells. *Chem. Mater.* **2009**, *21*, 1413-1417.
102. Walker, B.; Tamayo, A. B.; Dang, X.-D.; Zalar, P.; Seo, J. H.; Garcia, A.; Tantiwiwat, M.; Nguyen, T.-Q., Nanoscale Phase Separation and High Photovoltaic Efficiency in Solution-Processed, Small-Molecule Bulk Heterojunction Solar Cells. *Adv. Funct. Mater.* **2009**, *19*, 3063-3069.
103. Yoo, S.; Domercq, B.; Kippelen, B., Efficient thin-film organic solar cells based on pentacene/C60 heterojunctions. *Appl. Phys. Lett.* **2004**, *85*, 5427-5429.
104. Valentini, L.; Bagnis, D.; Marrocchi, A.; Seri, M.; Taticchi, A.; Kenny, J. M., Novel Anthracene-Core Molecule for the Development of Efficient PCBM-Based Solar Cell. *Chem. Mater.* **2008**, *20*, 32-34.
105. Li, Z.; He, G.; Wan, X.; Liu, Y.; Zhou, J.; Long, G.; Zuo, Y.; Zhang, M.; Chen, Y., Solution Processable Rhodanine-Based Small Molecule Organic Photovoltaic Cells with a Power Conversion Efficiency of 6.1%. *Adv. Energy Mater.* **2012**, *2*, 74-77.
106. Zhou, J.; Wan, X.; Liu, Y.; Long, G.; Wang, F.; Li, Z.; Zuo, Y.; Li, C.; Chen, Y., A Planar Small Molecule with Dithienosilole Core for High Efficiency Solution-Processed Organic Photovoltaic Cells. *Chem. Mater.* **2011**, *23*, 4666-4668.

107. Chiu, S. W.; Lin, L. Y.; Lin, H. W.; Chen, Y. H.; Huang, Z. Y.; Lin, Y. T.; Lin, F.; Liu, Y. H.; Wong, K. T., A donor-acceptor-acceptor molecule for vacuum-processed organic solar cells with a power conversion efficiency of 6.4%. *Chem. Commun.* **2012**, *48*, 1857-1859.
108. Shang, H.; Fan, H.; Liu, Y.; Hu, W.; Li, Y.; Zhan, X., A solution-processable star-shaped molecule for high-performance organic solar cells. *Adv. Mater.* **2011**, *23*, 1554-1557.
109. Sun, Y.; Welch, G. C.; Leong, W. L.; Takacs, C. J.; Bazan, G. C.; Heeger, A. J., Solution-processed small-molecule solar cells with 6.7% efficiency. *Nat. Mater.* **2011**, *11*, 44-48.
110. Kan, B.; Li, M.; Zhang, Q.; Liu, F.; Wan, X.; Wang, Y.; Ni, W.; Long, G.; Yang, X.; Feng, H.; Zuo, Y.; Zhang, M.; Huang, F.; Cao, Y.; Russell, T. P.; Chen, Y., A series of simple oligomer-like small molecules based on oligothiophenes for solution-processed solar cells with high efficiency. *J. Am. Chem. Soc.* **2015**, *137*, 3886-3893.
111. Ryu, S. U.; Abbas, Z.; Cho, A.; Lee, H.; Song, C. E.; Lee, H. K.; Lee, S. K.; Shin, W. S.; Moon, S. J.; Park, T.; Kim, H. I.; Lee, J. C., Strategic Halogen Substitution to Enable High-Performance Small-Molecule-Based Tandem Solar Cell with over 15% Efficiency. *Adv. Energy Mater.* **2020**, *10*, 1903846.
112. Wang, X.; Wang, J.; Han, J.; Huang, D.; Wang, P.; Zhou, L.; Yang, C.; Bao, X.; Yang, R., Over 15% efficiency all-small-molecule organic solar cells enabled by a C-shaped small molecule donor with tailororable asymmetric backbone. *Nano Energy* **2021**, *81*, 105612.
113. Green, M. A.; Dunlop, E. D.; Hohl - Ebinger, J.; Yoshita, M.; Kopidakis, N.; Ho - Baillie, A. W. Y., Solar cell efficiency tables (Version 55). *Prog. Photovolt.* **2019**, *28*, 3-15.
114. Cheng, P.; Li, G.; Zhan, X.; Yang, Y., Next-generation organic photovoltaics based on non-fullerene acceptors. *Nat. Photonics* **2018**, *12*, 131-142.
115. Yang, X.; Uddin, A., Effect of thermal annealing on P3HT:PCBM bulk-heterojunction organic solar cells: A critical review. *Renew. Sust. Energ. Rev.* **2014**, *30*, 324-336.
116. Zhao, F.; Wang, C.; Zhan, X., Morphology Control in Organic Solar Cells. *Adv. Energy Mater.* **2018**, *8*, 1703147.
117. Kwon, S.; Kang, H.; Lee, J.-H.; Lee, J.; Hong, S.; Kim, H.; Lee, K., Effect of Processing Additives on Organic Photovoltaics: Recent Progress and Future Prospects. *Adv. Energy Mater.* **2017**, *7*, 1601496.
118. Zhao, Y.; Chen, H.; Zhu, C.; Yuan, J.; Li, Y.; Hai, J.; Hu, Y.; Jiang, L.; Chen, G.; Zou, Y., Fine-tuning the energy levels and morphology via fluorination and thermal annealing enable high efficiency non-fullerene organic solar cells. *Mater. Chem. Front.* **2020**, *4*, 3310-3318.

119. Qiu, B.; Chen, Z.; Qin, S.; Yao, J.; Huang, W.; Meng, L.; Zhu, H.; Yang, Y. M.; Zhang, Z. G.; Li, Y., Highly Efficient All-Small-Molecule Organic Solar Cells with Appropriate Active Layer Morphology by Side Chain Engineering of Donor Molecules and Thermal Annealing. *Adv. Mater.* **2020**, *32*, e1908373.
120. Jin, C.; Olsen, B. C.; Luber, E. J.; Buriak, J. M., Nanopatterning via Solvent Vapor Annealing of Block Copolymer Thin Films. *Chem. Mater.* **2016**, *29*, 176-188.
121. Wessendorf, C. D.; Schulz, G. L.; Mishra, A.; Kar, P.; Ata, I.; Weidelener, M.; Urdanpilleta, M.; Hanisch, J.; Mena-Osteritz, E.; Lindén, M.; Ahlsweide, E.; Bäuerle, P., Efficiency Improvement of Solution-Processed Dithienopyrrole-Based A-D-A Oligothiophene Bulk-Heterojunction Solar Cells by Solvent Vapor Annealing. *Adv. Energy Mater.* **2014**, *4*, 1400266.
122. Gao, K.; Deng, W.; Xiao, L.; Hu, Q.; Kan, Y.; Chen, X.; Wang, C.; Huang, F.; Peng, J.; Wu, H.; Peng, X.; Cao, Y.; Russell, T. P.; Liu, F., New insight of molecular interaction, crystallization and phase separation in higher performance small molecular solar cells via solvent vapor annealing. *Nano Energy* **2016**, *30*, 639-648.
123. Zheng, Y.; Li, S.; Zheng, D.; Yu, J., Effects of different polar solvents for solvent vapor annealing treatment on the performance of polymer solar cells. *Org. Electron.* **2014**, *15*, 2647-2653.
124. Gu, Y.; Wang, C.; Russell, T. P., Multi-Length-Scale Morphologies in PCPDTBT/PCBM Bulk-Heterojunction Solar Cells. *Adv. Energy Mater.* **2012**, *2*, 683-690.
125. Hoven, C. V.; Dang, X. D.; Coffin, R. C.; Peet, J.; Nguyen, T. Q.; Bazan, G. C., Improved performance of polymer bulk heterojunction solar cells through the reduction of phase separation via solvent additives. *Adv. Mater.* **2010**, *22*, E63-E66.
126. Nguyen, T. L.; Choi, H.; Ko, S. J.; Uddin, M. A.; Walker, B.; Yum, S.; Jeong, J. E.; Yun, M. H.; Shin, T. J.; Hwang, S.; Kim, J. Y.; Woo, H. Y., Semi-crystalline photovoltaic polymers with efficiency exceeding 9% in a ~300 nm thick conventional single-cell device. *Energy Environ. Sci.* **2014**, *7*, 3040-3051.
127. Liu, C.; Hu, X.; Zhong, C.; Huang, M.; Wang, K.; Zhang, Z.; Gong, X.; Cao, Y.; Heeger, A. J., The influence of binary processing additives on the performance of polymer solar cells. *Nanoscale* **2014**, *6*, 14297-14304.
128. Wan, Q.; Guo, X.; Wang, Z.; Li, W.; Guo, B.; Ma, W.; Zhang, M.; Li, Y., 10.8% Efficiency Polymer Solar Cells Based on PTB7-Th and PC<sub>71</sub>BM via Binary Solvent Additives Treatment. *Adv. Funct. Mater.* **2016**, *26*, 6635-6640.

129. Gao, K.; Miao, J.; Xiao, L.; Deng, W.; Kan, Y.; Liang, T.; Wang, C.; Huang, F.; Peng, J.; Cao, Y.; Liu, F.; Russell, T. P.; Wu, H.; Peng, X., Multi-Length-Scale Morphologies Driven by Mixed Additives in Porphyrin-Based Organic Photovoltaics. *Adv. Mater.* **2016**, *28*, 4727-4733.
130. Cheng, P.; Zhan, X., Stability of organic solar cells: challenges and strategies. *Chem. Soc. Rev.* **2016**, *45*, 2544-2582.
131. Drakonakis, V. M.; Savva, A.; Kokonou, M.; Choulis, S. A., Investigating electrodes degradation in organic photovoltaics through reverse engineering under accelerated humidity lifetime conditions. *Sol. Energy Mater. Sol. Cells* **2014**, *130*, 544-550.
132. Yeom, H. R.; Heo, J.; Kim, G. H.; Ko, S. J.; Song, S.; Jo, Y.; Kim, D. S.; Walker, B.; Kim, J. Y., Optimal top electrodes for inverted polymer solar cells. *Phys. Chem. Chem. Phys.* **2015**, *17*, 2152-2159.
133. Cao, H.; He, W.; Mao, Y.; Lin, X.; Ishikawa, K.; Dickerson, J. H.; Hess, W. P., Recent progress in degradation and stabilization of organic solar cells. *J. Power Sources* **2014**, *264*, 168-183.
134. Schroeder, B. C.; Li, Z.; Brady, M. A.; Faria, G. C.; Ashraf, R. S.; Takacs, C. J.; Cowart, J. S.; Duong, D. T.; Chiu, K. H.; Tan, C. H.; Cabral, J. T.; Salleo, A.; Chabinyc, M. L.; Durrant, J. R.; McCulloch, I., Enhancing fullerene-based solar cell lifetimes by addition of a fullerene dumbbell. *Angew. Chem. Int. Ed.* **2014**, *53*, 12870-12875.
135. Lee, S.; Kong, J.; Lee, K., Air-Stable Organic Solar Cells Using an Iodine-Free Solvent Additive. *Adv. Energy Mater.* **2016**, *6*, 1600970.
136. Constantinou, I.; Lai, T. H.; Zhao, D.; Klump, E. D.; Deininger, J. J.; Lo, C. K.; Reynolds, J. R.; So, F., High efficiency air-processed dithienogermole-based polymer solar cells. *ACS Appl. Mater. Interfaces* **2015**, *7*, 4826-4832.
137. McAfee, S. M.; Dayneko, S. V.; Josse, P.; Blanchard, P.; Cabanetos, C.; Welch, G. C., Simply Complex: The Efficient Synthesis of an Intricate Molecular Acceptor for High-Performance Air-Processed and Air-Tested Fullerene-Free Organic Solar Cells. *Chem. Mater.* **2017**, *29*, 1309-1314.
138. Xu, Y.; Yao, H.; Ma, L.; Wang, J.; Hou, J., Efficient charge generation at low energy losses in organic solar cells: a key issues review. *Rep. Prog. Phys.* **2020**, *83*, 082601.
139. Yao, H.; Cui, Y.; Qian, D.; Ponseca, C. S., Jr.; Honarfar, A.; Xu, Y.; Xin, J.; Chen, Z.; Hong, L.; Gao, B.; Yu, R.; Zu, Y.; Ma, W.; Chabera, P.; Pullerits, T.; Yartsev, A.; Gao, F.; Hou, J., 14.7% Efficiency Organic Photovoltaic Cells Enabled by Active Materials with a Large Electrostatic Potential Difference. *J. Am. Chem. Soc.* **2019**, *141*, 7743-7750.

140. Zhang, G.; Chen, X. K.; Xiao, J.; Chow, P. C. Y.; Ren, M.; Kupgan, G.; Jiao, X.; Chan, C. C. S.; Du, X.; Xia, R.; Chen, Z.; Yuan, J.; Zhang, Y.; Zhang, S.; Liu, Y.; Zou, Y.; Yan, H.; Wong, K. S.; Coropceanu, V.; Li, N.; Brabec, C. J.; Bredas, J. L.; Yip, H. L.; Cao, Y., Delocalization of exciton and electron wavefunction in non-fullerene acceptor molecules enables efficient organic solar cells. *Nat. Commun.* **2020**, *11*, 3943.
141. Hinrichsen, T. F.; Chan, C. C. S.; Ma, C.; Palecek, D.; Gillett, A.; Chen, S.; Zou, X.; Zhang, G.; Yip, H. L.; Wong, K. S.; Friend, R. H.; Yan, H.; Rao, A.; Chow, P. C. Y., Long-lived and disorder-free charge transfer states enable endothermic charge separation in efficient non-fullerene organic solar cells. *Nat. Commun.* **2020**, *11*, 5617.
142. Wang, R.; Zhang, C.; Li, Q.; Zhang, Z.; Wang, X.; Xiao, M., Charge Separation from an Intra-Moiety Intermediate State in the High-Performance PM6:Y6 Organic Photovoltaic Blend. *J. Am. Chem. Soc.* **2020**, *142*, 12751-12759.
143. Huang, Y.; Kramer, E. J.; Heeger, A. J.; Bazan, G. C., Bulk heterojunction solar cells: morphology and performance relationships. *Chem. Rev.* **2014**, *114*, 7006-7043.
144. Li, G.; Yao, Y.; Yang, H.; Shrotriya, V.; Yang, G.; Yang, Y., “Solvent Annealing” Effect in Polymer Solar Cells Based on Poly(3-hexylthiophene) and Methanofullerenes. *Adv. Funct. Mater.* **2007**, *17*, 1636-1644.
145. Wang, D. H.; Kyaw, A. K. K.; Pouliot, J.-R.; Leclerc, M.; Heeger, A. J., Enhanced Power Conversion Efficiency of Low Band-Gap Polymer Solar Cells by Insertion of Optimized Binary Processing Additives. *Adv. Energy Mater.* **2014**, *4*, 1300835.
146. Liu, C.; Hu, X.; Zhong, C.; Huang, M.; Wang, K.; Zhang, Z.; Gong, X.; Cao, Y.; Heeger, A. J., The influence of binary processing additives on the performance of polymer solar cells. *Nanoscale* **2014**, *6*, 14297-14304.
147. Wan, Q.; Guo, X.; Wang, Z.; Li, W.; Guo, B.; Ma, W.; Zhang, M.; Li, Y., 10.8% Efficiency Polymer Solar Cells Based on PTB7-Th and PC<sub>71</sub>BM via Binary Solvent Additives Treatment. *Adv. Funct. Mater.* **2016**, *26*, 6635-6640.
148. Chen, L.-M.; Hong, Z.; Li, G.; Yang, Y., Recent Progress in Polymer Solar Cells: Manipulation of Polymer:Fullerene Morphology and the Formation of Efficient Inverted Polymer Solar Cells. *Adv. Mater.* **2009**, *21*, 1434-1449.

149. Woo, S.; Hyun Kim, W.; Kim, H.; Yi, Y.; Lyu, H.-K.; Kim, Y., 8.9% Single-Stack Inverted Polymer Solar Cells with Electron-Rich Polymer Nanolayer-Modified Inorganic Electron-Collecting Buffer Layers. *Adv. Energy Mater.* **2014**, *4*, 1301692.
150. Yan, Y.; Cai, F.; Yang, L.; Li, J.; Zhang, Y.; Qin, F.; Xiong, C.; Zhou, Y.; Lidzey, D. G.; Wang, T., Light-Soaking-Free Inverted Polymer Solar Cells with an Efficiency of 10.5% by Compositional and Surface Modifications to a Low-Temperature-Processed TiO<sub>2</sub> Electron-Transport Layer. *Adv. Mater.* **2017**, *29*, 1604044.
151. Liu, J.; Chen, S.; Qian, D.; Gautam, B.; Yang, G.; Zhao, J.; Bergqvist, J.; Zhang, F.; Ma, W.; Ade, H.; Inganäs, O.; Gundogdu, K.; Gao, F.; Yan, H., Fast charge separation in a non-fullerene organic solar cell with a small driving force. *Nat. Energ.* **2016**, *1*, 16089.
152. Yao, J.; Kirchartz, T.; Vezie, M. S.; Faist, M. A.; Gong, W.; He, Z.; Wu, H.; Troughton, J.; Watson, T.; Bryant, D.; Nelson, J., Quantifying Losses in Open-Circuit Voltage in Solution-Processable Solar Cells. *Phys. Rev. Applied* **2015**, *4*, 014020.
153. Sun, Y.; Seo, J. H.; Takacs, C. J.; Seifter, J.; Heeger, A. J., Inverted polymer solar cells integrated with a low-temperature-annealed sol-gel-derived ZnO Film as an electron transport layer. *Adv. Mater.* **2011**, *23*, 1679-1683.
154. Guérette, M.; Najari, A.; Maltais, J.; Pouliot, J.-R.; Dufresne, S.; Simoneau, M.; Besner, S.; Charest, P.; Leclerc, M., New Processable Phenanthridinone-Based Polymers for Organic Solar Cell Applications. *Adv. Energy Mater.* **2016**, *6*, 1502094.
155. Zou, Y.; Gendron, D.; Badrou-Aich, R. d.; Najari, A.; Tao, Y.; Leclerc, M., A High-Mobility Low-Bandgap Poly(2,7-carbazole) Derivative for Photovoltaic Applications. *Macromolecules* **2009**, *42*, 2891-2894.
156. Zhang, W.; Chen, Y., Visibility of subsurface nanostructures in scattering-type scanning near-field optical microscopy imaging. *Optics Express* **2020**, *28*, 6696-6707.
157. Stanciu, S. G.; Tranca, D. E.; Pastorino, L.; Boi, S.; Song, Y. M.; Yoo, Y. J.; Ishii, S.; Hristu, R.; Yang, F.; Bussetti, G.; Stanciu, G. A., Characterization of Nanomaterials by Locally Determining Their Complex Permittivity with Scattering-Type Scanning Near-Field Optical Microscopy. *ACS Appl. Nano Mater.* **2020**, *3*, 1250-1262.
158. van Hal, P. A.; Janssen, R. A. J.; Lanzani, G.; Cerullo, G.; Zavelani-Rossi, M.; De Silvestri, S., Two-step mechanism for the photoinduced intramolecular electron transfer in oligo(p-phenylene vinylene)-fullerene dyads. *Phys. Rev. B* **2001**, *64*, 075206.

159. Coffey, D. C.; Ferguson, A. J.; Kopidakis, N.; Rumbles, G., Photovoltaic Charge Generation in Organic Semiconductors Based on LongRange Energy Transfer. *ACS Nano* **2010**, *4*, 5437-5445.
160. Jia, B.; Dai, S.; Ke, Z.; Yan, C.; Ma, W.; Zhan, X., Breaking 10% Efficiency in Semitransparent Solar Cells with Fused-Undecacyclic Electron Acceptor. *Chem. Mater.* **2017**, *30*, 239-245.
161. Li, T.; Dai, S.; Ke, Z.; Yang, L.; Wang, J.; Yan, C.; Ma, W.; Zhan, X., Fused Tris(thienothiophene)-Based Electron Acceptor with Strong Near-Infrared Absorption for High-Performance As-Cast Solar Cells. *Adv. Mater.* **2018**, *30*, 1705969.
162. Hu, Z.; Wang, Z.; Zhang, F., Semitransparent polymer solar cells with 9.06% efficiency and 27.1% average visible transmittance obtained by employing a smart strategy. *J. Mater. Chem. A* **2019**, *7*, 7025-7032.

# RÉSUMÉ

## L'introduction

Actuellement, l'énergie utilisée de l'énergie repose principalement sur des combustibles fossiles non renouvelables et polluants, ce qui entraîne des conséquences non durables sur les problèmes sociaux, économiques, géopolitiques et environnementaux. L'énergie solaire est l'une des sources d'énergie renouvelable les plus prometteuses pour répondre à la demande énergétique mondiale, qui ne cesse de croître. Les cellules solaires, qui convertissent directement l'énergie solaire en électricité grâce à l'effet photovoltaïque (PV), ont été considérées comme l'une des technologies les plus propres et les plus prometteuses pour résoudre les problèmes énergétiques actuels. Depuis que la première cellule solaire en silicium, avec un rendement de 6%, a été mise en place avec succès par le Bell Lab en 1954, l'efficacité des cellules solaires n'a cessé d'être améliorée et différents types de cellules solaires ont été explorés. Aujourd'hui, les différentes cellules solaires inorganiques à base de silicium cristallin, de tellurure de cadmium ou de sélénite de cuivre, d'indium et de germanium (CIGS) obtiennent un rendement élevé de conversion d'énergie (PCE) d'environ 15 à 25%, et occupent la plupart des technologies PV disponibles dans le commerce. Cependant, le processus complexe de fabrication des cellules solaires inorganiques ci-dessus, le coût élevé des matières premières et les problèmes environnementaux connexes ont empêché leur déploiement à grande échelle. Ils encouragent la recherche intensive pour développer les technologies PV à haut rendement, à faible coût et respectueuses de l'environnement, dont les cellules solaires organiques (OSC) sont la solution de rechange prometteuse en raison de leurs remarquables avantages de faible coût, de la flexibilité, l'égéreté et simplicité dans le processus de fabrication des dispositifs. Aujourd'hui, le PCE certifié des OSC à jonction unique a atteint plus de 17% en laboratoire, ce qui les rend plus que jamais attrayantes pour d'éventuelles applications commerciales.

Cependant, certaines questions doivent être traitées avec soin avant que les CSP puissent être appliquées à grande échelle. Premièrement, l'efficacité des dispositifs des CSP est encore inférieure à celle des dispositifs en silicium. Il est difficile de régler avec précision la séparation de phase de l'hétérojonction en vrac afin de répondre à une dissociation d'exciton efficace ainsi qu'à une séparation de charge. Jusqu'à présent, il est difficile de prédire avec précision la morphologie optimisée du film photoactif, bien que de nombreux paramètres de traitement connexes aient été ajustés, notamment le recuit thermique, le recuit en vapeur de solvant et l'ingénierie des additifs de solvant. Parmi eux, l'ajout d'additifs de solvants est un moyen le plus simple et le plus efficace sans rendre la fabrication des CSP plus complexe, en particulier les additifs de solvants binaires. Cependant, le rôle du composant unique dans les additifs solvants binaires dans les rapports susmentionnés n'a pas été entièrement divulgué. Deuxièmement, bien que l'efficacité des CSP se soit considérablement améliorée, la plupart des CSP sont encore fabriqués dans une atmosphère inerte en

raison de la sensibilité à l'air des matériaux photovoltaïques organiques, des couches d'interface et des matériaux d'électrode. La capacité de traitement à l'air et la stabilité à long terme des CSP ont donc attiré davantage d'attention et certaines stratégies ont été mises en oeuvre, comme l'utilisation de la structure de dispositif inversée, les oxydes métalliques comme couches d'extraction d'électrons, les oxydes métalliques à haute fonctionnalité comme couches d'interface d'anode et la modification des films photoactifs. Toutefois, la stratégie la plus prometteuse et la plus efficace pour les CSP stables et à haut rendement consiste à explorer les matériaux photovoltaïques stables et pouvant être traités à l'air dans diverses conditions. En attendant, les performances des dispositifs correspondants doivent être encore améliorées et la stabilité à long terme de ces dispositifs traités à l'air dans différentes conditions ambiantes doivent être examinée en détail. Enfin, la percée des matériaux accepteurs autres que le fullerène fait progresser rapidement l'efficacité des dispositifs. Et la caractéristique la plus importante des dispositifs à haute performance à base de non-fullerène est la faible perte de tension et donc la séparation efficace des charges avec une force motrice faible (ou négligeable), qui est différente des dispositifs à base de dérivés du fullerène avec une force motrice importante. Jusqu'à présent, la plupart des recherches se sont principalement concentrées sur les nouveaux accepteurs sans fullerène pour les dispositifs à haute performance avec une perte de tension plus faible. La raison de la dissociation efficace de l'exciton sous une faible perte de tension (ou une faible force motrice) n'est pas tout à fait claire, et les facteurs d'influence doivent être étudiés. Par conséquent, pour régler les problèmes ci-dessus, cette thèse explore principalement les stratégies appropriées, les matériaux photovoltaïques, et les mesures.

## **Objectif de la thèse**

Selon les problèmes actuels susmentionnés dans le domaine des cellules solaires organiques, tels que la recherche d'un rendement plus élevé des dispositifs, la faible stabilité des performances des dispositifs et la séparation de charge controversée dans les dispositifs à base de non-fullerène, la thèse comprend principalement trois parties de recherche comme suit :

Partie I : Étude du mécanisme d'amélioration des performances photovoltaïques des cellules solaires à polymère par l'effet synergique d'additifs de solvants binaires (DIO et AA)

Comme on le sait, outre la conception de la structure des dispositifs et des couches d'interface, et la combinaison de nouveaux matériaux photovoltaïques avec une absorption de la lumière complémentaire, l'obtention de la morphologie idéale du film photoactif avec une séparation de phases et un réseau d'interpénétration appropriés est une autre stratégie importante pour améliorer l'efficacité des dispositifs photovoltaïques. Jusqu'à présent, il est difficile de prédire la morphologie optimisée, bien que de nombreuses méthodes aient été utilisées.<sup>33,38,143-144</sup> Parmi celles-ci, l'ingénierie des additifs aux solvants est

la méthode la plus simple et la plus efficace pour obtenir la morphologie idéale du film photovoltaïque. Cependant, la plupart des travaux se concentrent principalement sur l'effet de l'additif de solvant unique, sur l'efficacité du dispositif et quelques cas où l'additif de solvant binaire a amélioré l'efficacité du dispositif sont signalés.<sup>145-147</sup> De plus, le principe de l'additif de solvant binaire et la manière dont le composant unique de l'additif de solvant binaire affecte le dispositif ne sont pas clairs. Par conséquent, pour résoudre ce problème, un nouvel additif de solvant binaire (DIO et AA) est étudié, et le rôle du composant unique et le principe général de combinaison dans l'additif de solvant binaire sont étudiés en détail.

Partie II : Fabrication de cellules solaires organiques stables et traitées à l'air avec des performances plus élevées grâce à un matériau photovoltaïque stable à l'air (polymère PDPPPTD)

Au cours des dernières décennies, les travaux sur les cellules solaires organiques (CSO) ont principalement porté sur l'amélioration de l'efficacité des dispositifs. La plupart des fabrications de CSO sont effectuées dans une atmosphère inerte en raison de la sensibilité à l'air des matériaux organiques, qui n'est pas compatible avec les grands futurs procédés de fabrication. Bien que de nombreuses stratégies aient été explorées pour améliorer la stabilité des dispositifs photovoltaïques, telles que la structure inversée du dispositif, les matériaux d'interface stables et la modification de l'interface, les matériaux accepteurs plus stables et l'introduction du troisième composant.<sup>134-135,148-150</sup> Cependant, peu de recherches sur les donneurs de polymères stables à l'air sont signalées pour les dispositifs à haute stabilité. Ainsi, pour collaborer avec le groupe du professeur Mario Leclerc, le donneur de polymère PDPPPTD stable à l'air obtenu, des oxydes métalliques stables (ZnO) comme couche de transport d'électrons, et un additif solvant favorable (p-anisaldéhyde:AA) sont combinés pour obtenir un dispositif photovoltaïque à haut rendement et plus stable.

Partie III : Effet synergique de la propriété diélectrique et du transfert d'énergie sur la séparation des charges dans les cellules solaires sans plomb

Ces dernières années, grâce aux percées réalisées dans le domaine des matériaux accepteurs sans plomb, l'efficacité des dispositifs a été considérablement améliorée, et l'efficacité certifiée des dispositifs sans plomb a atteint plus de 17%.<sup>9</sup> Il est à noter que les caractéristiques remarquables des dispositifs à haut rendement sans plomb présentent une faible perte de tension et une séparation efficace des charges sous une faible force motrice.<sup>151</sup> Il est très différent des dispositifs traditionnels à base de dérivés du fullerène, pour lesquels une force d' entraînement suffisante (généralement >0.3 eV) est nécessaire pour la séparation des charges en raison de la faible propriété diélectrique des matériaux photovoltaïques organiques.<sup>152</sup> Bien que les recherches sur les facteurs dominants qui influencent la séparation efficace des charges des dispositifs à base de dérivés de fullerène à une force motrice faible avec une perte de tension réduite aient été menées, elles sont toujours contestées. D'après les processus physiques fondamentaux des dispositifs sans plomb, la diffusion efficace de l'exciton et les constantes diélectriques des films photovoltaïques sont

les paramètres physiques importants pour un processus efficace de séparation des charges. C'est pourquoi, en collaboration avec le groupe du professeur Maojie Zhang, les effets de la propriété diélectrique et du transfert d'énergie sur la séparation des charges dans les dispositifs à base de non-fullerène sont étudiés en détail.

Dans la première partie, un nouveau solvant binaire composé de DIO et d'AA a été exploré et utilisé dans les CSP, basé sur le donneur de polymère PffBT4T-2OD et l'accepteur PC<sub>61</sub>BM. Après avoir optimisé le rapport de concentration entre DIO et AA, l'efficacité du dispositif est passée de 9.11% à 10.64%, comme le montre la Figure R1. Le mécanisme correspondant a été sondé par la spectroscopie d'absorption optique, le GIXRD basé sur le synchrotron, le module AFM du DMT et le STEM. Comme le montre la Figure R2, Il a été constaté que l'AA améliorait principalement l'ordre du polymère PffBT4T-2OD avec une meilleure orientation de l'empilement et une cristallinité élevée. Différemment, l'IO pourrait faciliter la diffusion d'une plus grande quantité de PC<sub>61</sub>BM dans la matrice polymère. Ainsi, sur la base des différentes contributions de DIO et d'AA sur les films photoactifs, l'additif solvant binaire améliore encore l'ordre du polymère, maintient une cristallinité élevée et obtient une morphologie préférable du film photoactif (interfaces D-A plus efficaces), ce qui facilite un transport plus équilibré des porteurs de charge, et des probabilités plus élevées de dissociation des excitons et de collecte des charges comme le montre la Figure R3 et le Tableau R1, ce qui aboutit finalement à des CSP à haute performance. Le cas a introduit une nouvelle façon de concevoir un additif de solvant binaire avec des effets synergiques pour les CSP améliorés.

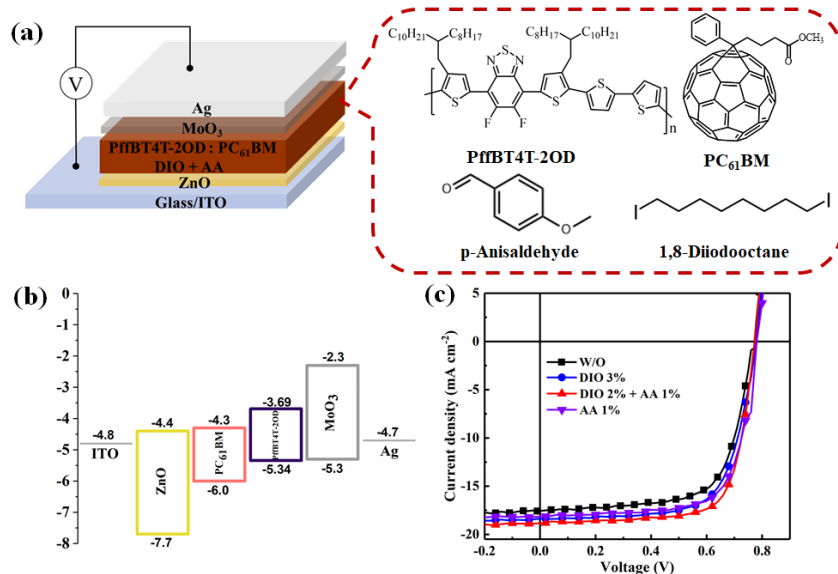


**Figure R1.** (a) Illustration schématique de l'architecture du dispositif inversé avec le film photoactif du PffBT4T-2OD:PC<sub>61</sub>BM, les structures moléculaires du PffBT4T-2OD, PC<sub>61</sub>BM, DIO et AA; (b) Diagramme du niveau d'énergie correspondant du dispositif, toutes les valeurs sont tirées des références; (c) Caractéristiques *J-V* des dispositifs PffBT4T-2OD:PC<sub>61</sub>BM avec/sans différents additifs de solvant (DIO 3 %, DIO 2 % + AA 1 %, et AA 1 %).

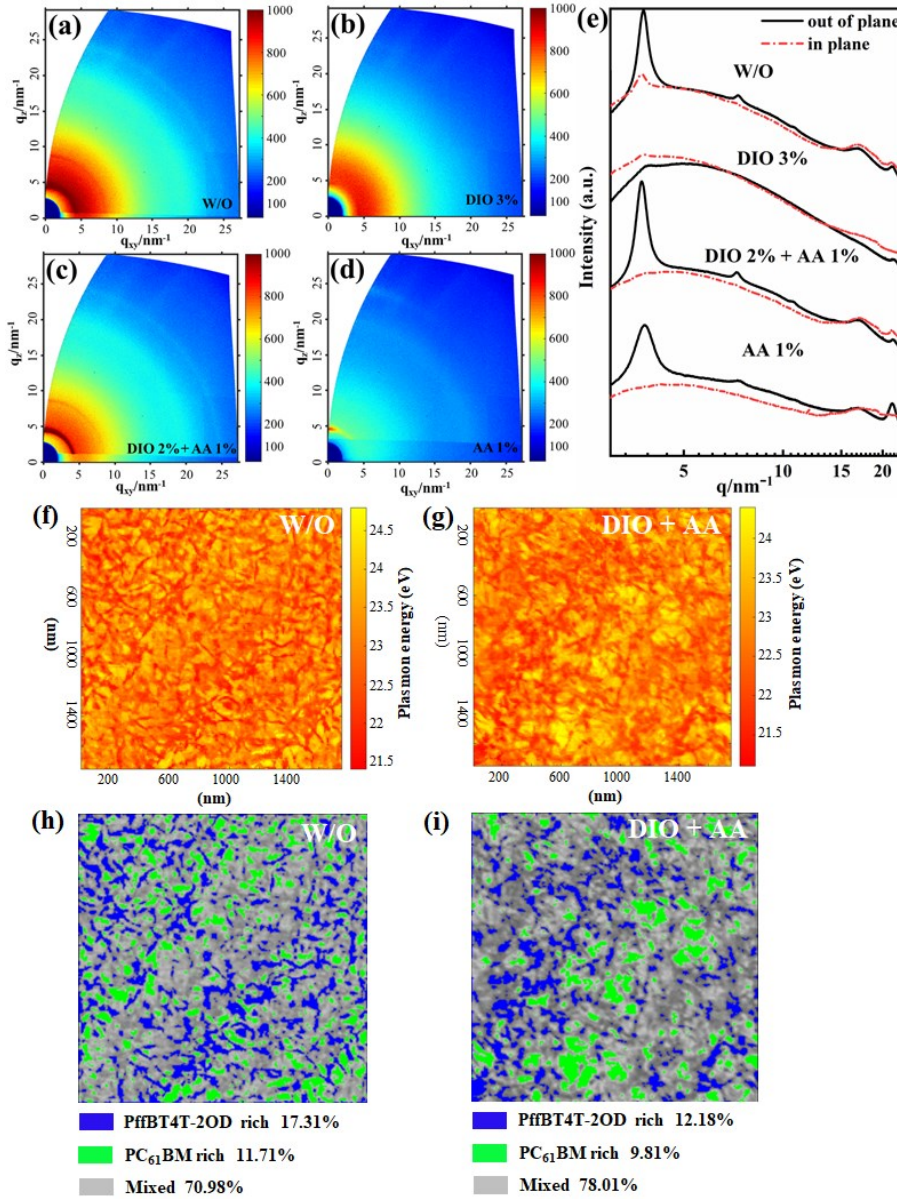


**Figure R2.** Motifs GIXRD 2D basés sur le synchrotron des films photoactifs PffBT4T-2OD:PC<sub>61</sub>BM avec/sans différents additifs de solvants : (a) W/O, (b) DIO 3%, (c) DIO 2% + AA 1%, et (d) AA 1%, respectivement; (e) Motifs GIXRD basés sur le synchrotron selon la géométrie de diffusion OOP et IP pour différents films photoactifs. Imagerie par déplacement d'énergie de plasma (PC<sub>61</sub>BM: 24.8 eV et PffBT4T-2OD: 21.4 eV) acquise en mode STEM des films photoactifs PffBT4T-2OD:PC<sub>61</sub>BM, (a) Sans additif de solvant, (b) Avec des additifs de solvant binaires (DIO 2% + AA 1%). (c) et (d) Segmentation de la cartographie de l'énergie plasmonique correspondante en domaines enrichis et mixtes, qui ont été obtenus à l'aide du logiciel ImageJ.

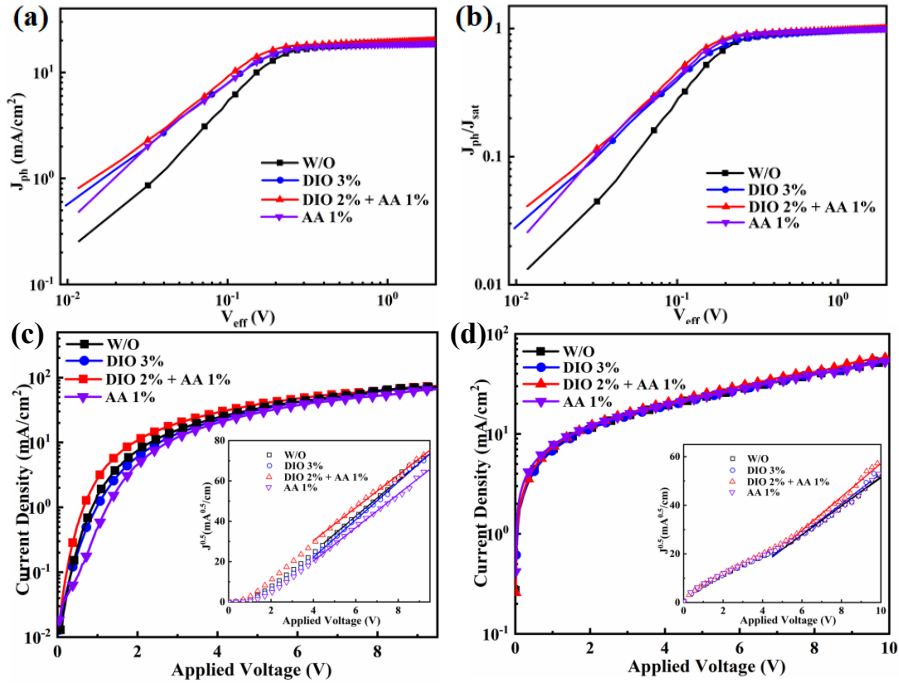


**Figure R3.** (a) Graphiques de  $J_{ph}$  par rapport à  $V_{eff}$  pour les dispositifs photovoltaïques avec/sans différents additifs de solvants (DIO 3%, DIO 2% + AA 1%, et AA 1%), (b) Graphiques correspondants de  $J_{ph}/J_{sat}$  par rapport à  $V_{eff}$  dans les dispositifs, (c) Caractéristiques  $JD-V$  des dispositifs à électrons seuls de ITO/ZnO/PffBT4T-2OD:PC<sub>61</sub>BM/LiF/Ag par le modèle SCLC, d) Caractéristiques  $Jd-V$  des dispositifs à trous seulement de ITO/PEDOT:PSS/PffBT4T-2OD:PC<sub>61</sub>BM/MoO<sub>3</sub>/Ag par le modèle SCLC. Les insets sont les caractéristiques  $J^{0.5}$ -V correspondantes pour les lignes de mobilité et d'appareillage des SCLC à porteuse unique.

**Tableau R1.** Valeurs calculées de la mobilité des électrons et des trous pour les dispositifs PffBT4T2OD : PC<sub>61</sub>BM sans ou avec différents additifs de solvants (DIO 3%, DIO 2% + AA 1%, AA 1%).

Solvent Additives	Electron mobility ( $\mu_e$ ) ( $\times 10^{-3} \text{ cm}^2 \text{ V}^{-1} \text{ s}^{-1}$ )	Hole mobility ( $\mu_h$ ) ( $\times 10^{-3} \text{ cm}^2 \text{ V}^{-1} \text{ s}^{-1}$ )	$\mu_e / \mu_h$
W/O	$5.84 \pm 0.26^a$	$2.50 \pm 0.48$	2.34
DIO 3%	$6.17 \pm 0.49$	$2.84 \pm 0.30$	2.17
DIO 2% + AA 1%	$5.27 \pm 0.18$	$3.17 \pm 0.38$	1.66
AA 1%	$5.16 \pm 0.57$	$2.50 \pm 0.42$	2.06

<sup>a</sup>Des valeurs moyennes sont obtenues dans quatre appareils.

Les résultats correspondants dans cette section sont publiés dans l'article suivante:

Pandeng Li, Yuliang Zhang, Ting Yu, Qingzhe Zhang, Jean-Philippe Masse, Yingguo Yang, Ricardo Izquierdo, Baoquan Sun, Dongling Ma, Unveiling Photovoltaic Performance Enhancement Mechanism of Polymer Solar Cells via Synergistic Effect of Binary Solvent Additives, *Sol. RRL* 2020, 2000239.

Dans la deuxième partie, nous avons combiné un nouveau polymère PDPPPTD à faible bande interdite et stable à l'air comme donneur et le PC<sub>61</sub>BM comme accepteur pour obtenir le dispositif photovoltaïque traité à l'air avec le PCE de 6.34% dans la Figure R4. Sans encapsulation ni modification de l'interface, la stabilité du dispositif dans différentes conditions ambiantes et les variations correspondantes de la morphologie des films photoactifs ont été vérifiées par diverses caractérisations, telles que la spectroscopie synchrotron GIXRD, AFM et FTIR. Comme le montre la Figure R5, les appareils traités à l'air non seulement présentaient une excellente stabilité thermique et une excellente photostabilité, mais aussi une stabilité supérieure dans l'atmosphère ambiante avec une humidité appropriée. L'utilisation de l'AA, un additif de solvant non toxique et sans iodé, a non seulement simplifié la fabrication des dispositifs et amélioré la reproductibilité des performances, mais également à amélioré la morphologie des films photoactifs, y compris les plus épais, ce qui a encore augmenté l'efficacité à 7.41% dans la Figure R6a, ce qui représente l'un des PCE les plus élevés des CSP traités à l'air et stables, y compris ceux fabriqués à l'aide du PC<sub>71</sub>BM plus coûteux. Un autre avantage important du traitement aux AA était l'amélioration de la stabilité du dispositif, comme le montre la Figure R6. Ce travail a suggéré que la conception de matériaux photovoltaïques stables à l'air était une tactique plus efficace pour les CSP traités à l'air et à haute performance.

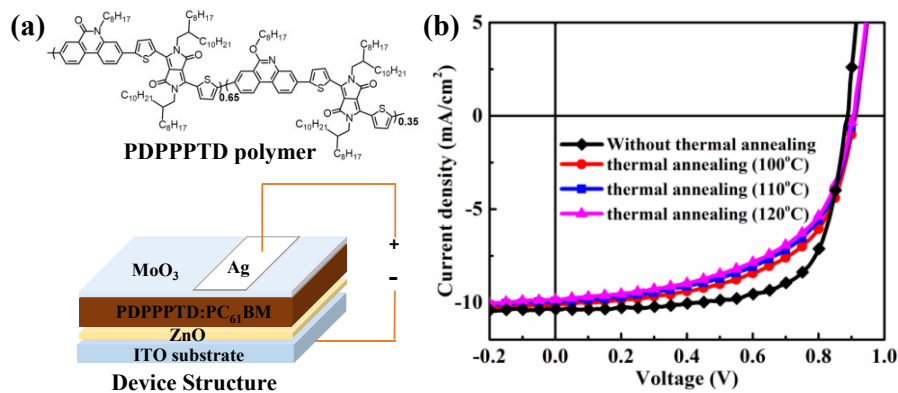


**Figure R4.** (a) Illustration de la structure du polymère PDPPPTD et de l'architecture des dispositifs de CSP inversés basés sur le film photoactif du PDPPPTD et du PC<sub>61</sub>BM, (b) Caractéristiques  $J$ - $V$  des dispositifs basés sur le film PDPPPTD/PC<sub>61</sub>BM non recuit et ceux subissant un recuit thermique à différentes températures sous irradiation AM 1.5G à 100 mW/cm<sup>2</sup> et dans l'obscurité.

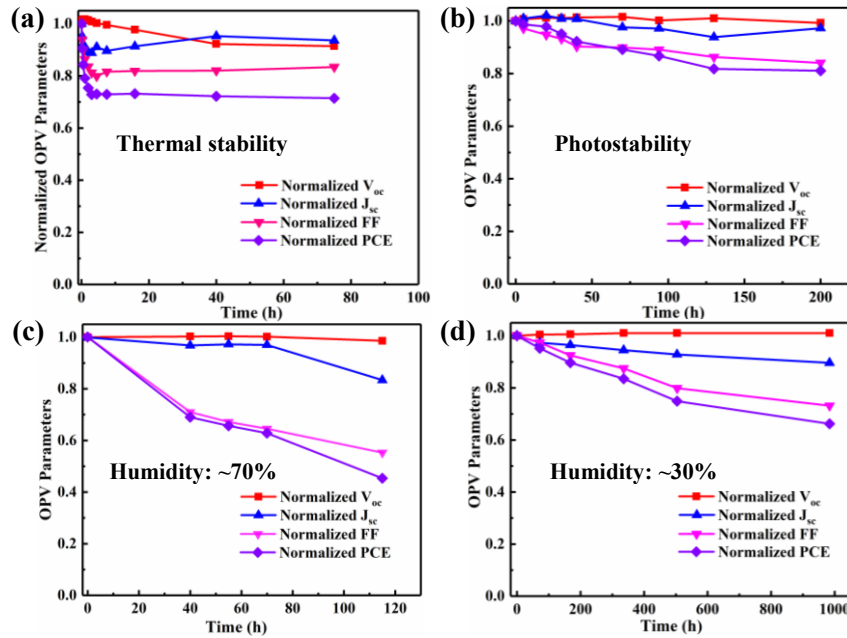


**Figure R5.** Stabilité des dispositifs PDPPPPTD/PC<sub>61</sub>BM (a) à 85 °C dans une boîte à gants, (b) Sous éclairage continu dans une boîte à gants, (c) Dans un air à forte humidité de 70% dans l'obscurité et (d) Dans un air à faible humidité de 30% dans l'obscurité.

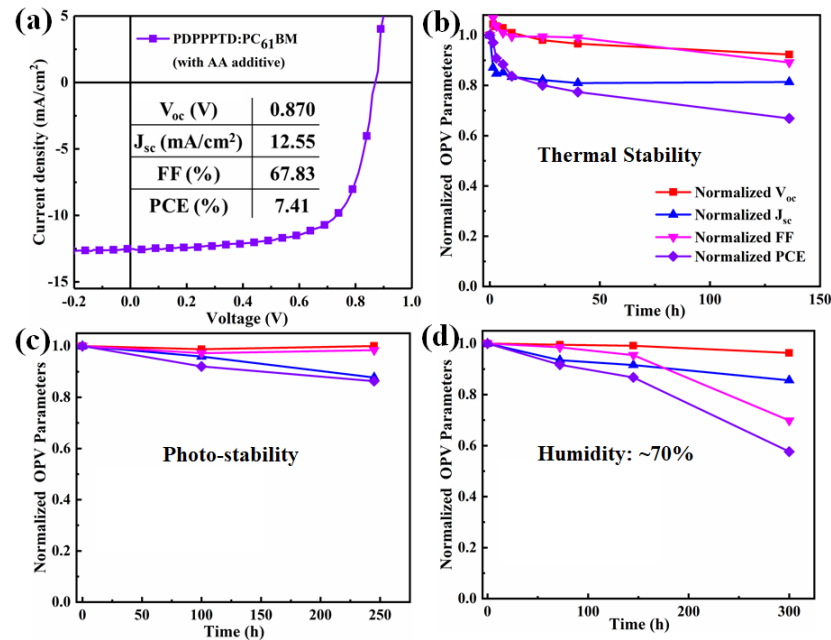


**Figure R6.** (a) Caractéristiques  $J$ - $V$  et paramètres photovoltaïques du meilleur dispositif, préparés en faisant intervenir l'AA comme additif, sous irradiation AM 1.5G à 100 mW/cm<sup>2</sup>. Mesures de stabilité des dispositifs PDPPPPTD/PC<sub>61</sub>BM après traitement additif avec AA: (b) à 85 °C dans une boîte à gants, (c) Sous éclairage continu dans une boîte à gants, (d) Dans un air à forte humidité de 70% dans l'obscurité.

Les résultats correspondants dans cette section sont publiés dans l'article suivante:

Pandeng Li, Mathieu Mainville, Yuliang Zhang, Mario Leclerc, Baoquan Sun, Ricardo Izquierdo, Dongling Ma, Air-Processed, Stable Organic Solar Cells with High Power Conversion Efficiency of 7.41%, *Small* 2019, 15, 1804671.

Dans la troisième partie, une nouvelle méthode a été mise au point pour sonder la variation des constantes diélectriques des dispositifs à base de non-fullerène, composés de PM6 comme donneur commun, et de ITIC, IT-4F, Y6 et IEICO comme matériaux accepteurs. Comme le montre la Figure R7, il a été constaté qu'à l'exception de l'IEICO, les accepteurs autres que le fullerène avaient des constantes diélectriques plus élevées que les dérivés du fullerène ( $PC_{61}BM$  et  $PC_{71}BM$ ) dans la gamme de fréquences de 100 Hz à ~MHz. Les films de mélange correspondants présentaient également des constantes diélectriques de mélange plus élevées, entraînant une recombinaison bimoléculaire réduite et une possibilité accrue de dissociation de charge avec de faibles pertes géminées. Les mesures de s-SNOM illustrées à la Figure R8 ont également confirmé la grande différence de constante diélectrique des films de mélange d'accepteurs autres que le fullerène et la constante diélectrique plus élevée des accepteurs autres que le fullerène dans la gamme des GHz, ce qui a conduit à une énergie de liaison des excitons plus faible et à une meilleure efficacité de dissociation des excitons. En outre, comme le montre la Figure R9, le chevauchement entre les spectres d'émission du donneur et les spectres d'absorption des accepteurs non producteurs de plein-lène apparentés, et la variation des spectres d'émission du donneur et des accepteurs non producteurs de plein-lène apparentés dans les films d'hétérojonction en vrac et les films d'hétérojonction bicouches suggèrent que le transfert d'énergie du donneur à l'accepteur pourrait se produire dans les dispositifs photovoltaïques non producteurs de plein-lène, ce qui étend la diffusion efficace de l'exciton pour des performances de dispositif préférables. Par conséquent, ces résultats interprètent bien les performances élevées du dispositif avec une force motrice minime. Sur la base de l'effet synergique de la propriété diélectrique et du transfert d'énergie plus élevés sur le processus de séparation/transfert de charge dans des dispositifs sélectionnés ne fonctionnant pas au fullerène, un autre mécanisme de travail photophysique intrinsèque de séparation/transfert de charge dans des dispositifs ne fonctionnant pas au fullerène a été présenté. En particulier, l'étendue de la contribution du transfert d'énergie à l'amélioration des performances photovoltaïques devra être étudiée plus en détail à l'avenir.

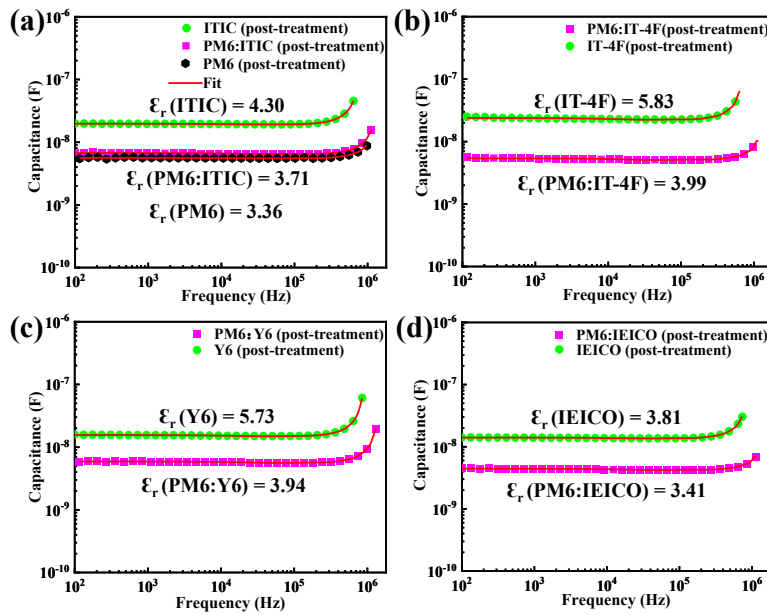


**Figure R7.** Graphiques de capacité en fonction de la fréquence pour (a) le film ITIC vierge et le film mélange PM6 et ITIC avec post-traitement, (b) le film IT-4F vierge et le film mélange PM6 et IT-4F avec post-traitement, (c) le film Y6 vierge et le film mélange PM6 et Y6 avec post-traitement, et (d) le film IEICO vierge et le film mélange PM6 et IEICO avec post-traitement. Les lignes rouges représentent les courbes d'ajustement simulées sur les données mesurées par fonction polynomiale.

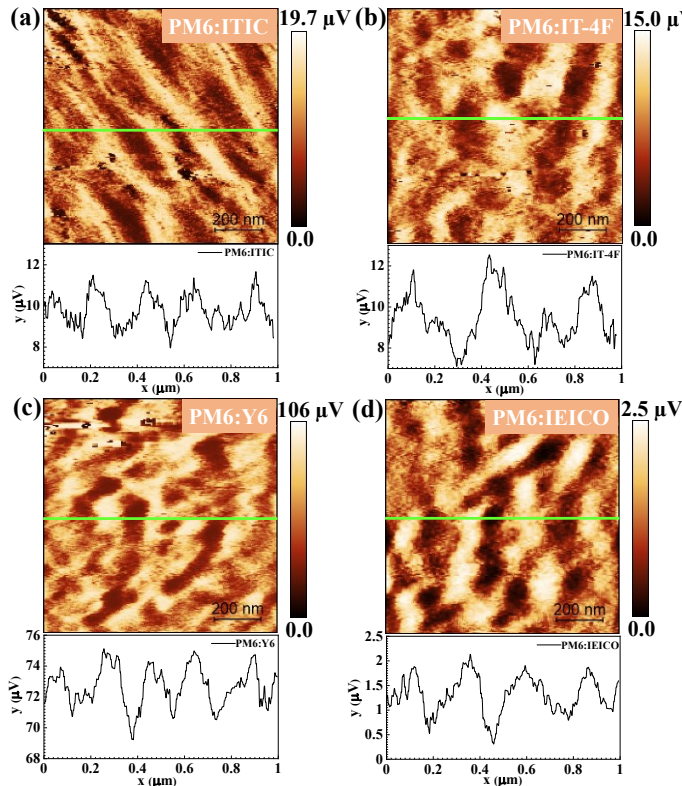


**Figure R8.** Images d'amplitude optique et profils de surface extraits correspondants de (d) film de mélange PM6 et ITIC avec post-traitement, (e) film de mélange PM6 et IT-4F avec post-traitement, (f) film de mélange PM6 et Y6 avec post-traitement, (g) film de mélange PM6 et IEICO avec post-traitement. Les images d'amplitude optique ont été dérivées du s-SNOM.

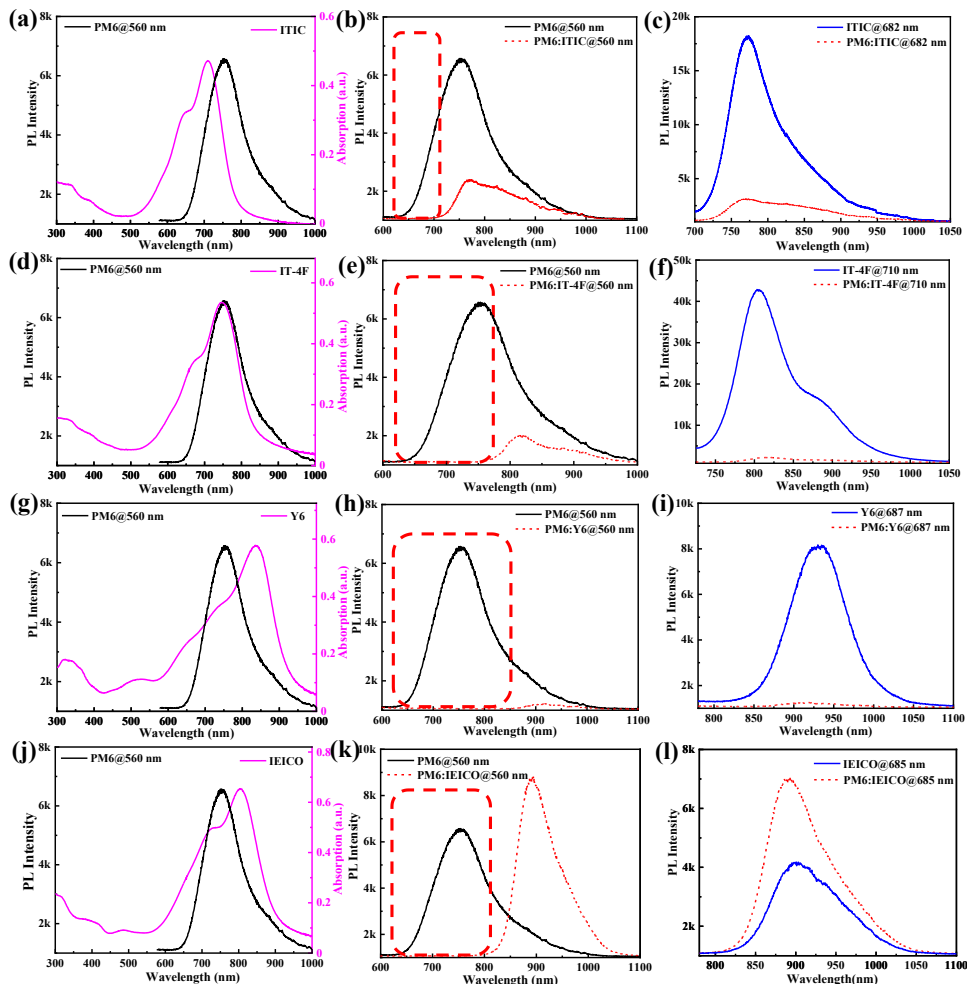


**Figure R9.** Spectres d'absorption et d'émission des donneurs de PM6 vierges, des accepteurs vierges et des films de mélange correspondants dans différentes combinaisons: (a)-(c) PM6: ITIC, (d)-(f) PM6:IT-4F, (g)-(i) PM6:Y6, et (j)-(l) PM6:IEICO (pompée à 560 nm pour la PM6 et les films de mélange correspondants, 682 nm pour l'ITIC et le film de mélange correspondant, 710 nm pour l'IT-4F et le film correspondant, 687 nm pour l'Y6 et le film correspondant, 685 nm pour l'IEICO et le film correspondant).

Ce travail est décrit dans l'article ci-dessous:

Pandeng Li, Jin Fang, Yusheng Wang, Sergei Manzhos, Lei Cai, Zheheng Song, Yajuan Li, Tao Song, Xuechun Wang, Xia Guo, Maojie Zhang, Dongling Ma, Baoquan Sun, Synergistic Effect of Dielectric Property and Energy Transfer on Charge Separation in Non-fullerene Based Solar Cells, *Angew. Chem. Int. Ed.* 2021, DOI: 10.1002/anie.202103357.